30

Accelerator-Based Neutron Brachytherapy

by

Haijun Song

B.S., Physics (1990)
University of Science and Technology of China

Submitted to the Department of Physics
in Partial Fulfillment of the Requirements for the Degree Of
Doctor of Philosophy in Physics

at the

Massachusetts Institute of Technology
September 1998

Signature of Author ....
Department of Physics
August 17, 1998

Certified by ....
Jacquelyn C. Yanch
Associate Professor of Nuclear Engineering
Thesis Supervisor

....
Lee Grodzins
Professor of Physics
Thesis Co-Supervisor

Accepted by ....
Professor Thomas J. Greytak
Associate Department Head for Education

Accelerator-Based Neutron Brachytherapy

by
Haijun Song

Submitted to the Department of Physics
on August 4, 1998 in partial fulfillment of the
requirements for the Degree of Doctor of Philosophy in
Physics

ABSTRACT

The feasibility of a new modality of radiation therapy, Accelerator-Based Neutron Brachytherapy (ABNBT), has been demonstrated through simulations and experimental work. The candidate nuclear reactions investigated are ^{9}Be(d,n)^{10}B, ^{9}Be(p,n)^{9}B, and ^{7}Li(p,n)^{7}Be, with charged particle beam energies of less than 4.1 MeV.

The focus of this work is the treatment of intracranial tumors which limits the diameter of the dose delivery needle tube to 6 mm. A prototype needle tube, a tube-in-tube design with cooling water running in between the inner and outer tubes to cool the beryllium target located at the tip of the inner tube, has been tested to a heat load near 150 Watts. The insertion length is 10 cm.

The dosimetric characteristics were simulated using the Monte Carlo code MCNP and the treatment times were then calculated for a given heat load. The simulations and calculations show that the fast neutron dose is the dominant dose component for all the candidate reactions. The ^{9}Be(d,n)^{10}B reaction at E_d=1.5 MeV is capable of delivering a therapeutic dose of 66 RBE.Gy to the boundary of a 4.5 cm diameter tumor in 7.3 minutes at a heat load of 150 Watts. The other two candidate reactions deliver a similar dose rate at the same heat load to the target at a beam energy near 4.0 MeV. However, they show higher potential for dose enhancement with the boron-10 neutron capture reaction due to their soft neutron spectra. For input into dosimetric simulations, the source gammas from a thick beryllium target bombarded by a 1.5 MeV deuteron beam were measured at 60° with a 76 mm x 76 mm NaI(Tl) detector. The prominent gammas range from 414 keV to 3.6 MeV.

Dose distributions in a water phantom were measured with the prototype needle tube using the dual-ion chamber technique for the ^{9}Be(d,n)^{10}B reaction at E_d=1.5 MeV. The measurements and simulations agree within uncertainties.

In conclusion this work has demonstrated the dosimetric desirability and the practical feasibility of ABNBT for the treatment of interstitial or intracavity tumors.

Thesis Supervisor:	Jacquelyn C. Yanch
Title:	Associate Professor of Nuclear Engineering
Thesis Co-Supervisor:	Lee Grodzins
Title:	Professor of Physics

ACKNOWLEDGEMENTS

I would like to thank my thesis supervisor, Professor Jacquelyn C. Yanch, for the opportunity to work on this project in the Laboratory for Accelerator Beam Applications (LABA), and for her insight, guidance, support, and patience.

I also want to express my appreciation to the members of my thesis committee, especially Professor Lee Grodzins and Professor Neil E. Todreas, for their advice and help.

Many thanks to Dr. Stephen G. Steadman for his advice and his agreeing to be a reader.

I regard it essential to have the collaboration with and advice from the members of Newton Scientific, Inc. I feel I have greatly benefited from working with Dr. Robert E. Klinkowstein. And special thanks go to him for his advice and help.

Dr. Richard Lanza has been accommodating through the course of the project. I want to thank him also for the helpful discussions with him.

I am also grateful to Peter Morley of MIT Machine Shop for his advice on machining designs and eagerness to help.

This work would not have been possible without the assistance of the other members of LABA. In particular, I would like to thank William Howard, Brandon Blackburn, and David Gierga for their help.

I am indebted to the MIT Reactor BNCT group for their help.

The people of the United States of America are one of the greatest peoples, who provide education to students all over the world. I am a beneficiary of that generosity.

Finally, I want to express my deepest appreciation to my family, Zhiming, Eric Weijie, and Edwin Weiwen, for their encouragement and trust.

Haijun Song

August 17, 1998

TABLE OF CONTENTS

ABSTRACT 2
ACKNOWLEDGEMENT 3
TABLE OF CONTENTS 4
LIST OF FIGURES 7
LIST OF TABLES 9

CHAPTER ONE INTRODUCTION 10
- 1.1. Accelerator-Based Neutron Brachytherapy 10
- 1.2. Methodology 11
- 1.3. Boron Neutron Capture Therapy 12
- 1.4. Other Tumor Sites 12

CHAPTER TWO GAMMA YIELD MEASUREMENT 15
- 2.1. Neutron Spectra Data 15
- 2.2. Gamma Yields Estimations 17
- 2.3. Gamma yield Measurement 19
  - 2.3.1. Beryllium Target Assembly and Beam Line 19
  - 2.3.2. Experimental Setup 19
  - 2.3.3. Target Current Integration 20
  - 2.3.4. Tuning of Electronics 20
  - 2.3.5. Energy Calibration 21
  - 2.3.6. Efficiency Calibration 21
  - 2.3.7. ^{9}Be(d,γ) Spectra 22
  - 2.3.8. Background between 3.5 and 5 MeV 24
- 2.4. Conclusions 25

CHAPTER THREE ION OPTICS 46
- 3.1. First Order Electric Cylindrical Lens 46
  - 3.1.1. Trajectory Equation of Ions in an Axially Symmetric Electrostatic Field 46
  - 3.1.2. First Order Approximation 47
  - 3.1.3. Optical Parameters 48
    - 3.1.3.a. Object and Image Planes. Linear and Angular Magnifications 48
    - 3.1.3.b. Focal Point and Focal Length 48
    - 3.1.3.c. The x Parameter and the Gaussian Relation 49
    - 3.1.3.d. Principal Plane 49
  - 3.1.4. Emittance 49
- 3.2. Transfer Matrix 50
  - 3.2.1. Drift Space 50
  - 3.2.2. Cylindrical Doublet and Triplet 50
  - 3.2.3. Acceleration Tube 50
  - 3.2.4. Magnetic Quadrupole 51
- 3.3. Beams and Profiles 53

3.3.1. Beam I 53
3.3.2. Beam II 54
3.3.3. Beam III 54

CHAPTER FOUR DOSE SIMULATIONS 66
4.1. Charged Particle Reactions 66
4.1.1. ^{7}Li(p,n)^{7}Be 66
4.1.2. ^{9}Be(p,n)^{9}B 67
4.1.3. ^{9}Be(d,n)^{10}B 68
4.2. Kerma 68
4.2.1. Kerma Factors 69
4.2.1.a. Neutron Kerma Factors 69
4.2.1.b. Photon Kerma Factors 70
4.2.1.c. ^{10}B Kerma Factors 70
4.2.2. MCNP's f6 Tally 71
4.3. RBE Values 71
4.4. Dosimetry Simulations 72
4.4.1. Dose Components 73
4.4.2. Boron Enhancement Ratio 74
4.4.3. Treatment Time 75
4.4.4. Kerma Factor vs. f6 Tally 75
4.4.5. Phantom Size Effect 75
4.5. Conclusions 76

CHAPTER FIVE PROTOTYPE I 94
5.1. Tissue Heating 94
5.2. Prototype I Design 95
5.3. Heat Removal Experiment 96
5.4. Applying to Lithium and Beryllium Target 96
5.5. Discussions and Conclusions 97

CHAPTER SIX PROTOTYPE II 105
6.1. Needle Tube Design 105
6.2. Target Design 105
6.3. Heat Removal Test on Copper Target 106
6.4. Heat Removal Test on Beryllium Target 107
6.5. Conclusions and Future Work 108

CHAPTER SEVEN DOSE MEASUREMENT 116
7.1. Experimental Setup 116
7.2. Dual Ion Chamber Method 116
7.3. Dose Measurement 118
7.4. Dose Simulation and Comparison with Measurements 119
7.5. Conclusions 121

CHAPTER EIGHT CONCLUSIONS AND FUTURE WORK 128

REFERENCES 130

APPENDIX A. C Code for Calculating the Double Differential Neutron Yield Spectra for the ^{7}Li(p,n) and ^{7}Li(p,n′) Reactions and Generating the SDEF for the MCNP Input File 135

APPENDIX B. The MCNP Input File for the ^{9}Be(d,n) Reaction at E_d=1.5 MeV 149

APPENDIX C. Algorithm for Operating the Angular Tilter 153

APPENDIX D. Heat Transfer Analysis 156

APPENDIX E. Dependence of the Effective Center of a Dosimeter on the Gradient of a Radiation Field 166

LIST OF FIGURES

Figure 1.1. Schematic illustration of ABNBT for brain tumors 13
Figure 1.2. Flow chart of investigating ABNBT. 14

Figure 2.1.a. Angle integrated neutron spectrum for ^{9}Be(d,n)at E_d=1.4 MeV. 31
Figure 2.1.b. Shifting ^{9}Be(d,n) at E_d=1.4 MeV to estimate E_d=1.5 MeV spectrum. 32
Figure 2.1.c. Estimated ^{9}Be(d,n) at E_d=1.5 MeV spectrum. 33
Figure 2.1.d. Spectrum of ^{9}Be(d,n) at E_d=1.5 MeV and at 0° by Guzek *et al.,*(1996). 34
Figure 2 2. Decay scheme of ^{10}B, Γ_γ/Γ ,and ^{9}Be(d,n')^{10}B* at E_d=1.5 MeV branching ratios. 35
Figure 2.3. Decay scheme of ^{10}Be and relative (^{9}Be+d-n) levels. 36
Figure 2.4.a. Needle tube Prototype II. The outer and inner tubes. 37
Figure 2.4.b. The Be target and positions of the two thermocouples. 38
Figure 2.5. Schematic of the gamma yield measurement setup. 39
Figure 2.6. Schematic of LogAMP. 40
Figure 2.7. Diagram of electroincs for the gamma yield measurements. 41
Figure 2.8. Diagram of a charge-sensitive mode PreAMP. 42
Figure 2.9. Energy calibration of NaI(Tl) detector with Co-60 and Cs-137. 43
Figure 2.10. The intrinsic peak efficiency of the 76 mm x 76 mm NaI(Tl) detector. 44
Figure 2.11. Spectra of gammas from 1.5 MeV deuterons hitting a thick Be target. 45

Figure 3.1. Illustration of the optical parameters. 57
Figure 3.2. Illustration of the emittance ellipse and waist condition. 57
Figure 3.3. Illustration of cylindrical triplet lens. 58
Figure 3.4. Illustration of acceleration tube. 58
Figure 3.5. The field of the magnetic quadrupole lens. 59
Figure 3.6. Optical components of the tandem electrostatic accelerator at LABA. 60
Figure 3.7. The beam line before installation of the switching magnet. 61
Figure 3.8. Envelopes of Beam I under different conditions. 62
Figure 3.9. The beam line (final version). 63
Figure 3.10. Envelopes of Beam II under different conditions. 64
Figure 3.11. Envelopes of Beam III under different conditions. 65

Figure 4.1. Double differential neutron spectra for ^{7}Li(p,n) and ^{7}Li(p,n') at E_p=4.1 MeV calculated from cross section data. 81
Figure 4.2. Neutron angular distributions for ^{7}Li(p,n) and ^{7}Li(p,n') at E_p=4.1 MeV. 82
Figure 4.3.a. Dose components and distributions for ^{7}Li(p,n) at E_p=4.1 MeV. 83
Figure 4.3.b. Dose components and distributions for ^{7}Li(p,n) at E_p=3.0 MeV. 84
Figure 4.3.c. Dose components and distributions for ^{7}Li(p,n) at E_p=2.5 MeV. 85
Figure 4.3.d. Dose components and distributions for ^{7}Li(p,n) at E_p=2.0 MeV. 86
Figure 4.3.e. Dose components and distributions for ^{9}Be(d,n) at E_d=1.5 MeV. 87
Figure 4.3.f. Dose components and distributions for ^{9}Be(p,n) at E_d=4.0 MeV. 88
Figure 4.3.g. Dose components and distributions for ^{9}Be(p,n) at E_d=3.7 MeV. 89

Figure 4.4.a. Boron Enhancement Ratio. 90
Figure 4.4.b. A close-up at small radius of Figure 4.4.a. 91
Figure 4.5. Treatment time vs. tumor radius. 92
Figure 4.6. The effect of phantom size on dose distribution. 93

Figure 5.1.a. Drawing of the needle tube Prototype I. 99
Figure 5.1.b. Picture of Prototype I being assembled. 100
Figure 5.2. Tip portion of Prototype I. 101
Figure 5.3.a. Picture of Prototype I with adjustment step motors. Side view. 102
Figure 5.3.b. Front view of Figure 5.3.a. 103
Figure 5.4. Target temperature measurements vs. heat load on target of Prototype I.. 104

Figure 6.1.a. Needle tube Prototype II. The base pieces. 110
Figure 6.1.b. Prototype II. The inner and outer tubes. 111
Figure 6.2.a. Picture of Prototype II. 112
Figure 6.2.b. Picture of Prototype II with outer tube taken apart. 113
Figure 6.3. Details of the tube-shaped target of Prototype II. 114
Figure 6.4. Temperature measurements on target of Prototype II vs. heat load. 115

Figure 7.1.a. Setup of dose measurement for ^{9}Be(d,n) E_d=1.5 MeV. 123
Figure 7.1.b. Illustration of matrix of points of dose measurements. 124
Figure 7.2. Neutron to gamma sensitivity ratio of TE ion chamber vs. neutron energy. 125
Figure 7.3.a. Measurement of photon dose distribution and comparison with simulation. 126
Figure 7.3.b. Measurement of neutron dose distribution and comparison with simulation. 127

Figure C.1. Demonstration of operating the angular tilter. 155

Figure D.1. A simple heat transfer system. 162
Figure D.2. Tip portion of Prototype I. Symbols and parameters for heat transfer analysis. 163
Figure D.3. Estimate of target-water surface temperature of Prototype I. 164
Figure D.4. Target of Prototype II. Symbols for heat transfer analysis. 165

Figure E.1. Illustration of dependence of effective center of dosimeter on radiation gradient. 167

LIST OF TABLES

Table 2.1. Maximum and minimum neutron energies from ^{9}Be(d,n′) reaction channels at E_d=1.4 and 1.5 MeV. 26
Table 2.2. Prediction of intensities of cascade gammas from ^{9}Be(d,n′) reactions. 26
Table 2.3. Intrinsic (gamma) peak efficiency of a 3"x3" Na(Tl) detector. 27
Table 2.4. Summary of NaI(Tl) efficiency measurement experiments. 28
Table 2.5. Measurements vs. predictions of gammas from ^{9}Be(d,γ). 29
Table 2.6. Summary of yields of prominent gammas from ^{9}Be(d,γ) at E_d=1.5 MeV. 30

Table 3.1. Envelope of last 10 inch of Beam I. 55
Table 3.2. Envelope of last 10 inch of Beam II. 55
Table 3.3. Envelope of last 10 inch of Beam II. 56

Table 4.1. Summary of neutron and gamma yields for the candidate reactions. 77
Table 4.2. Kerma factors for brain equivalent tissue. 78
Table 4.3. Kerma factors for photon. 79
Table 4.4. Kerma factors for 1 ppm of boron-10. 79
Table 4.5. Treatment times for a 4.5 cm diameter tumor under 100 Watts of heat load on the target. 80

Table 5.1. Treatment times for a 4.5 cm diameter tumor with Prototype I. 98

Table 6.1. Treatment times for a 4.5 cm diameter tumor with Prototype II. 109

Table 7.1. Measured neutron and photon dose distributions in a water phantom for ^{9}Be(d,n) at E_d=1.5 MeV. 122

CHAPTER ONE
INTRODUCTION

1.1. ACCELERATOR-BASED NEUTRON BRACHYTHERAPY

The proposed Accelerator-Based Neutron Brachytherapy (ABNBT) modality involves the interstitial or intracavity insertion of a narrow, evacuated, and needle-shaped tube with a neutron-producing target at the tip such that neutron radiation is generated within the tumor when the neutron-producing target is hit by a charged particle accelerator beam. The present work focuses on intracranial insertion, which is more restrictive on tube diameter than other tumor sites and hence more technically challenging. A schematic setup for intracranial insertion is drawn in Figure 1.1. Implementation of this therapy would require a sophisticated gantry system that allows freedom of positioning the therapy tube within the patient.

The potential of ABNBT was first proposed by Crawford, (1992) with the candidate nuclear reaction ^{7}Li(p,n)^{7}Be. There have been intermediate works on the development of ABNBT (Song *et al.,* 1996-1998). The present work concludes the feasibility studies of ABNBT through simulating the dose profiles for the candidate reactions (with the ^{9}Be(p,n)^{9}B and ^{9}Be(d,n)^{10}B reactions added), designing, constructing and testing prototypes of the therapy needle tube, and measuring the dose profile in a water phantom with a prototype for the ^{9}Be(d,n)^{10}B reaction at E_d=1.5 MeV and comparing with the simulations.

ABNBT has its roots in neutron brachytherapy using the neutron-emitting isotope ^{252}Cf (CfNBT). CfNBT has been used in treating bulky localized tumors for a few hundred patients since the1970s in the University of Kentucky Medical Center (UKMC). Maruyama, (1984) gives a review of CfNBT in UKMC till the year 1984. About 20 different tumor sites were treated. Cervical cancer constitutes more than half of the total cases. A few other tumor sites are listed here in the order of number of cases: uterus, brain, vagina, tonsil-oropharynx, etc. Maruyama *et al.*, (1991) reviews the treatment of cervical cancer to the year 1991. Chin *et al.*, (1991) reports that 85 patients with a diagnosis of malignant glioma have been treated with CfNBT. The results are encouraging due to the physical and radiobiological advantages of CfNBT. First, compared with external radiation, the tumor to healthy tissue dose ratio is large as a result of the r^{-2} fall off in dose from the source. Second, under-vascularized and under-oxygenated brain tumors are resistant to conventional photon radiation. This is where neutron radiation could play its role. It has high Linear Energy Transfer (LET) and hence high Relative Biological Effectiveness (RBE) and low Oxygen Enhancement Ratio (OER), and still maintains a large range similar to photon radiation. Third, tumor dose enhancement via neutron capture therapies is possible with neutrons but not with photon therapy. Maruyama, (1984) and Maruyama, (1991) provide comprehensive coverage of the radiobiology of CfNBT.

Accelerator-based NBT has further advantages over use of an isotope source. Neutron production can be turned off when not required, thereby avoiding the extensive shielding needed for storage and transport of ^{252}Cf sources. Also an accelerator source shows no loss in neutron production over time while ^{252}Cf decays with a half life of 2.5 years. Lastly, a variety of initial neutron spectra are available from accelerator-based nuclear reactions so that the neutron spectrum can be optimized for a given medical situation. This would provide the possibility of tailoring the beam energy for a particular tumor size or enhancing tumor dose by combining fast neutron therapy with Boron Neutron Capture Therapy (BNCT). In BNCT, the tumor is selectively loaded with a higher concentration of ^{10}B than healthy tissue and receives a high RBE dose from the thermal neutron capture reaction ^{10}B(n, α)^{7}Li. Hence, the advantage of combining ABNBT with BNCT is better exploited with a softer initial neutron spectrum and/or at a further distance from the neutron source so that more neutrons can be thermalized. Coupling with BNCT was proposed for CfNBT by Wierzbicki *et al.*, (1991). Investigation by Yanch and Zamenhof, (1992) shows that a maximum increase in tumor dose of 18% as a result of a 50 ppm boron concentration for CfNBT is possible. For ABNBT, 40 ppm boron can increase tumor dose by 150% for the optimum situation, as will be discussed in detail in Chapter Four.

The concept of inserting a needle tube through the skull for treatment of brain tumors is not novel. An accelerator-based x-ray source for interstitial radiosurgery (Photon Radiosurgery System (PRS), Photoelectron Corporation, Lexington, MA) (Dinsmore *et al.*, (1996)) was recently approved for treatment of intracranial tumors by the Food and Drug Administration. It uses a 40 keV electron beam to generate x-ray radiation from a gold target within the brain tumor. Due to its small size, the accelerator plus tube configuration is mounted directly onto a stereotactic frame. For ABNBT, a gantry system will be required to position the needle tube within the patient. However, while the PRS is useful for treating small tumors due to the limited range of the low energy x-rays, the neutron probe described here will be most useful in the treatment of considerably larger tumors.

1.2. METHODOLOGY

The tools of the investigation of ABNBT described here are Monte Carlo simulation and experiments, as shown in Figure 1.2.

The Monte Carlo code MCNP was used to simulate absorbed dose profiles in a tissue-equivalent phantom, using the source neutron and source gamma spectra as input. Methodology and results are provided in Chapter Four. The candidate nuclear reactions, ^{7}Li(p,n)^{7}Be, ^{9}Be(p,n)^{9}B, and ^{9}Be(d,n)^{10}B were chosen for their high neutron yields at low accelerator beam energies. The source neutron and source gamma yields were evaluated from published data except the ^{9}Be(d,n)^{10}B reaction, for which the source gamma yields were not known and were measured in the present work at a deuteron energy of 1.5 MeV (Chapter Two).

Tissue heating due to the heat load generated on the target by the incident accelerator beam was identified in preliminary assessments, and active cooling of the target was determined necessary. The focus of the present work is on the treatment of intracranial tumors, which limits the diameter of the dose delivery needle tube to a size compatible with intracranial insertion (6 mm). This imposes a major barrier on the heat removal capability of the target and hence on the delivery of a high dose rate. As a first test of the feasibility of ABNBT, the dosimetric characteristics were simulated with MCNP; the treatment times were then calculated for a given heat load, and two prototypes of the dose delivering needle tube with active cooling were designed to realistic dimensions for an intracranial insertion and constructed to test the heat removal capabilities. The dose rate achievable with Prototype I is not desirable (Chapter Five) although it could be useful for other tumor sites which are not as restrictive on the diameter of the needle tube as brain tumors. Prototype II improves upon Prototype I and is capable of delivering a therapeutic dose to a tumor of a few centimeters in diameter in only a few minutes (Chapter Six). Prototype II is also suitable for insertion into a phantom with an insertion length of 10 cm. The $^{9}Be(d,n)^{10}B$ reaction was then chosen to perform dose measurements in a water phantom using the dual-ion chamber methods. The comparison with dose simulations using MCNP was made (Chapter Seven).

Control of the accelerator beam and construction of beam lines are essential for the experiments in the present work. Chapter Three is devoted to a review of the ion optical elements used in the beam lines. The profiles of the beams used in the experiments were simulated.

1.3. BORON NEUTRON CAPTURE THERAPY

Boron Neutron Capture Therapy (BNCT) is a potential treatment of the disease Glioblastoma Multiforme (GBM). The basic mechanism is to deliver dose through the thermal neutron capture reaction $^{10}B(n, \alpha)^{7}Li$, which has a high cross section of 3838 barn and releases 2.4 MeV energy through the two product heavy ions, α and ^{7}Li. (For comparison, the thermal neutron capture reaction cross section for the most abundant element of human body, H, is 0.333 barn.) The success of BNCT depends on two key elements that have to work together: neutronics and selective drug delivery. There needs to be, at the site of the tumor, enough thermal neutrons and a sufficient ^{10}B concentration with such selectivity that healthy tissue is spared. BNCT clinical trials are now in the feasibility and safety study stage (Chadha *et al.*, (1997)).

1.4. OTHER TUMOR SITES

The present work has its focus on treating brain tumors, for which the size of the insertion tube is most restricted (6 mm in diameter chosen for the present work). For other tumor sites, e.g., cervical cancers and nasopharyngeal cancers, the tube diameter can be increased. As a result, heat removal from the target will be simpler and the therapy tube design will be correspondingly easier than the ones designed in this thesis.

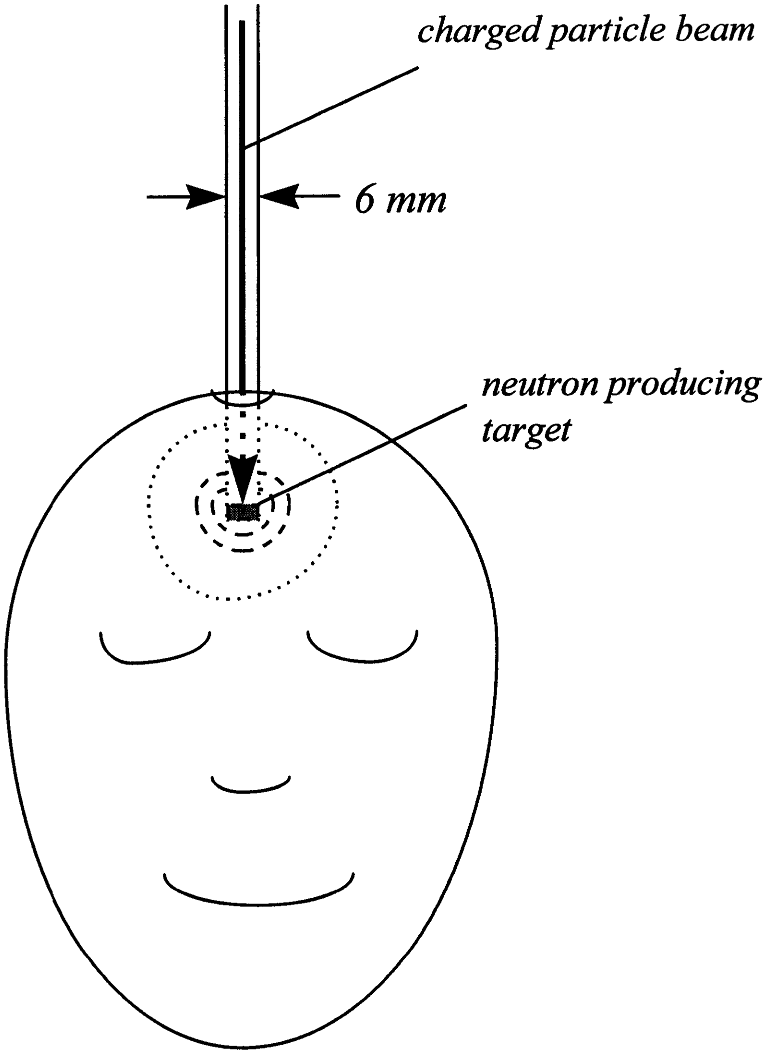

Figure 1.1. Schematic illustration of Accelerator-Based Neutron Brachytherapy (ABNBT) for brain tumors.

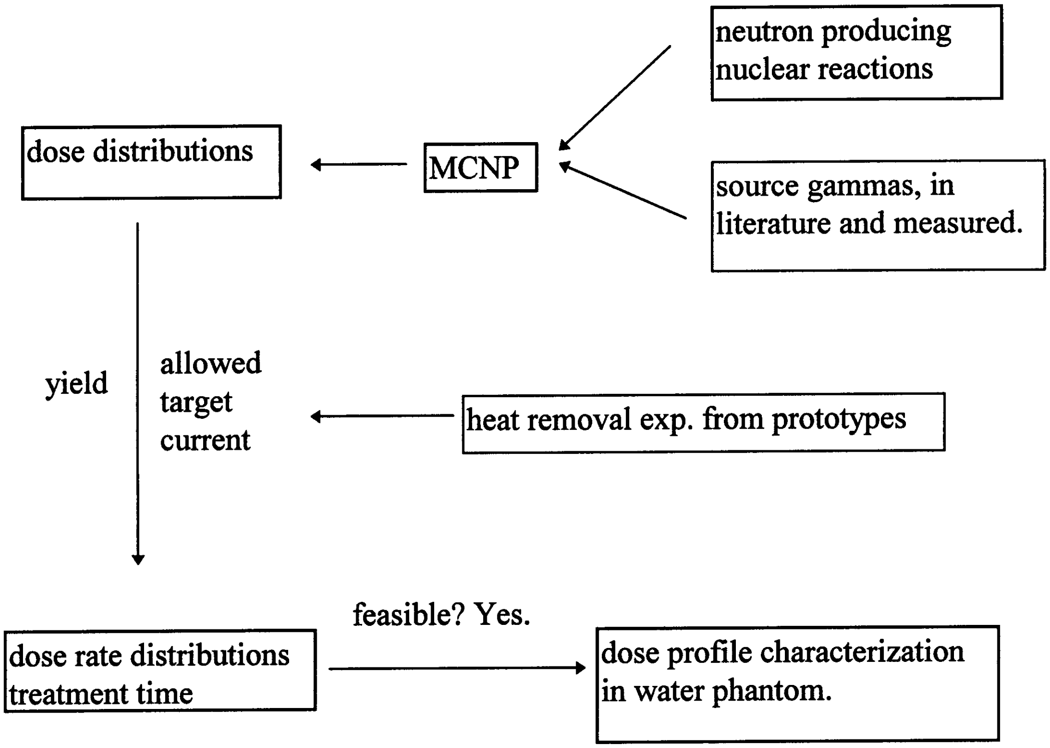

Figure 1.2. Flow chart of investigating ABNBT.

CHAPTER TWO
GAMMA YIELD MEASUREMENT

The nuclear reaction $^{9}Be(d,n)^{10}B$ at E_d=1.5 MeV is one of the most practical candidate reactions for Accelerator-Based Neutron Brachytherapy (ABNBT), as will be discussed in the following chapters. The yields of gammas from this reaction have not been directly measured, although the neutron spectrum and the nuclear structure of the nuclides involved suggest that gamma production could be abundant. To simulate the dose profile and compare it with dose measurement in a water phantom, the gamma yields are needed. So experiments were carried out with a NaI(Tl) (76 mm diameter x 76 mm) detector to measure the gamma yields.

2.1. NEUTRON SPECTRA DATA

The neutron spectrum provides a way of estimating the gamma yields per neutron from the $^{9}Be(d,n'\gamma)^{10}B^*$ reactions, which will be discussed in Section 2.2. This section gives an introduction and interpretation of the neutron spectrum data from different authors.

The nuclear reaction $^{9}Be(d,n)^{10}B$ has a positive Q value of 4.63 MeV. Interest in the $^{9}Be(d,n)$ reaction below 2 MeV deuteron energy results from the dose simulations in Chapter Four, which show that, at deuteron energies around 1.5 MeV, the dose rate is comparable with or better than that from the other two neutron prolific reactions Li(p,n) and Be(p,n) at a proton energy of 4.0 MeV. In terms of accelerator technology, 1.5 MeV is a great simplification over 4.0 MeV.

In the deuteron energy range of 1.4-2.8 MeV, there are three groups who have measured the neutron spectrum from the $^{9}Be(d,n)^{10}B$ reaction: Inada *et al.*, (1968), Whittlestone, (1977), and Guzek *et al.*, (1996). Both Inada and Whittlestone measured the spectra at E_d=1.4, 1.8, 2.3, and 2.8 MeV at angles of 0°, 30°, 45°, 60°, 90°, 120°, and 150°. The angle integrated spectrum for the E_d=1.4 MeV from Whittlestone, (1977) is read off the published curve and plotted in Figure 2.1.a. The spectrum is read in a neutron energy interval of 1/8 MeV except the first point which is 0.075 MeV, the experimental cut-off energy. The second data point is 0.25 (2/8) MeV and the third is 0.375 (3/8) MeV, etc. The neutron yields integrated (in this work) with the first two data points as the cut-off energies are:

$$Y_{En>0.075} = 5.5\ [\pm 7\%] \times 10^{8}\ n/\mu C \text{ for } E_n > 0.075 \text{ MeV}, E_d=1.4 \text{ MeV},$$

$$Y_{En>0.25} = 4.6\ [\pm 6\%] \times 10^{8}\ n/\mu C \text{ for } E_n > 0.25 \text{ MeV}, E_d=1.4 \text{ MeV}.$$

The errors are assigned as follows. Since they decrease with number of data points in summation, relative statistical errors in the neutron spectrum do not contribute to the errors in the integrated yields. The Whittlestone spectrum gives the sources of systematic errors (relative) as the following: 1) detector efficiency error, 5%; 2) spectrum normalization error, 3%; and 3) error from subtraction of background, significant only for E_n<0.2 MeV. An example of error 3) is given as 25% at E_n=0.1 MeV. Due to lack of details about error

3), a constant error of 25% is assumed for $0.25>E_n>0.075$ MeV in the present work and zero for $E_n>0.25$ MeV. For each of the three systematic errors, the linear sum of the absolute errors of all the data points is the corresponding absolute error for the neutron yield. As a result, the relative errors for the neutron yields are: 1) detector efficiency error, 5%; 2) normalization error, 3%; and 3) error from subtraction of background, 4% for $Y_{En>0.075}$ and 0% for $Y_{En>0.25}$. The binning uncertainty of the integration process is 2%. The total error of the integrated neutron yield is square root of the sum of the above four errors squared. The results are 6.2% for $Y_{En>0.25}$ and 7.3% for $Y_{En>0.075}$.

The total neutron yields, obtained by extrapolation to zero neutron threshold energy (8 keV, see Section 2.2 and Table 2.1), are (Whittlestone, (1977)):

$Y_{total} = 7.5 \times 10^8$ n/μC, E_d=1.4 MeV,

$Y_{total} = 8.0 \times 10^8$ n/μC, E_d=1.5 MeV.

These are in agreement with Inada *et al.*, (1968). However, integration of the Guzek spectrum gives the neutron yield above 0.25 MeV as:

$Y_{En>0.25} = 1.5 \times 10^9$ n/μC, E_d=1.5, (Guzek *et al.*, (1996)),

which almost doubles the total yield from Whittlestone. One possibility is that the Guzek spectrum is not their final version with efficiency calibration, so that the spectrum may have the correct shape but be off by scaling factors. (The spectrum for the Be(d,n) reaction at E_d=1.5 MeV was mentioned as have been measured in Guzek *et al.*, (1996) but not published. It was later relayed to us through second-hand private communication. For comparison, the Guzek spectrum at E_d=1.5 MeV and 0° is shown in Figure 2.1.d.)

Burrill, (1964) gives compiled total neutron yields but no information on neutron spectra for a variety of neutron producing reactions including the ^{9}Be(d,n)^{10}B reaction. The total neutron yield given is

$Y_{total} = 4.0 \times 10^8$ n/μC at E_d=1.5 MeV (Burrill, (1964)),

which is only half the value by Whittlestone, (1977) and Inada *et al.*, (1968). The Whittlestone, (1977) and Inada *et al.*, (1968) are deemed the most reliable due to the following reasons. First, their estimates of the total neutron yields agree with each other and their spectra show similar shapes. Second, there is a doubt about the efficiency calibration of the spectrum by Guzek *et al.*, (1996). Third, the data by Burrill, (1964) are based on measurements before 1964 and no neutron spectrum is given. Between Whittlestone, (1977) and Inada *et al.*, (1968), the Whittlestone spectrum data are more recent and will be used for the ABNBT studies in this thesis.

Before this decision to use the Whittlestone spectrum was made, the dose measurement in a water phantom (Chapter Seven) and gamma yield measurement (this chapter) had been done for the deuteron energy of 1.5 MeV due to the availability of the Guzek E_d=1.5 MeV neutron spectrum. To compare with the experimental work, the spectrum at E_d=1.5 MeV is needed. Therefore, an attempt was made to estimate the neutron spectrum for E_d=1.5 MeV from the Whittlestone E_d=1.4 MeV spectrum, as shown below.

The difference between the spectra for E_d=1.4 MeV and 1.5 MeV lies only in the high energy end of the spectrum for each neutron group. As discussed in Section 2.2 and shown in Table 2.1, the maximum neutron energy for each neutron group shifts by 0.1 MeV. A simplified estimation is to extend the high neutron energy end by 0.1 MeV for each neutron group, as illustrated by the dashed lines in Figure 2.1.b. Another step of simplification leads to simply shifting up the whole E_d=1.4 MeV spectrum by 0.1 MeV while holding the data point of the lowest neutron energy (0.075 MeV) the same for both spectra. The estimated spectrum for the E_d=1.5 MeV is shown in Figure 2.1.c. After the shifting, the first few data points on the E_d=1.5 MeV spectrum are 0.075, 0.35 (2/8+0.1), 0.475 (3/8+0.1) MeV, etc. The neutron yields with the first two data points as the energy cut-offs are:

$Y_{En>0.075} = 6.0\ [\pm 10\%]\ \times 10^8$ n/μC for E_n >0.075 MeV, E_d=1.5 MeV,

$Y_{En>0.35} = 4.6\ [\pm 9\%] \times 10^8$ n/μC for E_n >0.35 MeV, E_d=1.5 MeV.

The error resulting from the spectrum shifting is not known but should be less than the difference (6%) between the total neutron yields at neutron energies of 1.4 and 1.5 MeV as given by Whittlestone, (1977). In the neutron yields with cut-off energies as shown above, the errors are given as the sum of the errors for the E_d=1.4 MeV and half of the 6%. The real errors may be smaller. The errors given here are upper limits.

The neutron yield with a neutron energy cut-off of 0.1 MeV will be needed in Chapter Seven and is estimated as

$Y_{En>0.10} = 5.7\ [\pm 10\%]\ \times 10^8$ n/μC for E_n >0.1 MeV, E_d=1.5 MeV.

The error is the same as that of $Y_{En>0.075}$.

2.2. GAMMA YIELDS ESTIMATIONS

The ^{9}Be(d,n'γ)^{10}B* reaction occurs through many channels leading to different excited states of the product nuclide ^{10}B. The energy levels and the decay schemes of ^{10}B (Ajzenberg, (1979)) are shown in Figure 2.2 and are listed below: 0.718 MeV (1, first excited state), 1.740 (2), 2.154 (3), 3.587 (4), 4.774 (5), 5.11 (6), 5.16 (7), and 5.18 (8). Levels 6, 7, and 8 are close to each other and are referred to as group vi. Note from level 4.77 MeV and up, ^{9}Be(d,nα)^{6}Li competes with gamma cascade decay. The Γ_γ/Γ ratios for levels 6 and 7 are taken from Warburton *et al.*, (1963). Also shown in Figure 2.2 are the ratios of the reaction channels of ^{9}Be(d,n'γ)^{10}B* at E_d=1.5 MeV leading to excited states of ^{10}B, which are estimated from the neutron spectrum, as discussed below.

The neutron energy, E_n, at 0°, for the reaction channels is calculated using

$$\sqrt{E_n} = \{\sqrt{m_d m_n E_d} + \sqrt{m_d m_n E_d + (m_B + m_n)(m_B Q + (m_B - m_d)E_d)}\} / (m_B + m_n), \quad (2.1)$$

where m is the mass and E_d is the deuteron energy. Every reaction channel leading to a different excited state of ^{10}B has a different Q value. The neutrons from each channel start from a maximum energy, E_{nmax}, calculated from equation (2.1) with E_d = 1.5 MeV. As the deuteron beam attenuates in the thick beryllium target, lower energy neutrons are produced. Due to the motion of the center of mass, the neutrons have lower energies at higher angles and show as a low energy tail in an angle integrated spectrum. The minimum neutron energies for levels 0, 1, 2, 3, and 4, for which the Q values are positive, of ^{10}B are calculated by setting E_d = 0 in equation (2.1) due to isotropy at E_d = 0. (In reality, the deuteron has to overcome a low Coulomb barrier so the reaction does not happen at E_d = 0.) For level 5, 6, 7, 8, the Q values are negative. The neutron energy is minimum at E_d = E_{th} (threshold energy) and 180°. The relation between the minimum neutron energy, E_{nmin}, Q, E_{th}, and particle masses is:

$$E_{nmin} = (M_n M_d / M^2) E_{th} = (M_n M_d / (M M_{Be})) (-Q), \qquad (2.2)$$

where $M = M_{Be} + M_d = M_B + M_n$ is the total mass. Table 2.1 lists the E_{nmax} for the different reaction channels at E_d=1.4 and 1.5 MeV and E_{nmin}. The minimum neutron energy is 8 keV from level 5 and 16 keV from level group vi. The neutron energies are shifted by almost the same amount as are the deuteron energies.

When comparing the neutron energy ranges in Table 2.1 with the neutron peaks in Figure 2.1.c, the peaks could be assigned with reaction channels leading to states of ^{10}B: vi, 3.59, 2.15, and 0.718 MeV. The three levels in level group vi are not distinguishable from each other in the neutron spectrum. Notice the reaction does not lead to the ground state and 4.774 (5) MeV. They are probably not favored due to angular momentum transfer inhibition (both are 3+ states). The area under the assigned peaks is calculated and the branching ratios of the reaction channels are derived: 32.6%, 11.5%, 15.0%, and 40.9% for level 1, 3, 4, vi respectively, as shown on Figure 2.2.

Following the reaction channels and the decay schemes in Figure 2.2, the number of gammas per (d,n) reaction, i.e., source neutron, is derived and tabulated in Table 2.2. Gammas originating from level 7 have been found experimentally (Ajzenberg, (1979)): 3.028, 4.442, and 5.16 MeV. No gammas from level 6 and 8 have been observed. For level 6, the dominating α mode is enough to explain the lack of gammas ($\Gamma\gamma/\Gamma$ is < 0.05, see Figure 2.2). For level 8, either of the following two explanations is possible: the (d,n) reaction does not lead to it or its decay is dominated by the α mode. Since the channel ratio within the three levels of level vi is not known, intensities of the gammas are calculated for two conditions and are listed in Table 2.2: the (d,n) reaction channel to level vi leads either completely, or not at all, to level 7. Level 7 plays a big role in the intensities of the gammas below it through cascading. The difference in the intensity of the most prominent gamma of 718(1-0) keV for the two conditions will be .763/.534 = 1.4. Intensities of some other gammas are affected more. The intensity of high energy gammas from level 7 itself, 3.028(7-3), 4.442(7-1), and 5.16(7-0), will be a clearer indication whether the (d,n) reaction channel through level vi is dominated by level 7. The total number of gammas per neutron differs by almost a factor of 2 (sum of weight 1.7/0.88) under conditions with and without involvement of level 7. The relative intensities (normalized to the peak at 718 keV) are also listed in Table 2.2.

The experimentally obtained neutron cut-off energy of 0.075 MeV is higher than the minimum neutron energy of 16 keV from level group vi, but only neutrons leading to level group vi will be affected. The gamma measurements will show that level group vi decays do not produce gammas; therefore, the estimation of the relative gamma intensities without the contribution of level group vi will not be affected by the experimental neutron energy cut-off.

Other gammas could also be produced as follows.

^{9}Be(d,p)^{10}Be has a positive Q value of 4.5873 MeV. The decay scheme of the product nuclide ^{10}Be (Ajzenberg, (1979)) is shown in Figure 2.3. E_d = 1.5 MeV is above the first excited state (3.368 MeV) of ^{10}Be. The 3.368 MeV gamma peak is reported to be prominent for E_d = 4.0 MeV (Guzek *et al.*, (1996)), which is above the second excited state group (5.9583, 5.960, 6.179, 6.263 MeV) and the third excited state group (7.371, 7.542

MeV) of ^{10}Be. Whether 1.5 MeV deuterons will produce abundant 3.368 MeV gammas will be answered by the gamma yield measurement.

The 0.478 MeV gamma from the first excited state of ^{7}Li to the ground state following the ^{9}Be(d, $\alpha\gamma$)^{7}Li* reaction is comparable in intensity to the gammas from the (d,n) reaction channels at $E_d = 4.0$ MeV (Guzek *et al.*, (1996)). The same may happen at $E_d = 1.5$ MeV.

2.3. GAMMA YIELD MEASUREMENT

2.3.1. Beryllium Target Assembly and Beam Line

The dose delivering needle tube Prototype II with the beryllium target, as described in Chapter Six, was used for the gamma yield measurements. Here is a brief introduction.

Prototype type II was designed to deliver high dose rate neutron dose to large brain tumors at a heat load of more than 130 Watts with the Be(d,n) and Be(p,n) reactions. (For the gamma yield measurements, only a fraction of a Watt of heat will be produced.) The target assembly consists of the beryllium target (99.6% beryllium), the stainless steel needle tube, and an aluminum water-cooled aperture. (Abundance of ^{9}Be is 100%.), The schematic of the needle tube and target is borrowed from Chapter Six and shown in Figure 2.4.a, with the inner and outer tubes and in Figure 2.4.b, the dimensions of the target. The needle tube is a tube-in-tube design, both stainless steel. Deionized water runs between the two tubes to cool the target. (Deionized water enables electric insulation of the target and measurement of accelerator beam current from the target.) The cooling channel is formed with two bronze rods between the inner and outer tubes. The water cooled aperture limits the accelerator beam size going into the needle tube. The target itself is tube shaped. It is electrically insulated from the rest of the target assembly with a teflon sleeve, which is protected from being hit by the accelerator beam by an aluminum protection ring placed immediately before it inside the inner tube. A thermocouple with sheath is led out from the target to monitor the temperature. Target current is measured from the thermocouple sheath. In the text below, the "target" refers to the vacuum surface of 2 mm diameter at the bottom of the target tube where neutrons are produced. Due to the machining process, the surface is not flat but is V-shaped with a 120° angle.

The 1.5 MeV deuteron beam from the tandem electrostatic accelerator in the Laboratory for Accelerator Beam Applications (LABA) at MIT is described as Beam III in Chapter Three. The beam line elements, as shown in Figure 3.9, consist of an x-y steering magnet, a quadrupole doublet, and a switching magnet. The experiments use the center port of the switching magnet so the switching magnet acts as merely a drift space. The beam envelopes are shown in Figure 3.11. Under the best conditions, a maximum of 65% of total beam is expected to be delivered to the target.

2.3.2. Experimental Setup

The experimental setup is shown in Figure 2.5. To reduce the counting rate, the NaI(Tl) (76 mm x 76 mm) detector was set up 6 meters away at the same height of the target and at 60 degrees relative to the beam, which is the farthest distance possible in the target room. The detector (the crystal and the photomultiplier tube (PMT)) was shielded with 5 cm thick lead blocks, forming a collimation tunnel in front of the detector with an opening of 17 x 20 cm and a length of 41 cm. The detector and the collimation tunnel were aligned with the target by pointing a laser beam from the target to the detector. Lead bricks were used to reduce the background gammas generated from the aperture and the needle tube. The shielding was divided into three regions, I, II, and III, shielding the target, needle tube, and the aperture respectively, all 20 cm high, 15 cm thick along the line of detection, and 10 cm across. Spectra with combinations of lead I and II were taken with Lead III in place all the time. A rough rather than precise alignment was adopted in the setup. The shielding in front of the detector was larger than the detector size. Lead I covers the beryllium target and about 2 cm of the stainless steel tube so when Lead I is lifted and Lead II blocked, the spectrum should include some gammas produced from the needle tube (stainless steel and Al). When Lead I is blocked and Lead II lifted, all gammas from the Be target should be blocked.

The target and the detector were mapped to the floor using a plumb line and the distance between them was measured on the floor. The angle of detection was determined, also on the floor, to be 60° ±10°.

The efficiency calibration source, ^{137}Cs, was positioned using the laser beam so that it was on the central axis of the NaI(Tl) detector.

2.3.3. Target Current Integration

The gamma yields are normalized to the number of deuterons hitting the beryllium, or equivalently the electric charge collected from the target. The target current is converted to voltage by an arithmetic amplifier, as shown Figure 2.6. The conversion is as follows:

$$i = 10^{-(5+v/2)}, \; -5<v<5 \text{ v, or}$$

$$v=10 - 2\log(i), \; 3.16e\text{-}8<i<3.16e\text{-}3 \text{ A.} \qquad (2.3)$$

To reduce AC noise, e.g., 60 Hertz from power lines, the input has an RC circuit with cut-off frequency around 30 Hertz. A 30 meter long optical fiber relays the voltage signal to a personal computer where the conversion from the voltage signal to current and current integration to charge are all done by software. The current reading was checked against a multimeter. The agreement was within 0.8% in the current range of 0.1μA-3.0 mA. The experiments in this chapter used currents of 0.1-10 μA.

2.3.4. Tuning of Electronics

The diagram of the gamma spectrum recording electronics is shown in Figure 2.7. The signals formed from the anode of the PMT go through a PreAMP (ORTEC Model 113), a 30 meter long coaxial cable, a SpecAMP (ORTEC Model 471), and a Multi-Channel Analyzer (MCA) (Aptec) interfaced to a personal computer.

The negative pulses coming from the PMT anode are integrated by the PreAMP. The PreAMP mainly serves two functions: impedance reduction and stable charge-to-voltage conversion. The PMT has a high output impedance. The PreAMP takes this high impedance input and produces a 50 Ω impedance voltage signal which is matched to the SpecAMP. The PreAMP operates in the charge-sensitive mode as shown in Figure 2.8 (Knoll, (1989)). The charge-to-voltage conversion is done by the stable integration capacitor, C_f, which is independent of the unstable input capacitance, C_i (capacitance of the

PMT and the cable connecting the PMT and the PreAMP). For the same amount of charge, a smaller C_f converts a stronger signal; the following condition must be met for the circuit to work properly:

$$C_f >> C_i / A, \tag{2.4}$$

where A is the gain of the amplifier. A lower C_f allows the propagation of more high frequency noise. C_f was set to 100 pF, which is the next to zero option of the PreAMP. The discharge circuit is comprised of C_f and the discharge resistor, R_f, which is fixed in this PreAMP. The time constant of the RC circuit is around 50 μs, which is much longer than the decay time of the input signal (< 1 μs) to ensure full current integration. This long time constant results in the long tail of the output signal.

The SpecAMP is a narrow band pass filter adjusted to minimize noise. The gain was adjusted with a ^{60}Co source so that the spectrum covers the energy range of interest, 0-5.3 MeV. While the shorter the signal, the less the pile-up effect, the ADC of the MCA usually requires a rise time of more than 1 μs. For this undocumented MCA, the rise time was set to 4 μs and decay time to 6 μs. A spectrum with shorter times (1 μs rise and 2 μs decay) was later taken to compare the pile-up effect. The improvement on the pile-up effect was found to be 8%.

Special attention was paid to the high voltage supply (+850 volt used in the experiments) to the PMT. The current multiplication is very sensitive to the voltage on the dynodes. Besides the stability of the voltage itself, the current output must be much higher than the current of the multiplying electrons between the dynodes, which is on the order of 10-100 μA. The HV supply used in this experiment has a maximum current output of 5 mA. The PMT also comes with a magnetic shield to reduce the interference of stray magnetic fields on the electrons generated within the PMT dynodes. The stability of the whole electronics system was confirmed by non-distorted peaks after 6 hours of continuous counting.

2.3.5. Energy Calibration

Energy calibration was done with ^{60}Co and ^{137}Cs sources. At the time of the experiment, the activities were about 0.7 μCi for the ^{60}Co and 5 μCi for the ^{137}Cs. The energy of the single gamma from the ^{137}Cs is 661.7 keV. ^{60}Co has two cascade gammas: 1173.2 and 1332.5 keV. The ^{60}Co was placed touching the detector surface to maximize the sum peak of 2505.7 keV. The ^{137}Cs source was put at a distance of about 10 cm from the detector surface to get a comparable intensity. The energy calibration was based on the four points: 661.7, 1173.2, 1332.5, and 2505.7 keV, assuming a quadratic fit. The gain of the SpecAMP was adjusted so that the 4096 channel MCA corresponds to 5.29 MeV, higher than the expected most energetic gamma from the ^{9}Be(d,n'γ)^{10}B* of 5.16 MeV. The low energy cut-off was set at 30 keV. (Without this cut-off, the background noise would swamp the ADC.) The calibration spectrum is shown in Figure 2.9.

2.3.6. Efficiency Calibration

The intrinsic peak efficiency, ε_p, (ratio of registered photopeak to gammas entering the detector) of a 76 mm dia. x 76 mm NaI(Tl) detector is available for a source-to-detector distance of 9.3 cm in the energy range of 0.135-9.2 MeV from Neiler and Bell, (1965). Since the gammas of interest range from 414 keV to 5.16 MeV in the present work, the efficiency curve is read and tabulated in Table 2.3 for the energy range of 0.135-5.5 MeV and replotted in Figure 2.10. The intrinsic peak efficiency decreases from 50% at 0.4 MeV to 4% at 5.0 MeV. One of the major contributors to the efficiency curve in Neiler and Bell, (1965) is Jarczyk *et al.*, (1962), which gives an error of 8-12%. The error for the intrinsic peak efficiency used in this work is assumed to be 10%.

To apply the efficiency curve at a source-to-detector distance of 9.3 cm to 6 m as in this work, the edge effect needs to corrected. (When the source is close to the detector, all gammas entering the detector edge are not parallel to the crystal and do not see the whole depth of NaI(Tl), so the efficiency is lower than when the source is far away. This is called the edge effect.) To determine the distance at which the edge effect is minimal, the ^{137}Cs calibration source was placed at 44.2 cm and 100.0 cm away from the detector and counted. The results are summarized in Table 2.4. The solid angle, Ω, is calculated from

$$\Omega = 2\pi\,(1- \frac{d}{\sqrt{d^2+r^2}}), \tag{2.5.1}$$

$$= \pi\, r^2 / d^2,\ d>>r, \tag{2.5.2}$$

where r is the diameter of the NaI crystal and d is the source-to-detector distance. If the edge effect is absent, the counting rate is proportional to the solid angle the source sees of the detector, and the counting rate multiplied by d^2 is constant. This value is 23.46 cps. m^2 for the 100.0 cm source-to-detector distance and 23.20 cps. m^2 for 44.2 cm. They are within 1 %. Hence, it is concluded that the edge effect for this 76 mm x 76 mm NaI detector is minimal at a distance of 44 cm or farther. Table 2.4 also lists the calculated intrinsic peak efficiencies, .352 and .350, which are also very close. At a source-to-detector distance of 9.3 cm, the Neiler and Bell data read .328 for a 660 MeV gamma. An assumption is made to multiply the Neiler and Bell efficiency data by a scale factor of .352/.328 = 1.0732 for all energies, as shown Figure 2.10 and Table 2.3. The converted intrinsic peak efficiency will be used for the 6 m source-to-detector distance counting.

2.3.7. Be(d, γ) Spectra

The first set of two spectra was taken under two different blockings: 1) Lead I lifted, Lead II blocked, and 2) Lead I blocked, Lead II lifted. As explained in the experimental setup in Section 2.3.2, Spectrum I includes gammas from the beryllium target and a small portion of gammas from the needle tube (stainless and aluminum). All gammas from the beryllium target should be blocked from Spectrum II.

The two spectra were taken under similar beam conditions. The deuteron current on the target and the tube were around 0.20 (34% of total, as opposed to the predicted optimum of 65%) and 0.13 μA respectively. The current on the water-cooled aperture (shielded with lead block III) was around 0.25 μA. The counting time was 30 minutes each. The target current integration was synchronized with the spectrum taking. The ADC dead time was 9% for Spectrum I and 7% for Spectrum II. For comparison, the two spectra are plotted together in Figure 2.11. Distinguishable peaks are labeled with the fitted energies: 400, 462, 712, 1021, 1430, 1836, 2190, 2813, 3272, and 3473 keV. To get better statistics, Spectrum I was repeated for a counting time of 6.5 hours and a higher counting rate (dead time 12.5%) and called Spectrum III. This spectrum is also plotted in Figure 2.11. The improvement from Spectrum I is smoother peak shapes. The biggest improvement is seen in the peak at 3473 keV, which is barely identifiable in Spectrum I.

The gammas from level 7 of ^{10}B, 3.028 (7-3), 4.442(7-1), and 5.16 MeV (7-0), are not present in any of the three spectra. Therefore, it is concluded that the (d,n) reaction channel leading to level group vi of ^{10}B does not lead to level 7 and does not produce any cascading gammas. Since neutron energy cut-off affects only neutrons leading to level group vi (as discussed in Section 2.2), the neutron spectrum with a cut-off energy of 0.075 MeV should still give valid estimates of accompanying gammas.

The comparison between measured and predicted peaks is summarized in Table 2.5. The intensity predictions without the involvement of level 7, as discussed in Section 2.2 and listed in Table 2.2, are used. The energy of the matched peaks are within 3%. All the other predicted gammas, from the (d,n), (d,p), and (d,α) reactions are detected. Before going into intensity comparisons, keep in mind that the intensity estimates are for total gamma intensities and the measurements are at a fixed angle of 60 degrees, though strong angular dependence of the gammas is not expected at such a low deuteron incident energy. The peak at 1836 keV is deformed, probably by gammas from stainless steel and aluminum with similar energies. This peak shows equal strength in both spectra, and so is ignored. The "clean" (showing on Spectrum I but not II) peaks are: 718, 1022, 1433/1436, 2869, 3368, and 3587 keV. Peaks at 414 and 478 keV (overlapping) are seen in Spectra I and II, but much stronger in Spectrum II. It is not attempted to identify and separate sources other than beryllium. The 511 keV peak from positron annihilation is probably buried in the 478 keV peak. The net areas of the peaks at 414 and 478 keV, based on the good half peaks, should be overestimates. The peak at 1022 keV could include the 1022 keV positron annihilation. The peak at 2869 keV could include the escape peak of 3368 keV (3368 - 511 = 2857). The peak at 2154 keV shows in both Spectra I and II and could be obstructed by gammas of similar energies from stainless steel and aluminum reactions. The uncertainties mentioned above could explain the fact that the measured relative intensities (net peak area divided by the intrinsic peak efficiency of the detector) for peaks at 414, 478, 1022, 2154, 2869 keV are higher than the predictions. The other three gammas from the (d,n) reaction show good agreement between prediction and measurement: 1433/1466 and 3587 keV. The errors listed with raw peak areas in Table 2.5 are variations of peak fittings given different upper and lower background points. The error of 8% for the 2154 keV peak is assigned to the 414 and 478 peaks because they all have high interference gamma background.

Since there is no apparent contradiction between prediction and measurement of gammas from the (d,n) reactions, the predicted intensities relative to the 718 keV peak will be used to derive the absolute yields from the absolute yield of 718 keV since 718 keV is the only good, strong, and clean peak. For the 478 keV from the (d,α) reaction and 3368 keV from the (d,p) reaction, there is no prediction of the intensity, so the measured intensity will be used. As mentioned above, the 478 keV peak includes other gammas. Since the relative intensities of peaks 414 and 478 are similar between Spectra I and II, the real/raw ratio of .33 (.13/.393, see Table 2.5) for the peak at 414 keV will be applied to the peak at 478 keV. This is a best guess, but better than none.

The gamma yields are summarized in Table 2.6. The yields are normalized to the deuteron charge, which is corrected for the dead time. Spectrum III was recorded over 23293 seconds

(6.5 hours) of real time. The live time (MCA open to incoming pulses) was 20385 seconds. The dead time is (1-20385/23293) = 12.5%. The total deuteron charge collected from the beryllium target was 4810 μC. The corrected charge is 4810 μC x live/real time. For the strongest gamma, 718 keV, the differential yield is 2.366 x 10^7 /sr/μC.

Error analysis is as follows. For the 718 keV gamma, the error is dominated by the 10% peak efficiency error. The peak reading error is 1.8% (Table 2.5). The uncertainty with deuteron current measurement is 1%. The total relative error is 10%. The differential yield with two significant digits are:

$$dY_{g\,718}/d\Omega = 2.4\ (\pm 10\%) \times 10^7\ /\mathrm{sr}/\mu\mathrm{C},\ E_d=1.5\ \mathrm{MeV}.$$

For the other gammas, errors in the measured intensities are bigger since the peak reading errors and background interference are larger. The total errors for the 478 and 3368 keV gammas are calculated to be both 13%. The predicted intensities of the other gammas relative to the 718 keV peak carry the same 10% error as in the neutron yield integration. So the errors for the other gammas with the derived intensities carry a total error of 14%, as listed in Table 2.6.

Another source of error, which affects all gammas, is the uncertainty in the deuteron beam energy. The accelerator beam energy was calibrated against the threshold energy (1.8806 MeV) of the ^{7}Li(p,n) reaction (LABA log book, (1998)). The threshold energy was found to be 1.8666 MeV, 0.014 MeV lower than the accepted value. If the same energy shift applies to 1.5 MeV, the real energy should be 1.514 MeV. The uncertainties about the deuteron beam energy will not affect the comparison between the gamma dose simulations and measurements in Chapter Seven since the same nominal deuteron energy will be used in the dose measurements as used in the gamma yield measurements.

Without information about angular distribution of the 718 keV gamma, the total yield was obtained by multiplying the differential yield at 60° by 4π. The value is 2.97 x 10^8 /μC. The ratio to the neutron yield, $Y_{En>0.075}$ (error 10%), is 2.97/6.02 = 0.49, which is 8% lower than the estimate of 0.53 (Table 2.2). (Also note, as mentioned in Section 2.1, there have been significantly different estimates about the total neutron yields.) The loose agreement between estimates and measurements of relative gamma intensities and the absolute yield of the 718 keV gamma suggests that the gammas from the (d,n) reaction are largely isotropic. The total yields for the other gammas are calculated the same way as for the 718 keV gamma. The errors of the total yields are assumed to be the same as those of the differential yields. The justification is that the errors of the differential yields are probably much larger than those introduced by assuming an isotropy in the gamma angular distributions and equal the total errors.

2.3.8. Background between 3.5-5 MeV

It is noted that there is no peak above 3.5 MeV in Spectrum III. So the high background in the region between 3.5 and 5 MeV must be due to high energy gammas from neutron activation or pile-up of signals. The ratio of peaks at 718 and 4400 keV was set up to monitor the background change of the region 3.5-5 MeV. The higher the ratio, the lower the background. The ratio is 36 in Spectrum III.

In attempts to reduce the neutron activation, polyethylene slabs of 2.5 cm and 10 cm thick were put between the target and detector. Polyethylene attenuates fast neutrons quicker than gammas. For example, the mean free path is about 1 cm (shorter for lower energy neutrons) for a 1 MeV neutron but 10 cm for a 1 MeV gamma. However, the 718/4400 ratios were reduced (from 36) to 30 and 23 respectively with the 2.5 cm and 10 cm thick polyethylene slabs. One possible explanation is that the polyethylene moderates the fast neutrons and could increase the thermal neutron flux at the detector. Adding ^{10}B (high thermal neutron absorption cross section) to polyethylene may not help much since neutrons coming from the target are fast neutrons. When boronated polyethylene pellets (5% weight natural boron, ^{10}B abundance 19.9%), of rice grain size, of 10 cm thick were put between the target and detector, the 718/4400 ratio was reduced to 27.

To determine the pile-up effect, the time constants of the SpecAMP were reduced by a factor of 4 so that the output signal had a rise time of 1 μs, which is almost the minimum the ADC would take, and a decay time of 2-3 μs. The beam current was reduced so that dead time was reduced to 8.5% and 5.0% from 12.5% of Spectrum III, in two separate experiments. The 718/4400 ratio was increased to 38.8 and 39 respectively. The improvement is about 8%, which is not very significant. Since Spectrum III had been taken over a long counting time, Spectrum III was used for the yield analysis.

2.4. CONCLUSIONS

The yields of gammas from a thick beryllium target bombarded by 1.5 MeV deuterons have been measured at 60° to beam with a 76 mm diameter x 76 mm thick NaI(Tl) detector. Identified and measured are: 478 keV from ^{9}Be(d,$\alpha'\gamma$)^{7}Li*, 3368 keV from ^{9}Be(d,p'γ)^{10}Be*, and 414, 718, 1022, 1433/1436, 2154, 2869, 3587 keV from ^{9}Be(d,n'γ)^{10}B*.

The 718 keV peak, the transition from the first excited state of ^{10}B, is the most prominent peak. It is clean and well shaped. For the ^{9}Be(d,n'γ)^{10}B* reaction, predictions of gamma intensities relative to the 718 keV peak based on the neutron spectrum show no contradiction with measurements, and predicted values are used. About 40% of the reaction channels lead to the level group vi of level 6, 7, 8 of ^{10}B. Reaction channels through level 7 produce abundant 3028 and 4442 keV gammas. Reactions through level 6 or 8 produce almost no cascade gammas (e.g., level 6 decays through alpha mode >95%). Since 3028 and 4442 keV gammas are not seen, it is determined that the majority of the reaction channel through level vi does not lead to level 7 of ^{10}B and does not produce cascade gammas.

The comparison, assuming isotropic distribution of the gammas from the (d,n) reaction, between the measurements and estimates of relative gamma intensities and the absolute yield of 718 keV suggests that the gammas from the (d,n') reactions at E_d=1.5 MeV are largely isotropic.

The gamma yields will be used as input in dose simulations and compared to dose measurements in phantom in Chapters Four and Seven.

Table 2.1. The maximum and minimum neutron energies from the reaction channels $^{9}Be(d,n'\gamma)^{10}B^*$ at E_d=1.4 and 1.5 MeV. Unit is MeV.

^{10}B States	Q Value	E_d =1.4 E_{nmax}	E_d =1.5 E_{nmax}	E_{nmin}
g.s.(0)	4.36	5.709	5.814	3.964
0.718(1)	3.642	5.01	5.114	3.311
1.74(2)	2.62	4.009	4.111	2.382
2.154(3)	2.206	3.601	3.702	2.005
3.587(4)	0.773	2.169	2.268	0.703
4.774(5)	-0.414	0.936	1.035	0.008
5.11(6) (group vi) 5.16(7) 5.18(8)	-0.80	0.508	0.609	0.016

Table 2.2. Intensities of gammas from the reaction channels $^{9}Be(d,n'\gamma)^{10}B^*$ at E_d=1.5 MeV estimated from the neutron spectrum and decay scheme of ^{10}B under two assumptions about the reaction channel to level group vi (levels 6, 7, 8 of ^{10}B): either all or nothing to level vi leads to level 7.

Gamma Energy	none to level 7		all to level 7	
(MeV)	gamma/n	relative	relative	gamma/n
0.414((3-2)	.0671	.13	.21	.162
0.718(1-0)	.534	1	1	.763
1.022(2-1)	.0671	.13	.21	.162
1.433(4-3)	.0165	.031	.022	.0165
1.436(3-1)	.0355	.066	.11	.0856
2.154(3-0)	.0289	.054	.091	.0697
2.869(4-1)	.105	.20	.14	.105
3.028(7-3)	0	0	.24	.186
3.587(4-0)	.0285	.053	.037	.0285
4.442(7-1)	0	0	.11	.0844
5.16(7-0)	0	0	.021	.0157
Sum	0.88			1.7

Table 2.3. Intrinsic peak efficiency of a 3" dia x 3" NaI detector, at a source-to-detector distance of 9.3 cm, as a function of gamma energy, read off the curve from Neiler and Bell, (1965). The numbers for a source-to-detector distance of 1 m were scaled from the 9.3 cm. For the assumptions, see text. Also plotted in Fig. 2.10.

E(MeV)	9.3 cm	100 cm
0.135	0.940	1.009
0.150	0.920	0.987
0.165	0.900	0.966
0.180	0.880	0.944
0.200	0.845	0.907
0.215	0.820	0.880
0.225	0.800	0.859
0.250	0.760	0.816
0.260	0.740	0.794
0.280	0.700	0.751
0.300	0.660	0.708
0.335	0.600	0.644
0.350	0.580	0.622
0.370	0.550	0.590
0.400	0.515	0.553
0.410	0.500	0.537
0.450	0.465	0.499
0.500	0.420	0.451
0.550	0.385	0.413
0.600	0.360	0.386
0.620	0.350	0.376
0.660	0.328	0.352
0.700	0.315	0.338
0.730	0.300	0.322
0.800	0.280	0.301
0.900	0.250	0.268
1.000	0.227	0.244
1.150	0.200	0.215
1.500	0.158	0.170
1.800	0.135	0.145
2.000	0.122	0.131
2.500	0.100	0.107
3.000	0.0760	0.0816
3.500	0.0590	0.0633
4.000	0.0480	0.0515
4.500	0.0420	0.0451
5.000	0.0370	0.0397
5.500	0.0335	0.0360

Table 2.4. Summary of efficiency experiments with the ^{137}Cs (661.7 keV) source at 44.2 cm and 100.0 cm from the NaI(Tl) detector. The intrinsic peak efficiency at 9.3 cm from Neiler and Bell, (1965) is listed for comparison.

	100.0 cm	44.2 cm	9.3 cm (Neiler and Bell, (1965))
counting rate (cps)	23.46	118.8	
Ω	4.555e-3	2.321e-2	
$\Omega/4\pi$	3.625e-4	1.847e-3	
gamma entering detector (cps)	66.684	339.8	
intrinsic peak efficiency	.352	.350	.328
counting rate x d^2 (cps m^2)	23.46	23.20	

Table 2.5. Comparison between predictions and measurements of gamma yields from ^{9}Be(d,γ) at E_d=1.5 MeV and 60° .

Gamma energy comparison				Relative intensity comparison					
measu.	difference	prediction		prediction		measurement			
energy (keV)	1-meas/predi	energy (keV)	source	g/n	**g/718**	**g/718**	peak area (/1000)	ε_p	Comments
400	0.0338	**414**	(d,n)10B(3-2)	0.0571	**0.13**	**0.393**	2677 (±8%)	0.54	?include other gammas
712	0.0084	**718**	(1-0)	0.387	**1.000**	**1.000**	4164 (±1.8%)	0.33	
1021	0.0010	**1022**	(2-1)	0.0571	**0.13**	**0.244**	740 (±2.6%)	0.24	?include 1022 e-e$^+$ annihilation
1430	0.0021	**1433, 1436**	(4-3),(3-1)	0.0404	**0.097**	**0.104**	237 (±5.1%)	0.18	
2190	-0.0167	**2154**	(3-0)	0.0246	**0.054**	**0.067**	101 (±8.3%)	0.12	?interference from S.S., Al
2813	0.0195	**2869**	(4-1)	0.0651	**0.20**	**0.230**	267 (±7.1%)	0.092	?include escape peak of 3368
3473	0.0318	**3587**	(4-0)	0.0177	**0.053**	**0.038**	28 (±20%)	0.059	
		3028	(7-3)	0	0	0	0		
		4442	(7-1)	0	0	0	0		
		5160	(7-0)	0	0	0	0		
462	0.0335	**478***	(d,α)7Li			**0.780***	4628 (±8%)	0.47	?include 511 keV & others.
3272	0.0285	**3368**	(d,p)10Be			**0.132**	118 (±8.4%)	0.071	
1836			?s.s., Al						

*: Intensity to be reduced by the real/raw factor of .33 (=.13/.393) from peak 414.

Table 2.6. Yields of gammas from the ^{9}Be(d,γ) reactions at E_d=1.5 MeV and 60° to the deuteron beam.

Gammas (keV)	Intensity relative to 718 keV	dY/dΩ/μC (#/sr/μC)	Y/μC
414 (d,n)	0.13	3.08e6(±14%)	3.87e7(±14%)
718	1	2.37e7(±10%)	2.97e8(±10%)
1022	0.13	3.08e6(±14%)	3.87e7(±14%)
1433, 1436	0.097	2.30e6(±14%)	2.88e7(±14%)
2154	0.054	1.28e6(±14%)	1.61e7(±14%)
2869	0.20	4.74e6(±14%)	5.95e7(±14%)
3587	0.053	1.26e6(±14%)	1.58e7(±14%)
478(d,α)*	0.26*	6.16e6*(±13%)	7.73e7(±13%)
3368(d,p)	0.13	3.08e6(±13%)	3.87e7(±13%)

*: Intensity modified by an approximation factor. See section 2.3.7.

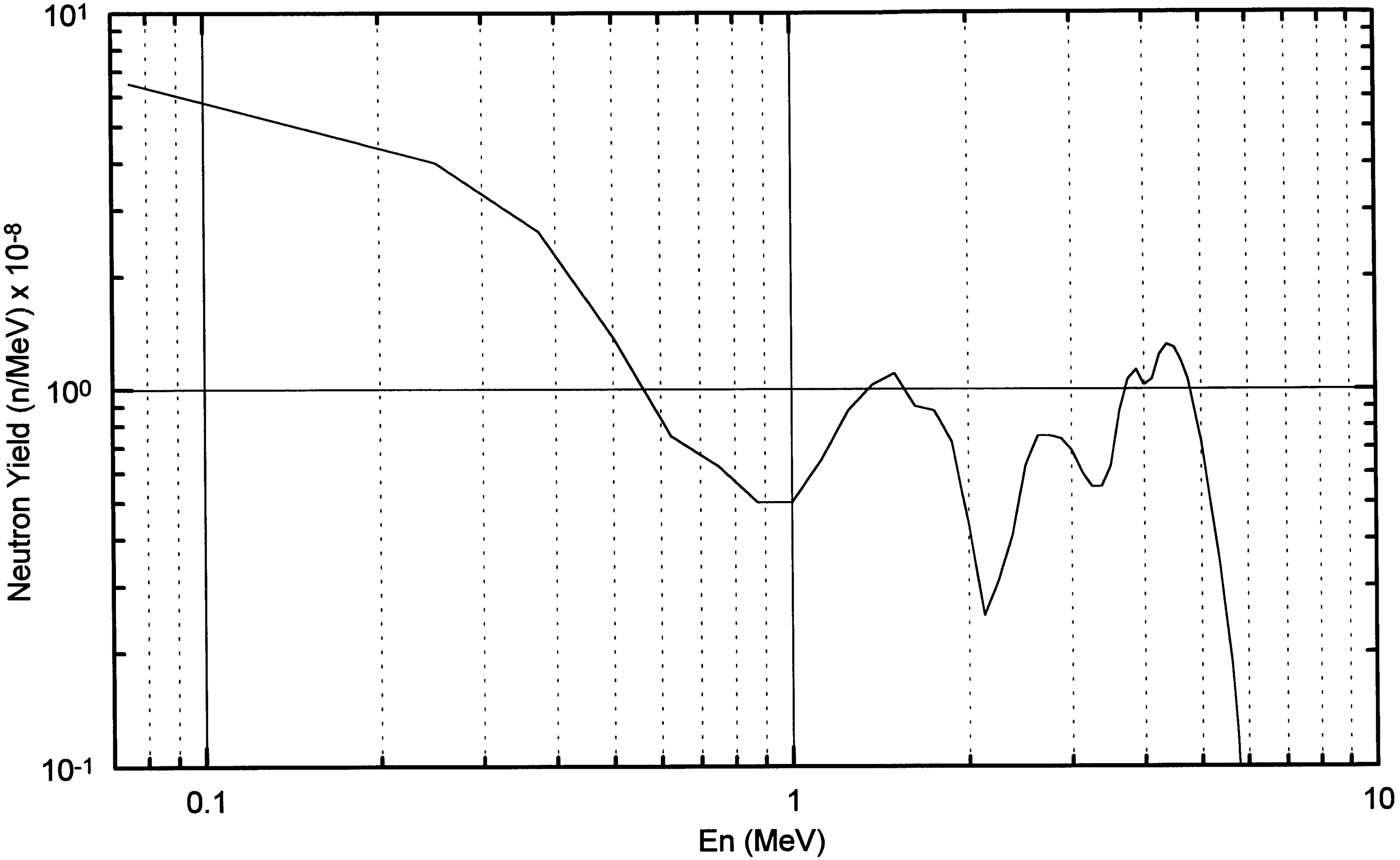

Figure 2.1.a. Angle integrated neutron spectrum for the $^9Be(d,n)^{10}B$ reaction at Ed=1.4 MeV (redrawn from Whittlestone, (1977)).

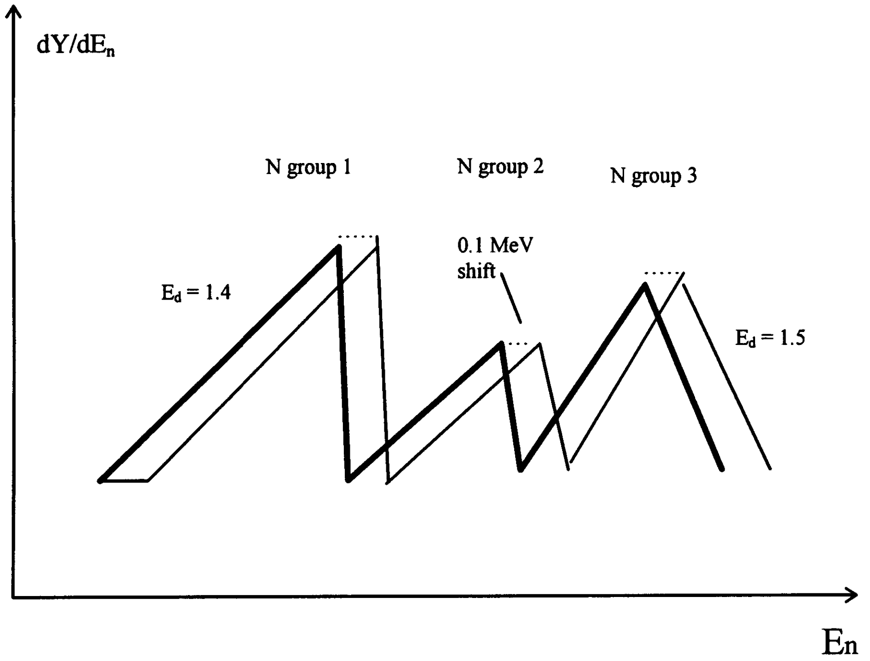

The thick line is an imaginary ^{9}Be(d,n)^{10}B at E_d=1.4 MeV neutron spectrum. Extension of each neutron group at the high energy end by 0.1 MeV is an estimate for the E_d=1.5 MeV spectrum. The thin line is an easier way of estimation.

Figure 2.1.b. Illustration of shifting the ^{9}Be(d,n)^{10}B at E_d=1.4 MeV spectrum to estimate the E_d=1.5 MeV spectrum.

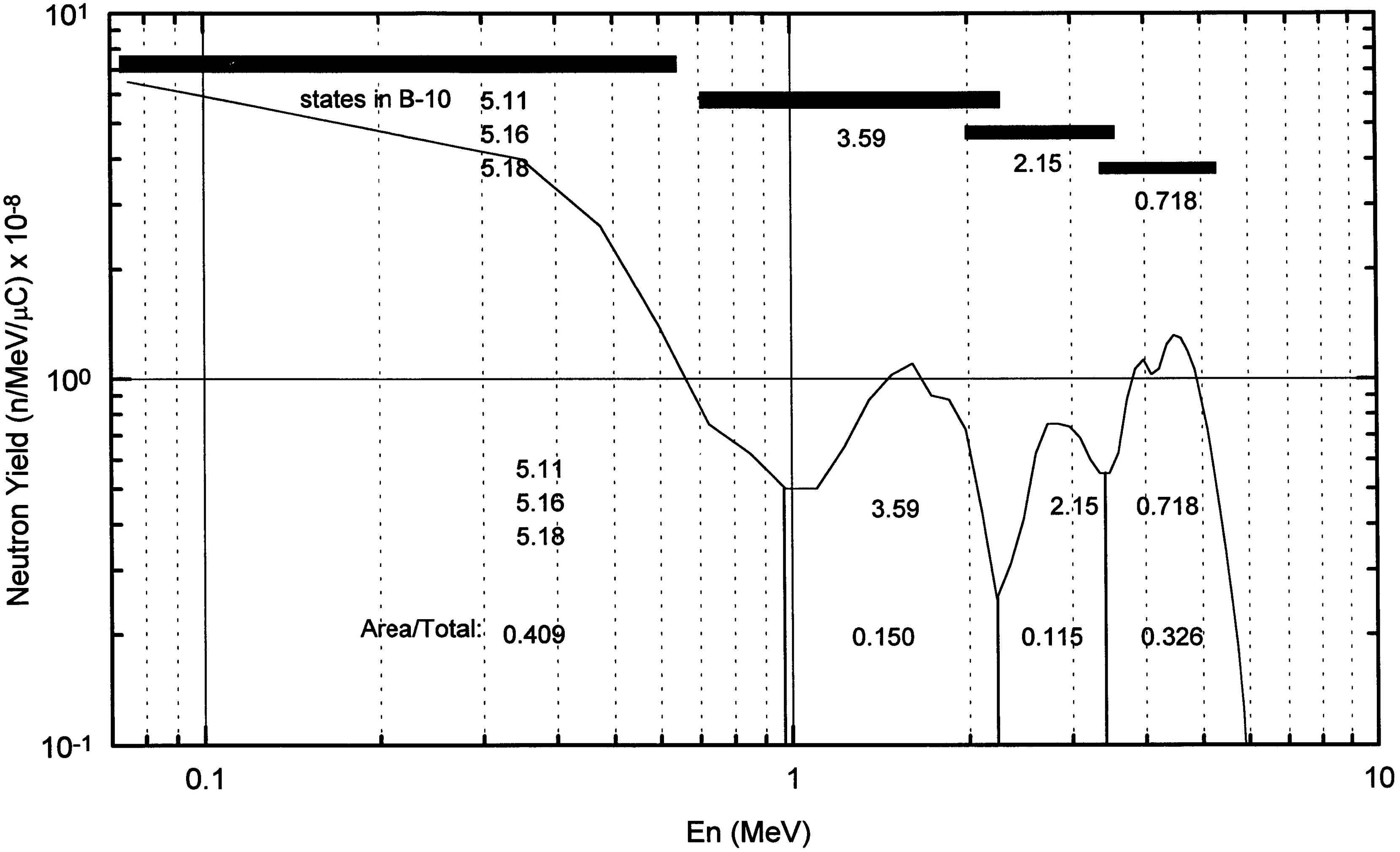

Figure 2.1.c. Estimation of the ^{9}Be(d,n)^{10}B reaction at Ed=1.5 MeV by shifting up 0.1 MeV the Ed=1.4 MeV spectrum shown in Figure 2.1.a. The peaks are labelled with the corresponding excited states of ^{10}B and the area under each peak divided by the total. The horizontal bars are the energy ranges of the neutron groups.

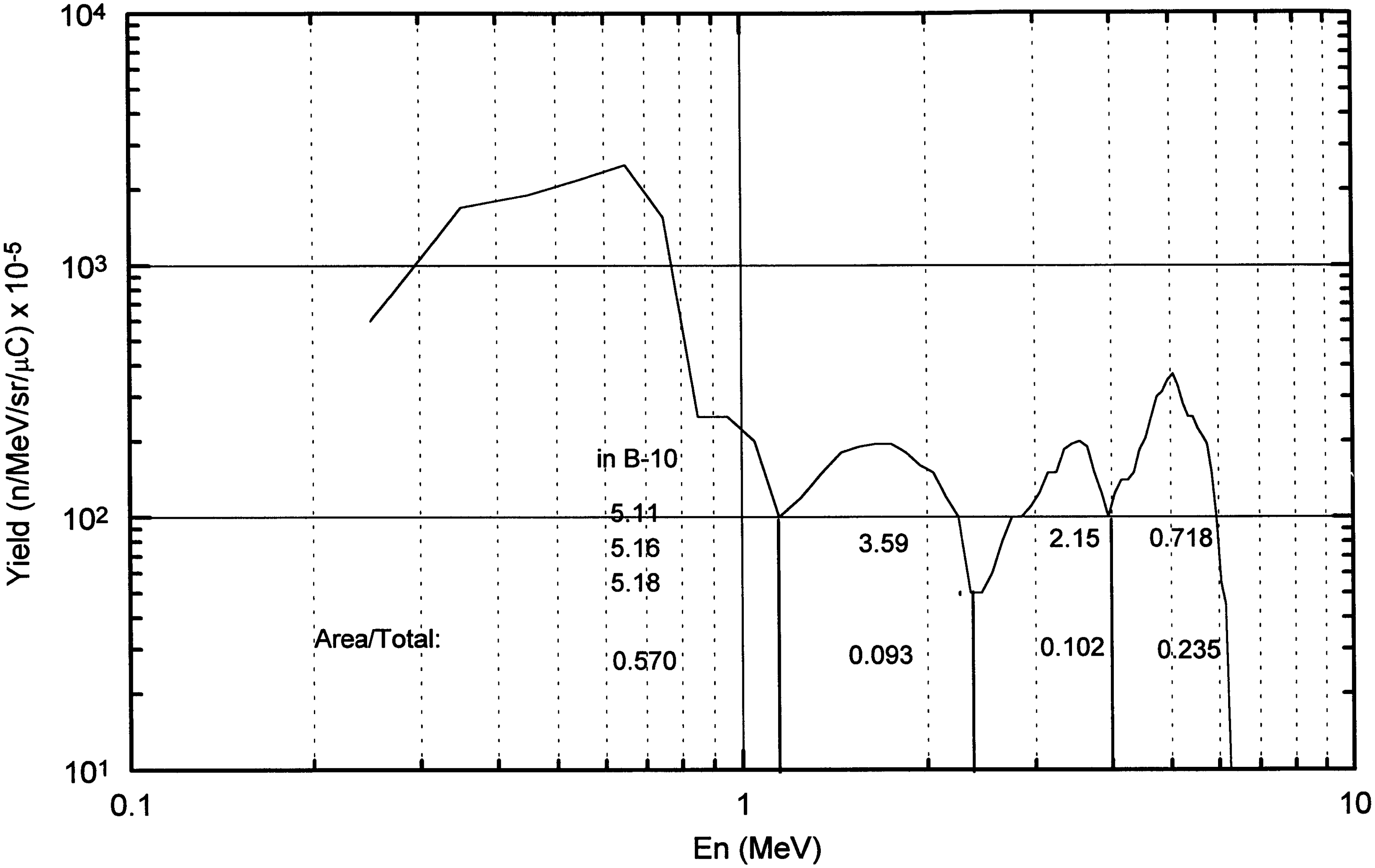

Figure 2.1.d. Neutron spectrum for the $^9Be(d,n)^{10}B$ reaction at Ed=1.5 MeV at 0° (redrawn from Guzek *et al.*, (1996)). The peaks are labelled with the corresponding excited states of ^{10}B and the area under each peak divided by the total.

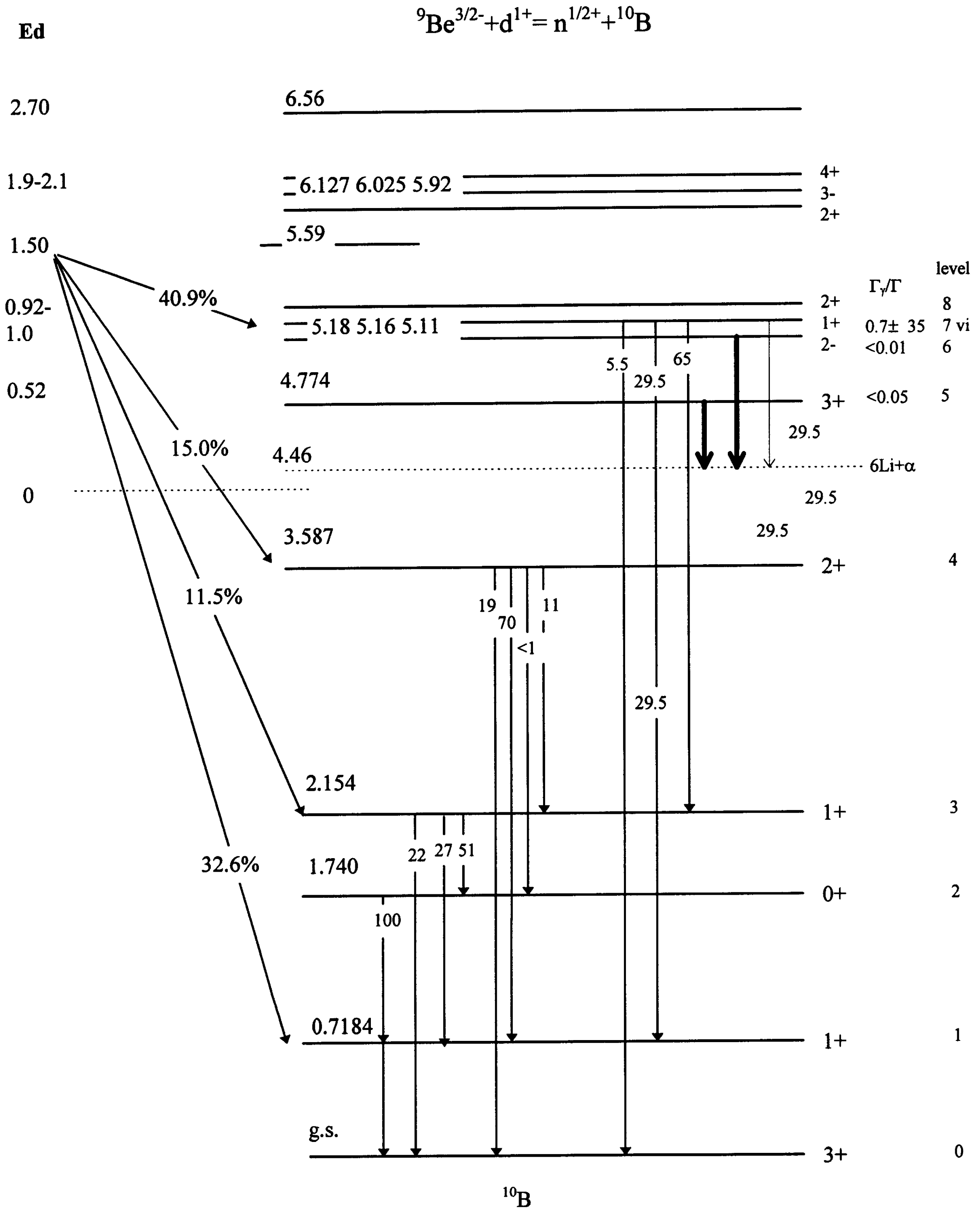

Figure 2.2. Decay scheme of ^{10}B (Ajzenberg, (1979)). The branching ratios of the ^{9}Be(d,n'γ)^{10}B* reaction at E_d=1.5 MeV reaction channels are estimated from the neutron spectrum as shown in Figure 2.1.c. Γ_γ/Γ ratios from Warburton *et al.*, (1963).

$^{9}Be^{3/2-} + d^{1+} = p^{1/2+} + {}^{10}Be$

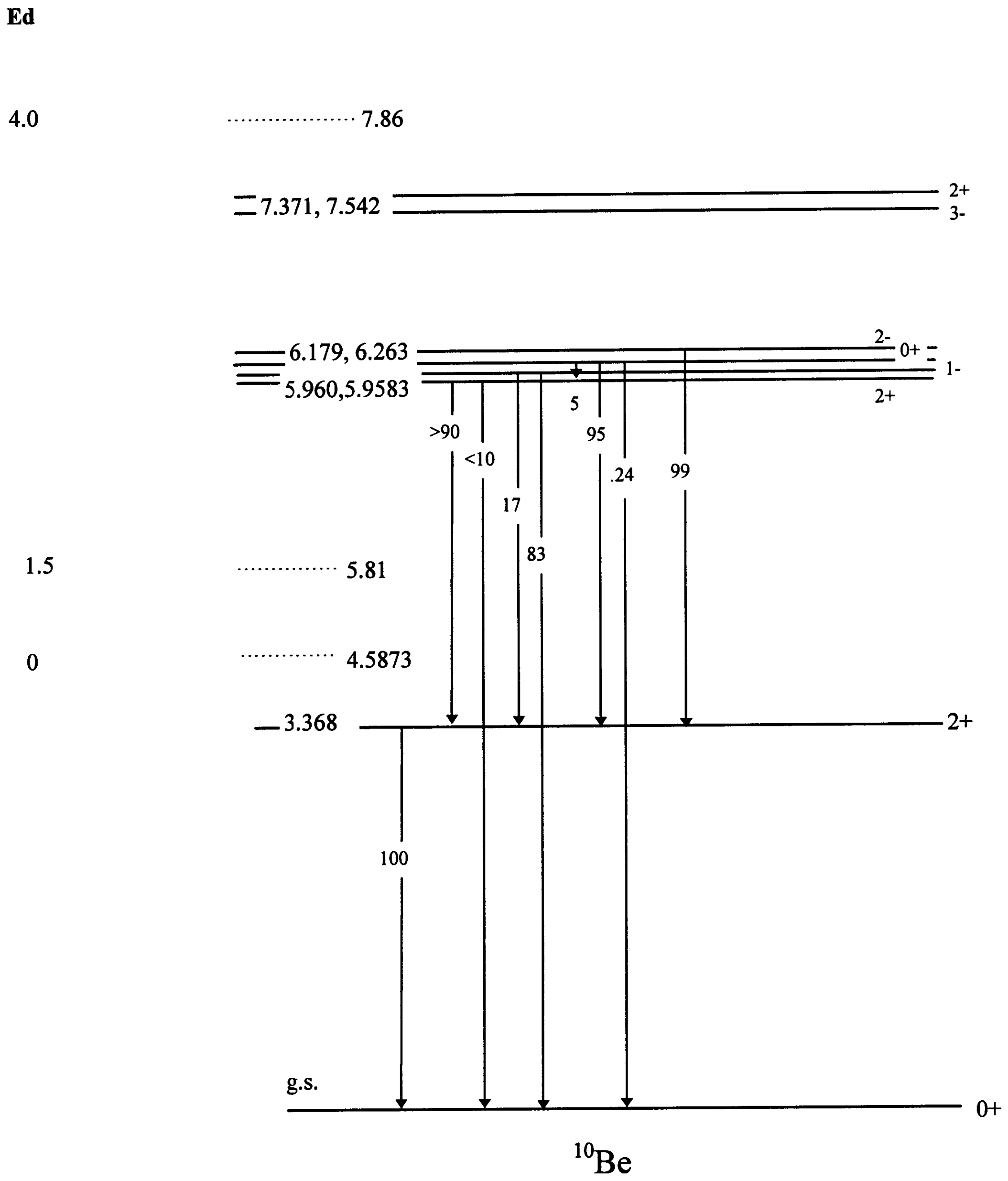

Figure 2.3. Decay scheme of ^{10}Be and levels of (^{9}Be+d-p) at E_d=0, 1.5, and 4.0 MeV relative to the ground state of ^{10}Be (Ajzenberg, (1979)).

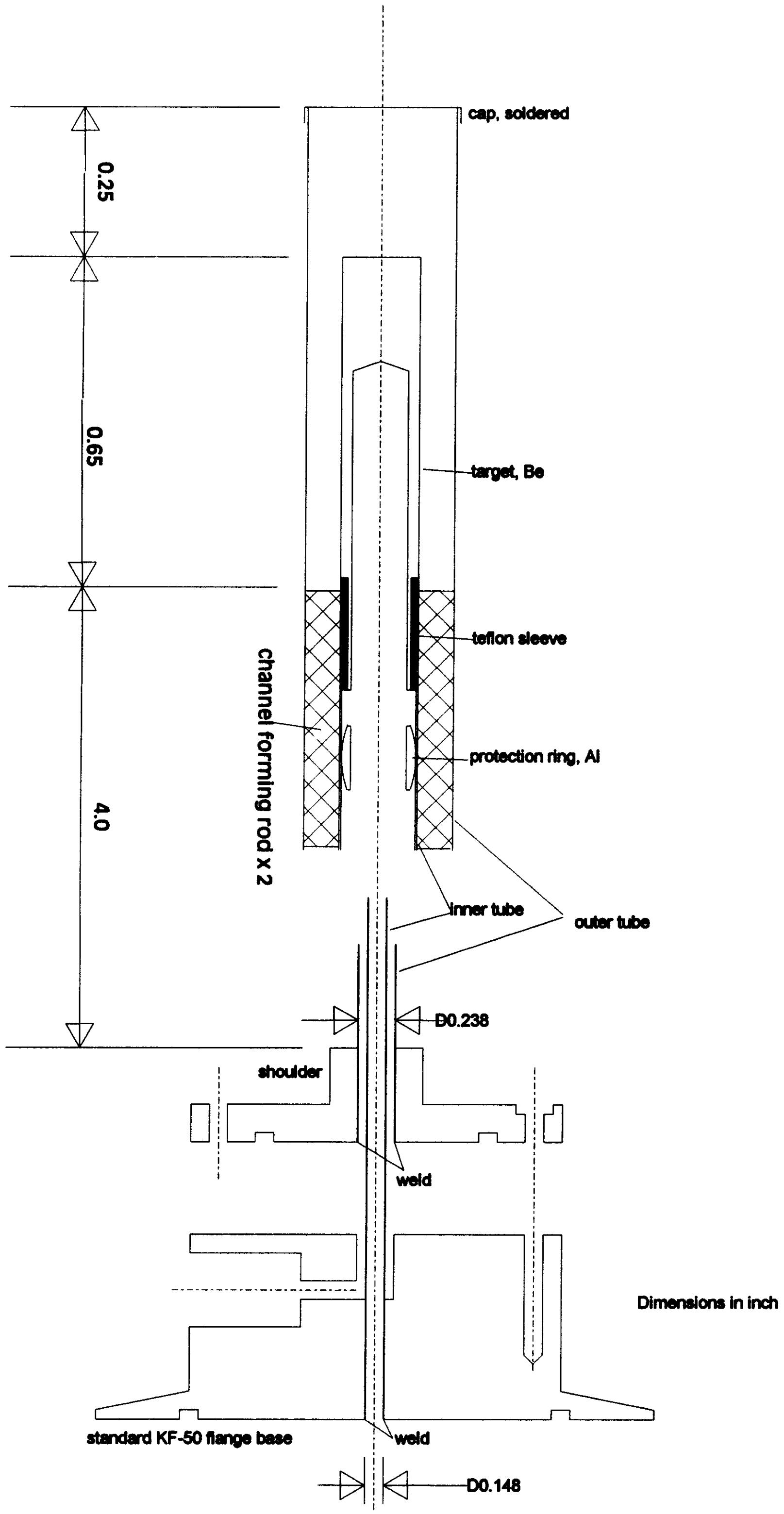

Figure 2.4.a. Needle tube Prototype II. The outer and inner tubes.

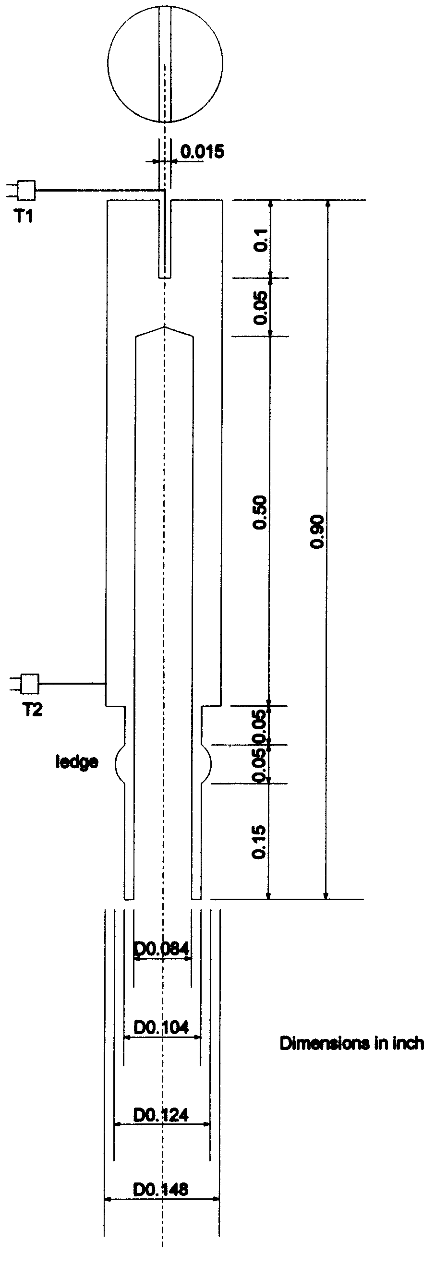

Figure 2.4.b. The Be target and positions of the two thermocouples.

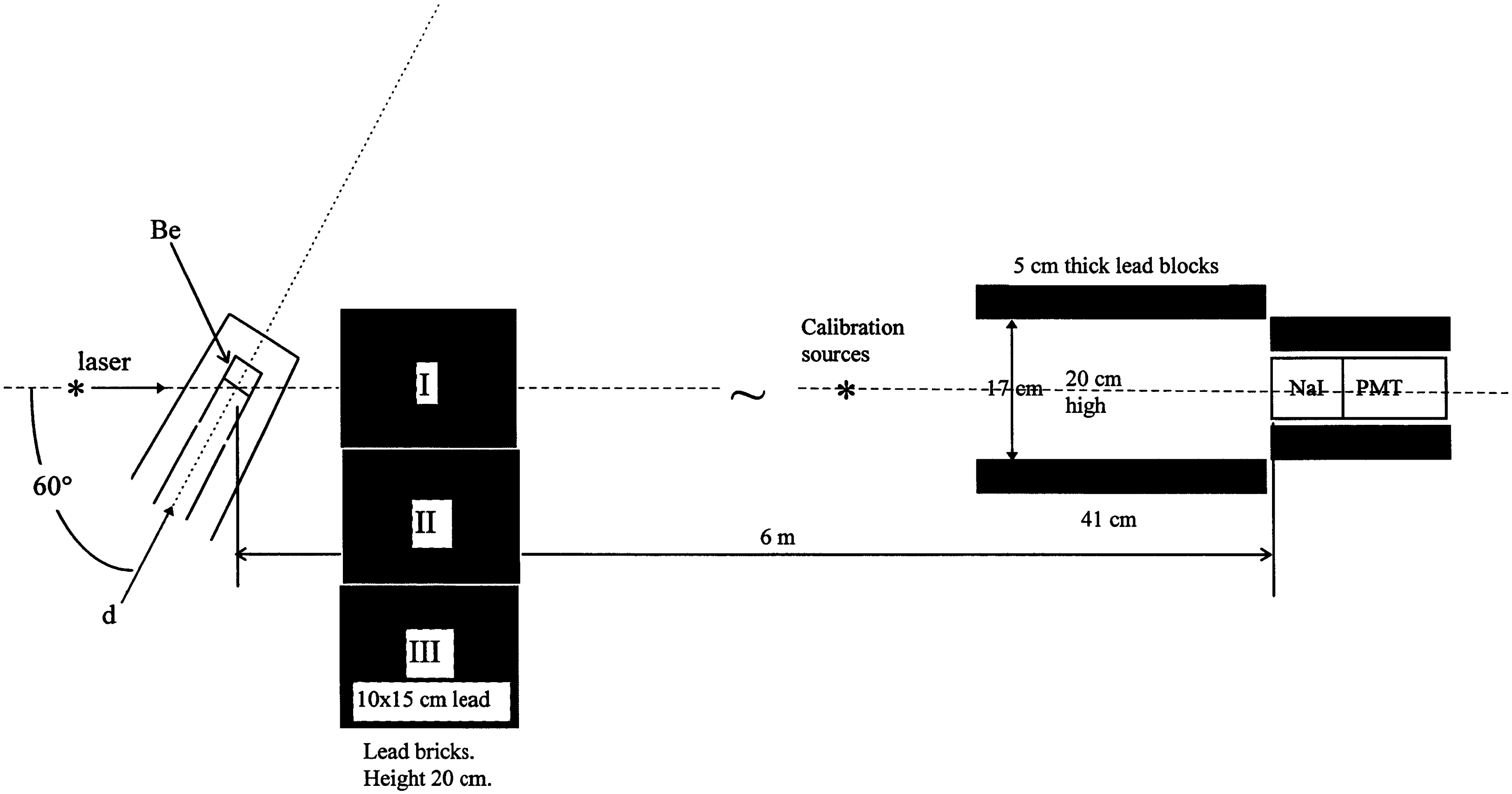

Figure 2.5. Schematic of the gamma yield measurement experiment. Top view. Arbitrary scale.

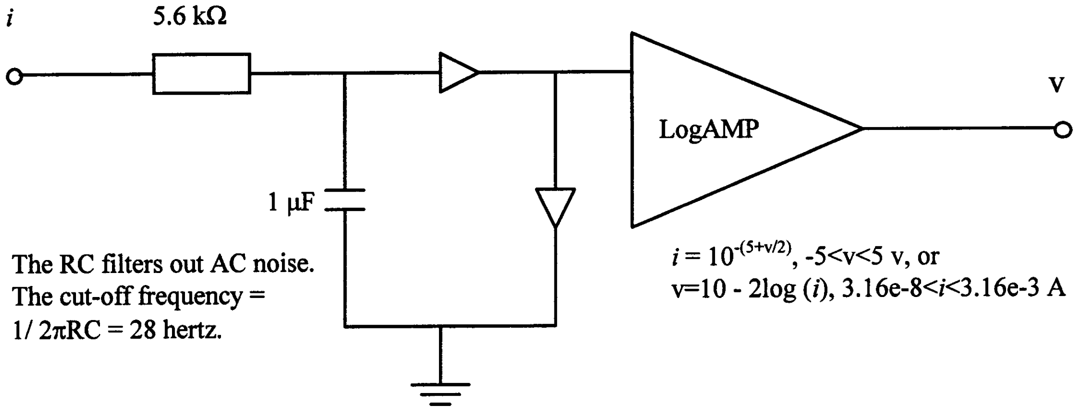

The RC filters out AC noise.
The cut-off frequency =
$1/2\pi RC = 28$ hertz.

$i = 10^{-(5+v/2)}$, $-5<v<5$ v, or
$v=10 - 2\log(i)$, $3.16e-8<i<3.16e-3$ A

Figure 2.6. The schematic of the LogAMP, which converts target DC currents to voltage signals for input into computer.

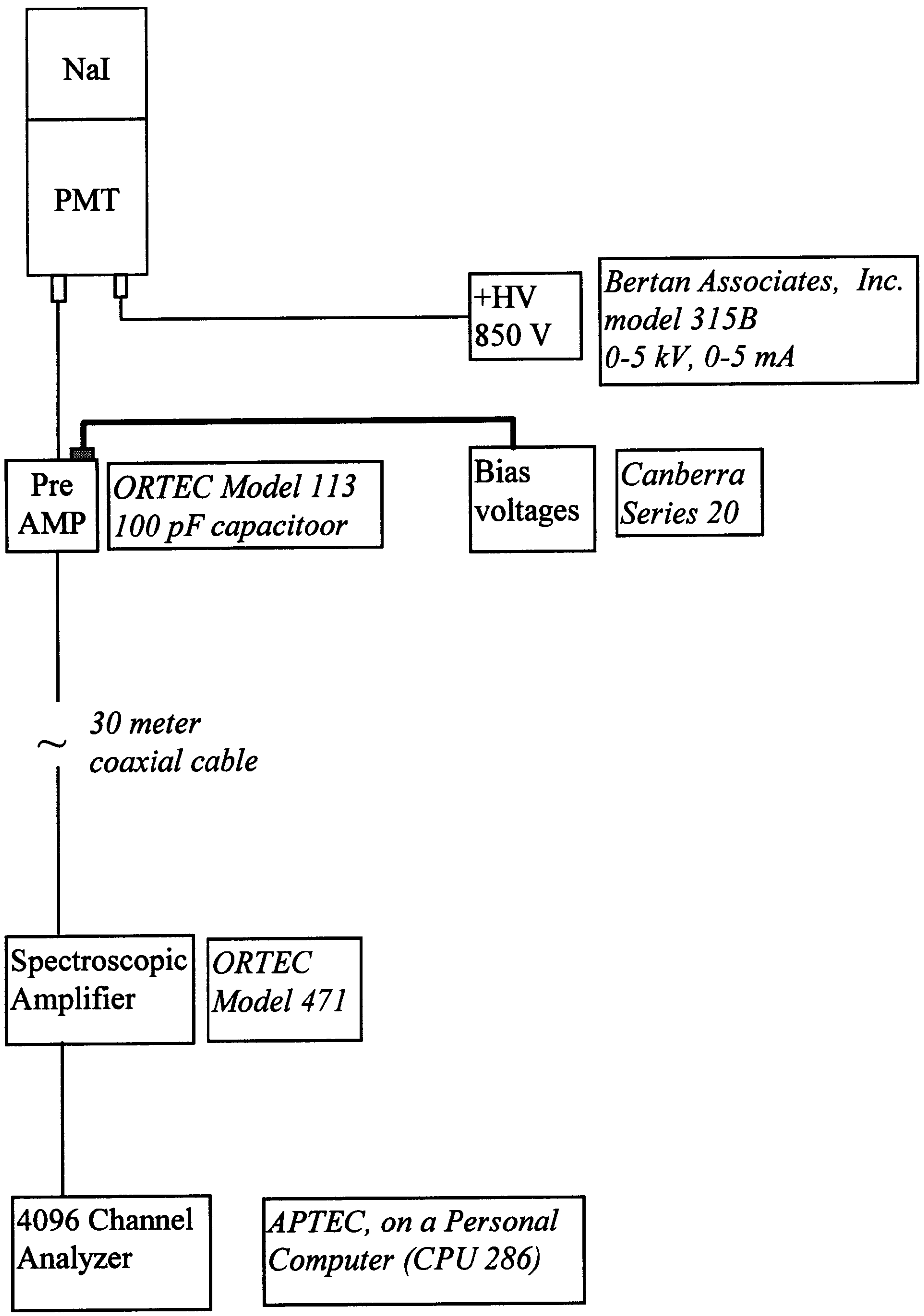

Figure 2.7. Diagram of electronics for the gamma yield measurements.

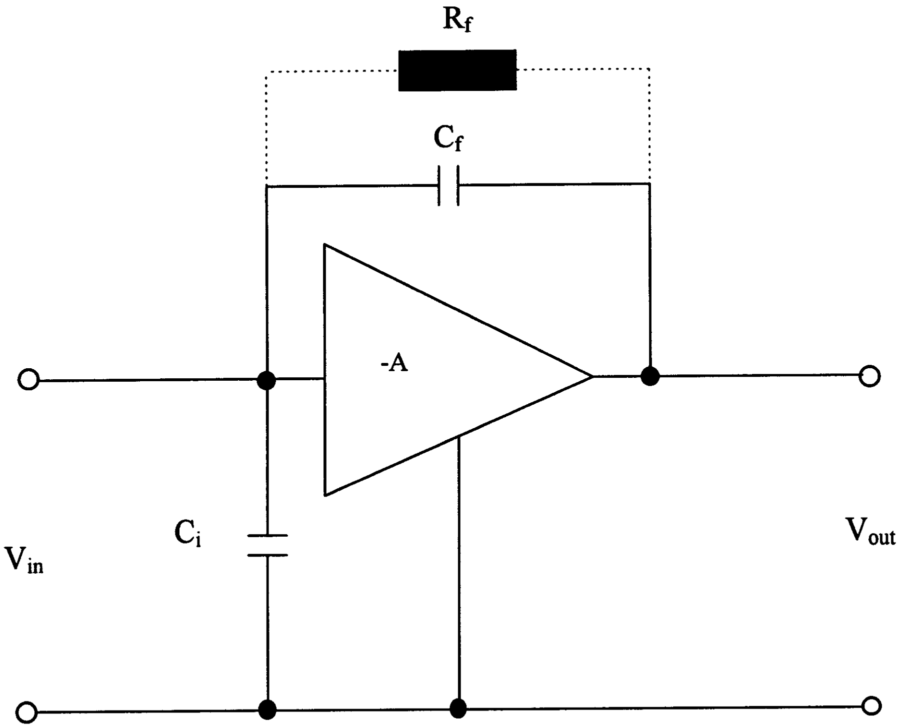

Figure 2.8. The diagram of a charge-sensitive mode PreAMP.

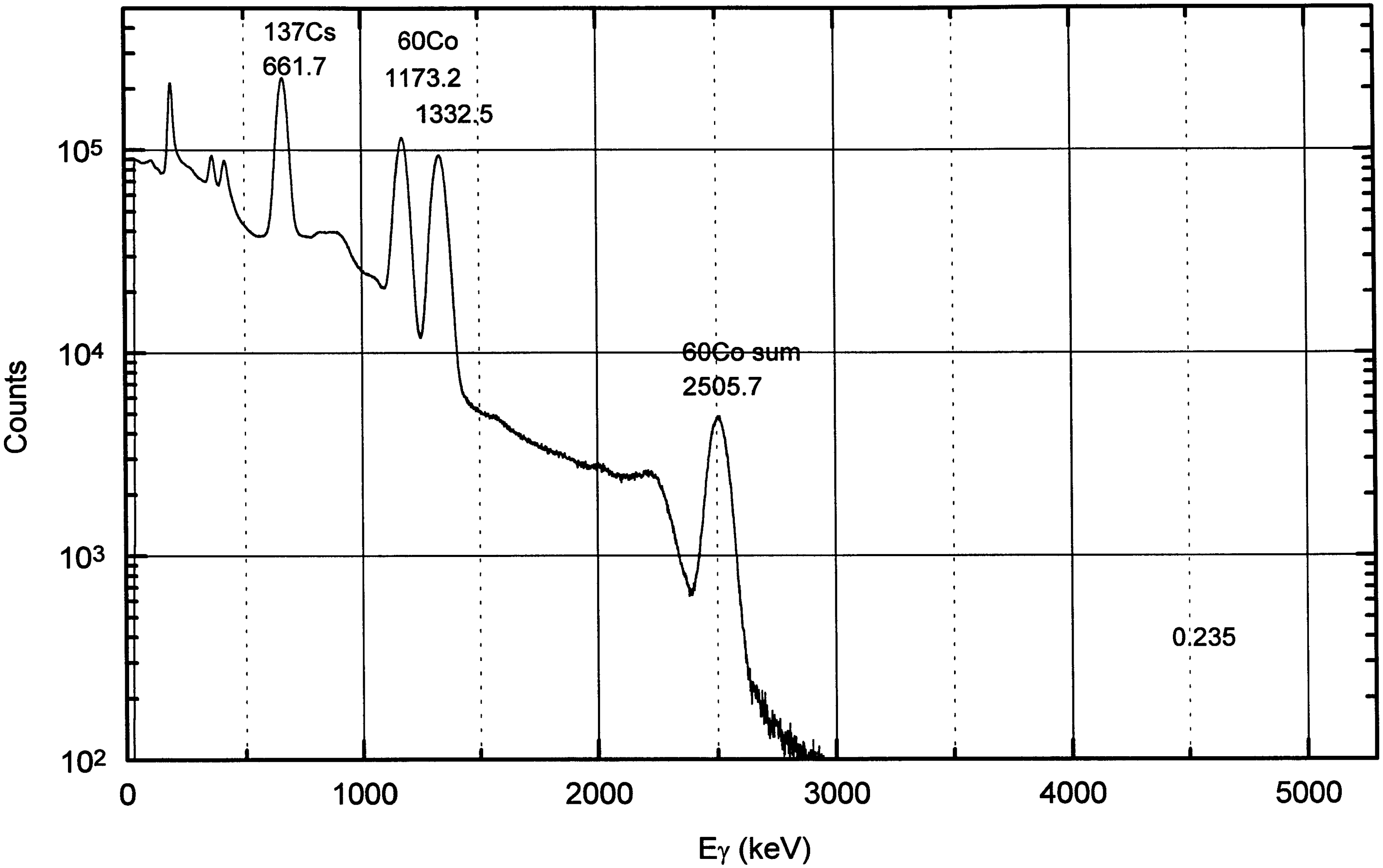

Figure 2.9. Spectrum of ^{60}Co and ^{137} Cs, for energy calibration of the NaI(Tl) detector.

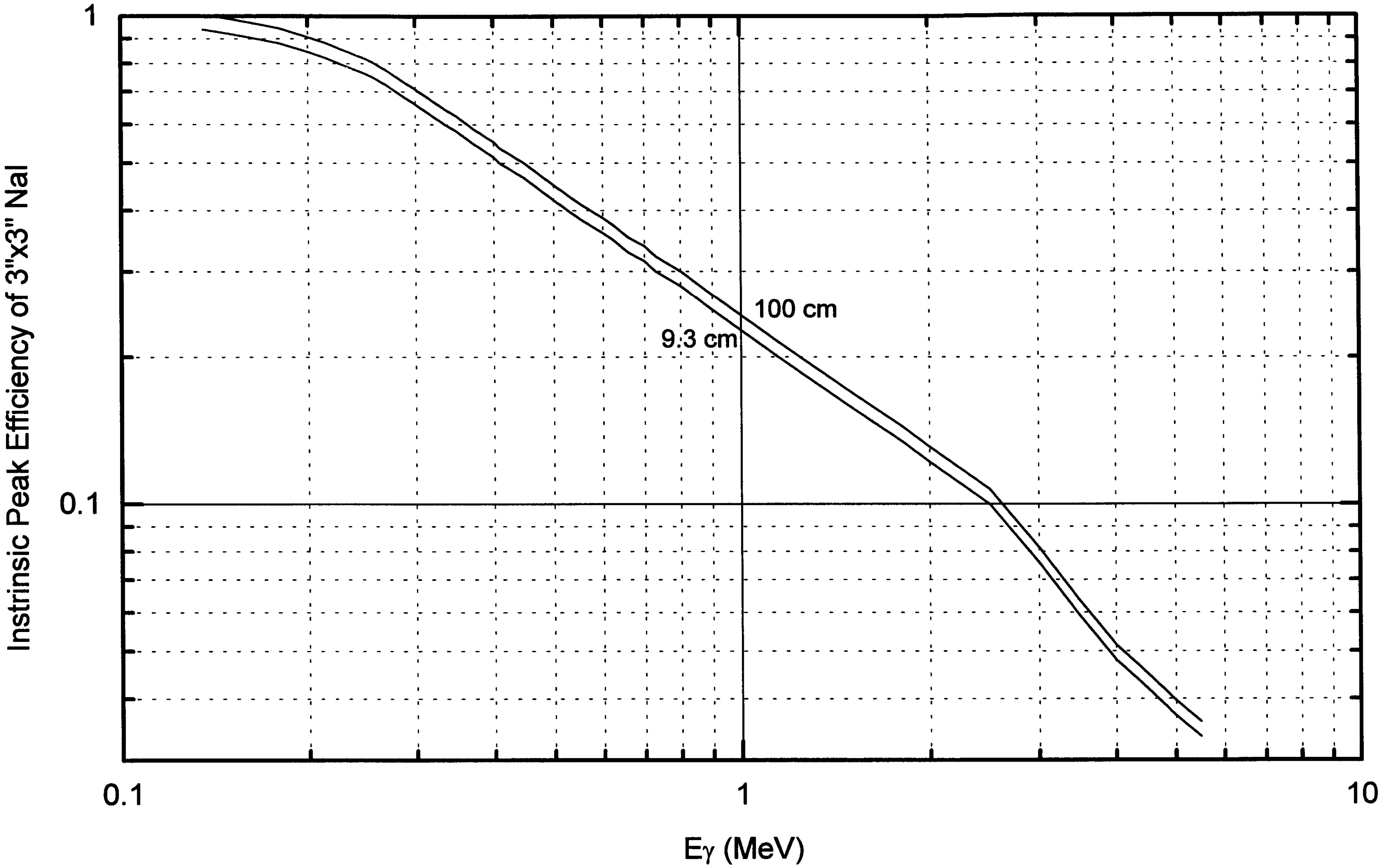

Figure 2.10. The intrinsic peak efficiency of a 76 x76 mm NaI detector, at a source-to-detector distance of 9.3 cm, as a function of gamma energy, replotted from Neiler and Bell, (1965). The curve for a source-to-detector distance of 1 m is scaled from the 9.3 cm curve (see text). Tabulated values are given in Table 2.3.

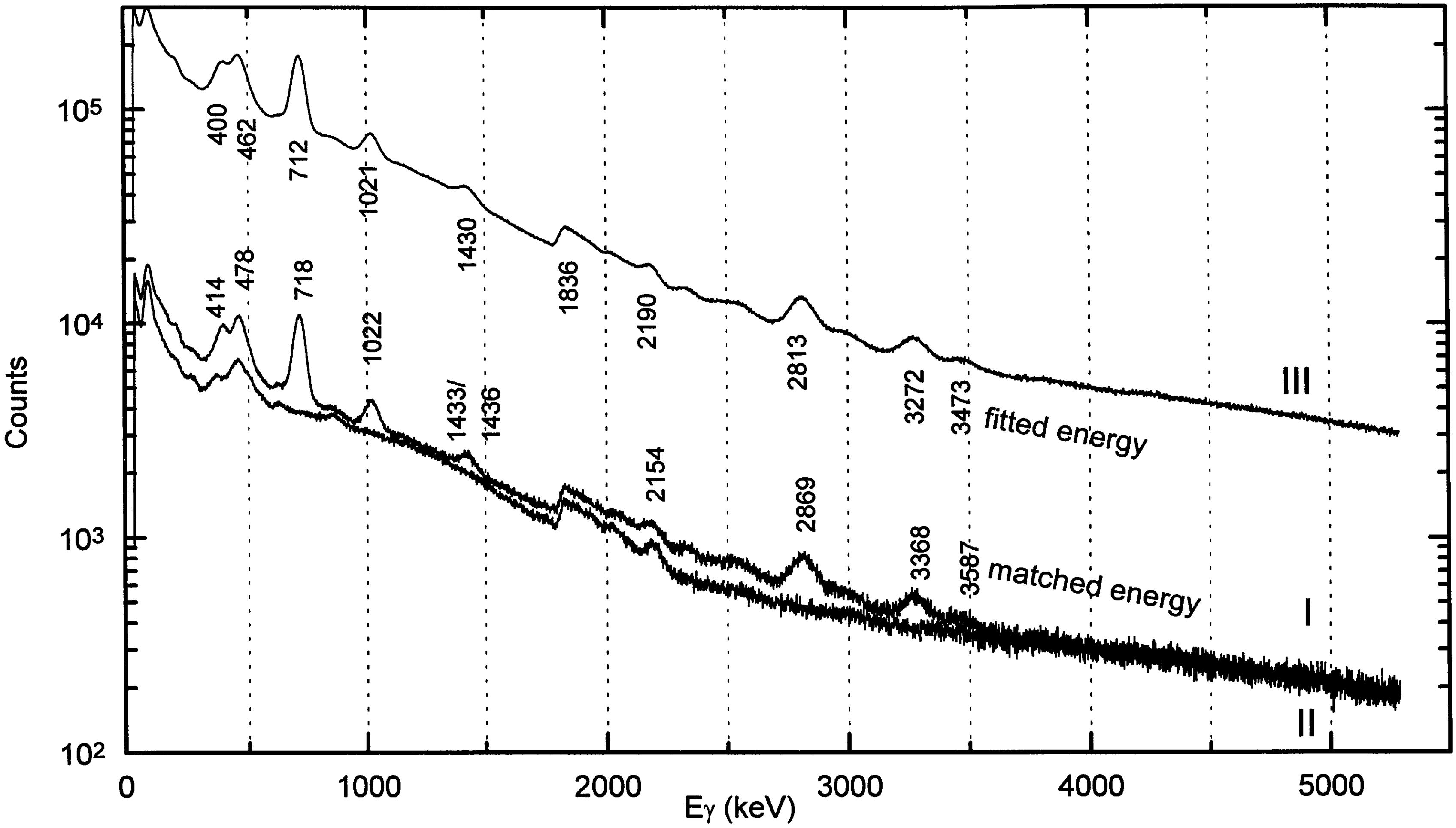

Figure 2.11. Spectra of gammas from 1.5 MeV deutrons hitting needle tube: I, gammas from the beryllium target and a small fraction from the needle tube (stailess steel and aluminum); II, gammas from the tube with the beryllium target blocked; III, longer counting version of I.

CHAPTER THREE

ION BEAMS

For Accelerator-Based Neutron Brachytherapy (ABNBT), delivery of accelerator beam to the target through the therapy tube is an essential part. The beam lines used to carry out all experiments on the prototype devices designed for ABNBT are investigated in this chapter, after an introduction of ion optics.

3.1. FIRST ORDER ELECTRIC CYLINDRICAL LENS

Examples of optical elements of this category are cylindrical lenses and acceleration tubes. This section intends to show, with the elements of this category, that ions behave in a way similar to light rays, and thereby validate the concept of "ion optics" which will be extended to cover other types of optical elements.

3.1.1. Trajectory Equation of Ions in an Axially Symmetric Electrostatic Field

The coordinate frame is placed so that the z axis resides on the beam and positive z points from the ion source towards the target, and the x, y axes reside in the plane perpendicular to the beam. (r, Θ) are the polar coordinates in (x, y) plane.

For an axially symmetric field, the static electric potential satisfies the Poisson equation:

$$\frac{\partial^2 P_e}{\partial z^2} + \frac{1}{r}\frac{\partial P_e}{\partial r} + \frac{\partial^2 P_e}{\partial r^2} = 0 , \qquad (3.1)$$

where P_e is the electric potential.

The equations of motion for the ion with electric charge Q are

$$m\ddot{r} = -Q\frac{\partial P_e}{\partial r}, \qquad (3.2.a)$$

$$m\ddot{z} = -Q\frac{\partial P_e}{\partial z}, \qquad (3.2.b)$$

where dotted variables are time derivatives.

The following equation can be either derived from equations (3.2) or directly from energy conservation:

$$\frac{1}{2}\,\mathrm{m}(\dot{r}^2 + \dot{z}^2) = -\mathrm{Q}\,\mathrm{P_e} + \frac{1}{2}\,\mathrm{m}\,\mathrm{V_0}^2, \qquad (3.3)$$

where V_0 is the initial velocity of the ion, and the ion source is at zero potential.

Let $-Q\,Pe + \frac{1}{2}\,m\,V_0^2 = |Q|\,P = q\,P$. Usually in real applications, the ion coming out of the ion source has near zero velocity compared with the final velocity and thus the initial motion can be ignored. Then P is the same as P_e for negative ions and the negative of P_e for positive ions. P is always positive and indicates the kinetic energy of the ion in both cases, thus called kinetic potential, or effective potential, effective voltage. One important feature of P should be pointed out here: P obeys the same equation (3.1) as P_e does. Using the new notation, we have

$$\frac{1}{2}\, m\,(\dot{r}^2+\dot{z}^2) = q\,P \quad . \tag{3.4}$$

To get the trajectory equation from the motion equations, we need to get rid of the dotted variables. The trajectory equation will have variables r and z only, taking P=P(z, r) as known. Take z as the independent variable. Primed variables are derivatives of z.

Substituting $\dot{r} = r'\,\dot{z}$ in equation (3.4), we obtain

$$\dot{z} = \left(\frac{2\,q\,P}{m\,(1+r'^2)}\right)^{1/2} \quad . \tag{3.5}$$

Transforming equation (3.2) using equation (3.5) and the following two transformations:

$$\ddot{r} = \dot{z}\,\frac{\mathrm{d}}{\mathrm{dz}}(\dot{z}\,r'),\ \ddot{z} = \dot{z}\,\frac{\mathrm{d}}{\mathrm{dz}}(\dot{z}),$$

we can obtain the trajectory equation,

$$\frac{\mathrm{d}}{\mathrm{dz}}\left(\frac{P^{1/2}}{(1+r'^2)^{1/2}}\,r'\right) - \frac{(1+r'^2)^{1/2}}{2P^{1/2}}\,\frac{\partial P}{\partial r} = 0. \tag{3.6}$$

The solution to this equation,

$$r = r(z),$$

is the trajectory of the ion, though the equation is hard to solve due to nonlinearity.

Without trying to solve this equation, readily observable is the independence of the trajectory on the charge-to-mass ratio of the ion. In other words, the trajectory is determined solely by the potential field regardless what the ion is. This is not surprising since the forces on the ion along the z and r directions are both proportional to the charge-to-mass ratio. The equivalence in the geometrical optics is the chromatic independence of the symmetric lenses. This independence on ion species will be lost in other fields such as a magnetic or electrostatic deflector, or a quadrupole magnetic lens.

3.1.2. First Order Approximation

One can expand P(z,r) into a power series of radius r about r=0:

$$P(z,r) = \sum_{k=0}^{\infty} A_{2k}(z)\,r^{2k} \quad . \tag{3.7}$$

Only even orders of r exist because of the symmetric relation

$$P(z,-r) = P(z,r). \tag{3.8}$$

Truncating the P(z,r) series, keeping the first two terms and substituting it into equation (3.1) gives

$$A_0(z) = V(z), \tag{3.9.a}$$

$$A_2(z) = -1/4\ V''(z), \tag{3.9.b}$$

where V(z) is the potential on the beam axis. Substituting equation (3.9) into equation (3.7) gives

$$P(z,r) = V(z) - 1/4\ V''(z)\,r^2 . \tag{3.10}$$

Substituting into the trajectory equation (3.6) gives

$$r'' + \frac{V'(z)}{2V(z)} r' + \frac{V''(z)}{4V(z)} r = 0. \tag{3.11}$$

In the process of simplification, terms containing r^2, r'^2, and $r r'$ are omitted, which constitutes the paraxial conditions: 1) $r' \ll 1$, which corresponds to a near parallel beam; and 2) r is small so that $V''(z)\, r^2 \ll 1$, which means a weak varying field along the z direction. An equivalent form is as follows:

$$\sqrt{V} \frac{d}{dz}(\sqrt{V}\, r') = -1/4\ V'' r. \tag{3.12}$$

This simplified equation, (3.11) or (3.12), is called the first order linear trajectory equation, also called the Gaussian trajectory equation.

3.1.3. Optical Parameters

The optical parameters are illustrated in Figure 3.1: object and image spaces separated by the field region, principal plane, H, focal plane, F, focal length, f, and x parameter (distance between the image and focal plane). Subscript "b" denotes the image side. The corresponding parameters on the object side are denoted by "a". The object and image planes are marked by "A" and "B", respectively.

The general solution to equation (3.11) can be written as

$$r(z) = r(A)\, u(z) + r'(A)\, v(z), \tag{3.13}$$

where u(z) and v(z) are two principal solutions satisfying the following initial conditions:

$$u(z{=}A) = 1,\ u'(z{=}A) = 0,$$
$$v(z{=}A) = 0,\ v'(z{=}A) = 1. \tag{3.14}$$

3.1.3.a. Object and Image Planes. Linear and Angular Magnifications.

If there exists a point z=B such that $B \neq A$ and v(B) =0, then r(B) = r(A) u(B). At this point, the trajectory is independent of the initial emerging angle $r'(A)$, i.e., all ions emerging from (z=A, r=r(A)) pass through the same point (z=B, r=r(B)). That is the concept of image. z=B is the image plane. The linear magnification is defined as

$$m_l = r(B) / r(A) = u(B). \tag{3.15}$$

The angular magnification is defined as

$$m_\alpha = v'(B) / v'(A) = v'(B)\,. \tag{3.16}$$

Both definitions of linear and angular magnifications are independent of the initial conditions.

3.1.3.b. Focal point and Focal Length.

The focal point is $z=F_b$ so that $u(F_b) = 0$. The proof is as follows. If $u(F_b) = 0$, then $r(F_b) = r(A)\, 0 + r'(A)\, v(F_b) = r'(A)\, v(F_b)$. For all rays emerging with zero angle $r'(A) = 0$, $r(F_b) = 0$, so they all pass through ($z=F_b$, r=0). By definition, F_b is the focal point. The focal length is:

$$f_b = -1 / u'(B). \tag{3.17}$$

Integrating equation (3.12) gives

$$\sqrt{V}\ u'|_{z=B} - \sqrt{V}\ u'|_{z=A} = \sqrt{V_b}\ u'(B) = -1/4 \int_{\text{region}}^{\text{field}} dz \frac{V''}{\sqrt{V}} r. \tag{3.18}$$

Under the thin lens approximation, i.e., the field region is small, object and image are both in field free space so that the potentials V_a and V_b are constants, and the trajectory changes only angle not radius in the field region so that in the field region, $r = u(A) = 1$, focal length is given by

$$1/f_b = 1/4\,(1/\sqrt{V_b}) \int_a^b dz \frac{V''}{\sqrt{V}}. \tag{3.19}$$

Now the integration is a function of the electric field only.

Similarly,

$$1/f_a = 1/4\,(1/\sqrt{V_a}) \int_a^b dz \frac{V''}{\sqrt{V}}. \tag{3.20}$$

A simple relation between the two focal lengths exists:

$$f_a / f_b = \sqrt{V_a} / \sqrt{V_b}. \tag{3.21}$$

3.1.3.c. The x Parameter and the Gaussian Relation

The parameter x_b is the distance between the image plane, B, and the focal point, F_b, and is given by

$$x_b = r(B) / r'(B) = u(B)\, r(A) / u'(B)\, r(A) = u(B) / u'(B). \tag{3.22}$$

It can be shown the optical Gaussian relation is valid in here:

$$x_a\, x_b = f_a\, f_b. \tag{3.23}$$

3.1.3.d. Principal Plane

The principal plane H_b is

$$H_b = F_b - f_b = F_b + 1 / u'(B). \tag{3.24}$$

3.1.4. Emittance

Emittance, ε, is defined as the area of the phase space (r,r') of an ion beam. The shape of (r,r') in phase space is usually assumed to be elliptical and at a waist at the exit of the ion source. The waist condition corresponds to a beam that is parallel to the axis at the beam edge and is at the maximum divergent angle at radius zero, as illustrated in Figure 3.2. Under the waist condition, the emittance is simply

$$\varepsilon = \pi\, r_{max}\, r'_{max}. \tag{3.25}$$

The ratio between emittance after and before optical transfer is equal to the multiplication of the linear and angular magnifications:

$$\varepsilon_b / \varepsilon_a = m_l\, m_\alpha = u(B)\, v'(B). \tag{3.26}$$

Using the geometrical relations in Figure 3.1, and Gaussian relation (3.23), it can be derived that:

$$u(B)\, v'(B) = f_a / f_b. \tag{3.27}$$

Under the thin lens approximation, combining equations (3.21), (3.26), and (3.27) gives

$$\varepsilon_b / \varepsilon_a = \sqrt{V_a} / \sqrt{V_b}. \tag{3.28}$$

Equation (3.28) is equivalent to statement that that $\sqrt{V}\,\varepsilon$ is conserved through the whole optical system. Normalized emittance is defined as

$$\varepsilon_n = \varepsilon\,\gamma\,v/c, \tag{3.29}$$

where γ is $1/(1-v^2/c^2)^{1/2}$, v is the speed of the ion, and c is the speed of light. For non-relativistic ions, conservation of normalized emittance is equivalent to the conserved quantity $\sqrt{V}\,\varepsilon$.

3.2. TRANSFER MATRIX

An equivalent expression of equation (3.13) is the following matrix:

$$\begin{bmatrix} r(z) \\ r'(z) \end{bmatrix} = \begin{bmatrix} u(z) & v(z) \\ u'(z) & v'(z) \end{bmatrix} \begin{bmatrix} r(A) \\ r'(A) \end{bmatrix}. \tag{3.30}$$

Denote $\begin{bmatrix} r(z) \\ r'(z) \end{bmatrix} = R(z)$, $\begin{bmatrix} u(z) & v(z) \\ u'(z) & v'(z) \end{bmatrix} = M(z, A)$, and a general form of the transfer matrix is written as

$$R(z_1) = M(z_1, z_0)\, R(z_0)\ . \tag{3.31}$$

In case of a series of n optical elements, each characterized by a transfer matrix, M_1, ..., M_n, the final vector $R(z_n)$ is

$$R(z_n) = M_n(z_n, z_{n-1})\ \ldots\ M_2(z_2, z_1)\ M_1(z_1, z_0)\ R(z_0) = M_{total}(z_n, z_0)\ R(z_0). \tag{3.32}$$

This expression is especially convenient for computer simulation.

Equation (3.30) defines a linear system. Trajectory tracing is usually used to calculate to higher orders.

Below are the transfer matrices for the optical elements to be used in the beam lines.

3.2.1. Drift Space

This is a field free space where the ions are under a constant effective electric potential.

$$M(z, 0) = \begin{bmatrix} 1 & z \\ 0 & 1 \end{bmatrix}. \tag{3.33}$$

3.2.2. Cylindrical Doublet and Triplet

A cylindrical triplet, as shown in Figure 3.3, can be broken into two mirrored doublets separated by a drift space, h. For a cylindrical doublet with a thin gap, g, between the two cylinders, the thin lens approximation applies and the lens itself occupies zero space along the z direction and changes only the direction of the beam. The matrix for a thin doublet is

$$M(g_+, g_-) = \begin{bmatrix} 1 & 0 \\ -1/f_b & 1 \end{bmatrix}. \tag{3.34}$$

The matrix for the triplet is

$$M(g_2, g_1) = \begin{bmatrix} 1 & 0 \\ -1/f_a & 1 \end{bmatrix} \begin{bmatrix} 1 & h \\ 0 & 1 \end{bmatrix} \begin{bmatrix} 1 & 0 \\ -1/f_b & 1 \end{bmatrix}, \tag{3.35}$$

where f_a and f_b are calculated by equations (3.19) and (3.20).

3.2.3. Acceleration Tube

An acceleration tube consists of three field regions: 1) low potential, V_a, zero field, $E_a=0$; 2) constant field, E_{acc}; and 3) high potential, V_b, zero field, $E_b=0$, as illustrated in Figure 3.4. The transfer matrix likewise can be separated into three parts, a thin lens at entrance (z_1), a constant acceleration region (z_1 -z_2), and a thin lens at exit (z_2).

The focal length, f_{1b} , for the thin lens at entrance can be calculated using equation (3.19):

$$1/ f_{1b} = 1/4\ (E_{acc} - E_a)/V_a = E_{acc} / (4V_a). \qquad (3.36)$$

Similarly, the focal length, f_{2b} , for the thin lens at exit is

$$1/ f_{2b} = 1/4\ (E_b - E_{acc})/V_b = -E_{acc} / (4V_b). \qquad (3.37)$$

Substituting the focal lengths into equation (3.34) gives the transfer matrices for the entrance and exit lenses, $M(z_{1+}, z_{1-})$, and $M(z_{2+}, z_{2-})$:

$$M(z_{1+}, z_{1-}) = \begin{bmatrix} 1 & 0 \\ -E_{acc} / (4V_a) & 1 \end{bmatrix}, \qquad (3.38)$$

$$M(z_{2+}, z_{2-}) = \begin{bmatrix} 1 & 0 \\ E_{acc} / (4V_b) & 1 \end{bmatrix}. \qquad (3.39)$$

Equation (3.19) is applicable to the constant acceleration region, where the integration is zero since the second derivative of potential is zero and so the focal length is infinite. From dynamics, we have

$$r(z_2) = r(z_1) + r'(z_1)\, 2\, d \sqrt{\frac{V_a}{V_b}},$$

(3.40.a)

$$r'(z_2) = r'(z_1) \sqrt{\frac{V_a}{V_b}},$$

(3.40.b)

under the condition $V_b >> V_a$, which is usually true when the accelerator tube is used.

Rewrite equation (3.40) in the matrix format:

$$M(z_{2-}, z_{1+}) = \begin{bmatrix} 1 & 2d\sqrt{V_a/V_b} \\ 0 & \sqrt{V_a/V_b} \end{bmatrix}. \qquad (3.41)$$

The total matrix for the acceleration tube is the multiplication of matrices (3.38), (3.39), and (3.41):

$$M(z_2, z_1) = M(z_{2+}, z_{2-})\, M(z_{2-}, z_{1+})\, M(z_{1+}, z_{1-}). \qquad (3.42)$$

3.2.4. Magnetic Quadrupole

In the first order approximation of the cylindrical lenses, the potential takes the form

$$P(z, r) = V(z) -1/4\ V''(z)\, r^2 . \qquad (3.10)$$

The r^2 term generates a force proportional to the distance from the central axis ("spring force") and is responsible that the ion moves like light rays. The quadrupole lenses generate fields of this nature directly along the transverse plane, thus are more efficient in beam maneuvering, while for electrical cylindrical lenses, the transverse force ($\propto V''(z)$) is only secondary to the axial force ($\propto V'(z)$).

Consider four infinite long magnetic poles with alternative senses placed every 90 degrees, as illustrated in Figure 3.5. The shortest distance from the pole surface to the central axis is R_0. The magnetic field is

$$\vec{B}(x,y,z) = (B_x, B_y, B_z) = (g\,y, g\,x, 0), \tag{3.43.a}$$

with a generating potential ($\vec{B} = -\nabla\Phi$)

$$\Phi = -g\,xy, \tag{3.43.b}$$

where g is a constant. To generate such a field, the poles follow the potential curves and form hyperbolae. The first order approximation trajectory equations are

$$x'' - k\,x = 0, \tag{3.44.a}$$

$$y'' + k\,y = 0, \tag{3.44.b}$$

with $k=q\,g/p_0$, where p_0 is the momentum of the particles, q the charge of ion. If $k>0$, the transfer matrices along x and y planes are:

$$M_x(z, 0) = \begin{bmatrix} \cos(kz) & 1/\sqrt{k}\sin(kz) \\ -\sqrt{k}\sin(kz) & \cos(kz) \end{bmatrix}, \tag{3.45.a}$$

$$M_y(z, 0) = \begin{bmatrix} \cosh(kz) & 1/\sqrt{k}\sinh(kz) \\ \sqrt{k}\sinh(kz) & \cosh(kz) \end{bmatrix}. \tag{3.45.b}$$

This lens converges the beam along the x direction and diverges along y. If k (or g) <0, the transfer matrices along x and y switch.

In case of finite length of the magnetic poles, L, the effect of the fringe field is approximated by introducing the effective length, L_{eff} (see, e.g., Grivet *et al.,* (1972)),

$$L_{eff} = L + 1.1\,R_0. \tag{3.46}$$

From the expression of k, it is obvious that the transfer matrices are a function of both ion charge and mass.

A quadrupole doublet consists of two quadrupoles of similar field strength stacked in series with a 90 degree phase shift of the poles. If along the x direction the first lens converges, then the second lens diverges, so the beam enters the second lens closer to the central axis than when it enters the first lens. The diverging field experienced by the beam in the second lens is weaker than the converging field in the first lens since the field is proportional to the distance from the central axis. Therefore, the net effect is convergence. Along the y direction, the first lens diverges and the second lens converges. The beam enters the second lens farther away from the central axis than it enters the first lens. So the beam experiences stronger converging fields than diverging fields. The net effect is also convergence. So the quadrupole doublet is capable of focusing beam along both directions.

Magnetic lenses can be used as "add-ons" to the beam line since they are in the air and not part of the whole voltage structure which generates the beam. Electric quadrupole lenses are equivalent in principle, however, the poles need to be in the vacuum.

3.3. BEAMS AND PROFILES

The optical system of the electrostatic tandem accelerator is about 140 inches (3.6 meter) long from the extraction aperture of the ion source to the end of the acceleration tube. Figure 3.6 shows a schematic of the accelerator optical system. It starts with the extraction electrode of a cylindrical triplet which prepares the beam for injection to the acceleration tube. The acceleration tube is divided into two parts by the high voltage terminal in the middle where the stripping foil is mounted. Two different sizes of stripping foils are used: 15.9 and 19.1 mm in diameter. Between the cylindrical lens and the accelerator, there is a pair of apertures of 1/4″ (6.35 mm) diameter, whose function is to define the acceptance and prevent stray electrons from entering the acceleration tube. The negative ions coming out of the ion source are accelerated toward the positive high voltage terminal, become positive ions after going through the stripping foil, and are repelled to the other end of the acceleration tube by the same high voltage terminal. However, in terms of effective voltage, the picture is very simple: the effective voltage is on a continuous increase.

The normalized emittance of the ion source is approximately $\varepsilon_n = 0.33\ \pi$ mm-mrad (Shefer and Klinkowstein, (1996)). At the beginning of the optical system (z=0), the effective voltage is around 20 kV and the maximum beam radius $r_{max} = 1$ mm. The maximum divergence, $r'_{max}= 0.0505$ rad, is derived from the following relation

$$\varepsilon_n = \pi\, r_{max}\, r'_{max}\, v/c. \qquad (3.47)$$

The velocity, v, is derived from the extraction voltage, V_{ext},

$$1/2\ m\, v^2 = q\, V_{ext}. \qquad (3.48).$$

The ideal beam profile has a minimum diameter (waist) at the apertures and the stripping foil position.

Two different beamlines were used for the experiments: before and after installation of the switching magnet. The beam profile is simulated with the code OPTIC II by Larson, (1988), which uses the first order transfer matrices. The beam profile is formed by tracing the two rays starting at (r_{max}, $r'=0$) and ($r=0$, r'_{max}) at z=0. OPTIC II uses the unit of inch for distance.

Different beams have been used for various experiments. These beams are all investigated in here and will be cited when they are used in the experiments described in other chapters.

3.3.1. Beam I

This beam was used before the switching magnet was installed. As shown in Figure 3.7, the beam line consists of an x-y steering magnet and a quadrupole doublet. Although the steering magnet plays a critical role in beam tuning, its effect on beam focusing is minimal for two reasons. First, steerers are weak lenses. Second, the optical system is assumed to be ideal to start with so steering is not needed in the simulation. The steering magnet is treated as drift space in the simulation.

The beam envelopes for 1.5 MeV proton beams under two injection conditions are shown in Figure 3.8. Under the two injection conditions, the voltage of the center cylinder of the injection cylindrical triplet differs by 5%, and the beam transport through the acceleration tubes varies from very strong to very weak focusing. The beam envelope has two minima inside the accelerator: one at the aperture before the acceleration tube and one at the stripping foil. The beam size is within the aperture diameters at both locations. The beam envelope is symmetric in the x-y plane until focused by the quadrupole doublet. To get to the target, the beam must travel a 10 cm long, 2.5 mm diameter tube. The beam envelope for the last 10 inches along the beam central axis is tabulated in Table 3.1. The biggest beam spot in the last 6 inches is 3.7 x 4.3 mm. Thus, under the best beam conditions, 39% (= 2.5 x 2.5 / (3.7 x 4.3)) of total beam is expected to be delivered to the target.

3.3.2. Beam II

This beamline with the switching magnet is the final version, as shown in Figure 3.9. The edges of the switching magnet poles are normal to the beam so there is no focusing effect. The experiments in this thesis were all carried out using the center port without using the bending function of the switching magnet. Thus, this beam is essentially the same as in Beam I except for the drift space occupied by the switching magnet.

The beam envelopes for 2.0 MeV proton beams under different injection conditions are shown in Figure 3.10. The two envelopes are produced by a 2% difference in the injection lens voltage adjustment. Compared with Beam I, the minimum beam diameter achievable is larger, probably due to the longer drift space after the quadrupole. However, for the same reason, the beam can be more parallel which could be an advantage for transporting the beam down a long thin tube. The beam dimensions in the last 10 inches of the beamline are tabulated in Table 3.2. The target to total current ratio is expected to be 63% (=2.5 x 2.5 / (4.1 x 2.4)).

3.3.3. Beam III

Beam III is the same as Beam II except the beam particles are 1.5 MeV deuterons. The beam profile under two different injection conditions are shown in Figure 3.11. The difference in the injection lens voltage adjustment is 5% . The beam dimensions in the last 10 inches of the beam line are tabulated in Table 3.3. The target to total current ratio is expected to 65% (=2.5 x 2.5/(4.0 x 2.4)).

Table 3.1. The minimum beam envelope of the last 10 inches to target of the 1.5 MeV proton beam without the switching magnet.

Distance	Dimension	
along central axis (inch)	x (mm)	y (mm)
-10	2.74	3.45
-9	2.79	2.74
-8	2.84	2.03
-7	2.90	1.32
-6	3.00	.863
-5	3.04	.914
-4	3.15	1.42
-3	3.30	2.13
-2	3.40	2.84
-1	3.55	3.55
target	3.71	4.31

Table 3.2. The minimum beam envelope of the last 10 inches to target of the 2.0 MeV proton beam.

Distance	Dimension	
along central axis (inch)	x (mm)	y (mm)
-10	3.66	2.29
-9	3.66	1.98
-8	3.71	1.73
-7	3.71	1.52
-6	3.76	1.42
-5	3.76	1.37
-4	3.81	1.47
-3	3.86	1.63
-2	3.91	1.83
-1	3.96	2.13
target	4.01	2.39

Table 3.3. The minimum beam envelope of the last 10 inches to target of the 1.5 MeV deuteron beam.

Distance	Dimension	
along central axis (inch)	x (mm)	y (mm)
-10	2.44	3.81
-9	2.34	3.05
-8	2.23	2.29
-7	2.18	1.63
-6	2.13	1.02
-5	2.13	0.81
-4	2.18	1.22
-3	2.29	1.88
-2	2.39	2.59
-1	2.49	3.35
target	2.69	4.11

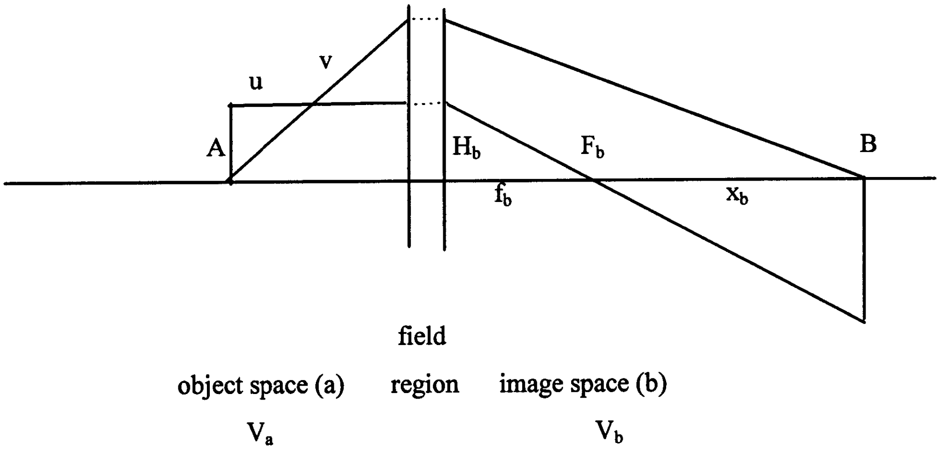

Figure 3.1. Illustration of the optical parameters.

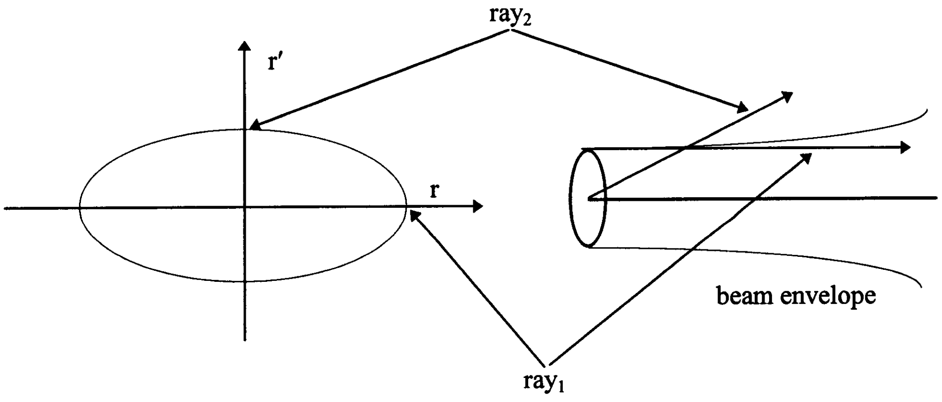

Figure 3.2. Illustration of the emittance ellipse and waist condition.

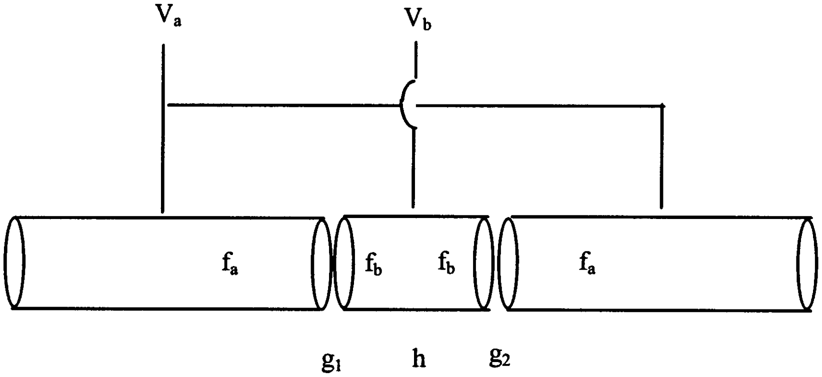

Figure 3.3. Illustration of the cylindrical triplet lens and its breakdown to two doublet and one drift space.

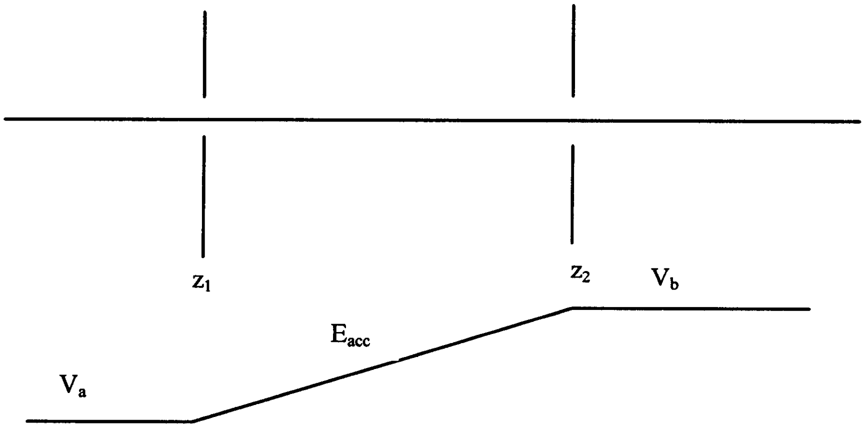

Figure 3.4. Illustration of acceleration tube.

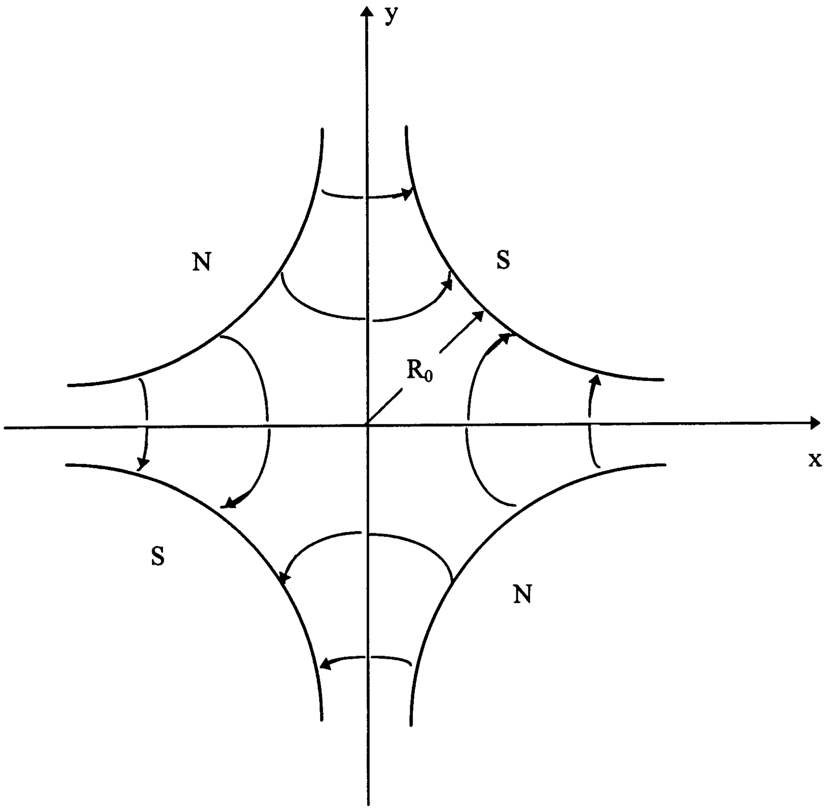

Figure 3.5. The cross section of the transverse plane of magnetic quadrupoles and the magnetic field lines. The z direction is perpendicular to the page.

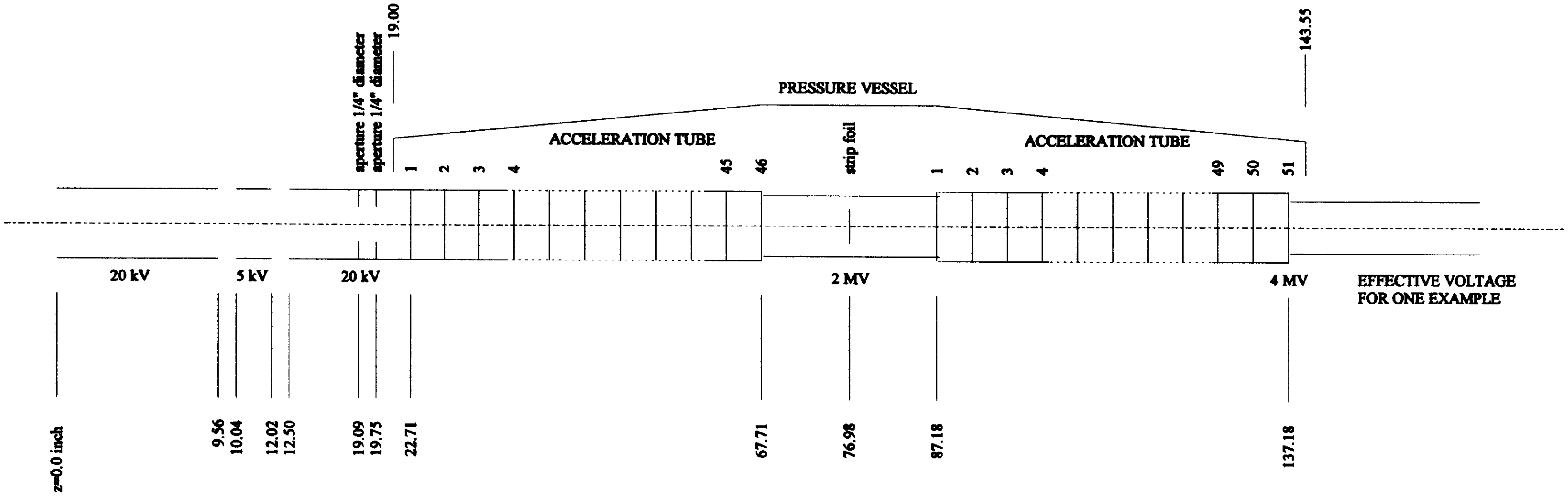

Figure 3.6. Schematic of the optical components of the tandem electrostatic accelerator at LABA.

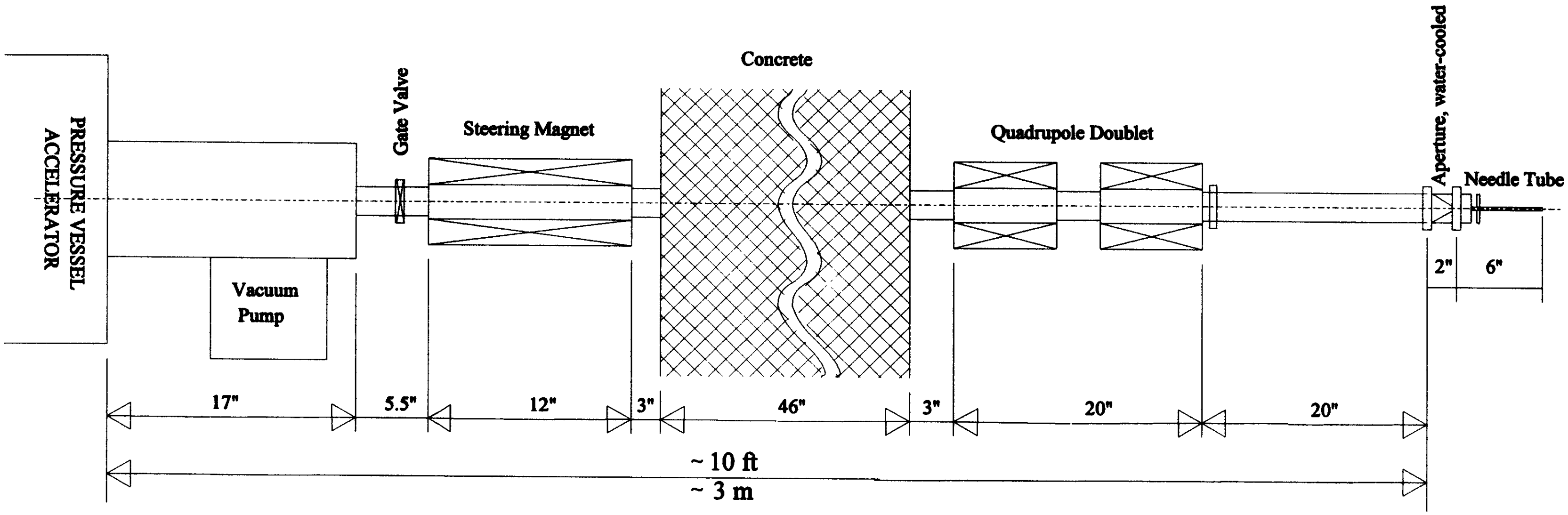

Figure 3.7. The beam line before installation of the switching magnet. Side view.

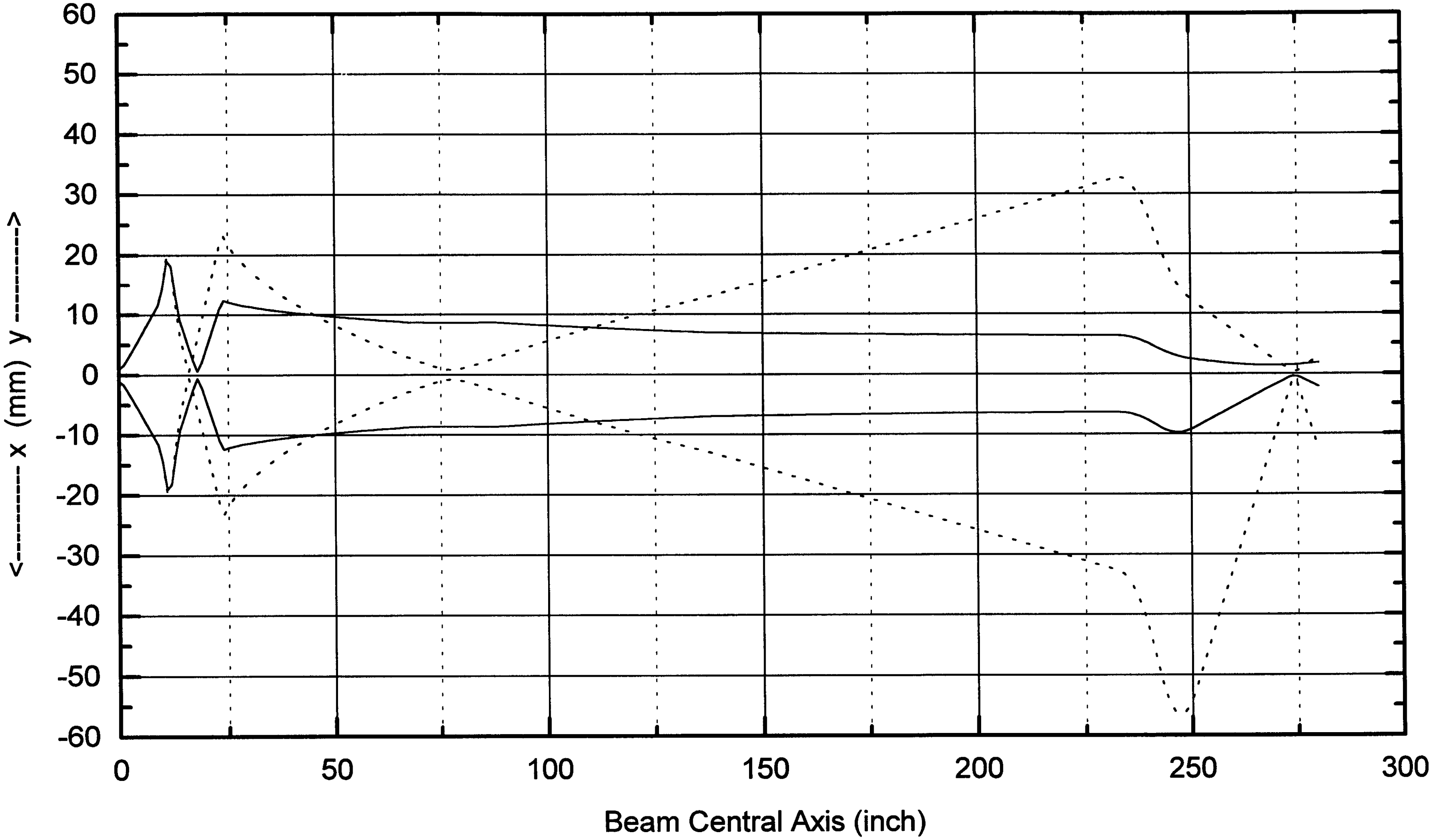

Figure 3.8. Envelopes of Beam I, the 1.5 MeV proton beams under different injection conditions, as described in Section 3.3.1.

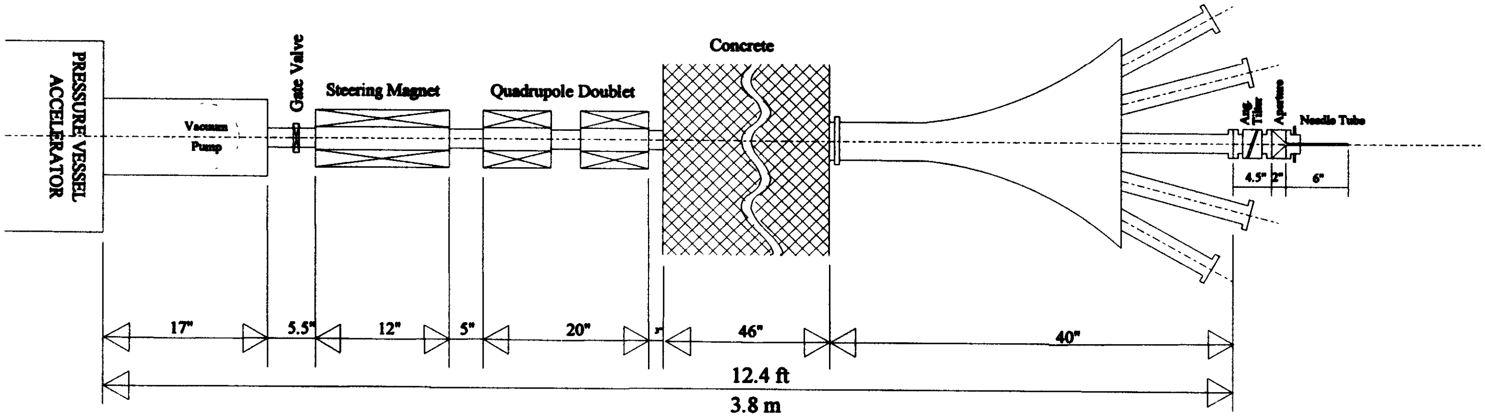

Figure 3.9. The beam line (final version). Top view.

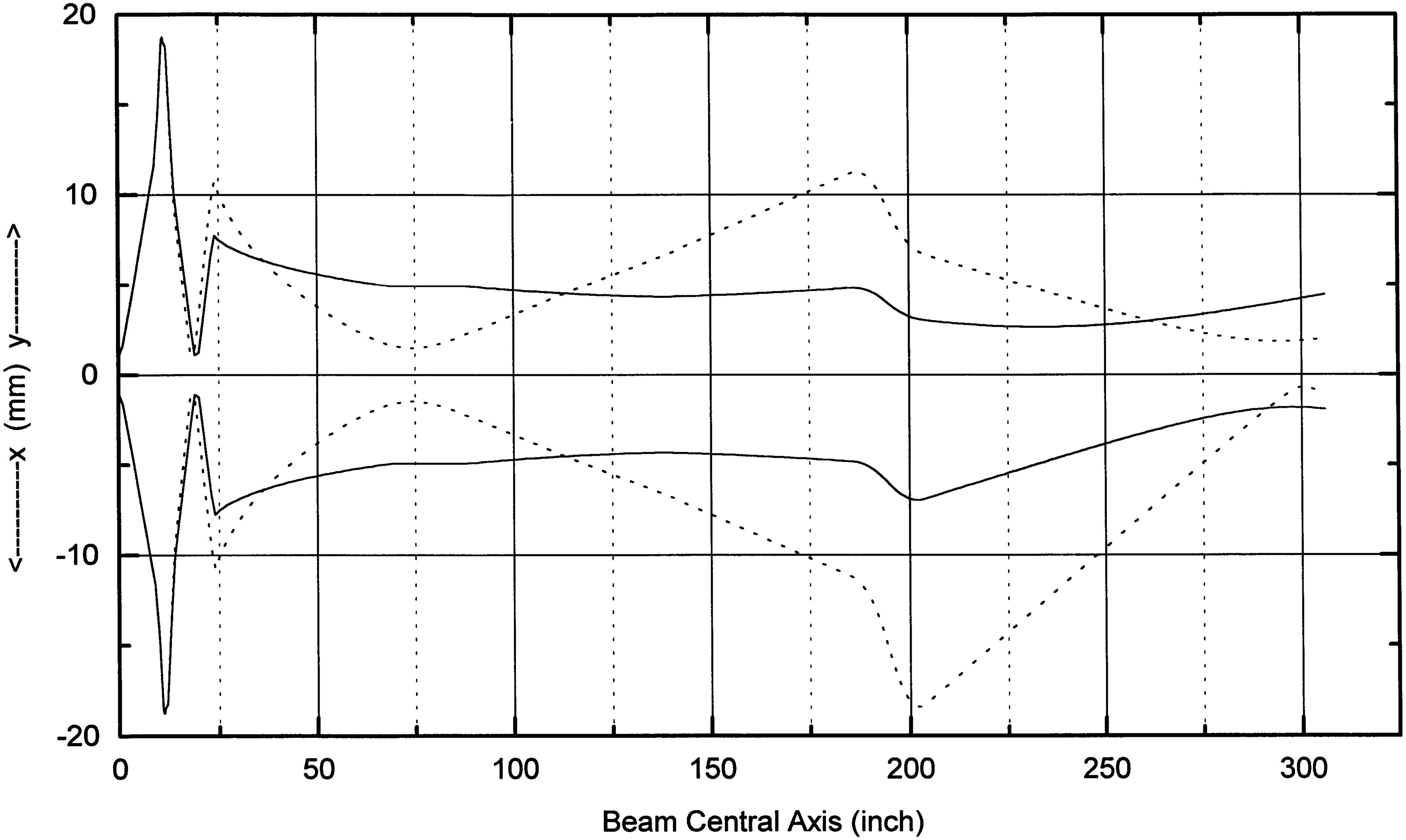

Figure 3.10. Envelopes of Beam II, the 2.0 MeV proton beams under different injection conditions, as decribed in Section 3.3.2.

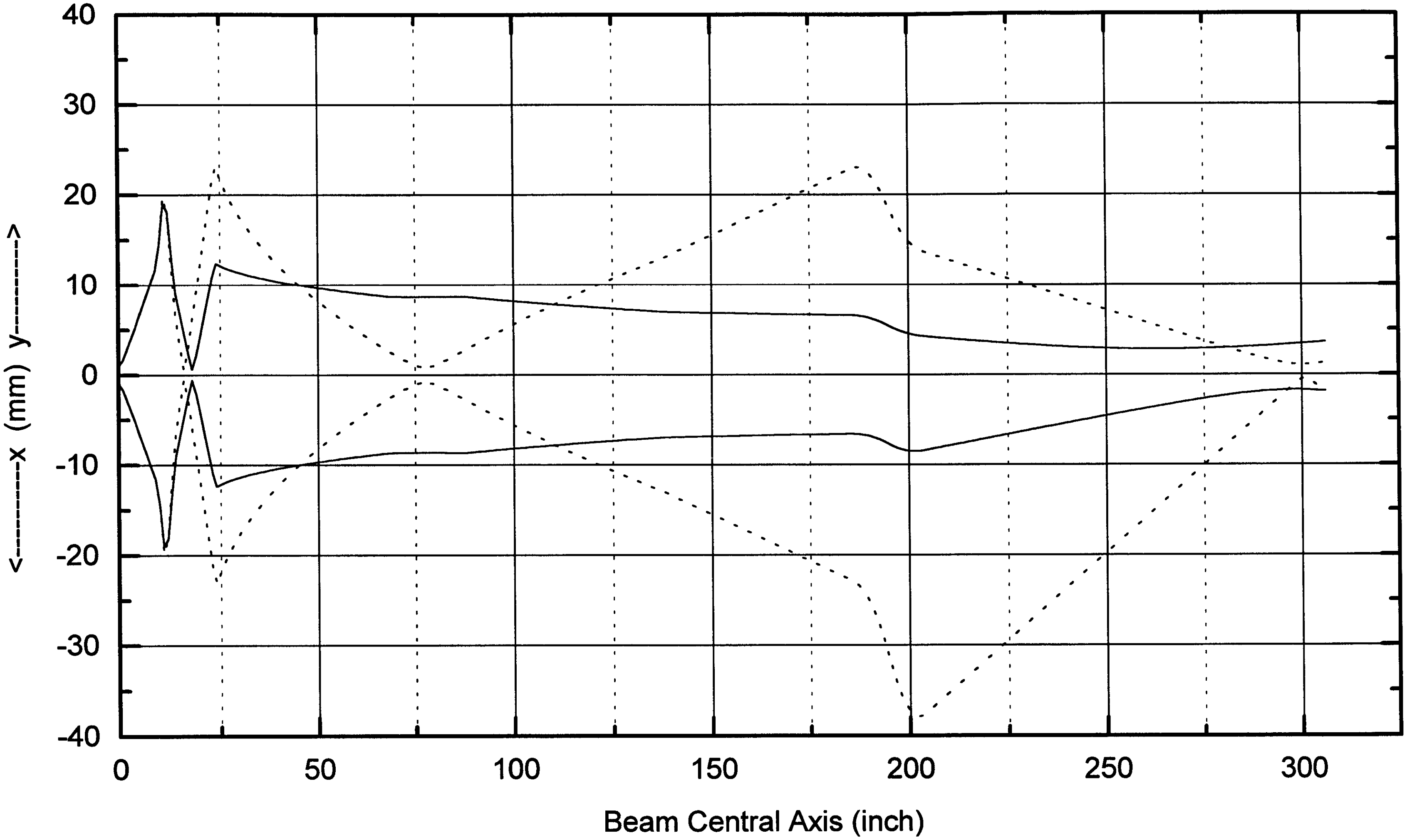

Figure 3.11. Envelopes of Beam III, the 1.5 MeV deuteron beams under different injection conditions, as decribed in Section 3.3.3.

CHAPTER FOUR
DOSIMETRY SIMULATIONS

One of the fundamental questions about Accelerator-Based Neutron Brachytherapy (ABNBT) is: can ABNBT deliver a dose rate high enough to be practical for radiation therapy? This question will be answered in two steps: calculation of dose distribution for the candidate nuclear reactions for a given heat load to the target and design of dose delivering devices that cope with a heat load that could deliver a practical dose rate. This chapter presents the dose simulations for all the candidate nuclear reactions. Chapter Five and Chapter Six will present two designs of the device. One of the candidate reactions will be chosen for comparison with dose measurement in Chapter Seven.

4.1. CHARGED PARTICLE REACTIONS

The primary criteria for candidate nuclear reaction selection are: high neutron yield and low charged particle energy; both reduce the requirements on accelerator technology. Other factors include the chemical, thermal, and mechanical properties of the target material, and dose enhancement by BNCT. Table 2.1 summarizes the neutron and source gamma yields for the candidate reactions under investigation. The charged particle energy is limited to be less than 4.1 MeV, which is the highest design energy of the tandem electrostatic accelerator (Shefer *et al.*, (1994)) in the Laboratory for Accelerator Beam Applications (LABA) at MIT.

4.1.1. ^{7}Li(p,n)^{7}Be

The ^{7}Li(p,n)^{7}Be reaction was suggested as a candidate reaction for ABNBT by Crawford, (1992).

Cross section data for the ^{7}Li(p,n)^{7}Be reaction from the threshold energy of 1.881 MeV to 7.0 MeV have been compiled by Liskien and Paulsen, (1975). At a proton energy of 2.373 MeV, a second neutron production channel starts: ^{7}Li(p,n')^{7}Be*. Neutron spectra from a thick natural lithium (92.5% ^{7}Li and 7.5% ^{6}Li) target can be calculated from the cross section data. The kinematics and conversion formulas for this reaction are summarized by Lee, (1997). The double differential neutron yield conversion formula is :

$$\frac{d^2Y}{d\Omega dE_n} = I_p/e\, N_{Li7} \frac{d\sigma}{d\Omega} \frac{dE_p}{dE_n} / \frac{dE_p}{dx}, \qquad (4.1)$$

where I_p is the proton current, e the electron charge, and N_{Li} the number density of lithium-7 in natural lithium.

A computer program in C has been written to carry out the conversions; for source code see Appendix A. The mass stopping power, S (MeV cm^2/g), is calculated from the formula:

$$S = -1/\rho \frac{dE}{dx} = \frac{A}{\beta^2} \left\{ \log\left(\frac{B\beta^2}{1-\beta^2}\right) - \beta^2 - \sum_{i=0}^{4} a_i \,[\log(E_p)]^i \right\}, \qquad (4.2)$$

where E_p is the proton energy in unit of keV, β is the proton speed in unit of speed of light, A, B, and a_0 to a_4 are fitted from experimental data for natural lithium by Anderson and Zeigler, (1985). The C code also integrates the spectra for total neutron yields and writes the source definition files for input into the Monte Carlo simulations.

In calculating the differential spectra and total yields, a low proton energy cut-off of 1.95 MeV was used for the ^{7}Li(p,n)^{7}Be reaction and 2.5 MeV for ^{7}Li(p,n')^{7}Be*, because they are the lowest energies for which the experimental cross section data are fitted in Liskien and Paulsen, (1975). The fact that the cut-off energies are above the backward threshold energies (1.920 and 2.423 MeV) of the two reaction channels allows simplicity in the yield spectrum calculations. Assuming a linear interpolation between the yield at the cut-off energy, the yields between the threshold and cut-off energies, $Y_{0Ep<1.95}$ and $Y_{1Ep<2.50}$, are estimated to be

^{7}Li(p,n)^{7}Be, $Y_{0Ep<1.95} = 3.27 \times 10^7$ n/μC,
^{7}Li(p,n1)^{7}Be*, $Y_{1Ep<2.50} = 2.23 \times 10^6$ n/μC.

As shown in Table 4.1, $Y_{0Ep(1.95\text{-}2.50)}$ is 8.10×10^8 n/μC, which is 25 times as large as $Y_{0Ep<1.95}$ and 360 times as big as $Y_{1Ep<2.50}$, while the yield $Y_{0Ep(1.95\text{-}2.00)}$ of 4.78×10^7 n/μC is comparable with $Y_{0Ep<1.95}$. However, as will be shown in Section 4.4, it will be proposed to use proton energies of 2.5 MeV and up for the ABNBT based on considerations of treatment time and gamma dose contamination, the effect of the proton energy cut-off will be insignificant.

The neutron spectra from the two reaction channels at angles of 0°, 45°, 90°, 135°, and 180° are plotted in Figure 4.1. The contours of the angular distribution of the yields integrated over neutron energy are plotted in Figure 4.2.

Significant accompanying source gammas are:

478 keV from ^{7}Li(p,p1)^{7}Li* and
429 keV from ^{7}Li(p,n1)^{7}Be*.

The yields from a thick natural lithium target have been measured at 55° relative to the incident proton beam by Kiss *et al.*, (1985). The total yield will be estimated by multiplying by 4π.

The Q value of the reaction ^{6}Li(p,n) is -5.070 MeV. A proton beam of 4.1 MeV does not produce neutrons on ^{6}Li. No significant source gamma was found (Kiss *et al.*, (1985)). So the presence of 7.5% ^{6}Li in natural lithium has no effect except reducing the effective neutron and source gamma yields per incident proton by 7.5% since ^{6}Li and ^{7}Li both attenuate the proton beam through ionization to the same extent.

4.1.2. ^{9}Be(p,n)^{9}B

The ^{9}Be(p,n)^{9}B reaction has a Q value of -1.8498 MeV. Neutron spectra and yields at proton energies of 3.7 and 4.0 MeV have been measured at angles of 0°, 20°, 40°, 60°, 80°, 110°, 115°, 120°, 125°, 130°, 135°, 145° and compiled between 0° and 148° by Howard, (1997). The neutron energy cut-off is 70 keV. An assumption of a constant spectrum between 145° and 180° is made for the present work to estimate total yield and spectrum over 0-180°. The new integrated yields are:

$Y_{En>0.070} = 1.13 \times 10^9$ n/μC, for E_p=4.0 MeV,

$Y_{En>0.070} = 8.22 \times 10^8$ n/μC, for E_p=3.7 MeV,

both about 7% higher than the values between 0° and 148° compiled originally by Howard, (1997). The integrated neutron yields are also listed in Table 4.1.

A significant source gamma of 3.562 MeV from the reaction ^{9}Be(p,αγ)^{6}Li is present. The yield has been measured by Kiss *et al.*, (1985) at 55° relative to the incident proton beam. The total yield will be estimated by multiplying by 4π.

4.1.3. ^{9}Be(d,n)B^{10}

Contrary to the ^{7}Li(p,n)^{7}Be and ^{9}Be(p,n)^{9}B reactions, the ^{9}Be(d,n)^{10}B reaction has a positive Q value of 4.36 MeV and can happen at a low accelerator energy. In the deuteron energy range of 1.4-2.8 MeV, there are three groups who have measured the neutron spectra: Inada *et al.*, (1968), Whittlestone, (1977), and Guzek *et al.*, (1996). As discussed in Section 2.1 of Chapter Two, the measurement of Whittlestone, (1977) is regarded as the most credible, but the measurement was performed for the deuteron energy of 1.4 MeV. The spectrum for E_d=1.5 MeV used in the present work was estimated by shifting up the E_d=1.4 MeV spectrum by 0.1 MeV, as discussed in Chapter Two and shown in Figure 2.1.c. The neutron yield is integrated in Chapter Two and listed in Table 4.1.

There are many gammas accompanying the (d,n) reaction. As discussed in Chapter Two, the gammas are: 0.414, 0.718, 1.022, 1.433, 1.436, 2.154, 2.869, and 3.587 MeV from the ^{9}Be(d,n'γ)^{10}B* reactions, 0.478 MeV from the ^{9}Be(d, α'γ)^{7}Li* reaction, and 3.368 MeV from the ^{9}Be(d,p'γ)^{10}Be reaction. The yields of these gammas at E_d=1.5 MeV were measured at 60° relative to the deuteron beam as described in Chapter Two and listed in Table 2.6. The total yields are estimated by multiplying the differential yields by 4π.

4.2. KERMA

Neutral particles react with media by two steps. First, charged particles are created through scattering or nuclear reactions. Second, the secondary charged particles cause ionization in the media. Kerma is defined as the sum of the initial kinetic energy transferred from the neutral particles to charged particles per unit mass, which is a result of the first step. In calculating kerma distribution, the energy sum takes place at the point where the energy transfer from the neutral particles to the charged particles occurs. Dose (absorbed dose) is defined as the energy deposition of the secondary charged particles and takes into account both steps. Under the condition of Charged Particle Equilibrium (CPE), when charged particles leaving a volume equal those entering, kerma equals absorbed dose. Inequality occurs in a region within the range of the charged particles from interfaces between different media. The range of electrons produced by gammas of interest to ABNBT (up to a few MeV) is up to around 1 cm in water. For the heavy charged particles (mostly protons) created by a few MeV neutrons in tissue, the range is less than 0.1 mm.

Calculation of kerma distribution can be done in two equivalent ways. First, kerma is the convolution between the neutral particle fluence (if given) and the fluence-to-kerma conversion factors. In the present work, the neutral particle fluence is calculated with the Monte Carlo code MCNP, Version 4A (Briesmeister, (1993)) using the f_4 tally. The f_6 tally of MCNP fulfills the definition of kerma and is the second way of calculating kerma. Both methods are used in the present work. The first method is used in this chapter. The simulation in Chapter Seven for comparison with dose measurements uses the second method. A comparison between the two methods will show that they differ by a factor of 3 on thermal neutron dose (for $E_n<0.36$ eV which is a negligible dose component for ABNBT) but give the same results for the other dose components.

4.2.1. Kerma Factors

4.2.1.a. Neutron Kerma Factors

The fluence-to-kerma conversion factors, or the kerma factors, for neutrons are calculated by Caswell *et al.*, (1980) from thermal neutron energy of 0.0253 meV to 30 MeV for 19 elements or nuclides: H, ^{6}Li, ^{7}Li, B, C, N, O, F, Na, Mg, Al, Si, P, S, Cl, Ar, K, Ca, and Fe. This study includes kinetic energy from the following reactions:

(i) Elastic scattering (n,n). The kinetic energy of the recoil nucleus is included in kerma without taking into account its charge status.

(ii) Inelastic scattering (n,n'). The nucleus usually de-excites by gamma emission which does not contribute to kerma.

(iii) Particle emission reactions: (n,2n), (n,n'p), $(n,n'\alpha)$, $(n,n'\alpha d)$, $(n,n'\alpha t)$, $(n,n'3\alpha)$, (n,p), (n,d), (n,t), (n, α), (n,2p), $(n,2\alpha)$, and $(n,p\alpha)$.

(iv) Radiative neutron capture (n,γ). The nucleus acquires kinetic energy from two sources: collision with incident neutrons and recoil from the gamma emission. At low neutron energies, the second term is more important. At high neutron energies, the first term dominates but the cross section for radiative capture reaction becomes negligible compared to other processes.

The cross section data used in the calculations are mainly from the Evaluated Nuclear Data File ENDF/B-4 (for neutrons below 20 MeV) maintained at Brookhaven National Laboratory, which combines evaluated experimental data with theoretical estimates. A preliminary version of ENDF/B-5 is used for carbon. The data ENDL (Livermore) are used for S, P, and Ar, and UKAEA for ^{11}B. Kerma estimates for the energy range 20-30 MeV are less accurate since extrapolated cross section data were used. However, the study of ABNBT is not affected; all neutrons will be below 20 MeV. The errors in kerma factors come mainly from the uncertainties in the cross section data. The error is 2% for hydrogen and around 10% for the other elements, both for $E_n < 20$ MeV (Caswell *et al.*, (1980)).

For neutrons below 100 keV, only exoergic reactions and elastic scattering are significant contributors to kerma since all the other reactions involve thresholds. The contribution from exoergic reactions usually increases with decreasing neutron energy since the cross section varies as $E_n^{-1/2}$ and the Q-value of the reaction is usually much bigger than the neutron energy. The important exoergic reactions include $^{14}N(n,p)^{14}C$, $^{10}B(n,\alpha)^7Li$, $H(n,\gamma)D$, and $^{17}O(n,\alpha)^{14}C$ for thermal neutrons. The average recoil energy is proportional to neutron energy and the cross section for elastic scattering is usually a weak function of the neutron energy. Hence elastic scattering contributes less to kerma with decreasing neutron energy.

When applying kerma factors to compounds rather than pure nuclides, new phenomena arise when the neutron energy approaches the first ionization potential of the molecules in the media. Firstly, should energy transfers below the ionization potential be excluded from kerma as they would not produce ionization? Secondly, chemical binding effectively increases the weight of the recoil nucleus and reduces the energy transfer from the neutron to medium. How should this be factored in the determination of kerma? Thirdly, as neutron energy (below 0.1 eV) approaches room temperature, thermal motions of nuclei become important. All the above three factors are ignored in the calculation of kerma factors for compounds. The authors point out, however, that the problems can be largely avoided if applying to compounds for neutron energies above 8 eV, as is done for 44 compounds in Caswell *et al.*, (1982).

The medium used in this ABNBT study is brain tissue (see Section 4.4 for elemental composition), the kerma factors of which are derived using simple element weighting of the kerma factors from Caswell *et al.,* (1980) and tabulated in Table 4.2 (Zhou, (1990)). As mentioned before in this section, the error of the neutron kerma factors are 2% for H and 10% for the others. For a compound comprised of H and other elements, the total error of the kerma factors should be dominated by the large error components. Therefore, the error for the kerma factors listed in Table 4.2 is taken to be 10%.

Comparison with MCNP simulations using the f_6 tally will show that the fast neutron dose (for E_n>0.36 eV) agrees within 1% while the thermal neutron dose calculated with the f_6 tally is 3 times as large. The simulations will also show that the thermal neutron is negligible for ABNBT. Therefore, the disagreement in the thermal neutron dose calculation with the two different methods does not affect the conclusion about ABNBT.

4.2.1.b. Photon Kerma Factors

Calculation of photon kerma factors are much simpler than that of neutron kerma factors. The only secondary charged particles are negative and positive electrons. Photons cause ionization in matter through three mechanisms: photoelectric process, Compton scattering, and electron pair production. Compton scattering dominates in water in the energy range of 0.1-10 MeV. Most gammas of importance to ABNBT fall within this energy range. Compton scattering cross sections can be calculated with the Klein-Nishina formula. The error in the kerma factor calculation should be very small and is assumed to be zero in the present work. (The error in photon dose will be dominated by errors from the neutron and source gamma yields.) The interaction of these photons with medium depends largely on the electron density, not on the elemental composition. As a result, the photon kerma factors calculated for one medium apply to other media. For a tissue with a density of 1.00 g/cm^3 and an elemental composition (by weight) of 71.39 % O, 14.89% C, 10.00% H, 3.47% N, 0.10% Cl, and 0.15% Na, the photon kerma factors are calculated by Zamenhof *et al.*, (1975) for the energy range of 0.055 -9.5 MeV and are tabulated in Table 4.3. These kerma factors are applied to the brain tissue in the present work without modification. Comparison with MCNP simulations using the f_6 tally for the brain tissue will show an agreement of better than 1%.

4.2.1.c. ^{10}B Kerma Factors

The reaction $^{10}B(n,\alpha)^7Li$ is the key to BNCT. Neutron kerma factors for 1 ppm boron-10 (1 μg of ^{10}B in 1 gram of tissue) have been compiled by Zhou, (1990) from the data of

Zamenhof *et al.*, (1975) and Caswell *et al.*, (1982), and are tabulated in Table 4.4. The error is not given in Zhou, (1990) nor in Zamenhof *et al.*, (1975). However, the methodology in calculating the boron-10 kerma factors should be the same as for other elements (10%) as done in Caswell *et al.*, (1982). Therefore, the error for the boron-10 kerma factors is taken to be 10%.

Comparison with MCNP simulation using the f_6 tally will show an agreement of 3%.

4.2.2. MCNP's f_6 Tally

MCNP calculates neutron and photon kerma through the f_6:n and f_6:p tallies. The energy spectrum of the kerma is available through the energy card. The f_6:n tallies for neutron energies below and above 0.36 eV are the thermal and fast neutron kermas. In the simulations in Chapter Seven, the f_6:n tally will be divided at 0.1 MeV to compare with dose measurements. The total f_6:p tally is the photon kerma. The boron-10 kerma is the total f_6:n tally with the boron-10 concentration in the medium subtracted by the total f_6:n tally without boron-10 in the medium.

The errors for the dose components per source particle are expected to be the same as those calculated with kerma factors as discussed in Section 4.2.1, i.e., 10% for fast neutron dose, 10% for thermal neutron dose, 0% for photon dose, and 10% for boron-10 dose.

4.3. RBE VALUES

The Relative Biological Effectiveness (RBE) is defined as the ratio between doses from a reference photon radiation and the radiation under investigation (e.g., neutron) to achieve the same endpoint (e.g., cell death) of irradiation. The RBE of gammas is a weak function of the gamma energies and is taken to be 1 in the present work. Neutron and boron-10 RBE values are taken from two different sources: ^{252}Cf brachytherapy for brain tumors (Miller *et al.*, (1991)) and BNCT clinical trials (Coderre *et al.*, (1993) and Morris *et al.*, (1994), summarized in Chada *et al.*, (1997)).

The average neutron energy in ABNBT is similar to that of ^{252}Cf (2.2 MeV). The therapeutic dose and RBEs from the ^{252}Cf therapy for the endpoint of tumor eradication will be adopted for ABNBT. The RBE for fast neutrons from ^{252}Cf has been determined to be between 5.0 and 6.0 and a value of 5.5 is taken for ABNBT. The unit RBE.Gy will be used to indicate an RBE weighted dose. A neutron dose of 12 Gy from Cf-252 was found to cause necrosis and eradication of Glioblastoma Multiforme (GBM). The therapeutic dose for ABNBT is

$$\text{Therapeutic Dose} = 12\ \text{Gy} \times \text{RBE} = 12 \times 5.5 = 66\ \text{RBE.Gy}.$$

In the ^{252}Cf studies, the thermal neutron dose is ignored, presumably, since it is not significant. Even the photon dose is ignored due to the fast neutron dominance (Wierzbicki, (1997)). The RBE of photon dose for ABNBT is 1.

Coupling between ABNBT and BNCT will be looked into. From the BNCT studies, the RBEs are taken to be 3.8 for the boron-10 dose and 3.2 for the thermal neutron dose.

In summary, the RBE values adopted for ABNBT are: fast neutron, 5.5; photon, 1; thermal neutron, 3.2; and boron-10, 3.8.

4.4. DOSIMETRY SIMULATIONS

Dosimetry simulations are carried out using MCNP (Version 4A) (Briesmeister, (1993)) to calculate the neutron and photon fluence distributions, which are converted to kerma (dose) distributions with the kerma factors. The results are dose distributions per source particle. Multiplying dose per source particle by the yield of the source particle of the particular reaction under investigation gives dose rate per charged particle beam current.

In the simulations, the radiation starts from an idealized point source at the center of a sphere of brain equivalent material (the tumor tissue is the same as the healthy tissue in terms of elemental composition). The elemental composition of gray and white matter has been published by Brooks *et al.*, (1980). The brain equivalent material is composed of 50/50% by weight average of gray and white matter and the elemental composition by weight is: 10.57% H, 13.97% C, 1.84% N, 72.59% O, 0.14% Na, 0.39% P, 0.14% Cl, and 0.39% K. The sphere has a diameter of 16 cm (the size of an average human head) and is divided into 16 spherical shells 0.5 cm apart along the radius. To determine the additional effect possible with BNCT, boron-10 dose converted with kerma factors for 40 ppm ^{10}B from the thermal neutron fluence without explicitly modeling the boron-10 content in the Monte Carlo simulations. (The thermal neutron absorption by the 40 ppm boron-10 is less than 12%, as will be shown in Section 4.4.2.) Dose resulting from neutron interactions is divided into four components: fast neutron (En>0.36 eV), induced photon, thermal neutron, and boron dose. The dose from source gamma(s) comprises the fifth dose component. As the first test of the feasibility of ABNBT, the dose distributions are averaged over spherical shells ignoring the angular distribution details.

The candidate reactions are investigated at the following energies.

(i) $^{7}Li(p,n)^{7}Be$, at proton energies of 2.0, 2.5, 3.0, and 4.1 MeV.

The energy of 4.1 MeV is the highest design energy of the tandem electrostatic accelerator in the Laboratory for Accelerator Beam Applications (LABA) at MIT. The energy of 2.0 MeV is near the threshold of 1.881 MeV. The energy of 2.5 MeV is near the threshold energy (2.37 MeV) of the $^{7}Li(p,n')^{7}Be^{*}$ reaction. A point between 2.5 and 4.1 MeV was chosen to be 3.0 MeV arbitrarily.

The source gamma yields are measured at proton energies of 1.7, 2.4, 3.1, 3.8, and 4.2 MeV (Kiss *et al.,* (1985)) and are interpolated linearly (Table 4.1).

(ii) $^{9}Be(p,n)^{9}B$, at proton energies of 3.7 and 4.0 MeV.

These energies are chosen because the spectra are directly available from measurements (with minor modifications). The source gamma yields are measured at proton energies of 1.7, 2.4, 3.1, 3.8, and 4.2 MeV (Kiss *et al.,* (1985)) and are interpolated linearly (Table 4.1).

(iii) $^{9}Be(d,n)^{10}B$, at deuteron energy of 1.5 MeV.

As explained in Chapter Two, Section 2.1, a deuteron energy of 1.5 MeV was chosen because the neutron spectrum was available from a very recent measurement (Guzek *et al.*, (1996)). The gamma yields were also measured at this energy and listed in Table 2.6 in Chapter Two. Later another spectrum (Whittlestone, (1977)) which was felt more reliable was used instead. But the spectrum is available for a deuteron energy of 1.4 MeV only, the next closest energy being 1.8 MeV. An estimate of the 1.5 MeV spectrum was made by shifting up the 1.4 MeV spectrum by 0.1 MeV. The $^9Be(d,n)^{10}B$ reaction at E_d=1.5 MeV will be chosen to perform dose measurements in a water phantom in Chapter Seven.

The MCNP input file for the reaction $^9Be(d,n)^{10}B$ at E_d=1.5 MeV is shown in Appendix B. For the other candidate reactions, only the source definition part is different.

4.4.1. Dose Components

Simulated dose rate components, with RBE weighting, as a function of distance from the neutron source in tissue are plotted in Figure 4.3.a-g for the candidate reactions. The dose rates are normalized to 100 Watts of power on the target. For every thousand protons or deuterons hitting the target, less than one would produce a nuclear reaction. The others lose all the kinetic energy through ionization and generate heat, which is a simple multiplication of the beam energy and the current, in the target. Since heat load is the main concern in the target design, the candidate reactions are compared with respect to the same amount of heat load. As will be shown in Chapter Six, 130 Watts were removed from the beryllium target in the prototype needle tube; 100 Watts is chosen as the heat load to which all the dose rates will be normalized. The spherical shells 0.5 cm apart in radius are represented by the mid point of the shell on the plots. For example, the data point at radius of 0.75 cm on the plots represents the dose averaged over the shell between 0.5 and 1.0 cm in radius. The total doses with and without boron contribution are sums of the RBE weighted dose components.

The $^7Li(p,n)^7Be$ reaction at E_p= 2.0 (Figure 4.3.d) is distinctively different from the other reactions in that the dose from source gammas is comparable to that from neutrons. The source gamma dose (all dose below refers to RBE weighted dose) constitutes 23% of the total dose without boron contribution at 0.25 cm of radius and 67% at 7.75 cm. The source gamma dose will still be prominent after correction for neutrons below the proton energy cut-off. The calculation underestimates the real doses from the neutrons due to the proton energy cut-off of 1.95 MeV in the neutron spectrum calculations. While neutrons between the threshold of 1.881 MeV and 1.95 MeV are negligible for the other proton energies (2.5, 3.0, and 4.1 MeV), it is comparable for 2.0 MeV: $Y_{0Ep<1.95} = 3.27 \times 10^7$ n/μC and $Y_{0Ep1.95\text{-}2.0}= 4.78 \times 10^7$ n/μC. The ratio of the two yields is 0.7 and the neutrons from the former group are less energetic. So these excluded neutrons are expected to at most increase the doses from neutrons by 70%. This reaction will be dropped from candidacy for ABNBT since a neutron therapy is desired rather than a photon therapy. (The long treatment time will be another reason that this reaction is not favored, as will be shown below.)

For the other reactions, the source gamma dose constitutes less than 8% of the total dose. More specifically, the source gamma dose as a percentage of the total dose without boron increases with radius since fast neutrons attenuate faster than gammas. The ranges of the source gamma doses as a percentage of the total doses are: 1-3%, 1-5%, and 2-8% for the $^7Li(p,n)^7Be$ reaction at proton energies of 4.1, 3.0, and 2.5 MeV; 0.7-2% and 0.7-3% for the $^9Be(p,n)^9B$ reaction at proton energies of 4.0 and 3.7 MeV; and 3-5% for the $^9Be(d,n)^{10}B$ reaction at a deuteron energy of 1.5 MeV. It follows from the low percentage of source gamma dose over the total dose that the errors in the estimation of total source gamma yields by multiplying the differential yields at 55° and 60° with 4π should have minimal effects on the dosimetry.

The other dose components follow a very similar pattern. The fast neutron dose dominates the region close to the source but decreases rapidly with distance partly due to the r^{-2} effect. Thermal neutron dose is negligible throughout the whole range. However, reactions between thermal neutrons and boron make a contribution comparable to that from the induced photons. The induced gamma, boron, and thermal neutron dose components are generated from within tissue rather than from the source and are less affected by the r^{-2} factor, so they show a smaller decrease with distance. Fast neutron dose still dominates the whole region except for the ^{7}Li(p,n) reaction at E_p=2.5 MeV, where a transition from fast neutron dominance to that of boron dose occurs at a radius of about 5 cm, due to the softness of the neutron spectrum.

As will be explained in the next section, with the boron-10 content (a thermal neutron absorber) in the medium explicitly modeled, the boron-10 dose will decrease by up to 12% depending on the size of the tumor.

4.4.2. Boron Enhancement Ratio

The Boron Enhancement Ratio (BER) is defined here as the ratio between the total dose with and without the contribution from the ^{10}B(n,α)^{7}Li reaction. BER is a measurement of the potential coupling of fast neutron brachytherapy and BNCT. BERs for the candidate reactions as a function of tumor radius are plotted in Figure 4.4.a. Starting from unity at zero radius, BER increases with radius before decreasing. This behavior is directly related to that of thermal neutron fluence. The source neutrons start as fast neutrons and thermalize through interacting with nuclei in the medium. At large radii, neutron dominance gives way to photon, and all neutron effects are minimized. So for a softer source neutron spectrum, BER has a higher peak. The near threshold reaction ^{7}Li(p,n)^{7}Be at E_p= 2.0 has some merit in this aspect: it has the highest BER peak of 3.05. The BER peaks for the other reactions range from 1.3 for the hardest spectrum of ^{9}Be(d,n)^{10}B at E_d= 1.5 MeV to 2.5 for the softest spectrum of ^{7}Li(p,n)^{7}Be at E_p= 2.5 MeV. The radius where the peaks occur is between 6-7.5 cm. While 6-7.5 cm radius is much larger than that of a single solid tumor, the boron-10 dose boost to those distant dispersed tumor sites (if any) could be very beneficial. A close look at the region of small radius is shown in Figure 4.4.b. For a tumor of 4.5 cm diameter, which corresponds to 2.25 cm in radius, BER ranges from 1.04 to 1.20, i.e., a tumor of 4.5 cm diameter with 40 ppm of boron will get between 4 and 20 percent more dose at the boundary than the healthy tissue without boron concentration would. This may make a big difference in the patient prognosis. In brachytherapy, the central portion of the tumor is usually "overkilled" since dose decreases quickly with distance from the source. The most difficult part is the boundary with healthy tissue where the tumor and healthy tissue receive the same dose and the cure relies on the lower tolerance of tumor cells. Any additional dose selectively delivered to the tumor while sparing healthy tissue at the boundary may be significant.

In calculating the boron-10 doses given above, the boron nuclei are not modeled in the medium. Inclusion of the borons in the medium should decrease the thermal neutron fluence since boron is a good thermal neutron absorber and so the boron-10 dose should decrease proportionally. To explicitly model the boron content, a separate MCNP run is needed for every tumor size. For example, for a tumor of 4.5 cm diameter, 40 ppm boron-10 will be added to the medium for radius < 2.5 cm and 0 ppm boron-10 for 2.5<radius<8 cm. Assuming a uniform 40 ppm boron-10 in the 8 cm radius medium will cause the most reduction of thermal neutron fluence. This lower limit case is compared with no modeling of boron-10 in the medium and the boron-10 dose is around 12% lower for the $^{7}Li(p,n)^{7}Be$ reaction at E_p=2.5 MeV. It is expected to be similar for the other reactions.

4.4.3. Treatment Time

Treatment time is defined as the time required to deliver the therapeutic dose to the boundary of tumor. (The total dose decreases with radius so the tumor tissue within the boundary will get over dosed.) The treatment time is calculated without boron contribution. The treatment times per 100 Watts of heat load on the target as a function of tumor radius are plotted in Figure 4.5. The $^{7}Li(p,n)^{7}Be$ reaction at E_p = 2.0 MeV has a long treatment time relative to the other reactions due to its low neutron yield and is thus not a good candidate for the therapy. The treatment times for a 4.5 cm diameter tumor are listed in Table 4.5. They are around 10 minutes for both the $^{7}Li(p,n)^{7}Be$ reaction at E_p= 4.1 MeV and the $^{9}Be(d,n)^{10}B$ reaction at E_d= 1.5 MeV, and 25 minutes for the $^{9}Be(p,n)^{9}B$ reaction at E_p= 4.0 MeV.

4.4.4. Kerma Factor vs. f_6 Tally

The f_6 tally of MCNP is a direct way of calculating kerma. The four different dose components are calculated using the f_6:p tally and f_6:n tally with energy cards, as described in Section 4.2.2. MCNP provides options of using different evaluated spectra data for neutron reactions including the cross section data (mainly ENDF) used in the kerma factor calculations by Caswell *et al.*, (1980). The cross section data for photon interactions used in MCNP and the photon kerma factors from Zamenhof *et al.* (1975) are different but the dose from photons of interest to ABNBT is not element dependent. Therefore, the two methods are expected to give similar results for all the four dose components (fast neutron, thermal neutorn, boron-10, and photon doses). A comparison is made for the $^{7}Li(p,n)^{7}Be$ reaction at E_p= 2.5 MeV. The photon dose calculated with f_6 tally is higher by up to 0.9%. The fast neutron dose (f_6 tally) is higher by up to 0.5%. The thermal neutron dose (f_6 tally) is higher by 200%, i.e., 3 times the value calculated with the kerma factors. The boron-10 dose (f_6 tally) is lower by 3%. It is expected to be similar for the other reactions. The above comparison shows that while the two methods of kerma calculation agree well for fast neutron and photon dose, the disagreement for thermal neutron kerma is significant. The disagreement in the thermal neutron dose calculation could be a result of the approximations made for low neutron energies in calculating the kerma factors (see Section 4.2.1.a). However, as demonstrated before, the thermal neutron dose is negligible for ABNBT and the disagreement does not affect the conclusions of ABNBT.

4.4.5. Phantom Size Effect

To see the effect of phantom size on dose distributions, a comparison is made between the 16 diameter phantom (approximating the size of a head) and a 40 cm diameter phantom (approximating the size of a torso) for the ^{7}Li(p,n)^{7}Be reaction at E_p= 2.5 MeV, as shown in Figure 4.6. The thermal neutron, boron, and induced gamma dose in the 16 cm meter diameter phantom are all lower than those in the 40 cm diameter phantom. The reason is that the phantom material in the outer radius reflects thermal neutrons so that a bigger size phantom increases the thermal neutron fluence at a small radius. With increasing radius, the medium outside decreases. So the thermal neutron fluence decreases with radius and becomes lower than that in a 40 cm diameter phantom by a larger amount. The boron dose and the induced gamma dose are all directly related to the thermal neutron fluence and should show similar behavior as the thermal neutron fluence. The dose component ratios between the 40 and 16 cm diameter phantoms increases with distance and maximizes at the boundary of the 16 cm diameter phantom. The ratios are 1.1 - 3.8 for thermal neutron dose, 1.1 - 3.7 for boron dose, and 1.6 - 2.9 for induced photon dose. The effect on fast neutron dose is very small. The agreement is within 0.5% up to 5 cm radius between the two phantoms. The difference also increases with radius and reaches a maximum of 10% at the boundary of the 16 cm diameter phantom. The effect of phantom size on the total dose is small because fast neutron dose is the dominant dose component, the thermal neutron dose is negligible, and the photon dose induced by neutrons are much less than that from source gammas. However, the effect on the Boron Enhancement Ratio (BER) can not be ignored.

4.5. CONCLUSIONS

The simulations show that at a heat load of 100 Watts to the target, all the three reactions, ^{7}Li(p,n), ^{9}Be(p,n), and ^{9}Be(d,n) are capable of delivering a therapeutic dose in a fraction of an hour for a tumor of a few centimeters in diameter. They are the candidate reaction pool for ABNBT. Heat removal experiments on the prototype ABNBT devices (Chapters Five and Six) will show that 100 Watts at target can be reasonably handled.

From the point view of dose rate, the ^{9}Be(d,n) reaction is the favorite because it offers a dose rate similar to or better than that of the Li(p,n) and Be(p,n) reactions at a much lower beam energy. However, the ^{9}Be(d,n) reaction has a harder spectrum. As a result, the benefit of coupling with BNCT is minimal.

The neutron dose dominance (over 90% of the total dose) indicates that ABNBT is mainly a fast neutron therapy. Accompanying gamma dose is generally a few percent, the most abundant being from the ^{9}Be(d,n)^{10}B reaction at E_d= 1.5 MeV (4-6%).

The boron enhancement depends on hardness of the neutron spectrum. The softer the neutron beam, the greater the dose enhancement. But a softer neutron spectrum is associated with a lower neutron yield at a lower charged particle beam energy and a longer treatment time. To benefit from BNCT, a balance needs to be made between the boron enhancement and the treatment time. For a tumor of 4.5 cm diameter, the additional dose from 40 ppm of boron-10 ranges from 4%, for the hardest neutron spectrum from the ^{9}Be(d,n)^{10}B reaction at E_d= 1.5 MeV, to 20%, for the softest neutron spectrum from the ^{7}Li(p,n)^{7}Be reaction at E_p= 2.5 MeV among the candidate nuclear reactions considered.

The next two chapters will cover two prototype designs mainly for determination of the heat removal capacity. Treatment times will be calculated and discussed in the corresponding chapters.

Table 4.1.Neutron yield (n/μC) and differential gamma yield (n/sr/μC) for the candidate reactions. References in Section 4.1.

Ep or Ed	Li(natural)+p				9Be+p		9Be+d	
(MeV)	(p,n)	(p,n1)	(p,p'γ)478keV	(p,n'γ) 429 keV	(p,n)	(p,α γ)3562keV	(d,n)	(d, γ)
0.50			(at 55°)	(at 55°)	En cutoff	(at 55°)	En cutoff 75 keV	Table 2.6
1.50					70 keV		6.02E+08 (±10%)	(at 60 °)
1.95	cutoff							
2.00	4.78E+07		1.56E+07					
2.05	9.71E+07							
2.10	1.50E+08							
2.15	2.15E+08							
2.20	2.98E+08							
2.25	4.02E+08							
2.30	5.09E+08							
2.35	6.01E+08							
2.40	6.78E+08							
2.45	7.46E+08							
2.50	8.10E+08	cutoff	3.13E+07					
2.60	9.33E+08	5.08E+06						
2.70	1.05E+09	1.37E+07						
2.80	1.17E+09	2.68E+07						
2.90	1.29E+09	4.55E+07						
3.00	1.40E+09	6.93E+07	5.05E+07	7.40E+06				
3.10	1.52E+09	9.69E+07						
3.20	1.63E+09	1.27E+08						
3.30	1.75E+09	1.59E+08						
3.40	1.87E+09	1.92E+08						
3.50	1.99E+09	2.24E+08						
3.60	2.12E+09	2.57E+08						
3.70	2.25E+09	2.88E+08			8.22E+08	4.59E+06		
3.80	2.38E+09	3.18E+08						
3.90	2.52E+09	3.48E+08						
4.00	2.67E+09	3.78E+08			1.13E+09	5.63E+06		
4.10	2.83E+09	4.09E+08	1.05E+08	3.15E+07				

Table 4.2. Kerma factors (rad cm^2) for brain tissue. From Zhou, (1990) and Caswell *et al.*,(1980). The error is 10%.

En/MeV	brain	En/MeV	brain	En/MeV	brain
2.53E-08	1.49E-11	2.50E-01	1.17E-09	4.60E+00	4.44E-09
3.60E-08	1.26E-11	2.70E-01	1.23E-09	5.00E+00	4.69E-09
6.30E-08	9.53E-12	2.90E-01	1.27E-09	5.40E+00	4.57E-09
1.10E-07	7.22E-12	3.10E-01	1.32E-09	5.80E+00	4.79E-09
2.00E-07	5.36E-12	3.30E-01	1.36E-09	6.20E+00	4.90E-09
3.60E-07	3.99E-12	3.50E-01	1.42E-09	6.60E+00	5.03E-09
6.30E-07	3.03E-12	3.70E-01	1.47E-09	7.00E+00	5.24E-09
1.10E-06	2.29E-12	3.90E-01	1.53E-09	7.40E+00	5.51E-09
2.00E-06	1.72E-12	4.20E-01	1.67E-09	7.80E+00	5.45E-09
3.60E-06	1.30E-12	4.60E-01	1.69E-09	8.20E+00	5.41E-09
6.30E-06	1.02E-12	5.00E-01	1.65E-09	8.60E+00	5.57E-09
1.10E-05	8.38E-13	5.40E-01	1.71E-09	9.00E+00	5.67E-09
2.00E-05	7.50E-13	5.80E-01	1.77E-09	9.40E+00	5.72E-09
3.60E-05	7.83E-13	6.20E-01	1.83E-09	9.80E+00	5.84E-09
6.30E-05	9.70E-13	6.60E-01	1.89E-09	1.05E+01	5.98E-09
1.10E-04	1.39E-12	7.00E-01	1.95E-09	1.15E+01	6.39E-09
2.00E-04	2.29E-12	7.40E-01	2.00E-09	1.25E+01	6.38E-09
3.60E-04	3.94E-12	7.80E-01	2.06E-09	1.35E+01	6.61E-09
6.30E-04	6.76E-12	8.20E-01	2.11E-09	1.45E+01	6.86E-09
1.10E-03	1.17E-11	8.60E-01	2.17E-09	1.55E+01	7.03E-09
2.00E-03	2.10E-11	9.00E-01	2.24E-09	1.65E+01	7.08E-09
3.60E-03	3.75E-11	9.40E-01	2.34E-09	1.75E+01	7.21E-09
6.30E-03	6.44E-11	9.80E-01	2.52E-09	1.85E+01	7.32E-09
1.10E-02	1.09E-10	1.05E+00	2.56E-09	1.95E+01	7.44E-09
2.00E-02	1.89E-10	1.15E+00	2.54E-09	2.10E+01	7.59E-09
3.60E-02	3.13E-10	1.25E+00	2.64E-09	2.30E+01	7.56E-09
6.30E-02	4.86E-10	1.35E+00	2.73E-09	2.50E+01	7.51E-09
8.20E-02	5.77E-10	1.45E+00	2.78E-09	2.70E+01	7.54E-09
8.60E-02	6.07E-10	1.55E+00	2.85E-09	2.90E+01	7.41E-09
9.00E-02	6.26E-10	1.65E+00	2.96E-09		
9.40E-02	6.45E-10	1.75E+00	3.00E-09		
9.80E-02	6.63E-10	1.85E+00	3.13E-09		
1.05E-01	6.95E-10	1.95E+00	3.15E-09		
1.15E-01	7.37E-10	2.10E+00	3.24E-09		
1.25E-01	7.78E-10	2.30E+00	3.29E-09		
1.35E-01	8.17E-10	2.50E+00	3.42E-09		
1.45E-01	8.54E-10	2.70E+00	3.57E-09		
1.55E-01	8.90E-10	2.90E+00	3.71E-09		
1.65E-01	9.23E-10	3.10E+00	3.84E-09		
1.75E-01	9.56E-10	3.30E+00	4.18E-09		
1.85E-01	9.86E-10	3.50E+00	4.27E-09		
1.95E-01	1.02E-09	3.70E+00	4.37E-09		
2.10E-01	1.06E-09	3.90E+00	4.30E-09		
2.30E-01	1.12E-09	4.20E+00	4.43E-09		

Table 4.3. Kerma factors (rad cm^2) for gamma. Error should be small and is assumed to be zero. From Zamenhof *et al.*,(1975).

Eg /MeV	kerma
9.50	2.45E-09
8.50	2.25E-09
7.50	2.05E-09
6.50	1.85E-09
5.50	1.64E-09
4.50	1.43E-09
3.50	1.21E-09
2.50	9.63E-10
1.50	6.71E-10
0.75	3.82E-10
0.30	1.51E-10
0.055	7.42E-11

Table 4.4. Neutron kerma factors (rad cm^2) for 1 ppm (weight fraction) boron-10. Error is 10% for all. From Zhou, (1990), Zamenhof *et al.*,(1975), and Caswell *et al.*,(1982).

En/eV	kerma
2.03E+03	3.27E-14
7.49E+02	5.48E-14
2.75E+02	8.99E-14
1.01E+02	1.47E-13
37.3	2.33E-13
13.7	4.00E-13
5.00	6.56E-13
1.86	1.09E-12
0.684	1.78E-12
0.251	2.92E-12
0.036	7.27E-12
0.025	8.724E-12
0.01	1.379E-11
0.001	4.362E-11

Table 4.5. Time required to deliver 66 RBE.Gy to the boundary of a 4.5 cm diameter tumor at a heat load of 100 Watts on the target. Not all digits in the treatment time are significant, but kept for scaling to different target heat loads in the future.

Particle Reactions	Bombarding Energy (MeV)	Treatment Time (min.100W)
^{7}Li(p,n)^{7}Be	2.0	1049
	2.5	39.40
	3.0	19.32
	4.1	8.05
^{9}Be(p,n)^{9}B	3.7	33.27
	4.0	24.27
^{9}Be(d,n)^{10}B	1.5	11.02

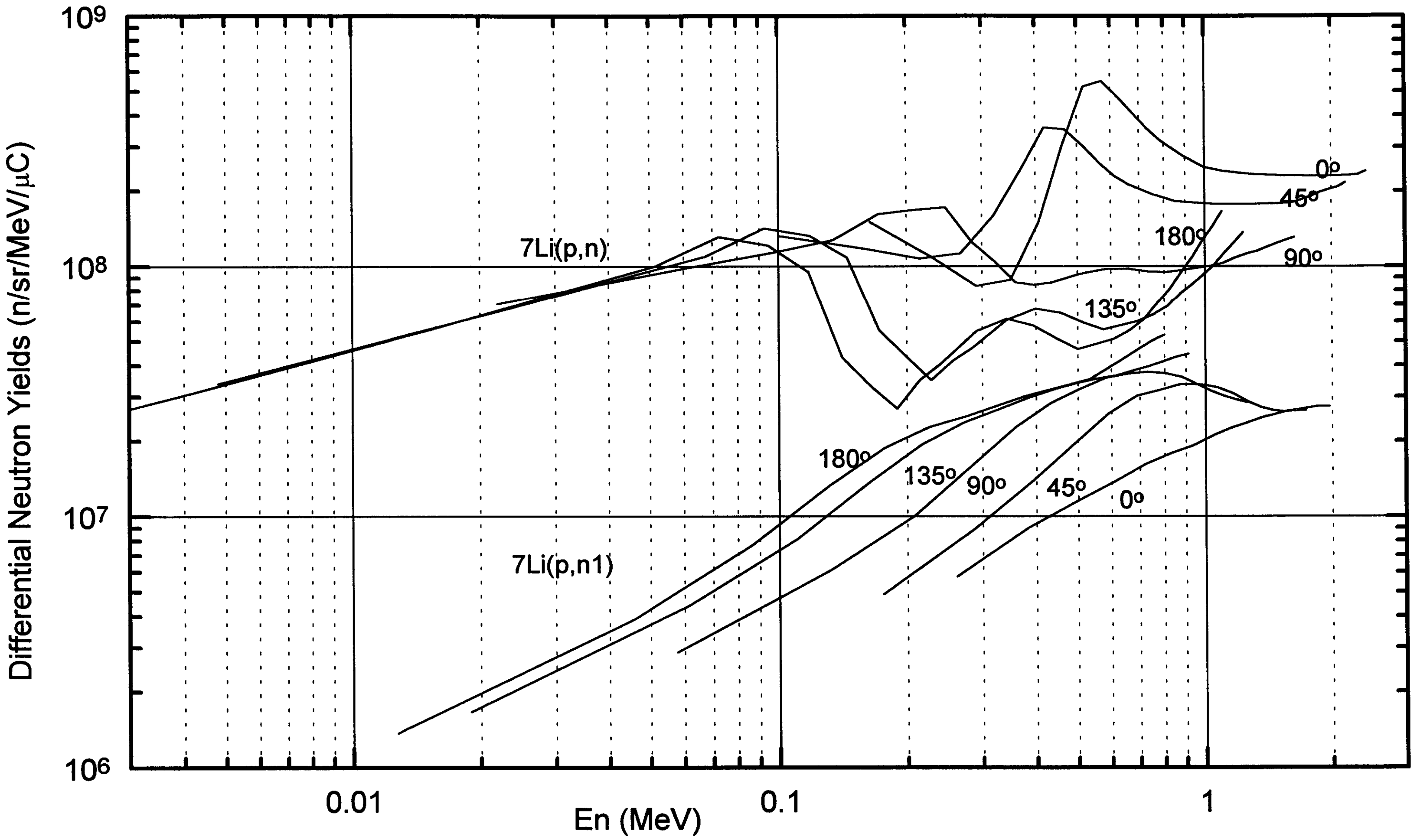

Figure 4.1. Spectra of neutrons from the ^{7}Li(p,n) and ^{7}Li(p,n1) reactions with a thick natural lithium target bombarded by 4.1 MeV protons at angles of 0, 45, 90, 135, and 180 degrees. The proton cut-off energies used in the calculations for the two reactions are 1.95 MeV and 2.5 MeV respectively.

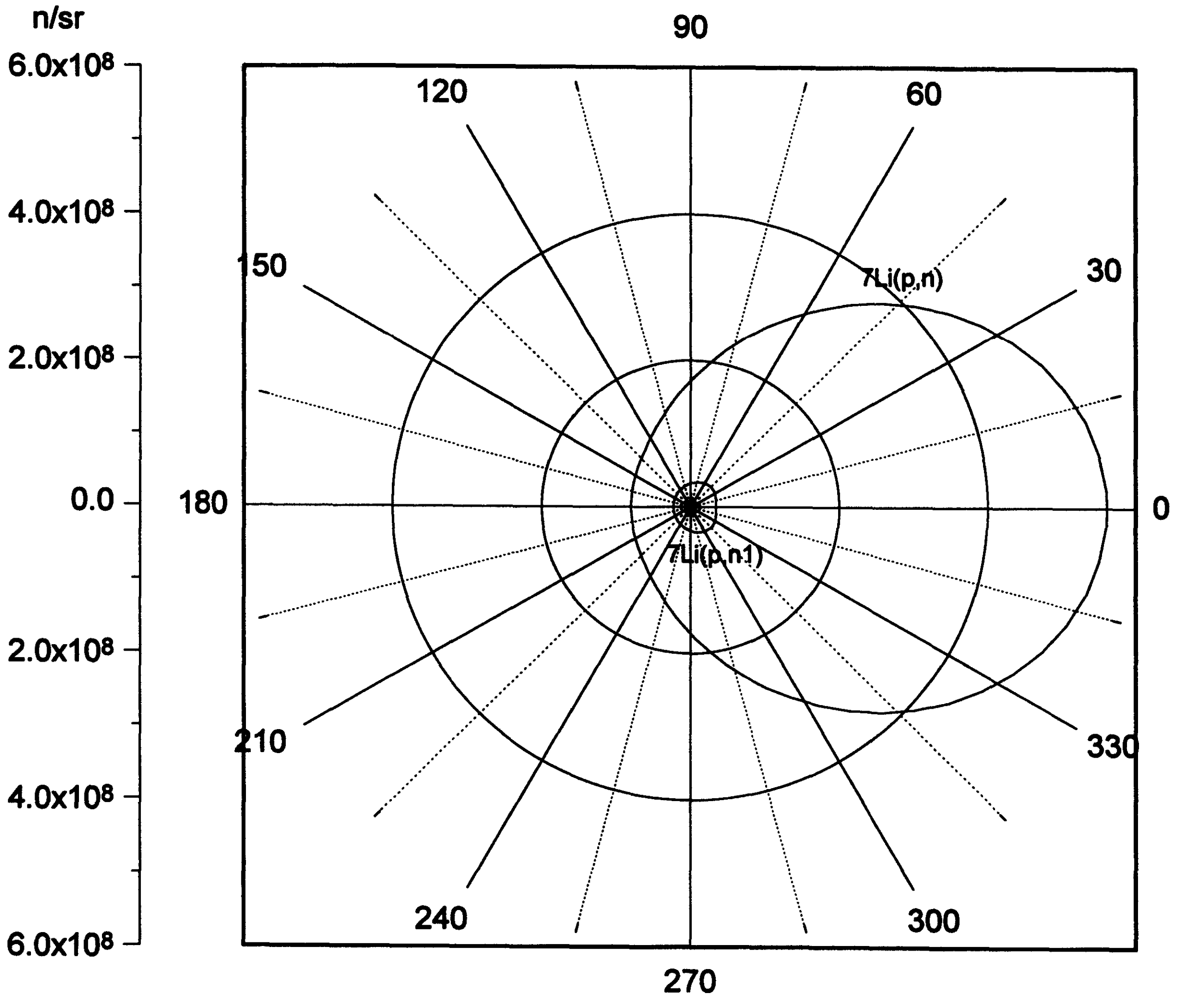

Figure 4.2. Neutron angular distributions (intergrated over neutron energy) for the ^{7}Li(p,n) and ^{7}Li(p,n1) reactions at Ep=4.1 MeV.

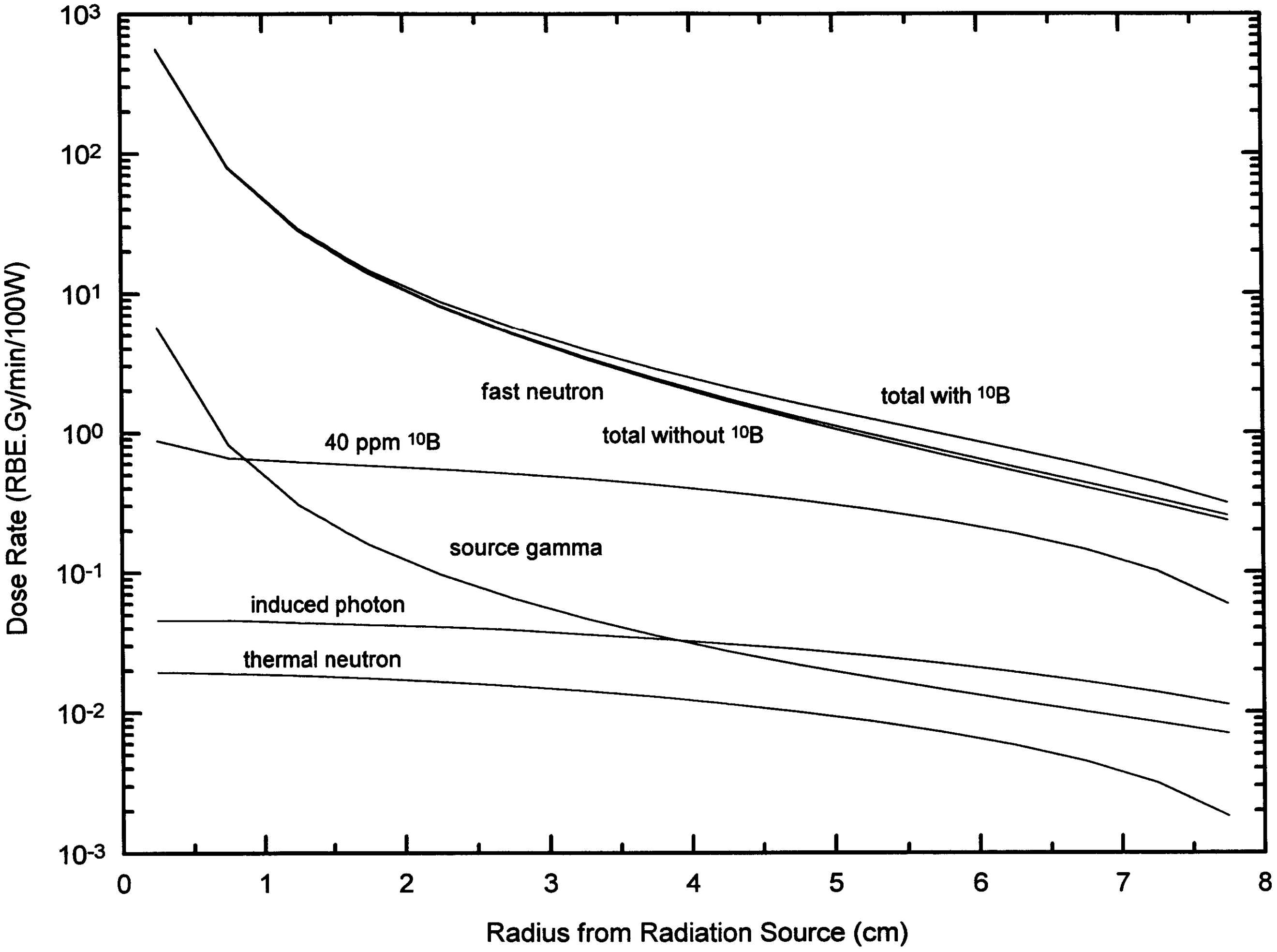

Figure 4.3.a. Dose components as a function of distance from the source in a brain tissue phantom for the reaction $^{7}Li(p,n)$ at Ep=4.1 MeV.

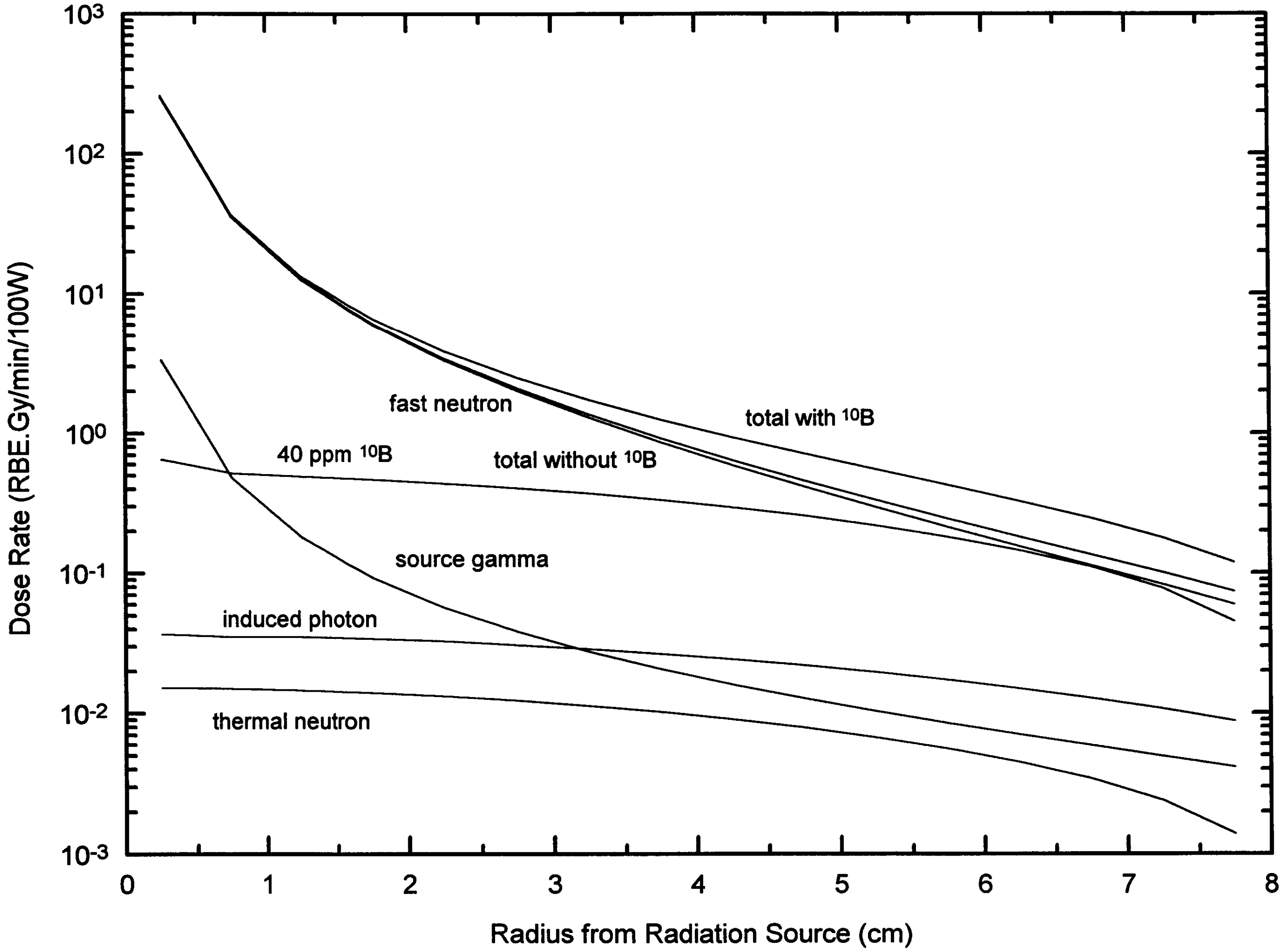

Figure 4.3.b. Dose components as a function of distance from the source in a brain tissue phantom for the reaction ^{7}Li(p,n) at Ep=3.0 MeV.

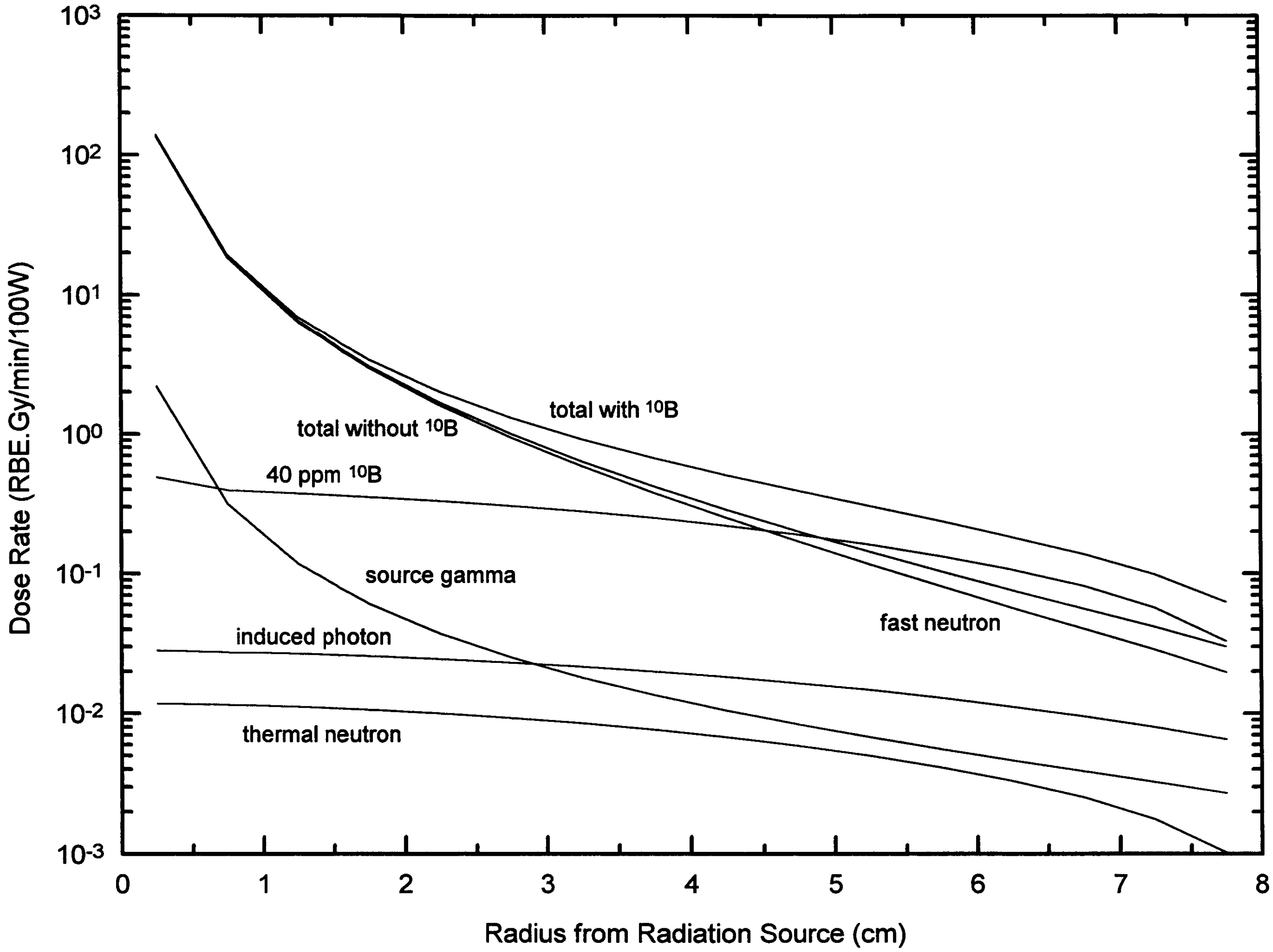

Figure 4.3.c. Dose components as a function of distance from the source in a brain tissue phantom for the reaction ^{7}Li(p,n) at Ep=2.5 MeV.

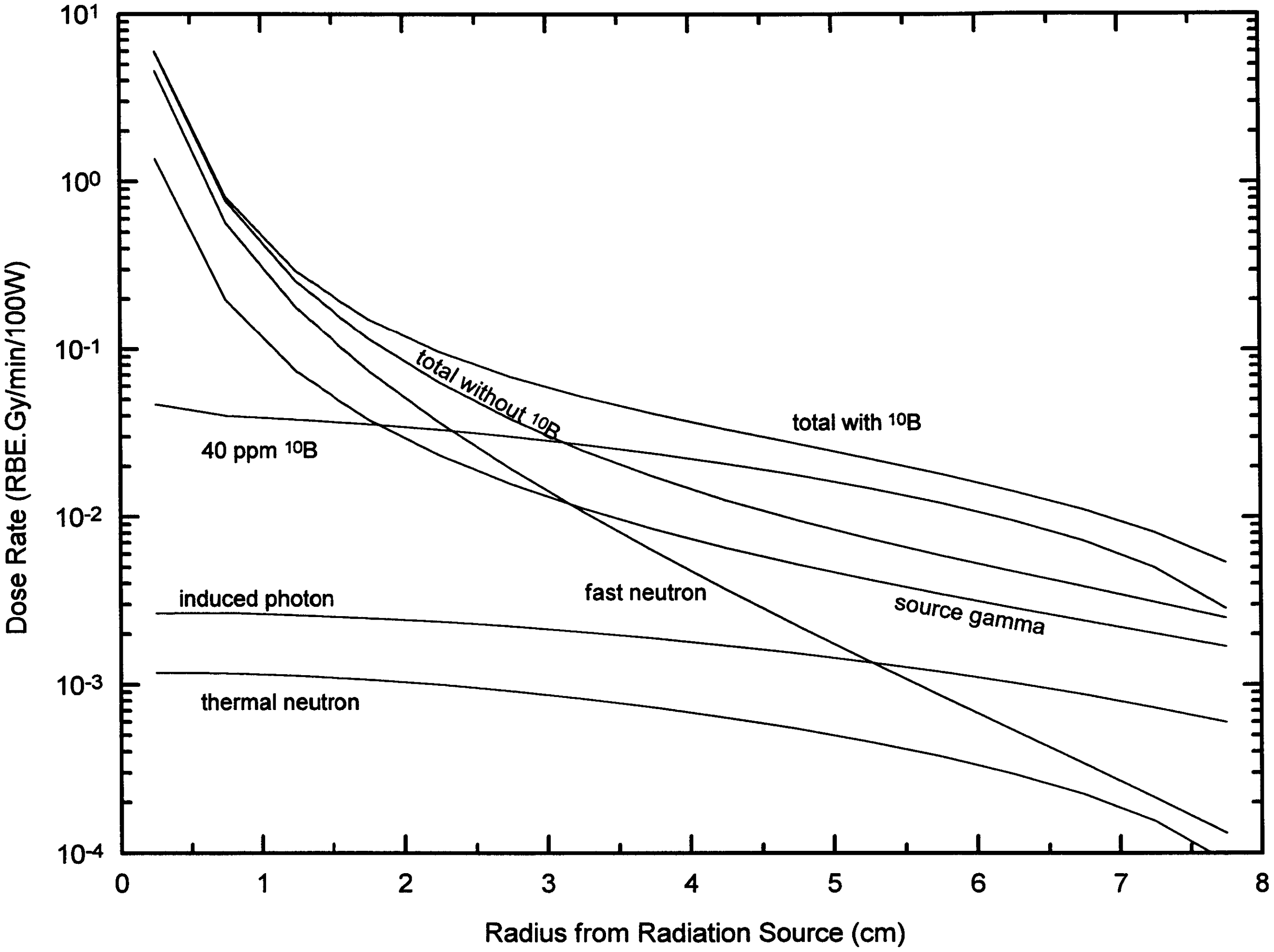

Figure 4.3.d. Dose components as a function of distance from the source in a brain tissue phantom for the reaction ^{7}Li(p,n) at Ep=2.0 MeV.

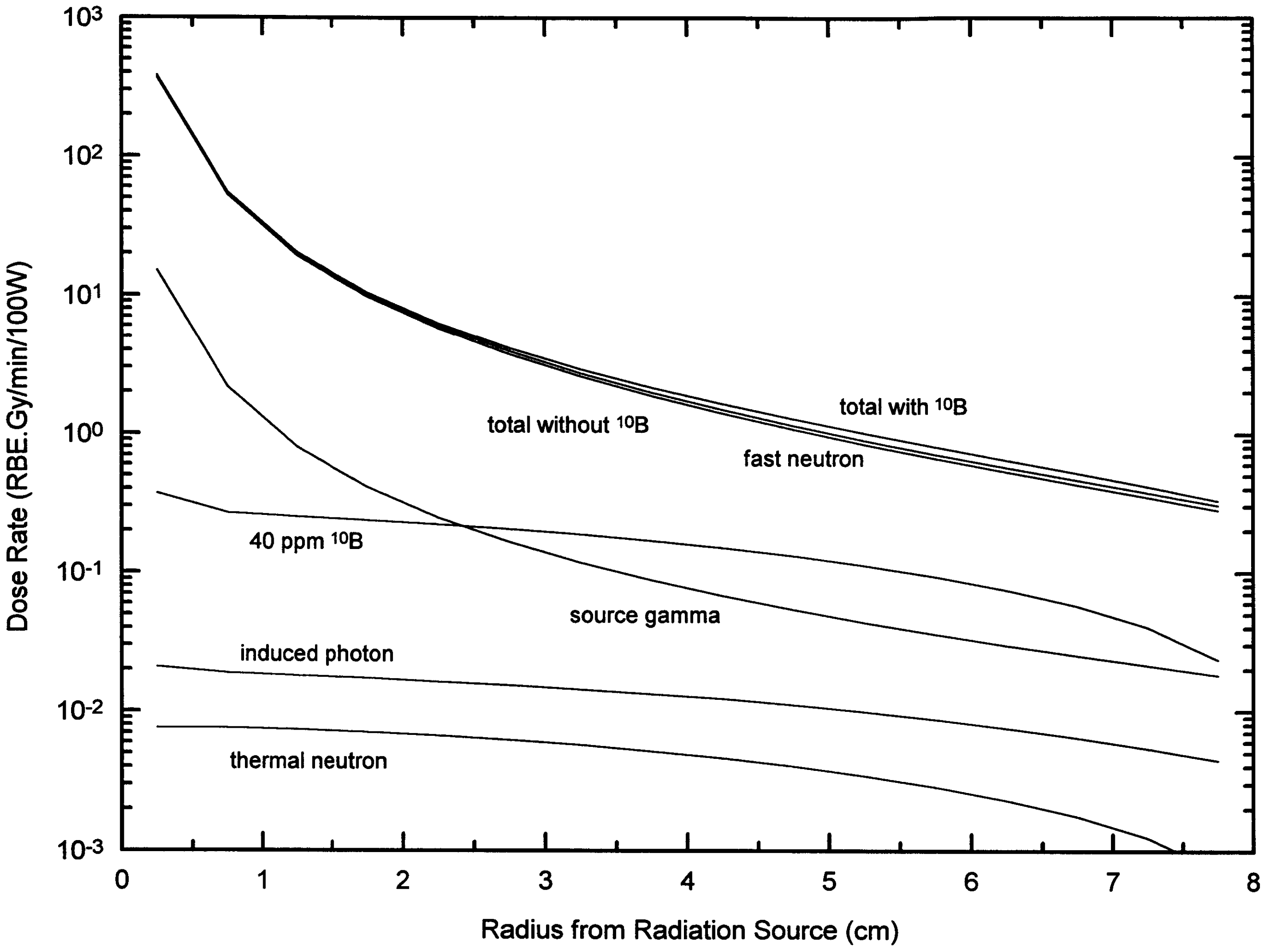

Figure 4.3.e. Dose components as a function of distance from the source in a brain tissue phantom for the reaction ^{9}Be(d,n) at Ed=1.5 MeV.

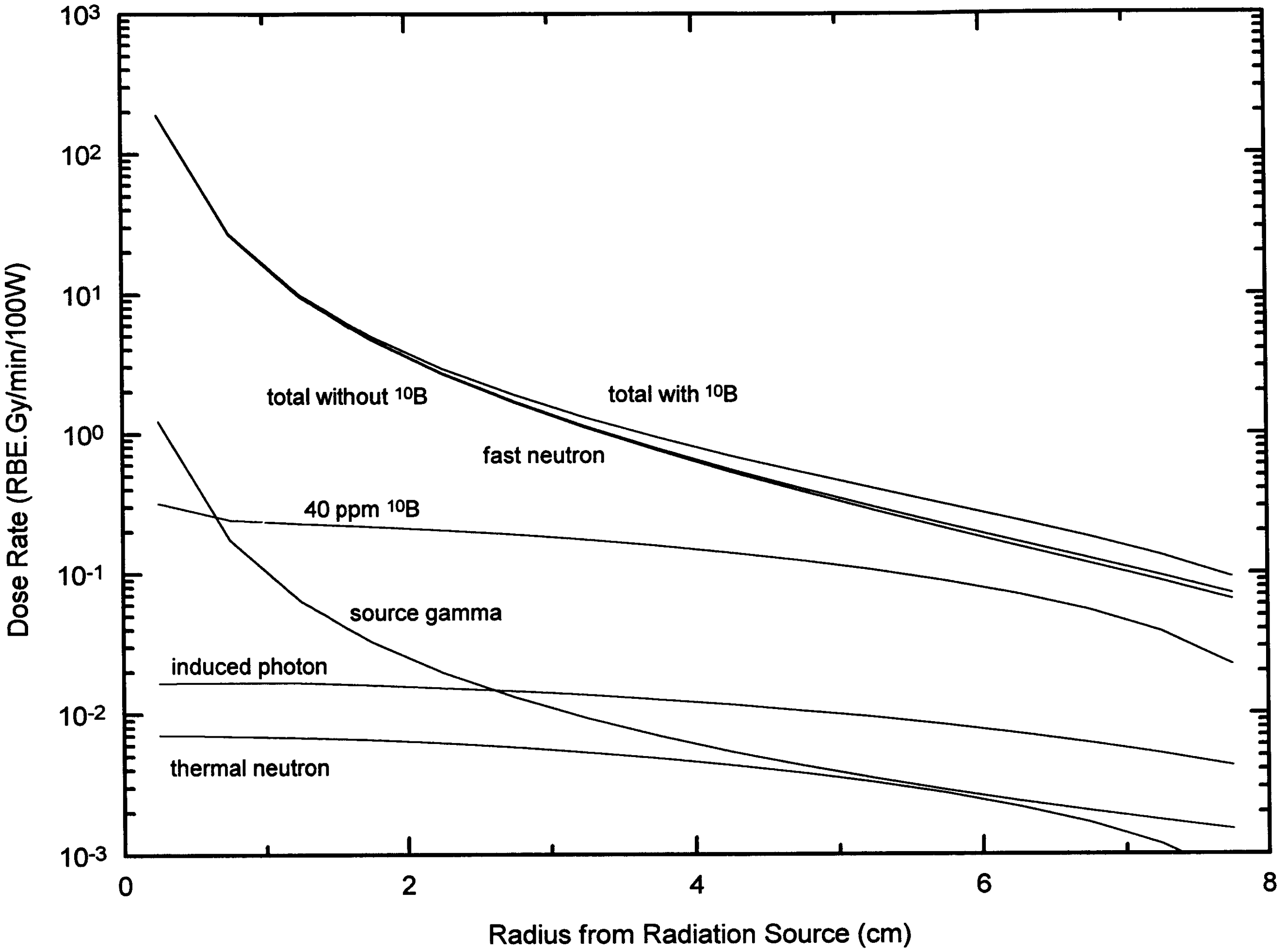

Figure 4.3.f. Dose components as a function of distance from the source in a brain tissue phantom for the reaction $^9Be(p,n)$ at Ep=4.0 MeV.

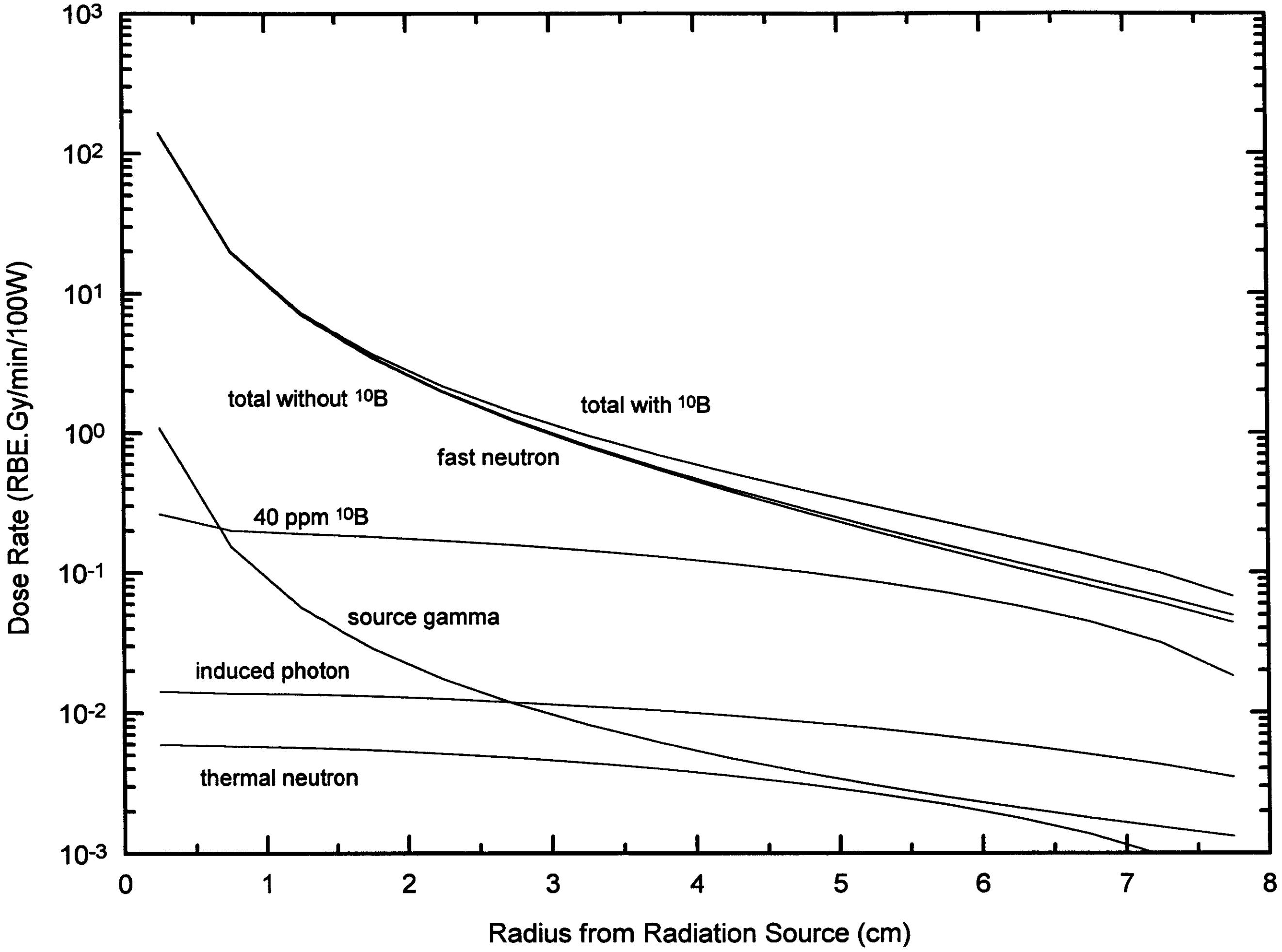

Figure 4.3.g. Dose components as a function of distance from the source in a brain tissue phantom for the reaction ^{9}Be(p,n) at Ep=3.7 MeV.

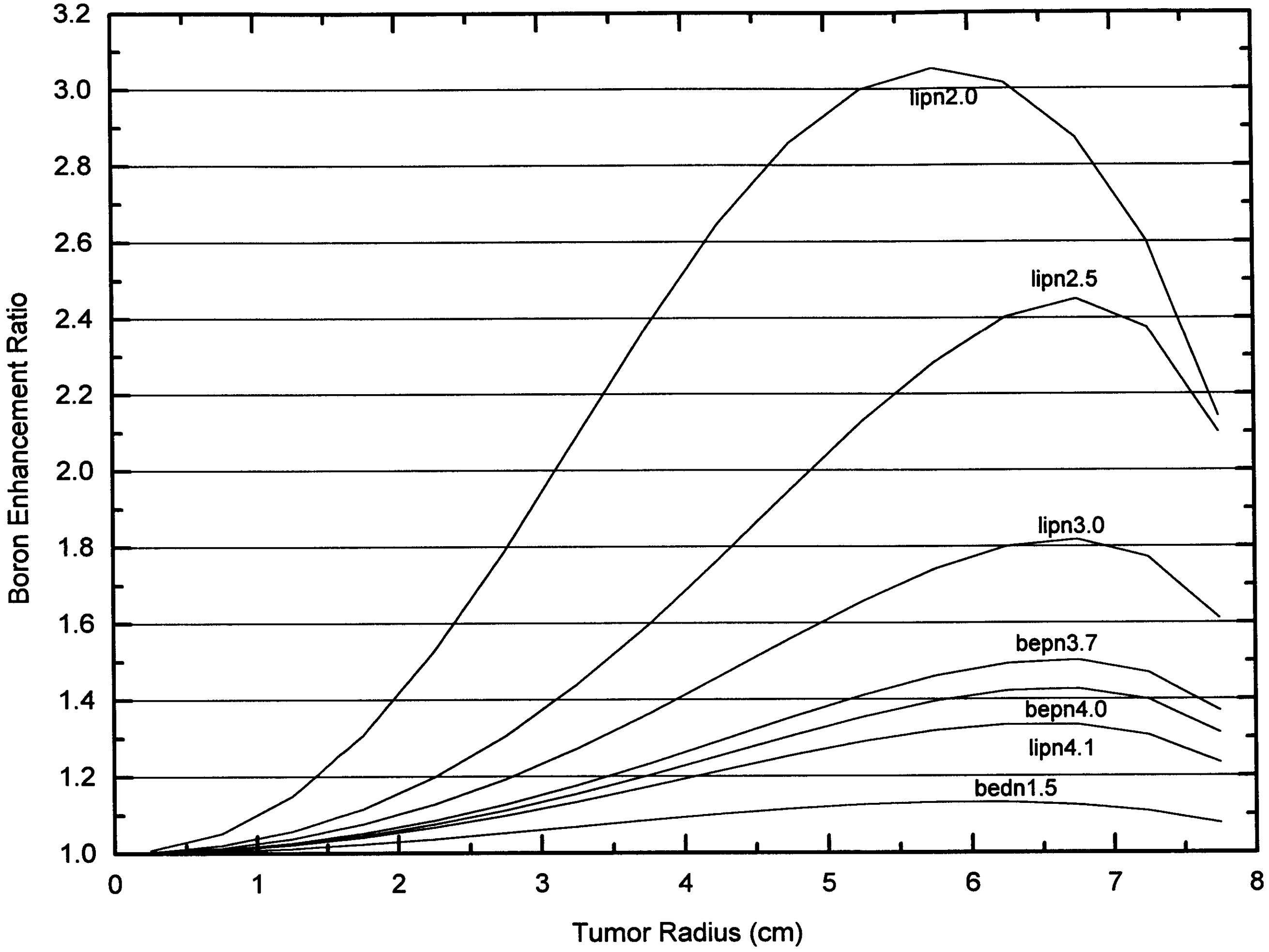

Figure 4.4.a. Boron Enhancement Ratio as a function of tumor radius for the candidate reactions, for a boron-10 concentration of 40 ppm.

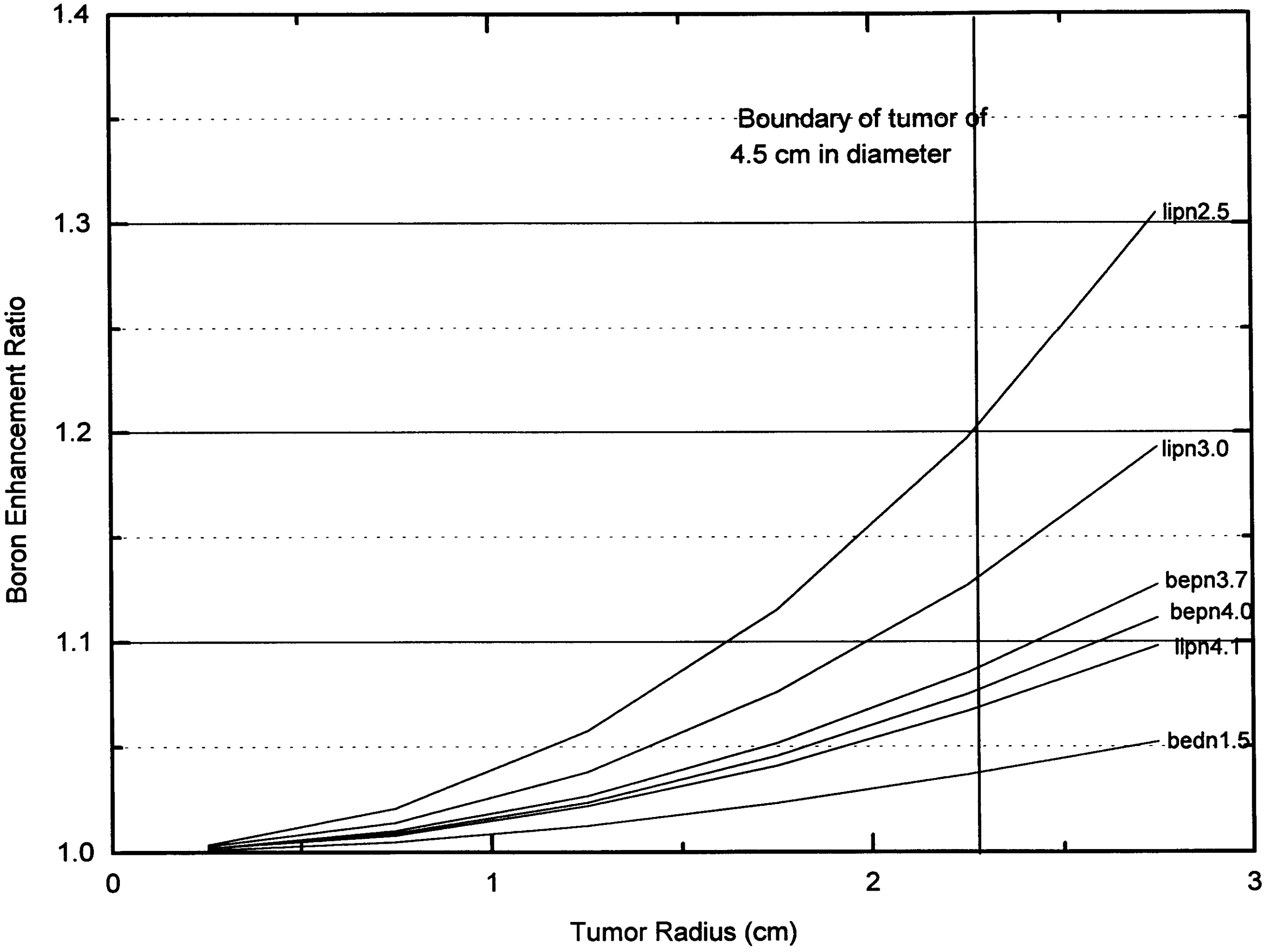

Figure 4.4.b. Boron Enhancement Ratio, a close-up at small radius of Figure 4.4.a.

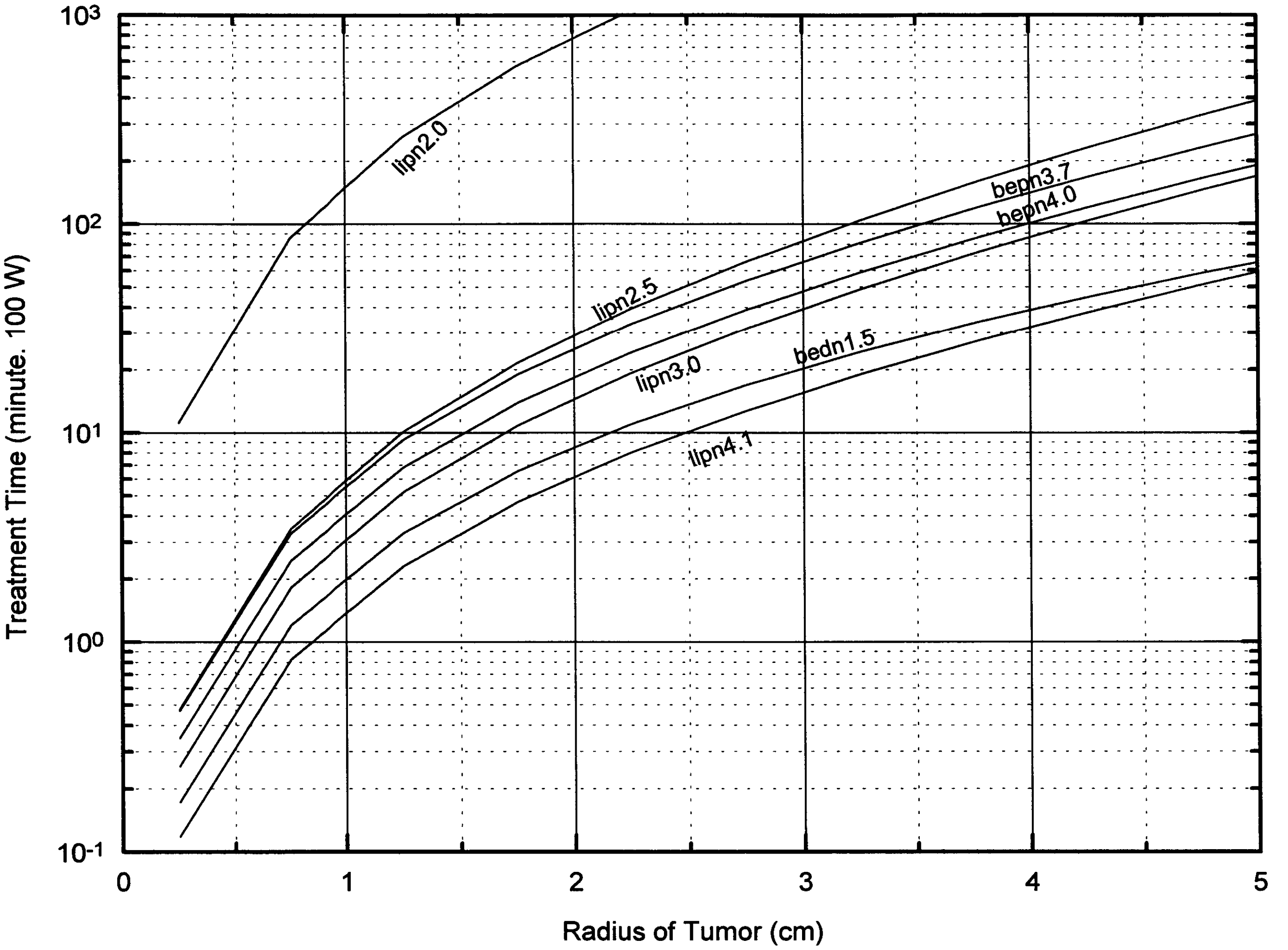

Figure 4.5. Time to deliver a therapeutic dose to the boundary of tumor, at a target heat load of 100 Watts, for the candidate reactions.

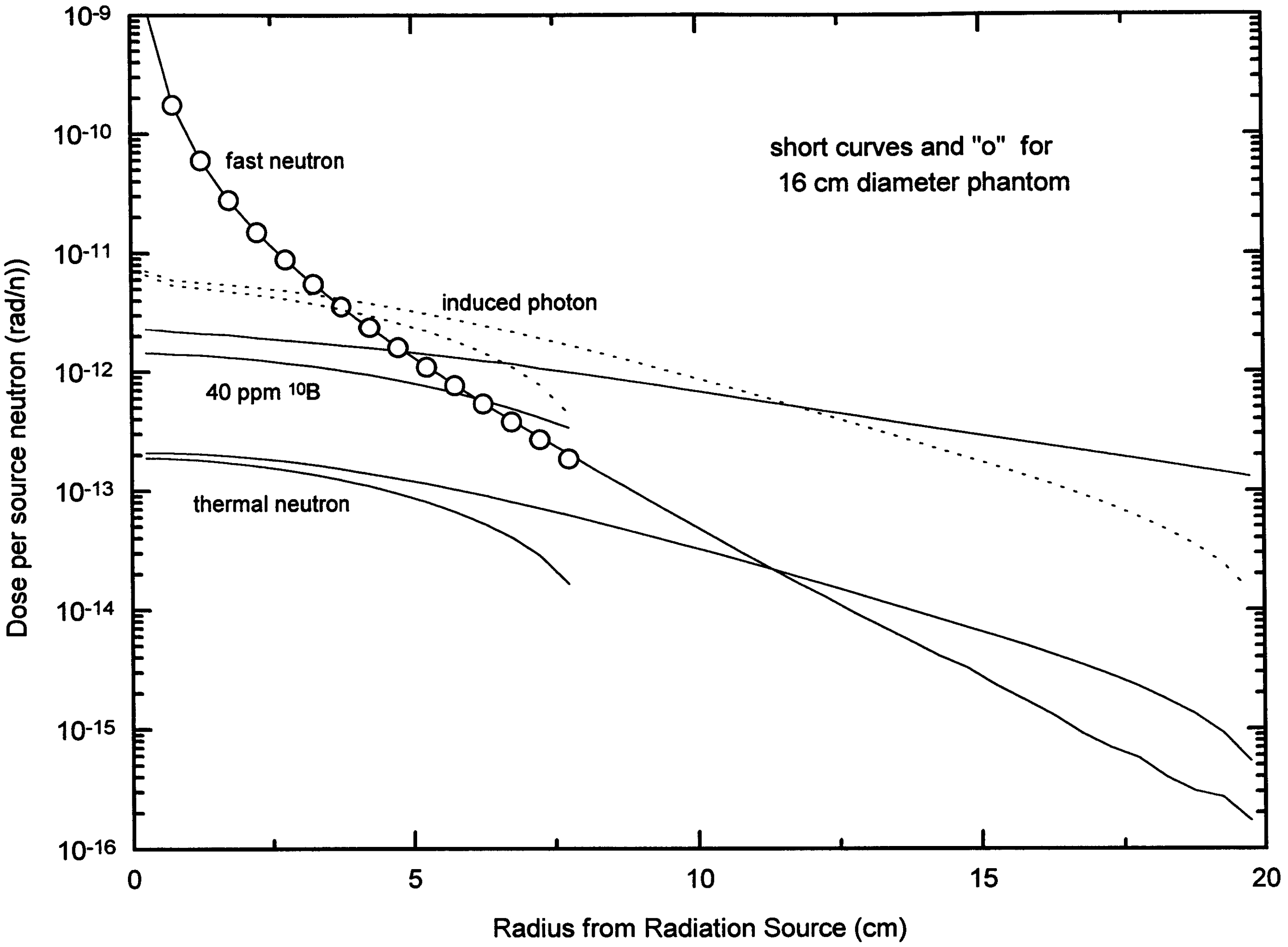

Figure 4.6. Comparison of dose components between a 16 and 40 cm diameter phantom, for the reaction ^{7}Li(p,n) at Ep=2.5 MeV.

CHAPTER FIVE
PROTOTYPE I

For Accelerator-Based Neutron Brachytherapy (ABNBT), the dose rate is proportional to the heat load in the neutron-producing target (beryllium and lithium for the candidate reactions). So it is desirable to have a target that can handle large amount of heat in pursuit of high dose rates and short treatment times. Due to the small size (6 mm diameter) of the dose delivering tube of ABNBT, limited by insertion into the tumor through a patient skull, a high power density can be created in the target for a medium amount of heat deposition. Heat removal capability of the target needs to determined by experiments. This chapter presents the design of a prototype dose delivering needle tube, Prototype I, and preliminary heat removal experiments using a proton beam as the heat source. Chapter Six will present Prototype II with a higher heat removal capability and more features.

5.1. TISSUE HEATING

For every thousand protons or deuterons, less than one will produces a nuclear reaction in the target. The majority lose all their kinetic energy through ionization and generate heat in the target, within a depth of a fraction of a millimeter for protons of a few MeV. The power (Watts) is calculated by

$$\text{Power} = I \times E, \qquad (5.1)$$

where I (μA) is the current of the charged particle beam and E (MeV) is the beam energy.

The following models the heat dissipation within tissue. Assume that a heat source of radius r_0 is at the center of an infinite body of tissue with a mass density, ρ_t, specific heat, C_t, heat conductivity, k_t, and blood flow per tissue mass, f. The blood has mass density, ρ_b, and specific heat, C_b. Energy conservation in a small tissue with mass, dm, and volume, dv, (notice $\rho_t = dm/dv$,) dictates that the temperature change (from normal body temperature), $T_c(r, \theta, \varphi, t)$, in the tissue due to the heat source obeys:

$$dm\, C_t\, \frac{\partial}{\partial_t}(T_c(r, \theta, \varphi, t)) + \nabla\cdot\vec{q}(r, \theta, \varphi, t)\ dv + f\ dm\ \rho_b\, C_b\, T_c(r, \theta, \varphi, t) = 0, \qquad (5.2)$$

where $\vec{q}(r, \theta, \varphi, t)$ is the heat flux and defined as

$$\vec{q}(r, \theta, \varphi, t) = -k_t\ \nabla T_c(r, \theta, \varphi, t)\ . \qquad (5.3)$$

The first term in (5.2) is the internal energy change in the tissue, the second term is outflow of heat through heat conduction, and the third is the heat carried away by circulating blood.

We are interested in the steady state solution, so let $\frac{\partial}{\partial_t}(T_c(r, \theta, \varphi, t)) = 0$. Also $T_c(r, \theta, \varphi, t)$ can be reduced to $T_c(r)$ due to spatial symmetry of the problem. Then (5.2) is reduced to

$$\nabla^2 T_c(r) = \beta^2 T_c(r)\ , \qquad (5.4)$$

where $\beta^2 = f\ \rho_b\ C_b\ \rho_t\ /\ k_t$. $\beta^2 = 4.2 \times 10^4\ m^{-2}$ for the combination of the following parameters:

$C_b = 4.2$ J/gram/°C, specific heat for water,
$\rho_b = \rho_t = 1.0\ g/cm^3$, density for water,

f = 30 ml/min/100 gram of tissue (Mattsson and Peterson, (1979)), and
k_t = 0.5 W/m/ °C, thermal conductivity for water.

The solution to equation (5.4) is

$$T_c(r) = \text{Power} \frac{e^{\beta r_o}}{4\pi k_t(1+\beta r_o)} \frac{1}{r} e^{-\beta r} . \tag{5.5}$$

To get solution (5.5), the following boundary condition has been used:

$$q(r) = \text{Power}/(4\pi r^2), \text{ at } r = r_o . \tag{5.6}$$

r_o is taken to be 3 mm, corresponding to the 6 mm diameter of the needle tube.

For example, for a heat load of only 10 Watts, the temperature change will be 130 °C at 0.5 cm and 0.5 °C at 2.5 cm. For a higher heat load, the temperature change will be proportionally higher. Of course, at these high temperatures, tissue boiling would have occurred and the model would have become invalid. It demonstrates, however, that the human body alone can not cope with such a heat load via heat conduction through tissue and convection by circulating blood. And, as shown in Chapter Four, a heat load of 100 Watts and up is desirable for ABNBT. Thus, active cooling of the target is needed.

5.2. PROTOTYPE I DESIGN

As shown in Figure 5.1.a, Prototype I is a tube-in-tube design with de-ionized water running in between the inner and outer tubes. (De-ionized water is needed so that the target is electrically insulated from the rest of the apparatus and the current from the target can be measured.) The outer tube has an outer diameter of 6 mm. The water inlet and outlet are welded to the outer tube. The insertion length, from the water inlet and outlet to the end of the outer tube, is 10 cm. The inner tube is 3 mm in diameter with the target at the tip. The whole tube assembly is welded to a KF-50 flange base. The tubes are stainless steel 316. The end cap of the outer tube is made of aluminum. A thermocouple, T_{target}, is led through the hole at the center of the end cap, electrically insulated with a teflon ring. The thermocouple is a miniature type (OMEGA Engineering, Inc., Stamford, CT) with a sheath of 0.25 mm diameter. The thermocouple wire and the junction are covered by the sheath and electrically insulated from the sheath with MgO powder. Thus the sheath can be used as a separate conductor for the measurement of beam current on the target. A second thermocouple, T_{liquid}, is used to measure the temperature of cooling water in the region close to the target. The cooling channel is formed by four evenly displaced rods fitted between the inner and outer tubes. Figure 5.1.b shows the process of assembling the parts.

The candidate reactions for ABNBT, $^7Li(p,n)^7Be$, $^9Be(p,n)^9B$, and $^9Be(d,n)^{10}B$, use two different targets: lithium and beryllium. Both are difficult to handle and expensive to make. For preliminary testing of heat removal, a copper target was used.

The copper target is plug-shaped, 2.5 mm diameter and 3.8 mm in length, and electrically insulated from inner tube by a teflon sleeve, as shown in Figure 5.2. The teflon sleeve also provides the vacuum seal. An aluminum protection sleeve (shown Figure 5.1.a) inside the inner tube protects the teflon ring from being hit by the accelerator beam.

Alignment of the needle tube relative to the accelerator beam is carried out with two remotely controlled step motors which apply pressure to the tip of the outer tube in orthogonal directions, as shown in Figure 5.3.a and b. While this approach is adequate for initial heat removal experiments it is not suitable for a clinical situation and an improved method has been developed for Prototype II.

5.3. HEAT REMOVAL EXPERIMENT

The testing of heat removal on the copper target was done using as the heat source a proton beam of 1.5 MeV from the tandem electrostatic accelerator in the Laboratory for Accelerator Beam Applications (LABA) at MIT, described as Beam I in Chapter Three. The beam line elements, as shown in Figure 3.7, consist of an x-y steering magnet and a quadrupole doublet. A water-cooled aperture (2.5 mm diameter opening, the same size as the target) right in front of the needle tube limits the beam size going into the needle tube. The beam envelopes are shown in Figure 3.8. Under the best conditions, a maximum of 39% of total beam is expected to be delivered to the target.

Getting the proton beam down to the 2.5 mm diameter target through the 10 cm long tube was done in two steps. First, the x-y steerer and the quadrupole lenses were tuned to get a good ratio of total beam through the water-cooled aperture. Then the beam current on the target was maximized by turning the two step motors in increments of the order of 0.1 mm. During the process of maximization, the beam (so the heat load) to the target increased from near zero and data points of temperature vs. heat load were recorded. Up to 20% of the total 1.5 MeV proton beam hit the target and 12% of the total beam hit the inner tube. The remainder of the beam was stopped by the water-cooled aperture.

The cooling water source was branched from the cooling and deionizing unit for the ion source of the tandem electrostatic accelerator. The pressure was around 1 atmosphere. The temperature was room temperature (~20°C). The flow to the needle tube was measured to be 0.8 l/min.

The temperatures, T_{target} and T_{liguid} , as a function of heat load are plotted in Figure 5.4. T_{target} increases linearly with heat load to a maximum of 120°C at the maximum heat load of 38 Watts. T_{liquid} stays low.

5.4. APPLYING TO LITHIUM AND BERYLLIUM TARGETS

According to the heat transfer analysis in Appendix D, at the heat load of 38 Watts, the heat transfer may have passed the transition from one phase to two phase heat transfer and be in the subcooled nucleation boiling regime. The temperature profile along the copper target is estimated to be 146 °C on the vacuum surface and about 100 °C on the target-water surface.

If the copper plug is used as the backing for a lithium metal target, the highest temperature inside the lithium will be higher than 146°C due to the temperature gradient within the lithium metal and the temperature difference across the lithium-copper interface. The fact that the melting point of lithium metal, 181°C, is within a few tens of degrees of 146 °C means that lithium would not be an attractive target for use in this prototype device unless cooler and/or higher cooling flow were used. In addition, lithium metal is very difficult to handle due to its chemical properties. Lithium fluoride is more stable but compromises the advantage of high neutron yield.

It is more practical to replace the copper target with an identical beryllium metal piece. Metal beryllium is chemically stable, has good mechanical strength, and a high melting point (1290°C). According to the heat transfer analysis in Appendix D, the temperature of such a beryllium target will be 247 °C on the vacuum surface and 100 °C on the target-water surface at a heat load of 38 Watts. The highest temperature of 247 °C in the beryllium target is far below the melting point of beryllium, however it poses a danger to the teflon sleeve. In fact this temperature approaches the point at which the ability of teflon to form a good vacuum seal is compromised. In other words, 38 Watts is about the maximum heat removal achievable with the target design of Prototype I under the cooling conditions.

At the heat load of 38 Watts, the time to treat a 4.5 cm diameter solid tumor to a therapeutic dose of 66 RBE.Gy for the candidate nuclear reactions is calculated from Table 4.5 and listed in Table 5.1. For example, using the $^{9}Be(p,n)^{9}B$ reaction at E_p=4.0 MeV, the treatment time is 64 minutes. It is 29 minutes for the $^{9}Be(d,n)^{10}B$ at E_d=1.5 MeV and 21 minutes for the $^{7}Li(p,n)^{7}Be$ reaction at E_p=4.1 MeV.

5.5. DISCUSSIONS AND CONCLUSIONS

While a treatment time of 29 minutes or 64 minutes from beryllium target may be acceptable, a shorter treatment time would be more desirable.

The $^{9}Be(d,n)^{10}B$ reaction at E_d=1.5 MeV is the favorite among the candidate reactions, because a beryllium target is easier to handle than a lithium target and Be(d,n) reaction delivers high dose rate at energies lower than those for the Be(p,n) and Li(p,n) reactions.

In this investigation, the outer diameter of the needle tube was limited to 6 mm to allow insertion into the brain. If applied to cavity tumors, e.g., cervical or nasopharyngeal cancers, the diameter of the outer tube can be significantly increased. For example, if the outer tube diameter is increased from 6 to 18 mm (a factor of 3), and the diameter of the inner tube and the target quadrupled (this will still leave a bigger cooling channel), the same heat flux on the target surface will result from a heat load 16 times as high. The heat removal capability is expected to increase by a factor of 16, as are the achievable dose rates.

Table 5.1. Time required to deliver 66 RBE.Gy to the boundary of a 4.5 cm diameter tumor at a heat load of 38 Watts, the achieved heat removal from the target of Prototype I.

Particle Reactions	Bombarding Energy (MeV)	Treatment Time (min)
$^{7}Li(p,n)^{7}Be$	2.5	104
	3.0	51
	4.1	21
$^{9}Be(p,n)^{9}B$	3.7	88
	4.0	64
$^{9}Be(d,n)^{10}B$	1.5	29

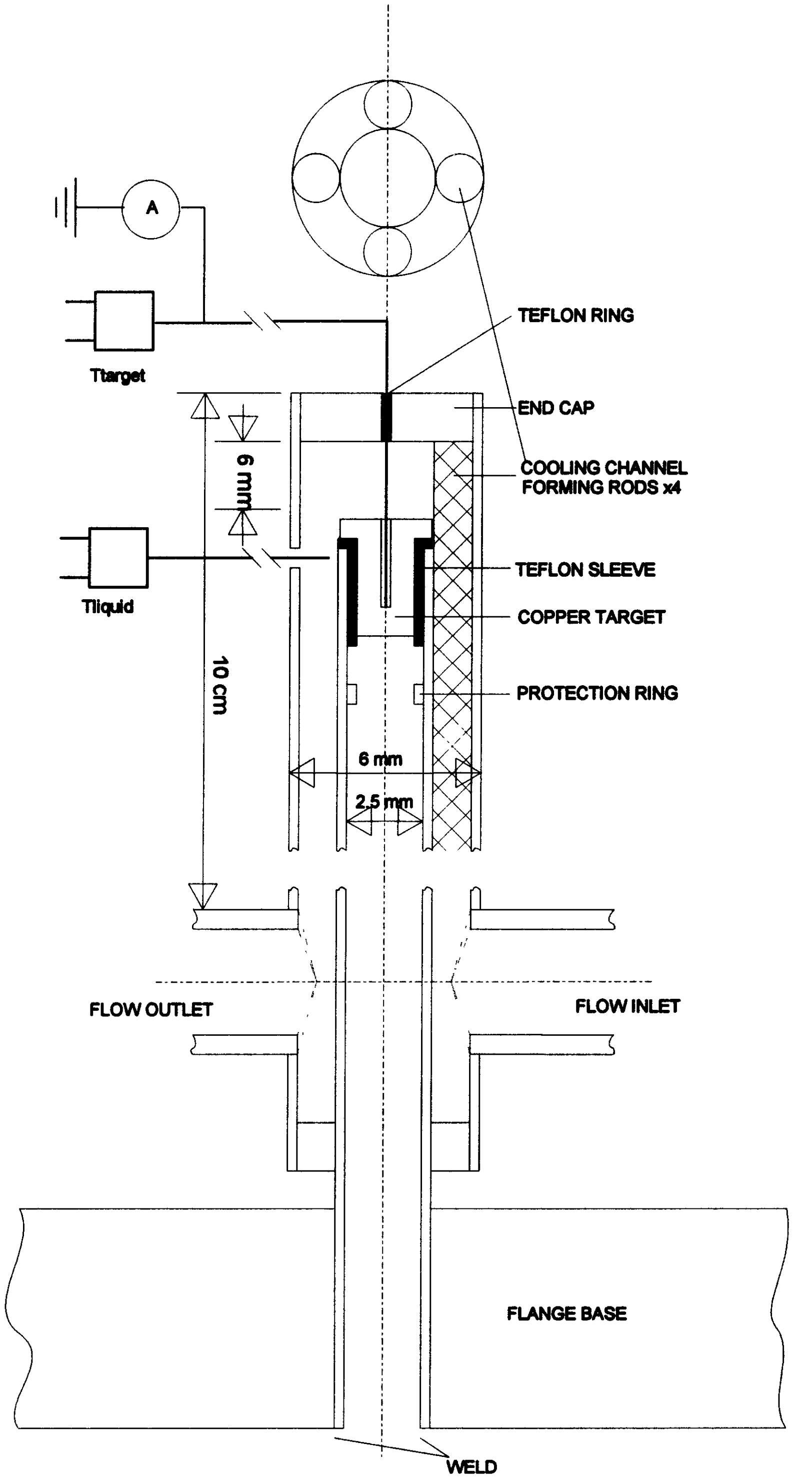

Figure 5.1.a. Drawing of the needle tube prototype I.

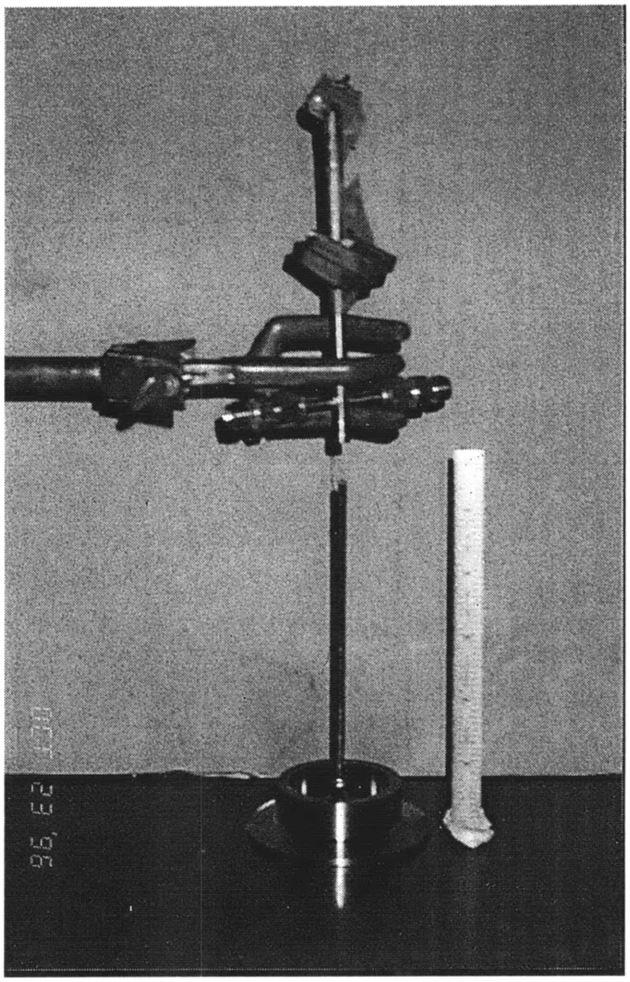

Figure 5.1.b. Assembly of the needle tube Prototype I. The inner tube has been welded to the flange base. The outer tube is about to be mounted. The thermocouple T_{target} is being attached.

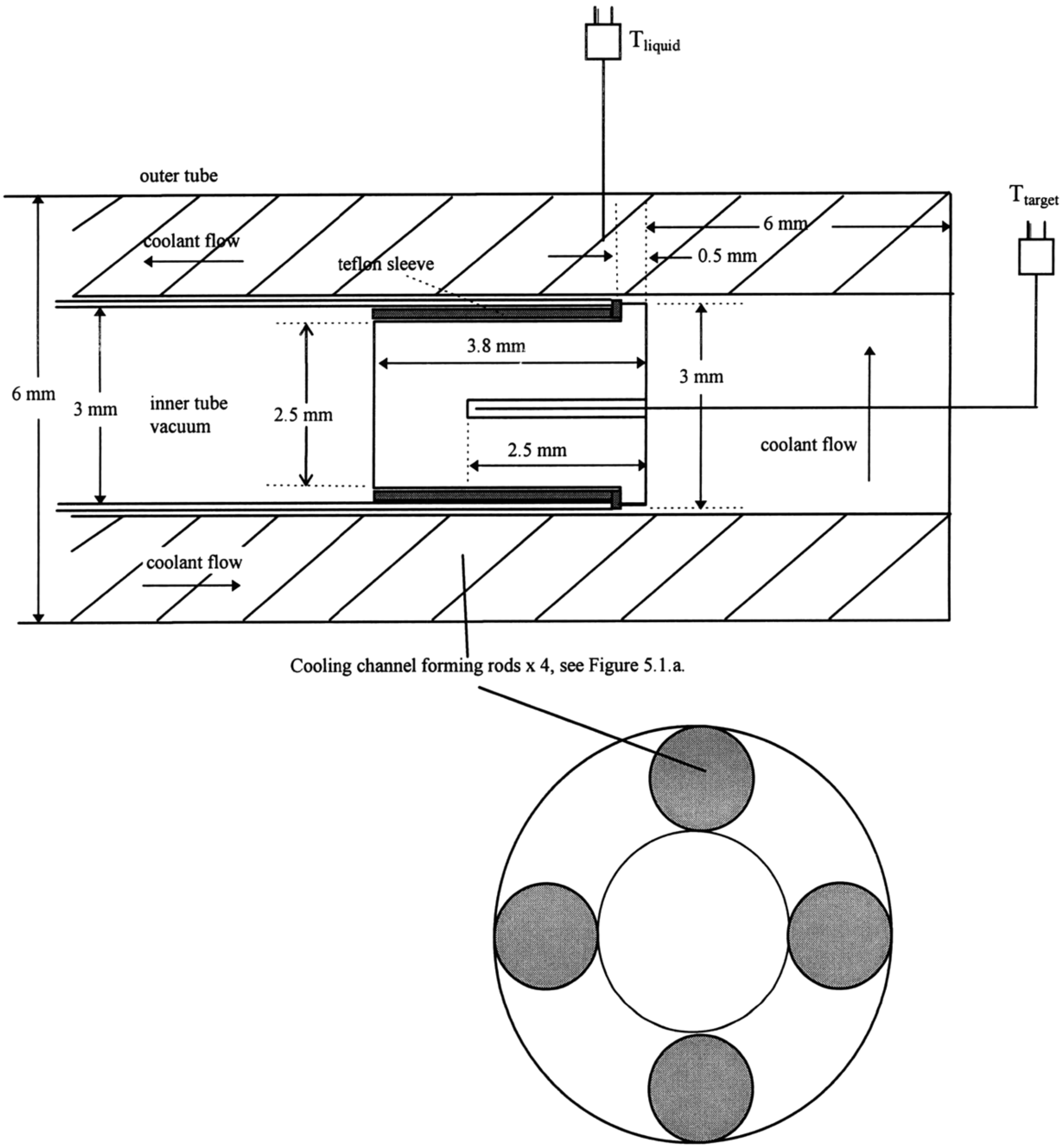

Figure 5.2. Schematic of the tip portion of the needle tube Prototype I, including the plug-shaped target. The cooling water runs between the inner and outer tubes.

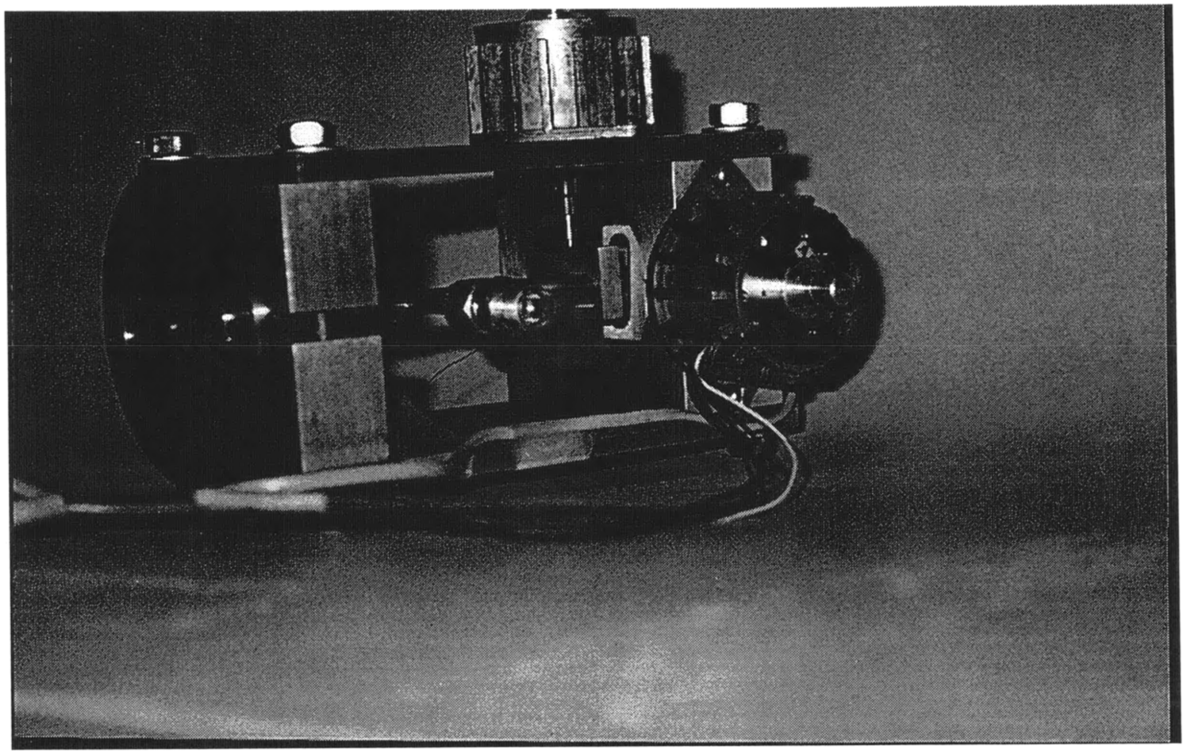

Figure 5.3.a. The needle tube Prototype I with the two step motors mounted. The flange base is to the left and the target to the right at the end of the needle tube. The step motor mount clamps on the flange base.

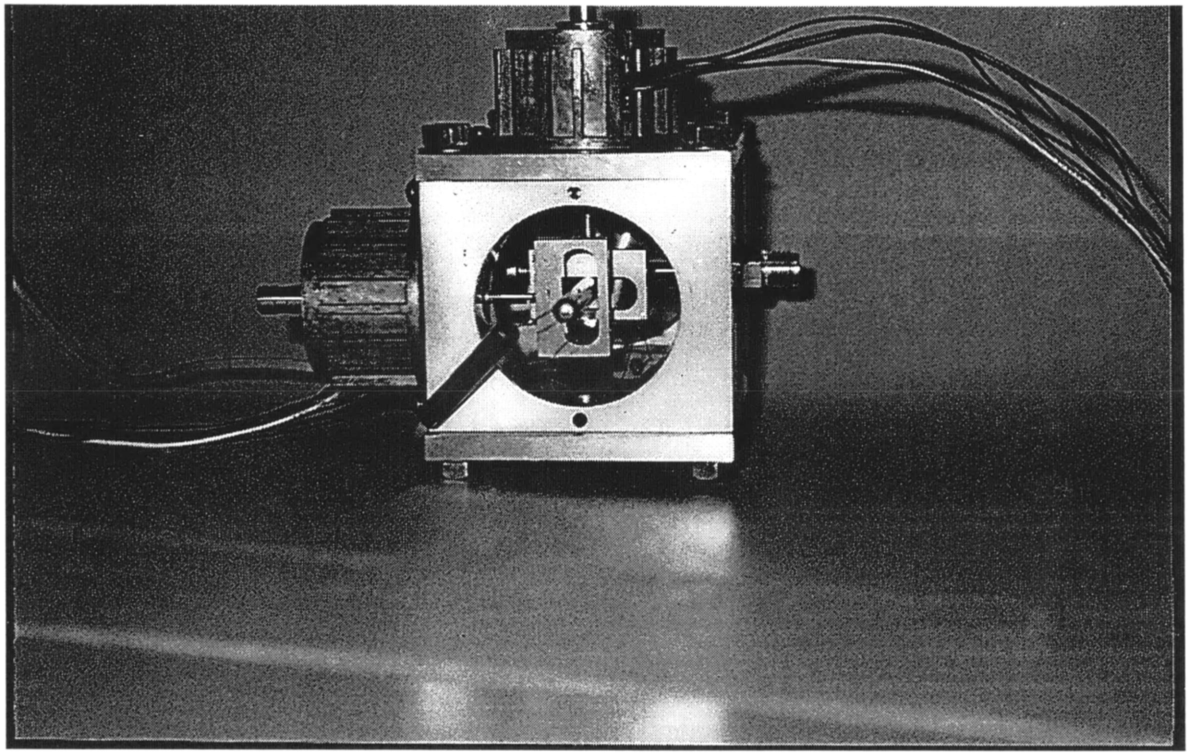

Figure 5.3.b. Front view of the needle tube Prototype I with the two step motors mounted. The tip of the needle tube is shown. The thermocouple wire comes out of the tip. The two brackets the step motors pulling and pushing the needle tube with are shown.

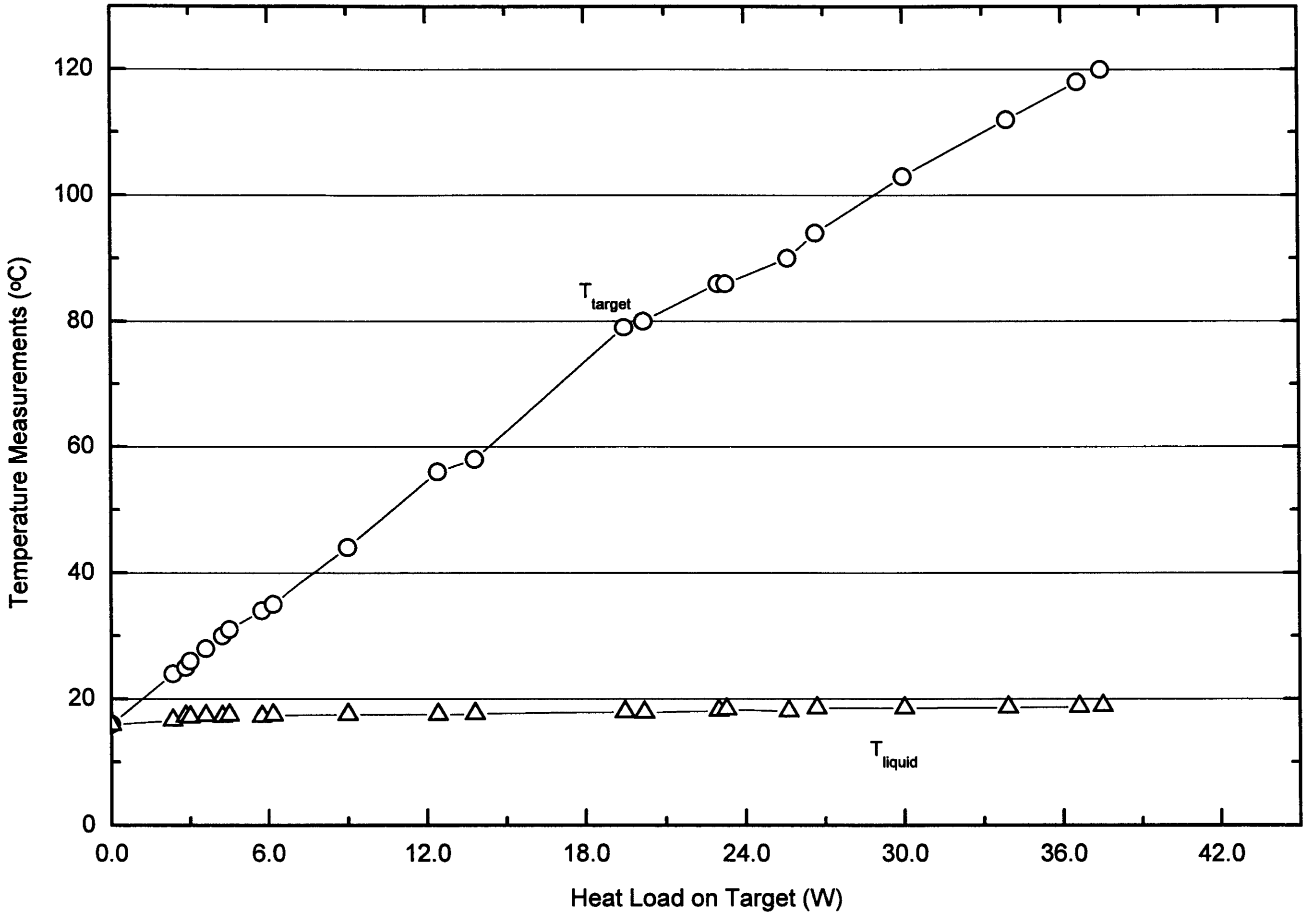

Figure 5.4. Temperatures as a function of heat load on target in prototype I. T_{target} and T_{liquid} are measured at locations indicated in Figure 5.1.a. and 5.2.

CHAPTER SIX
PROTOTYPE II

A prototype of the dose delivery needle tube, Prototype I, for Accelerator-Based Neutron Brachytherapy (ABNBT) was presented in Chapter Five. Prototype I needs to be improved in the following aspects. First, the dose rate allowed by the maximum heat removal of 38 Watts achievable with Prototype I may be acceptable but not satisfying. Second, the alignment of the tube of Prototype I to the accelerator beam is done with two step motors pressing directly on the tip of the needle tube. The needle tube is not suitable for insertion into a phantom with the two step motors mounted. Third, the thermocouples in Prototype I are led out of the tip of the tube and in the way of insertion. Prototype II improves upon all the three aspects.

6.1. NEEDLE TUBE DESIGN

Prototype II is, similar to Prototype I, a tube-in-tube design with de-ionized water running in between the inner and outer tubes. (De-ionized water is needed so that the target is electrically insulated from the rest of the apparatus and the current from the target can be measured.) The drawings are shown in Figure 6.1.a and b. The diameters of the inner and outer tube are the same as those of Prototype I, 3 mm and 6 mm. The flange base is made of two pieces, one holds the inner tube and one holds the outer tube. The inner tube is guided through a 1.6 cm length and welded to the flange base so that the inner tube is rigid and perpendicular to the flange surface. The guidance for the outer tube is 1.2 cm. The flange base has a protruding shoulder of 1.27 cm (0.5 inch) diameter and 0.76 cm (0.3 inch) deep, which serves as the water seal interface for insertion into a phantom. The inlet and outlet of the cooling channel are machined into the flange base. The cooling channel is formed with two rods between the inner and outer tubes. The thermocouple wires are led through the cooling channel. Pictures of Prototype II are shown as assembled in Figure 6.2.a and with the outer tube taken apart in Figure 6.2.b.

To introduce an ion beam to the target through the inner tube, the needle tube needs to be adjustable relative to the beam. The alignment is achieved with an motorized angular tilter (Huntington Mechanical Laboratories, Inc., Mountain View, CA). The angular tilter consists of two slanting rings grinding against each other. When mounted between the beam tube and the flange base of the needle tube, it is capable of pointing the needle tube to any position within a 10 degree cone. For operational principles, see Appendix C.

Since the angular tilter is mounted between the accelerator beam tube and the flange base of Prototype II, and the thermocouple wires are led through the cooling channel instead of the tip of the outer tube, the outside of the outer tube is now fully exposed. Therefore, Prototype II is suitable for insertion into a phantom.

6.2. TARGET DESIGN

The heat removal of Prototype I is limited by the fact that the teflon sleeve is in contact with the surface directly struck by the incident beam. Prototype II moves the teflon sleeve away from this heated surface. The target, illustrated in Figure 6.3, is now tube shaped. The teflon sleeve and the heating surface are separated by a water-cooled, thin, and long wall. Hence, most of the heat will be removed by the cooling water without reaching the teflon sleeve. An aluminum protection ring is placed immediately before the target inside the inner tube to prevent the teflon from being hit by the accelerator beam (Figure 6.1.b). The ledge is to insure a good vacuum seal from the teflon sleeve. To insure the electrical insulation of the target from the tube, the teflon sleeve has a shoulder so that the target tube shoulder does not contact the inner tube.

Temperature is monitored at two positions: T_1, at the center and inside the target bottom, and T_2, on the target tube wall immediately before the teflon sleeve. Thermocouple T_1 is inserted into the groove at the bottom of target and held in position by stuffing the groove with aluminum foil. (Commonly used epoxy glue does not insure electrical conduction. Electrically conductive epoxy glue and solder interferes with heat transfer.) Thermocouple T_2 is glued to the target tube wall with commercial epoxy. Target current is measured with the sheath of thermocouple T_1.

Heat transfer theory predicts that, at low heat flux, the heat transfer across the target-water surface is by single phase convection and the target surface temperature, hence T_1 and T_2, should increase linearly with heat load. When the surface is higher than but within around 5°C of the saturation temperature of the coolant, nucleation is initiated and two phase heat transfer occurs. This will initially result in improved heat transfer so that the surface temperature and hence T_1 and T_2 will increase with heat flux at less than a linear rate. However, for sufficiently high heat fluxes, a limiting value will be reached, the critical heat flux, a condition under which heat transfer deteriorates. This should happen before T_2 could get too hot and endanger the teflon sleeve. Therefore, heat removal of Prototype II will likely be limited by heat removal capability, instead of failure of the teflon seal.

6.3. HEAT REMOVAL TEST ON COPPER TARGET

Same as with Prototype I, a copper target was made to test the heat removal of Prototype II as the first step since it is easier to make than a beryllium one.

A 2.0 MeV proton beam from the tandem electrostatic accelerator in the Laboratory for Accelerator Beam Applications (LABA) at MIT was used as the heat source. The 2.0 MeV proton beam was described as Beam II in Chapter Three. The beam line elements, as shown in Figure 3.9, consist of an x-y steering magnet, a quadrupole doublet, and a switching magnet. The experiments used the center port of the switching magnet so the switching magnet acts as merely a drift space. A water-cooled aperture (2.5 mm diameter opening, about the same size as the target, shown in Figure 3.9) right in front of the needle tube limits the beam size going into the needle tube. The beam envelopes are shown in Figure 3.10. Under the best conditions, a maximum of 63% of total beam is expected to be delivered to the target.

Similar to that with Prototype I, maneuvering the proton beam to the target was done in two steps. First, the beam current through water-cooled aperture was maximized using the x-y steerers and quadrupole lenses. Next, the beam current to the target was maximized by turning the angular tilter. However the beam tuning was much more tedious than with Prototype I. For Prototype I, the flange base was solidly fixed to the accelerator beam tube and not moved by the step motors pushing the needle tube at the tip. So, there was no interference between the two steps and sequential execution of the two steps usually gave good results. With Prototype II, the whole needle tube assembly including the water-cooled aperture was mounted on the angular tilter and moves with the angular tilter. There is a correlation between the two steps. It usually took a few recursions of the two steps back and forth to get the proton beam down to the target. During the escalation of current onto the target, temperatures, T_1 and T_2, were recorded as a function of heat load. The maximum percentage of total proton beam put onto the target was 45%, when the percentages to the needle tube and the water-cooled aperture were 11% and 44%.

At 0.8 l/min of 1 atm and 30 °C water flow, T_1 increases with heat load linearly until 70 Watts, as shown in Figure 6.4. In a subsequent experiment, the cooling flow rate was increased to 1.4 l/min and 2 atm with a 1/4 horse power pump, and a heat removal of 150 Watts was still in the linear range. The experiments stopped at this point because of difficulty in getting more current to the target. At the achieved heat load of 150 Watts, T_1 is at a maximum of 142°C. As expected, T_2 remained low (<50°C) throughout all these experiments. For a beryllium target in similar situations, a similar T_2 is expected and so the teflon sleeve will be at a safe temperature.

At the heat load of 150 Watts, the treatment times for a 4.5 cm diameter tumor for the candidate reactions are calculated from Table 4.5 and listed in Table 6.1. They are 5 minutes for the ^{7}Li(p,n)^{7}Be reaction at E_d=4.1 MeV, 7 minutes for the ^{9}Be(d,n)^{10}B reaction at E_d=1.5 MeV, and 16 minutes for the ^{9}Be(p,n)^{9}B reaction at E_d=4.0 MeV. The treatment times are short enough to be practical. A decision was made at this point to make a beryllium target of the same dimensions. (With the same argument as with Prototype I, a beryllium target is favored over a lithium target which is much more difficult to handle.)

According to Appendix D, at the heat load of 150 Watts in the copper target, the heat transfer is likely by one phase convection across the target surface close to the teflon sleeve and by subcooled nucleate boiling across the surface close to the heated surface. The highest temperature, on the heated surface, is estimated to be 163 °C .

6.4. HEAT REMOVAL TEST ON BERYLLIUM TARGET

Heat removal tests were performed on the beryllium target the same way as with the copper target except the cooling conditions were better. A separate chiller (cooling and compression) with a deionization unit was used. The water pressure was increased from about 2 atm to 3-4 atm. The water temperature was kept constant by the chiller at about 23°C (30°C for the copper target heat removal test). The cooling flow rate was 1.4 l/min, the same as that for the copper target. The temperature increases with the heat load. The maximum of T_1, 220 °C, occurs at the maximum heat load of 127 Watts. T_2 remains lower than 40°C. The maximum percentage of total proton beam put onto the target was 36% when the percentages to the needle tube and the water-cooled aperture were 28% and 36%. The discontinuation of the test was due to the difficulty in getting more proton beam to the target.

The treatment times for a 4.5 cm diameter tumor for the candidate reactions at 130 Watts are calculated and listed in Table 6.1. (The lithium reactions are also listed for comparison.) The numbers are close to those at the 150 Watts with the copper target.

The regimes for heat transfer across the target-water surface is similar to that for the copper target. The highest temperature in the beryllium target, on the heated surface, is estimated to be 307 °C at a heat load of 130 Watts (Appendix D), which is much lower than the melting point (1290 °C) of metal beryllium.

6.5. CONCLUSIONS AND FUTURE WORK

Prototype II has been demonstrated to be capable of delivering high dose rate irradiation with a beryllium target. The design allows insertion into phantom. It is used in the dose profile measurements in a water phantom in Chapter Seven and the gamma yield measurement in Chapter Two for the ^{9}Be(d,n)^{10}B reaction at E_d=1.5 MeV.

The heat removal test on the target of Prototype II has not been carried out to near heat removal failure. Computer simulation of heat transfer (an analytical calculation is not possible due to the complex geometry of the target) or heat removal test at higher heat loads is needed to determine the safety margin, which is important to know for use in a medical situation.

Table 6.1. Time required to deliver 66 RBE.Gy to the boundary of a 4.5 cm diameter tumor at heat loads of 150 and 130 watts, the achieved heat removals from the copper and beryllium targets of Prototype II.

Particle Reactions	Bombarding Energy (MeV)	Treatment Time (min) at 150 watts	Treatment Time (min) at 130 watts
$^{7}Li(p,n)^{7}Be$	2.5	26	30
	3.0	13	15
	4.1	5.4	6.2
$^{9}Be(p,n)^{9}B$	3.7	22	26
	4.0	16	19
$^{9}Be(d,n)^{10}B$	1.5	7.3	8.5

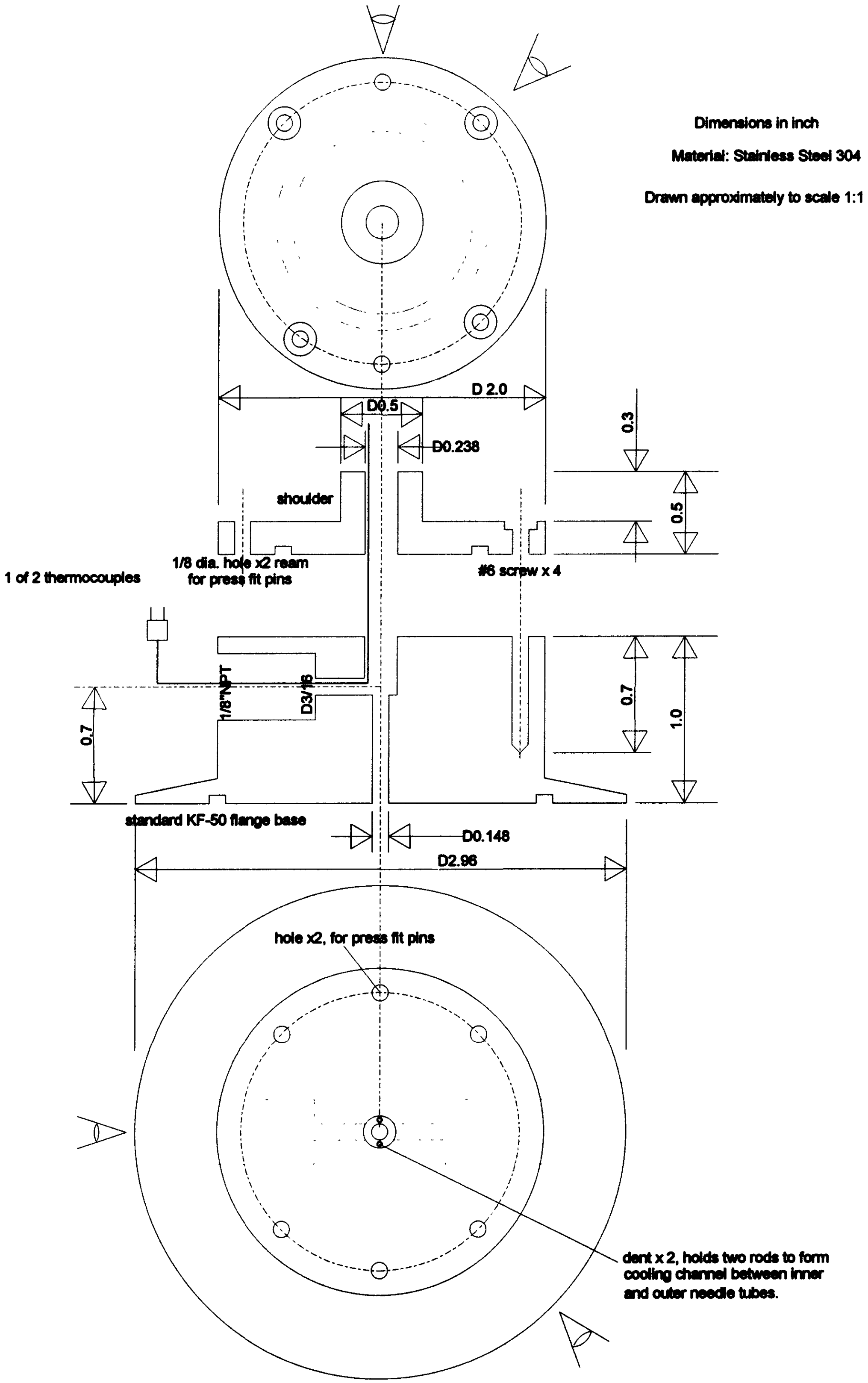

Figure 6.1.a. Needle tube Prototype II. The two base pieces, held together with precision by two press fit pins and four screws.

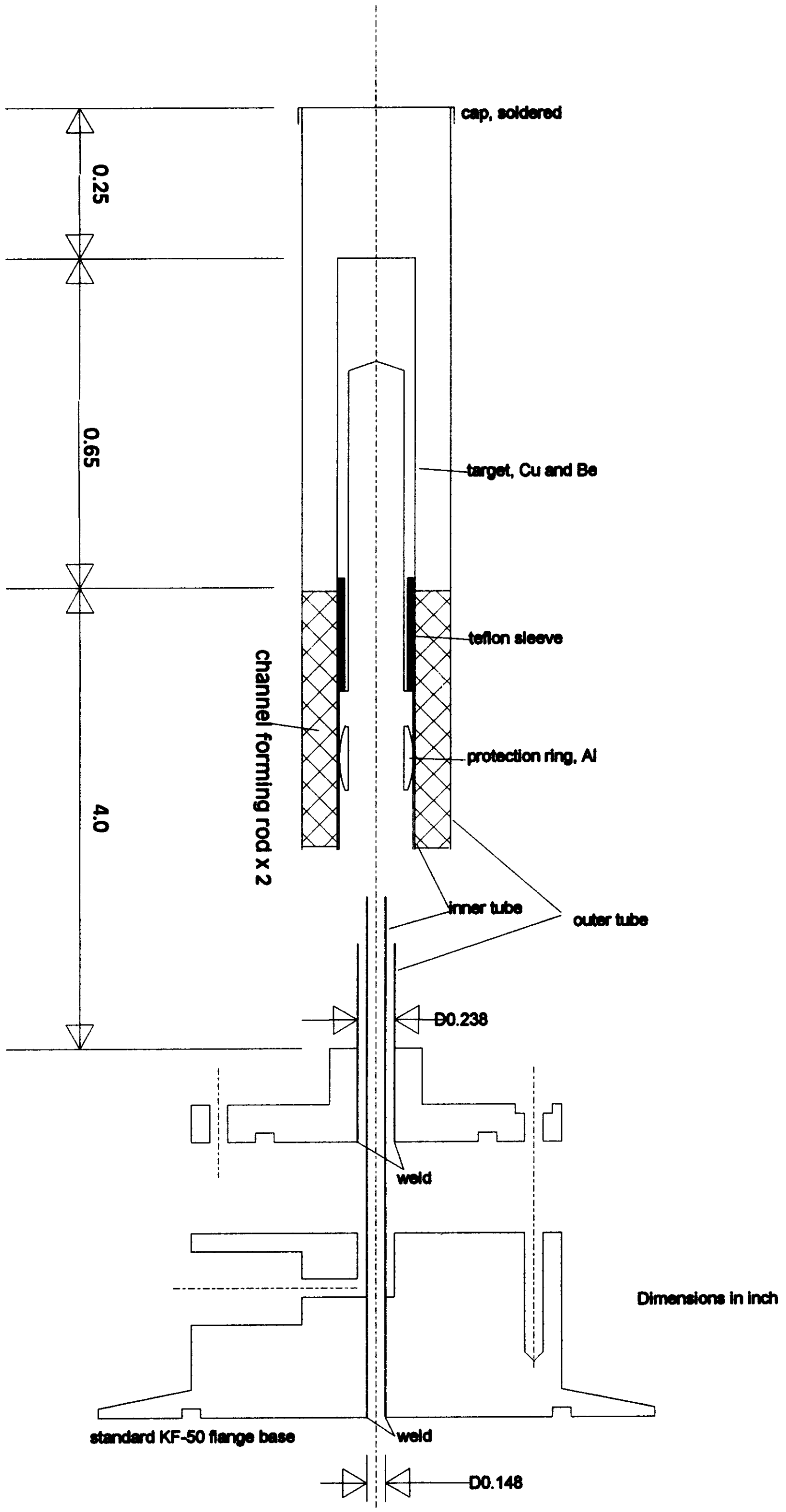

Figure 6.1.b. Needle tube Prototype II. The inner and outer tubes.

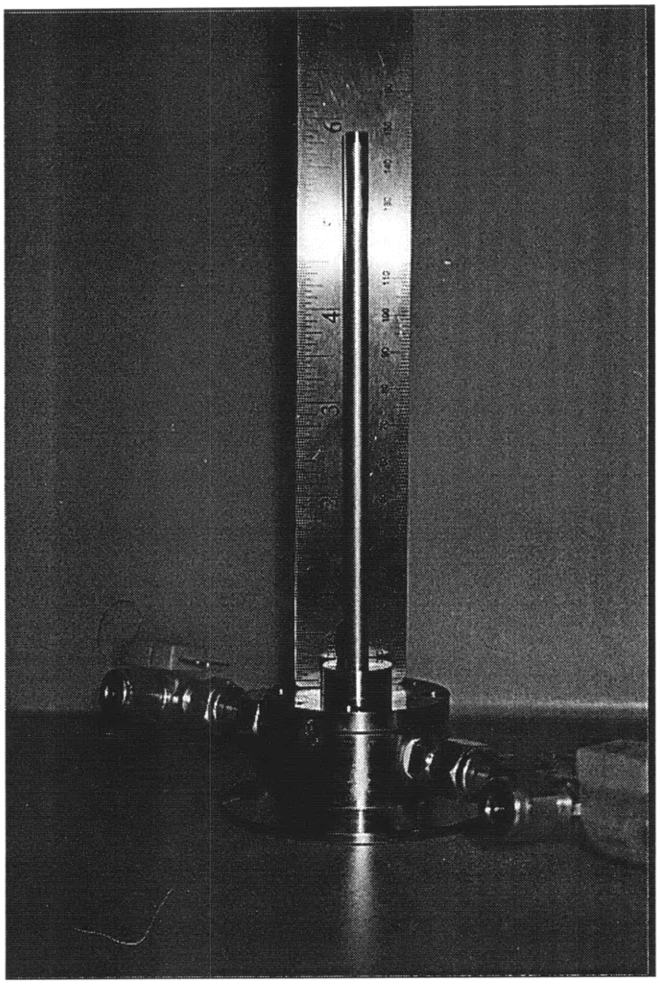

Figure 6.2.a. Picture of the needle tube Prototype II. Shown from top down are: outer tube, shoulder, and two base pieces. The two thermocouples are led out of the coolant inlet and outlet.

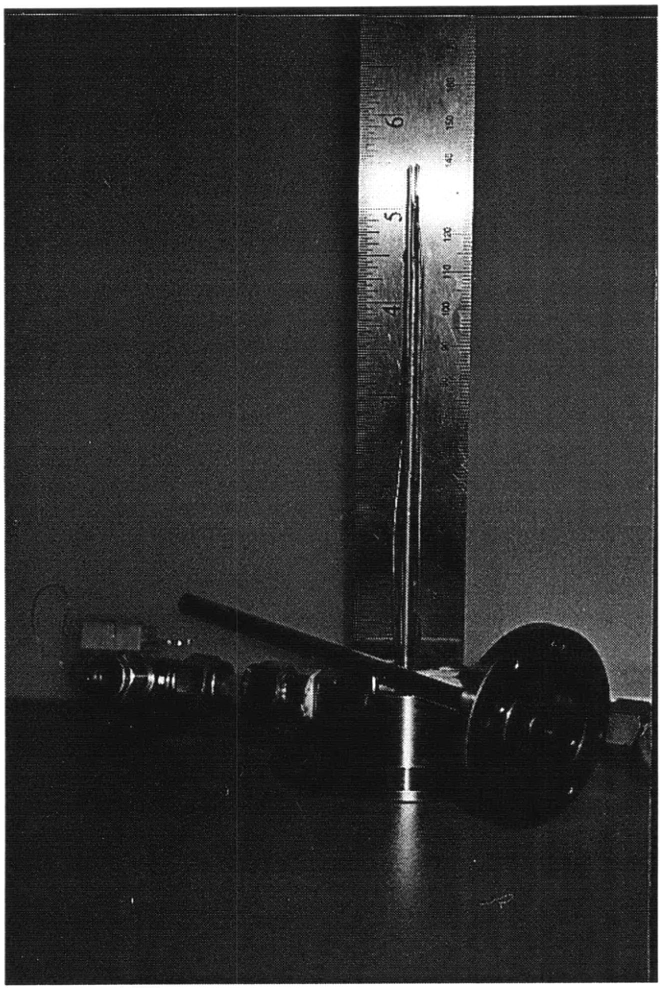

Figure 6.2.b. Picture of the needle tube Prototype II with the outer tube taken apart. The inner and outer tubes are welded separately to the two base pieces. The thermocouple wires go along the inner tube. At the top is the target. The two cooling channel forming rods are shown.

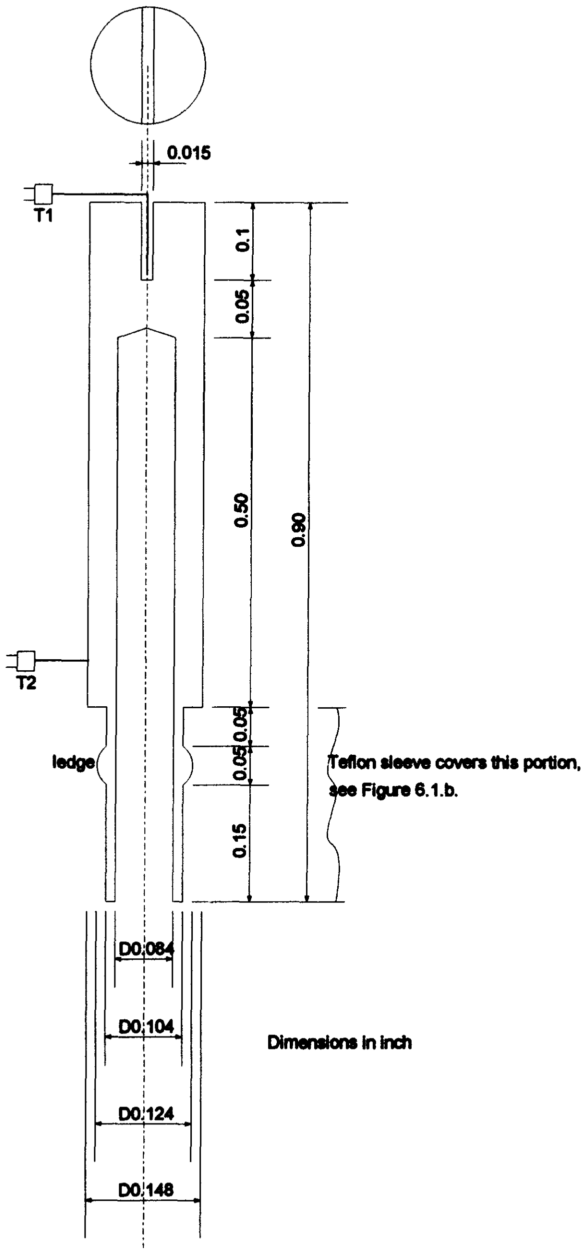

Figure 6.3. The target of Prototype II. Cu and Be targets were made. Also shown are positions of the two thermocouples, T1 and T2.

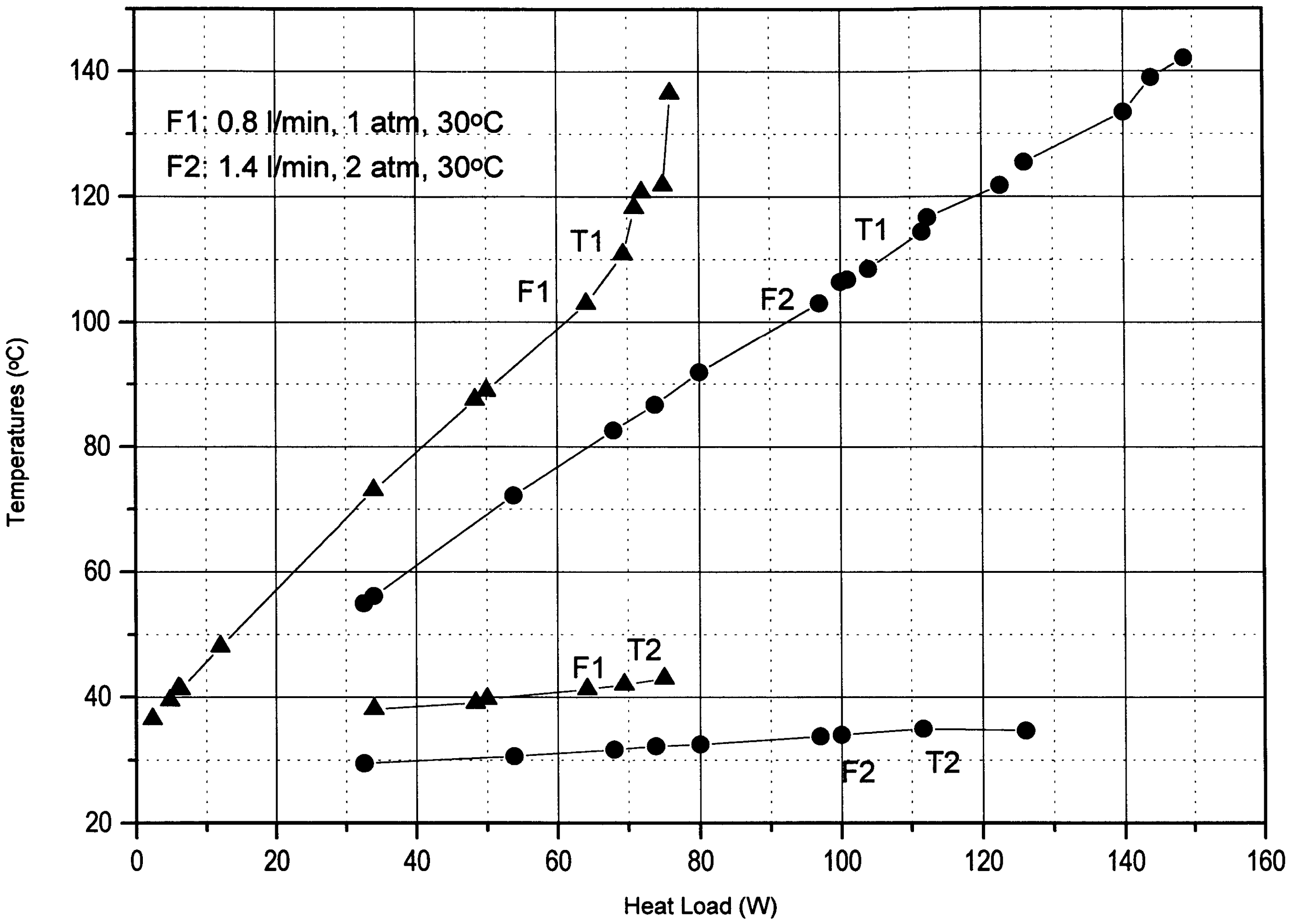

Figure 6.4, Temperatures from the copper target of Prototype II as a funtion of the heat load on the target under two different cooling flows, F1 and F2. Temperatures T1 and T2 are measured at the two locations in the target as shown in Fig. 6.3.

CHAPTER SEVEN
DOSE PROFILE MEASUREMENT

Dose profile measurements for the reaction $^{9}Be(d,n)^{10}B$ at E_d=1.5 were performed with Prototype II in a water phantom using the dual-ion chamber method. These measurements are presented in this chapter and are compared with Monte Carlo simulations using MCNP.

7.1. EXPERIMENTAL SETUP

A polyethylene tank of 30 x 30 x 30 cm^3 filled with water was used as the water phantom, as shown in Figure 7.1.a. The matrix of points where the dose measurements were taken is shown in Figure 7.1.b. The needle tube was inserted through one side wall of the phantom. A cone shaped plastic piece was used to make a water-proof seal. The plastic piece, being stretchable and flexible, allows small adjustments of the needle tube relative to the accelerator beam while in the tank. The beryllium target of the needle tube was centered in the tank along the x and y directions as shown in Figure 7.1.a. Limited by the 10 cm insertion length of the needle tube, the beryllium target can be extended up to 10 cm into the tank.

The tank is open from the top where the ion chambers access the radiation field. The ion chambers are not water resistant, so a water tight butyrate tube of 1.25 cm diameter is used. A polyethylene slab of 2.5 x 5 x 40 cm, fixed onto the tank edge with two C-clamps, holds the butyrate tube into the water-filled phantom.

7.2. DUAL ION CHAMBER METHOD

The dual ion chamber method for mixed field dosimetry utilizes two ion chambers with very different sensitivities, A and B, to photon and neutron doses, D_γ and D_n:

$$Q_i=A_i\, D_\gamma + B_i\, D_n,\ i=1,2, \tag{7.1}$$

where Q_i is the charge collected from the ion chambers. Take two measurements at the same location in the phantom with the two ion chambers and solve the two equations to get the photon and neutron doses.

The ion chamber pair used for this experiment is on loan from the MIT BNCT group. The development of the dual-ion chamber method for BNCT dosimetry is the work of the PhD thesis of Rogus, (1994). It is a comprehensive protocol for mixed field dosimetry, primarily for epithermal neutron beams. The thermal neutron flux is measured by gold foil activation. Dose from boron-10 concentration is calculated from the thermal neutron flux and the known kerma factors for boron-10. The responses of the ion chambers to thermal neutrons are pre-determined experimentally and subtracted. The two dose components left are photon and fast neutron doses which can be solved from equation (7.1). The definition of fast neutron is different from that in Chapter Four, which is above 0.36 eV. As will be discussed below, for use with the dual-ion chamber method, a fast neutron is defined as one with E_n > 0.1 MeV.

One ion chamber is made of A-150 plastic. The A-150 plastic, which has a 10.13 % weight H, close to the 10.6% H of brain tissue and 10.2% H of ICRU muscle, is called a tissue equivalent chamber (TE). The other ion chamber is a carbon graphite (0% H) chamber (CG). Both chambers are from the 18 series ion chambers from Far West, CA. The sensitivities to photon radiation, A_{TE} and A_{CG}, are determined by a Co-60 exposure calibration at a dosimetry calibration laboratory accredited by the American Association of Physicists in Medicine (AAPM). The different sensitivities to neutron radiation, B_{TE} and $B_{CG,}$ are achieved by the different hydrogen content of the chamber wall material (fast neutrons deliver dose mainly through collision with hydrogen). The neutron to gamma sensitivity ratio of the TE chamber, $(B/A)_{TE}$, as a function of neutron energy, E_n, is calculated (Rogus, (1994)) for brain tissue and is resketched in Figure 7.2. For $E_n < 0.1$ MeV, $(B/A)_{TE}$ shows large differences between using the W values (the average energy per ion pair) and extrapolated values from two different authors, Goodman and Coyne, (1980) and Leonard and Boring, (1973). For $0.1<E_n<10$ MeV, $(B/A)_{TE}$ is almost a flat function. The average is 0.92 for $0.1<E_n<10$ MeV. The dose simulations in this chapter will show that $E_n > 0.1$ MeV is the dominant (95%) dose component. So the uncertainty in $(B/A)_{TE}$ for $E_n < 0.1$ MeV will not have a significant effect on the uncertainty of the dose measurements. For the CG chamber, the neutron to photon sensitivity ratio, $(B/A)_{CG}$, is expected to be small due to the lack of hydrogen content. The average value of 0.044 is determined experimentally on a largely thermal neutron beam with thermal neutron part excluded (Ashtari, (1982)). Although the neutron dose being investigated here comes mainly from fast neutrons, it will be shown in the error analysis section after the dose measurements that the dose components are insensitive to the ratio $(B/A)_{CG}$. The numerical values of the A and B values are listed below (unit = coulomb/rad):

$$A_{TE} = 4.821\text{e-}11,\ B_{TE} = 4.435\text{e-}11,\ (B/A)_{TE} = 0.92;$$
$$A_{CG} = 7.591\text{e-}11,\ B_{CG} = 3.340\text{e-}12,\ (B/A)_{CG} = 0.044. \tag{7.2}$$

Special gases matching the ion chamber wall materials flush through the ion chambers at a rate of 20 cm^3/min and vent through the butyrate tube. For the TE chamber, the gas is tissue equivalent gas consisting of 64.4% CH_4, 32.4% CO_2, and 3.2% N_2 by partial pressure. The CG chamber uses CO_2 of 99.98% certified purity. The center of the ion chambers are biased at +250 volts as suggested by the manufacturer.

The two ion chambers have identical dimensions except the thimble (the actual chamber with the A-150 plastic or carbon graphite wall where ionization takes place). The thimbles are cylindrical with a rounded cap. The TE thimble has an outer diameter of 0.96 cm, a length of 1.50 cm, and a wall thickness of 0.251 cm. The CG thimble has an outer diameter of 0.787 cm, a length of 1.50 cm, and a wall thickness of 0.165 cm. The wall thickness of the thimbles is not enough to provide charged-particle equilibrium (CPE) (~ 1 cm for 2.2 MeV gamma). Water in the phantom will provide extra medium for CPE when the measurements are away from boundaries. The thimbles are mounted on a aluminum stem of about 25 cm long. The HV wire, signal wire, and the flushing gas tube are bundled to the aluminum stem. The ion chambers are not water proof, and inserted in a water tight butyrate tube of 1.25 cm diameter, 25 cm long to access depth in the water phantom. During the experiments, the ion chamber and the butyrate tube are filled with the flushing gas.

The 1.5 MeV deuteron beam from the tandem electrostatic accelerator in the Laboratory for Accelerator Beam Applications (LABA) at MIT is described as Beam III in Chapter Three. The beam line elements, as shown in Figure 3.9, consist of an x-y steering magnet, a quadrupole doublet, and a switching magnet. The experiment uses the center port of the switching magnet so the switching magnet acts as merely a drift space. The beam envelopes are shown in Figure 3.11. Under the best conditions, a maximum of 65% of the total beam current is expected to be delivered to the target. The beam was also used for the gamma yield measurements in Chapter Two.

Prototype II needle tube assembly consists of a water-cooled aperture, the needle tube base, and the beryllium target, as described in Chapter Six.

7.3. DOSE MEASUREMENT

The measurements were performed in the x=0 and y>0 plane only (for reference frame, see Figure 7.1.a) since the dose distribution is angularly symmetric. The position x=0 and z=0 was determined by looking down from top of the butyrate tube and aligning it to the spot of the needle tube which had been marked as the beryllium target. The different z values were achieved by sliding the polyethylene slab on the tank. The different y values were achieved by moving the butyrate tube up and downward. Dose profiles were characterized for a matrix of y and z positions in the x=0 plane, as shown in Figure 7.1.b. The z values were -8, -6, -4, -2, 0, 2, 4, 6, 8 cm. Along the y direction, parameter d, as shown in Figure 7.1, is defined as the distance between the bottom of the butyrate tube and the outer surface of the needle tube and values of 0, 1, 3, 5, 7 cm were used. The relation between y and d is

$$y = d+\Delta, \tag{7.3}$$

where Δ is the sum of the space of the butyrate bottom cap (.32 cm), the needle tube radius (.32 cm) and the distance between the ion chamber tip and the effective center of the ion chamber. The ion chamber thimble is a 1.50 cm long cylinder with a rounded tip. It collects ionization charge from the whole sensitive volume and is an average over the sensitive volume. For the measurement of a gradient radiation field, it is a question how to present the sensitive volume on a chart with a single point (the effective center). For convenience, the mid point of the cylindrical axis of the ion chamber thimble is assigned as the effective center of the ion chamber, which adds 0.75 cm to the value of Δ and makes a value of 1.39 cm for Δ. However, assigning the effective center as above introduces two errors: 1) The mid point of the cylindrical axis of the ion chamber thimble is not the geometric center since the thimble has a rounded tip; and 2) The effective center of the ion chamber is dependent on the gradient of the radiation field, as illustrated in Appendix E. The uncertainty in the effective center of the ion chamber will be addressed in the error analysis section below.

The measurements were carried out in many sessions in a course of days.

For each point on the matrix of z-d, charge was collected from both ion chambers for five minutes, and the deuteron current was integrated over the same time. The accelerator deuteron currents were similar for all sessions: 10, 7, and 20 μA to the beryllium target, needle tube and the water-cooled aperture before the needle tube, respectively. (A typical target/total current ratio is 27% as opposed to the predicted maximum of 65%.) The weakest signal (at the farthest point in phantom from the source) from the ion chambers was 0.08 nC/5min. The dark currents of the ion chambers were taken at the start and end of each session. The absolute value of the dark currents (could be either positive and negative) ranged from 0.09 to 5.99 pC/5 minutes. The weakest signal was 13.4 times as strong as the highest dark current. Although the dark current is not predictable, its effect should be minimal in this experiment.

For each point on the z-d matrix, equation (7.1) was solved, assuming all the neutron contributions are from E_n>0.1 MeV (see justification from dose simulations in next section). The fast neutron (En>0.1 MeV) dose, $D_{n>0.1,}$ and photon dose rate, $D_{\gamma,}$ distributions are summarized in Table 7.1.

Several trends can be readily observed. There is a mirror symmetry between the columns on both sides of the z=0 column, which means the dose distribution is isotropic in the whole phantom. For comparison with simulations, doses will be averaged over the two mirrored points. The dose rate decreases with either z and d, consistent with the fact that dose decreases with distance, R, from the source. The relation between R, z, d, and y is

$$R= \sqrt{z^2+y^2} = \sqrt{z^2+(d+\Delta)^2}\,. \qquad (7.4)$$

R ranges from 1.39 to 11.6 cm when Δ takes the value of 1.39 cm.

Quantitatively, the dose rate will be compared with Monte Carlo simulations.

7.4. DOSE SIMULATION & COMPARISON WITH MEASUREMENT

The kerma (dose) distribution can be calculated from the neutron and photon fluence, which are simulated with the Monte Carlo Code MCNP, Version 4A (Briesmeister, (1993)), with the kerma factors. An alternative is to use the f_6 tally of MCNP. As described in Chapter Four, while the two methods show significant difference for the thermal neutron dose, they agree within 1% for fast neutron and photon dose calculations. In Chapter Four, the first method is used for the dose simulations. In this chapter, the f_6 tally of MCNP will be used to simulate the dose components that will be compared to the dose measurements.

The dual ion chamber method has a well defined sensitivity for neutrons above 0.1 MeV and for all the gammas. The neutron dose is separated to be $D_{n<0.1}$ for E_n <0.1 MeV and $D_{n>0.1}$ for E_n >0.1 MeV.

The simulations tried to be realistic with simplifications in geometry that would greatly reduce the complexity in modeling. The phantom is a water sphere of 20 cm radius, which mimics the distance from the beryllium target to the front wall of the water tank. (In the real phantom, it is longer than 20 cm from the beryllium target to some tank corners, and shorter to other walls. As shown in Chapter Four, phantom size affects thermal neutron but not fast neutron dose.) The source is idealized to be a centrally located point source of neutrons and gammas.

The neutron spectrum from the reaction $^9Be(d,n)^{10}B$ at E_d=1.5 MeV is estimated by shifting up E_d=1.4 MeV neutron spectrum from Whittlestone, (1977) by 0.1 MeV, as described in Chapter Two. The neutron yield for En>0.1 MeV is estimated to be

$$Y_{En>0.10} = 5.7\ [\pm 10\%] \times 10^8\ n/\mu C \quad \text{(Chapter Two).}$$

The source gamma yields are measured at 60° to the accelerator beam, as described in Chapter Two. The total gamma yields are obtained by multiplying the differential yields at 60° by 4π and are listed in Table 2.6.

The dose measurements have shown the dose distribution is isotropic. So the simulation did not try to get angular distribution information. The phantom was divided into spherical shells, 0.5 cm apart, and represented in plotting by the mid point of the shell. To be more specific, the spherical shells are divided along radius of 0.5, 1.0, 1.5, ..., and 20.0 cm and represented as 0.25, 0.75, 1.25, ... , and 19.75 cm. The doses were averaged over the whole shell. Since the length of the ion chambers is 1.5 cm, the doses were then averaged over every neighboring 3 shells (1.5 cm in space) to compare with the ion chamber measurements.

The simulation shows that $D_{n>0.1}$ ranges from 99.8% to 95% of the total neutron dose throughout the whole radius of 20 cm. As discussed earlier in this chapter, the neutron to gamma sensitivity ratio of the TE ion chamber, $(B/A)_{TE}$, is flat and around 0.9 for E_n>0.1MeV. For E_n<0.1MeV, $(B/A)_{TE}$ varies between zero (case one, using the W and extrapolated values of Leonard and Boring, (1973)) and 1.5 (case two, using the W and extrapolated values of Goodman and Coyne, (1980)) (see Figure 7.2). If case one is true, the fast neutron doses listed in Table 7.1 equal $D_{n>0.1}$. If case two is true, the fast neutron doses listed in Table 7.1 are roughly 5% more than $D_{n>0.1}$. The uncertainty in $(B/A)_{TE}$ is thus taken as an error of 0 to -5% to $D_{n>0.1}$.

The comparisons between the simulation and measurement of D_γ and $D_{n>0.1}$ are shown in Figure 7.3.a and 7.3.b. The measured data points are plotted with error bars, which include the following components: dual-ion chamber method (electrometer ±0.5%, gamma dose calibration ±2.0%, and B/A ratios) (Rogus, (1994)) and the error of deuteron current measurement ±1% (Chapter Two). The errors from the B/A ratios are given as $(B/A)_{CG}$ ±3% and $(B/A)_{TE}$ ±1% for photon dose and $(B/A)_{CG}$ ±4% and $(B/A)_{TE}$ ±6% for neutron dose. The total errors are thus ±4% for the photon dose and ±8% for the neutron dose, as shown in the error bars in Figure 7.3.a and 7.3.b.

There is uncertainty in the positioning of the ion chambers. The dual-ion chamber method requires the two chambers measure at the same spot. Uncertainty in placing the two chambers at the same position is estimated to be 2 mm. This uncertainty results in error in the dose calculations and dose versus distance determinations, especially in a gradient radiation field as in the present work. The uncertainty in determining the distance from the beryllium target to the butyrate tube cap is estimated to be 2 mm, the major source resulting from the fact that the polyethylene tank top edge is not smooth. For convenience, the mid point of the cylindrical axis of the ion chamber thimble was assigned as the effective center of the ion chambers, as discussed in Section 7.3. In the dose measurements, the ion chambers were placed upright at all measurement points rather than pointing to the beryllium target. This adds a variation to the gradient of the radiation field the ion chamber sees and thus adds another uncertainty to the effective center. A best guess of the uncertainty in the effective center of the ion chamber is 5 mm (the length of the ion chamber thimble is 15 mm). The three sources of position uncertainty are independent from each other. The total uncertainty in the position of the dose measurement is therefore 5.7 mm, i.e., ±0.29 cm.

The uncertainties in dose rate simulations are from errors in kerma calculations and neutron and source gamma yields. Kerma calculation error for neutron dose is 10% and 0% for photon dose (Chapter Four). The errors in the neutron yield is ±10% and ±14% for the source gammas (Chapter Two). Therefore, the total uncertainties are: ±14% for neutron dose and ±14% for photon dose. The two thin lines in Figure 7.3.a and 7.3.b are two variations of the simulated dose rates for the following two cases: lower line, lower by 14% and shifted 0.29 cm to the left; and upper line, higher by 14% and shifted by 0.29 cm to the right.

The measured data points fall well within the upper and lower limits of the simulated lines for the photon dose, as shown in Figure 7.3.a. The measured neutron dose data points are lower than the simulation. The dashed line in Figure 7.3.b is calculated with a neutron yield 30% lower than the neutron yield $Y_{En>0.10}$, which is estimated in the present work (Chapter Two) from the neutron yield measurement by Whittlestone, (1977). The -30% line agrees well with the measured data points. Therefore, the neutron yield (4.0=5.7 x (1-30%)) for E_n>0.1 MeV to match the dose rate measurement of the present work is

$Y_{En>0.10}$=4.0 x 10^8 n/μC (to match dose rate measurements)

for the ^{9}Be(d,n) reaction at E_d=1.5 MeV. The total neutron yield at E_d=1.5 MeV is compiled by Burrill, (1964) to be

Y_{total}=4.0 x 10^8 n/μC (Burrill, (1964)).

The neutron yield with a neutron energy cut-off of 0.1 MeV will be less. So the $Y_{En>0.10}$ to match the dose rate measurements is between the neutron yield estimates by Whittlestone, (1977) and Burrill, (1964). Considering the possible -5% error in the dose measurements due to the uncertainty of the TE ion chamber's sensitivity to neutrons below 0.1 MeV (earlier in this section), the neutron yield to match the dose measurement could go down further by 5%.

Error analysis of $(B/A)_{CG}$ was performed on the data set at z=0, d=0, 1, 3, 5, and 7 cm. From the arguments of Section 7.2, $(B/A)_{CG}$ is expected to be a small number. The number of 0.044 used in the above calculations was derived from a largely thermal beam. If this ratio is set to zero, the gamma dose changes by +(6.2-8.8)% and the neutron dose by -4.8%. If this ratio is doubled to 0.088, the gamma dose changes by -(6.9-9.8%) and the neutron dose by +5.3%. This analysis shows that the dose calculations are very insensitive to the ratio $(B/A)_{CG}$.

7.5. CONCLUSIONS

The dose distribution for the reaction ^{9}Be(d,n)^{10}B at E_d=1.5 in a water phantom has been measured with the dual ion chamber method at distances between 1.39 and 11.6 cm from source. A good agreement was shown between the photon dose measurements and Monte Carlo simulation using the gamma intensities measured in Chapter Two. The neutron yield for E_n>0.1 MeV to match the measured neutron dose is around 30% less than that estimated from the spectrum by Whittlestone, (1977) in Chapter Two and higher than the estimate by Burrill, (1964).

Table 7.1. The fast neutron and photon dose rate distributions in a water phantom for the reaction $^{9}Be(d,n)^{10}B$ at E_d=1.5. The dose rate unit is Gy/min per 100μA of deuteron current.

Fast Neutron									
d (cm)	z=-8	z=-6	z=-4	z=-2	**z=0**	z=2	z=4	z=6	z=8
0	0.053836	0.097441	0.209453	0.757951	**2.381066**	0.969443	0.286904	0.108399	0.046991
1	0.051341	0.098782	0.213628	0.540781	**1.02859**	0.506363	0.208121	0.098588	0.048874
3	0.040063	0.071676	0.120929	0.205015	**0.268039**	0.195738	0.116094	0.068238	0.037682
5	0.027611	0.045418	0.066456	0.089947	**0.106326**	0.085511	0.060533	0.044554	0.026221
7	0.01928	0.028578	0.037512	0.045274	**0.052468**	0.041249	0.030468	0.026569	0.017248
Photon									
0	0.03934	0.074019	0.176178	0.412988	**1.566938**	0.416811	0.14599	0.072234	0.043698
1	0.044629	0.073858	0.136425	0.293507	**0.511702**	0.267277	0.119113	0.065186	0.041095
3	0.037027	0.054625	0.083703	0.121616	**0.144087**	0.11383	0.07851	0.051592	0.035396
5	0.028796	0.038917	0.052498	0.064934	**0.06655**	0.062517	0.050429	0.038025	0.028783
7	0.021533	0.027637	0.034703	0.039812	**0.036741**	0.039787	0.034455	0.027863	0.022235

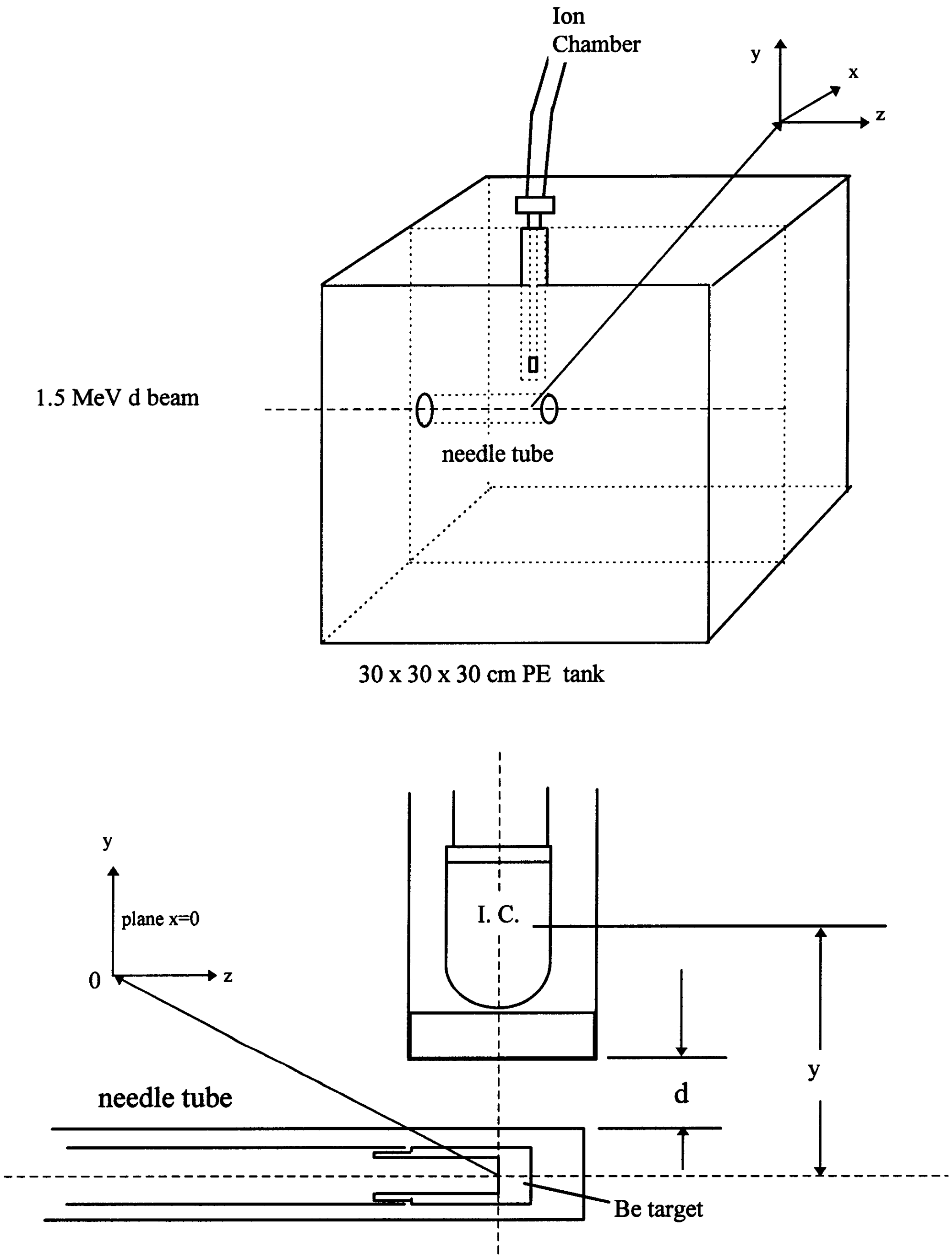

Figure 7.1.a. Schematic of the dose profile measurement in a water phantom. The measurements were made in the x=0 plane. Definition of the parameter d is shown.

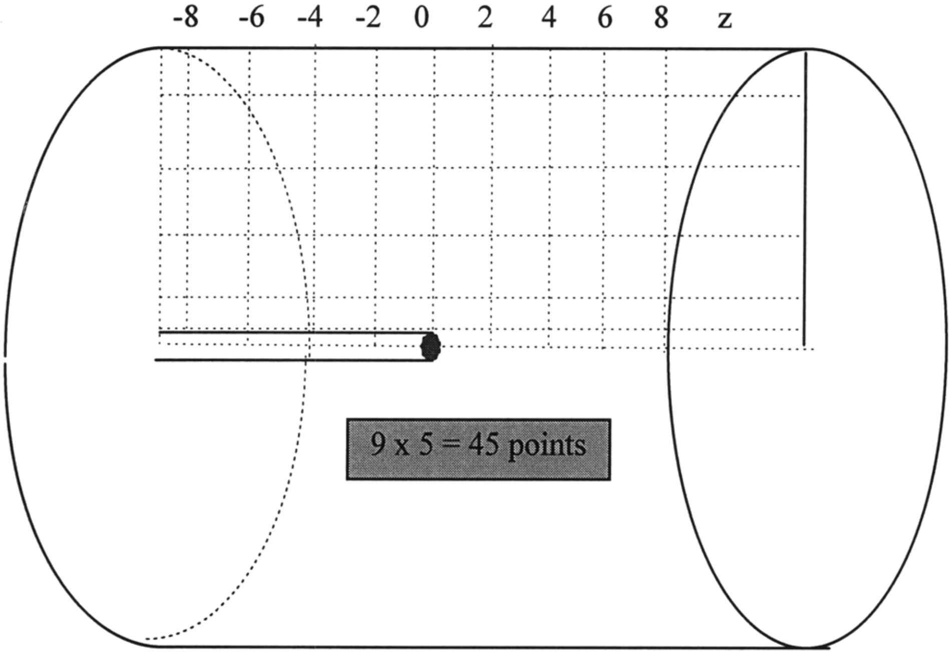

Figure 7.1.b. The matrix of points where the dose measurements were taken.

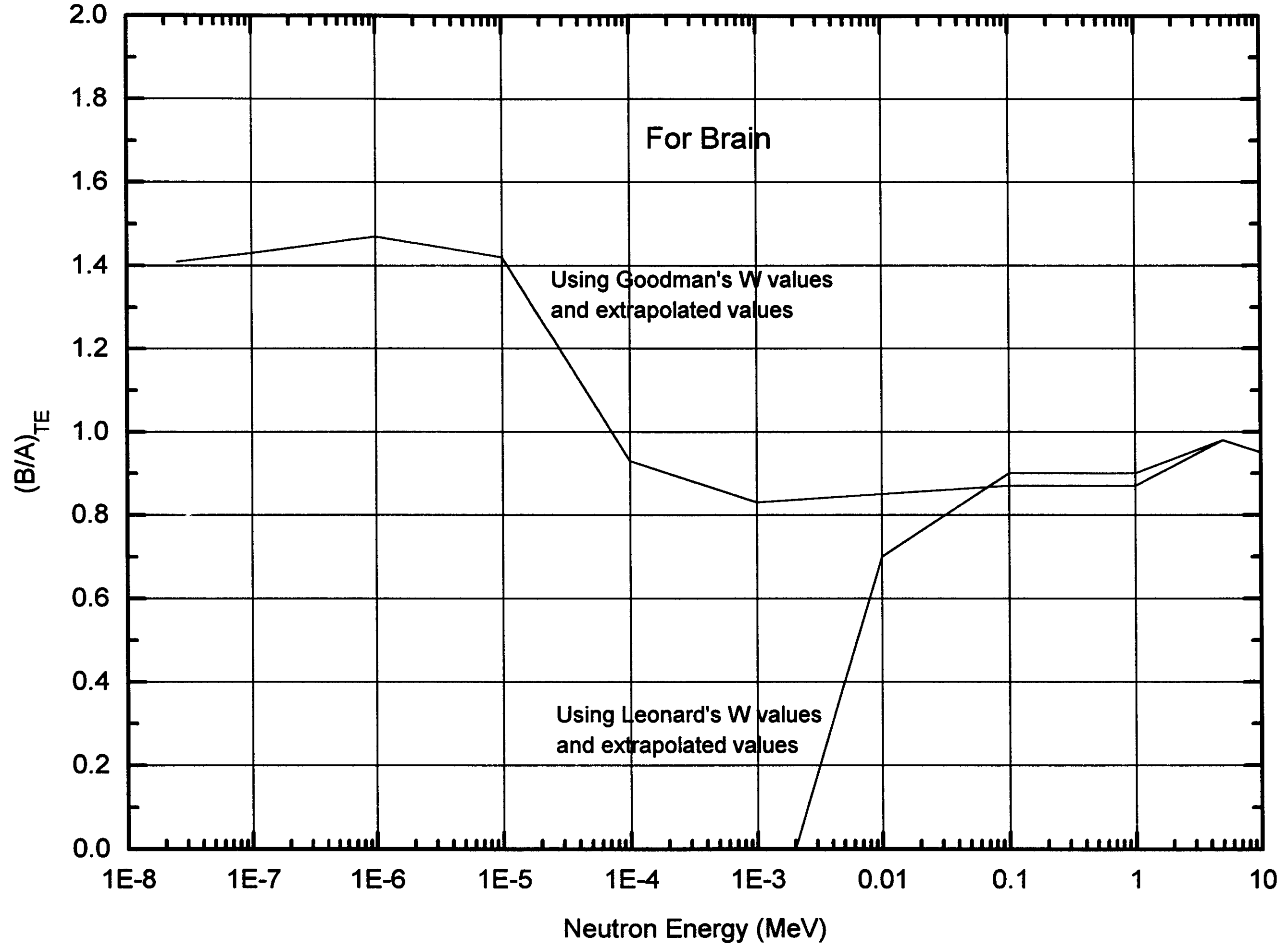

Figure 7.2. The neutron to gamma sensitivity ratio for brain and the tissue equivalent ion chamber as a function of neutron energy. The two curves are calculated using the different W and extrapolated values from Goodman and Leonard. The two curves diverge at below 0.1 MeV. Redrawn from Rogus, (1994).

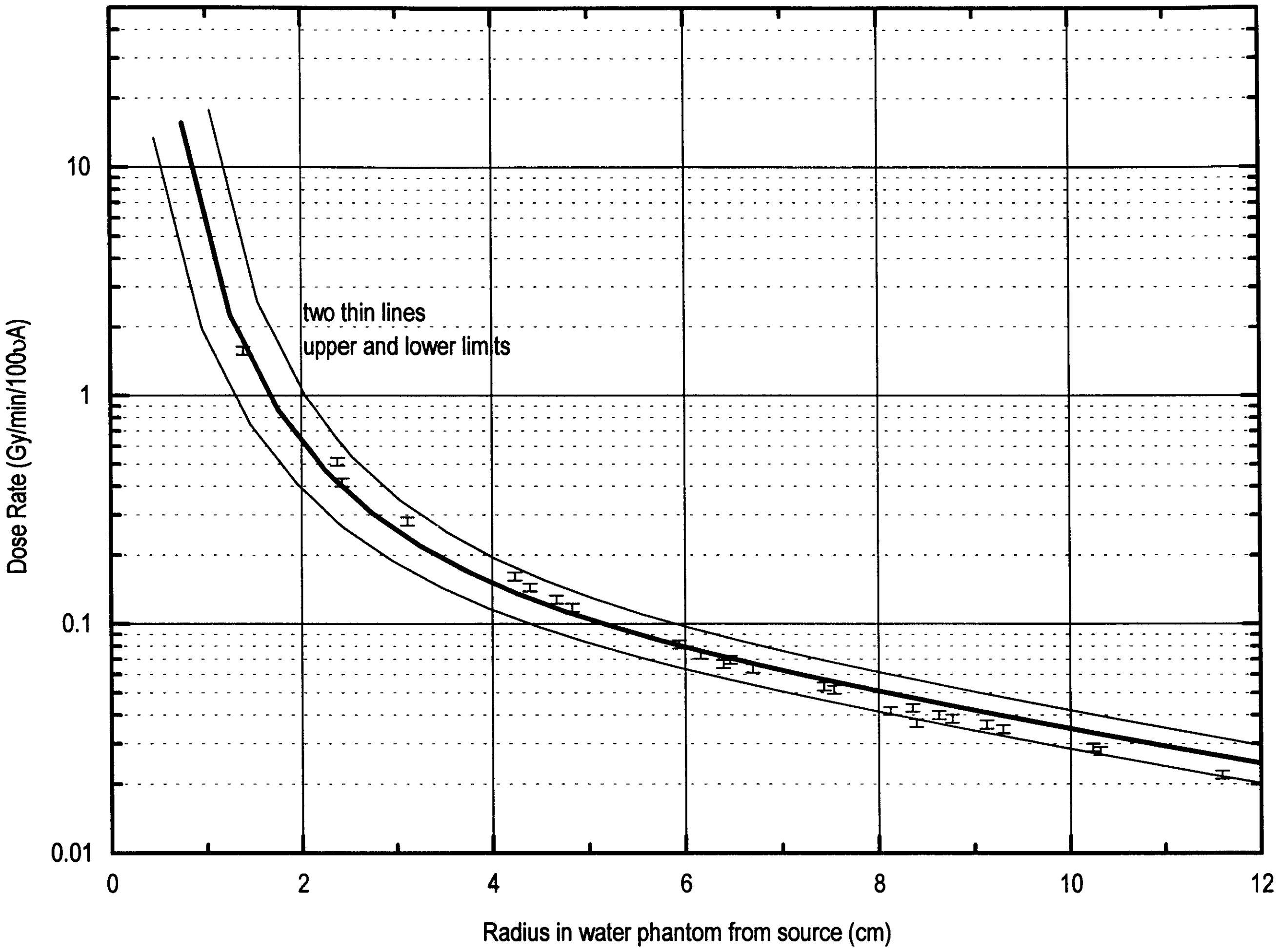

Figure 7.3.a. Dose distribution in a water phantom for the reaction ^{9}Be(d,n) at Ed=1.5 MeV. Comparison between simulation and measurement of the photon dose.

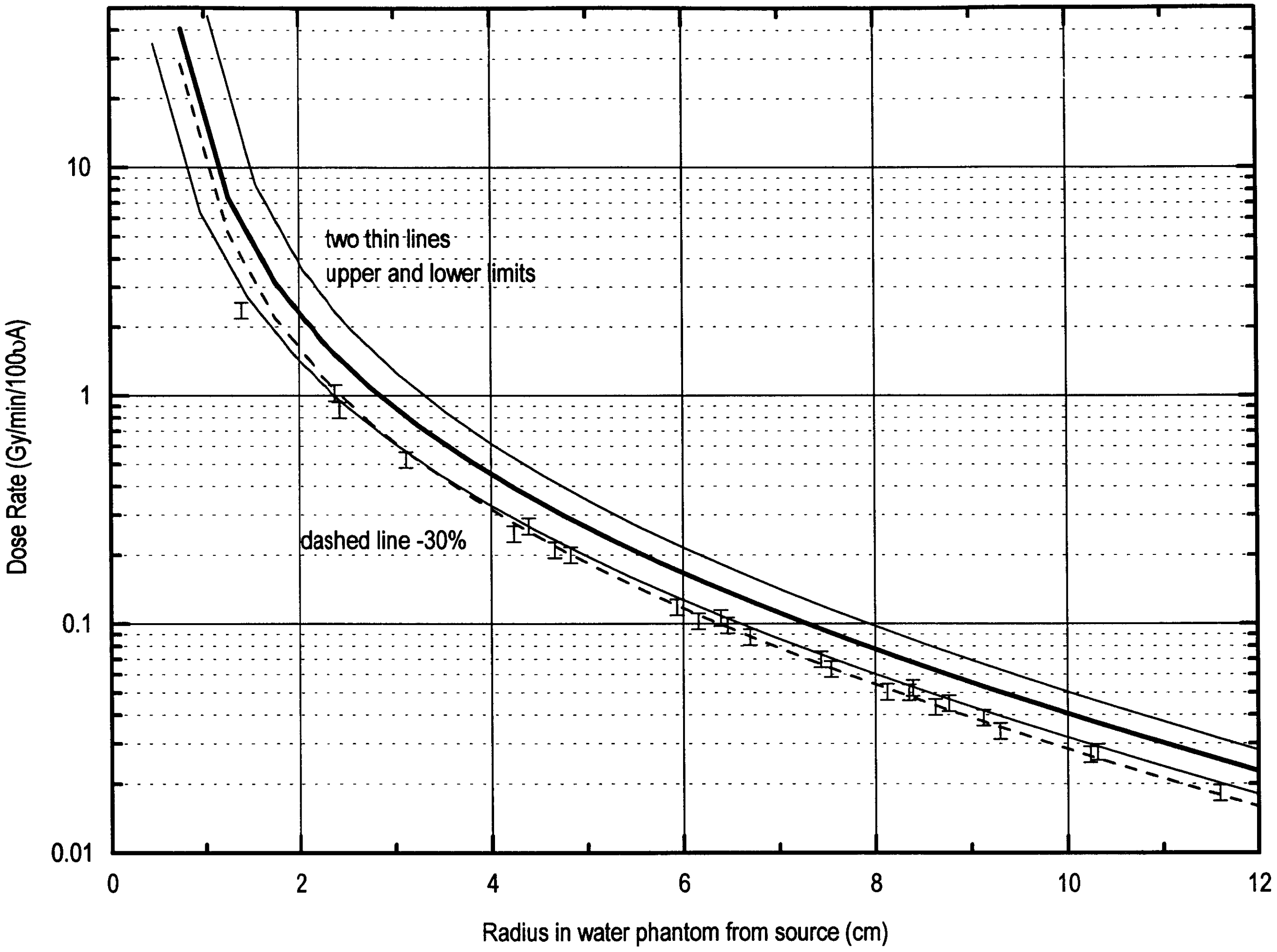

Figure 7.3.b. Dose distribution in a water phantom for the reaction ^{9}Be(d,n) at Ed=1.5 MeV. Comparison between simulation and measurement of the fast neutron (En>0.1 MeV) dose.

CHAPTER EIGHT
CONCLUSIONS AND FUTURE WORK

The feasibility of Accelerator-Based Neutron Brachytherapy (ABNBT) has been demonstrated through simulations and experimental work. The candidate nuclear reactions are $^{9}Be(d,n)^{10}B$, $^{9}Be(p,n)^{9}B$, and $^{7}Li(p,n)^{7}Be$. For the $^{9}Be(d,n)^{10}B$ reaction at E_d=1.5 MeV, with the Prototype II needle tube, a therapeutic dose of 66 RBE.Gy can be delivered to the boundary of a 4.5 cm diameter tumor in 7.3 minutes based on a power level of 150 Watts to the target. For the other two reactions, the proton beam energy must be near 4.0 MeV to deliver a similar dose rate at the same heat load to the target. However, they have more potential of coupling with BNCT with their softer neutron spectra.

The focus of the present work is on the treatment of intracranial tumors, which limits the dose delivery needle tube to a smaller size (6 mm in diameter) than other tumor sites would allow and imposes a major barrier on heat removal capability of the target and hence delivery of high dose rate. A copper target in the shape of a plug was made for Prototype I and tested to 38 Watts of heat load. It was determined that 38 Watts is probably the maximum heat removal achievable with the design of the target of Prototype I when applying to a lithium or beryllium target. At such a heat load, the treatment time for a 4.5 cm diameter tumor can be within half an hour (based on input from dose simulation work). However, the heat removal capability of the target can be improved significantly in a situation where the diameter of the needle tube can be increased; the dose rate can be correspondingly higher. Prototype II used a tube-shaped target which has been tested to a heat load of 150 Watts. The treatment time for a 4.5 cm diameter tumor can be as short as a few minutes. Besides the improvement in dose rate over Prototype I, Prototype II is suitable for insertion into a phantom. After the heat removal test on a copper target, a beryllium target of identical dimensions was made and also tested to similar heat loads.

The $^{9}Be(d,n)^{10}B$ reaction at E_d=1.5 MeV was chosen to perform dosimetry measurements in a water phantom with Prototype II using the dual-ion chamber method. Fast neutron and photon doses were measured and compared with simulations. The agreement is good for the photon dose. The measured fast neutron dose distribution as a function of distance from the beryllium target has a shape similar to that from the simulations. But the neutron yield to match the measured fast neutron dose rates is around 30% lower than the estimate based on data by Whittlestone, (1977). However, the neutron yield to match the measured fast neutron dose rates is higher than the estimate by Burril, (1964). The agreement between the simulations and the measurements supports the belief that the errors in the MCNP simulations mainly come from the input spectrum and yield data and the nuclear reaction cross section data used by the MCNP code.

The differential yields of the source gammas from a thick beryllium target bombarded by a 1.5 MeV deuteron beam have been measured in the present work at 60° with a 76 mm x 76 mm NaI(Tl) detector. The beryllium target used was the target of Prototype II. The prominent gammas are 414, 718, 1022, 1433, 1436, 2154, 2189, and 3587 keV from the $^{9}Be(d,n')^{10}B^{*}$ reaction, 3368 keV from $^{9}Be(d,p')^{10}Be^{*}$, and 478 keV from $^{9}Be(d,\alpha')^{7}Li^{*}$.

The sum of the yields is comparable with the neutrons from the ^{9}Be(d,n)^{10}B reaction. Another determination was that levels 6, 7, and 8 of ^{10}B, to which around 40% of the ^{9}Be(d,n')^{10}B* reaction channels lead, do not produce cascade gammas, probably due to dominance of the α-decay mode of these levels.

In the dose simulations, dose calculations using the fluence-to-kerma conversion factors and using the f_6 tally of MCNP were compared. A good agreement was found for the calculation of the fast neutron, photon, and boron-10 dose components, while the thermal neutron dose calculated using the f_6 tally is substantially higher than that calculated using the kerma factors. The difference may be a result of the approximations used in calculating the kerma factors at the thermal neutron energies.

For the clinical applications for ABNBT, there is more work ahead. To develop a therapy aimed at treating cervical cancers, a new prototype with a tube design of Prototype II and a target design of Prototype I but with a larger diameter could be useful. The heat removal test on the new design will be done first and dosimetry measurement in a water phantom and comparison with simulations are to follow. The possibility of applying ABNBT to other tumors sites, e.g., nasopharyngeal tumors, should also be looked into.

Prototype II has been tested to a heat load that allows a practical treatment time for a large tumor. However, safety margin of the heat removal needs to be determined either by heat testing at higher heat loads or simulation. Meanwhile, animal cell eradication trials could begin right away.

A gantry system, which allows the freedom of positioning the needle tube within a patient, will be needed for human clinical trials.

REFERENCES

Ajzenberg-Selove, F. (1979). “Energy levels of light nuclei A=5-10.” Nuclear Physics, A320, pp. 1-224.

Andersen, H.H. and J.F. Zeigler (1985). “Hydrogen: Stopping powers and ranges in all elements.” Pergamon Press, New York.

Ashtari, M. (1982). “Biological and Physical Studies of Boron Neutron Capture Therapy.” Ph.D. Thesis, MIT.

Briesmeister, J. (1993). “MCNP - A general Monte Carlo code for neutron and photon transport.” Version 4A, LA7396-M Rev.2, Los Alamos National Lab, Los Alamos, NM.

Brooks, R., G. DiChiro, and M.R. Keller (1980). “Explanation of cerebral white-gray contrast in computed tomography.” J. Comp. Asst. Tomog. **4**(4): 489-491.

Burrill, E.A. (1964). “Neutron Production and Protection.” High Voltage Engineering Corp., Burlington, MA.

Caswell, R.S., J.J. Coyne, and M. L. Randolph (1980). “Kerma factors for neutron energies below 30 MeV.” Radiation Research **83**: 217-254.

Caswell, R., J. Coyne, and M. Randolph (1982). “Kerma factors of elements and compounds for neutron energies below 30 MeV.” Int. J. Appl. Radiat. Isot. **33**: 1227-1262.

Chadha, M., J. Capala, J.A. Coderre, E.H. Elowitz, L. Wielopolski, and A.D. Chanana (1997). “Correlation of clinical outcome to the estimated radiation dose from BNCT.” Advances in Neutron Capture Therapy, Volume II, Chemistry and Biology, (Editors: B. Larsson, J. Crawford, and R. Weinreich): 575-579.

Chin, H.W., Y. Maruyama, R. Patchell, and A.B. Young (1991). “Cf-252 neutron brachytherapy for maglignant glioma: Retrospective and prospective views for future trials.” Nuclear Science Applications, Vol 4, pp. 261-271.

Coderre, JA, Makar MS, Micca PL, Nawrocky MM, Liu HB, Joel DD, Slatkin DN, and Amols HI (1993). “Derivations of the RBE for the high-LET radiations produced during boron neutron capture irradiations of the 9L rat gliosarcoma in vitro and in vivo.” Int J Radiat. Oncol. Biol. Phys. 27, pp. 1121-1129.

Crawford, J. (1992). “The potential of internal neutron sources in capture therapy.” Progress in Neutron Capture Therapy for Cancer, (Edited by B. Allen, Published by Plenum, NY, 1992): 203-205.

Dinsmore, M., K.J. Harte, A.P. Sliski, D.O. Smith, P.M. Nomikos, M.J. Dalterio, A.J. Boom, W.F. Leonard, P.E. Oettinger, and J.C. Yanch (1996). "A new miniature x-ray source for interstitial radiosurgery: Device description." Medical Physics **23**(1): 45-52.

Goodman, L.J. and J.J. Coyne (1980). "Wn and Neutron Kerma for Methane-Based Tissue Equivalent Gas," Rad. Res. 82, pp.13-26.

Grivet, P., M.-Y. Bernard, F. Bertein, R. Castaing, M. Gauzit, and A. Septier (1972). "Strong Focusing Lenses." Electron Optics, 2nd edition, Part 1: Optics, Chapter 10. Pergamon Press Ltd.

Guzek, J., U.A.S. Tapper, W.R. McMurray, and J.I.W. Waterson (1996). "Characterization of the ^{9}Be(d,n)^{10}B reaction as a source of neutrons employing commercially available RFQ linacs." Proceedings of the 5th International Conference on Applications of Nuclear Techniques (Crete, June 1996), pp. 509-512. (Edited by G. Vourvopoulos)

Holman, J.P. (1981). Heat Transfer. McGraw-Hill, Inc.

Howard, W.B. (1997). "Accelerator-based BNCT." Ph.D. Thesis, MIT. And Private communications.

Inada, T., K. Kawachi, and T. Hiramoto (1968). "Neutrons from thick target beryllium (d,n) reactions at 1.0 to 3.0 MeV." Journal of Nuclear Science and Technology, 5, pp. 22-29.

Kiss, Á.Z., E. Koltay, B. Nyakó, E. Somorjai, A. Anttila, and J. Räisänen (1985). "Measurement of relative thick target yields for PIGE analysis on light elements in the proton energy interval 2.4-4.2 MeV." J. of Radioanalytical and Nucl. Chem., Articles **89**(1): 123-141.

Knoll, G.F. (1989). "Radiation Detection and Measurement," Second Edition, pp. 590, 1989. (John Wiley & Sons, Inc.)

LABA Log Book, March, 1998

Larsson, J.D. (1988). "OPTIC II". Free distribution.

Lee, C. (1997). "Thick target doubly differential neutron yields for the 7Li(p,n)7Be reaction near threshold." Department of Nuclear Engineering of MIT.

Leonard, B.E. and J.W. Boring (1973). "The Average Energy per Ion Pair, W, for hydrogen and oxygen ions in a Tissue Equivalent Gas." Rad. Res. 55, pp.1-9.

Lekakh, B. (1996). "Mechanisms and limitations for water-cooling of high heat flux surfaces." Ph.D. thesis, MIT.

Liskien, H. and A. Paulsen (1975). "Neutron production cross sections and energies for the reaction ^{7}Li(p,n)^{7}Be and ^{7}Li(p,n)^{7}Be*." Atomic Data and Nuclear Data Tables **15**: 57-84.

Maruyama, Y. (1984). " Cf-252 neutron brachytherapy: An advance for bulky localized cancer therapy." Nuclear Science Applications, Vol 1, pp. 677-748.

Maruyama, Y. (1991). "Clinical radiobiology of Cf-252 for bulky tumor therapy." Nuclear Science Applications, Vol 4. pp. 29-43.

Maruyama, Y., J. Yoneda, and J. Wierzbicki (1991). "Methods for treatment of cervix cancer using Cf-252 neutron brachytherapy." Nuclear Science Applications **4**: 213-227.

Mattsson, J. and H. Peterson (1979). "Irradiation and tumor blood flow." Tumor Blood Circulation, (Edited by H. Peterson,, CRC Press, Florida, 1979.): 137-141.

Miller, J.P., R. Patchell, R. Yaes, H.W. Chin, B. Berner, J. Wierzbicki, R.J. Kryscio, Y. Maruyama, and A.B. Young (1991). "Preliminary report on Cf-252 neutron interstitial implant therapy for glioblastoma multiforme: A phase I trial." Nuclear Science Applications **4**: 281-289.

Morris GM, Coderre JA, Hopewell JW, Micca PL, Nawrocky MM, Liu HB, and Bywaters A (1994). "Response of central nervous system to boron neutron capture irradiation: Evaluation using the rat spinal cord model." Radiother. Oncol. 32, pp. 249-255.

Neiler, J.H. and P.R. Bell (1965), "The Scintillation Method." Alpha-, Beta- and Gamma-ray Spectroscopy, (edited by Kai Siegbahn), Volume 1, pp. 245-302. (North-Holland Publishing Company, Amsterdam.)

Rogus, R. (1994). "Design and dosimetry of epithermal neutron beams for clinical trials of BNCT at the MITR-II reactor." Ph.D. Thesis, MIT.

Shefer, R.E., R.E. Klinkowstein, J.C. Yanch, and W.B. Howard (1994). "Tandem electrostatic accelerators for BNCT." Proceedings of the 1st International Workshop for Accelerator-Based Neutron Sources for BNCT, INEL CONF-940976: 89-97.

Shefer, R.E. and R.E. Klinkowstein (1996). Newton Scientific, Inc., Cambridge, MA. Private communication.

Song, H., J. Yanch, and R. Klinkowstein (1996). "An accelerator-based interstitial neutron source for fast neutron brachytherapy." Medical Physics **23**: 1497.

Song, H., J. Yanch, and R. Klinkowstein (1996). "An accelerator-based neutron source for fast neutron brachytherapy." Proceedings of the 14th International Conference on the Application of Accelerators in Research & Industry, part two, pp. 1273-1276, (1996). (Edited by J. L. Duggan and I. L. Morgan. Published by the American Institute of Physics Press, New York, 1996.).

Song, H., J. Yanch, and R. Klinkowstein (1996). "An accelerator-based neutron source for fast neutron brachytherapy." Proceedings of the 14th International Conference on the Application of Accelerators in Research & Industry, (Edited by J. L. Duggan and I. L. Morgan. Published by the AIP Press, NY, 1996): Part Two, 1273-1276.

Song, H., J. Yanch, and R. Klinkowstein (1996). "An interstitial accelerator-based neutron source for fast neutron brachytherapy." Proceedings of the 1996 American Nuclear Society Topical Meeting: Radiation Protection and Shielding, (Published by ANS, Inc., La Grange Park, Illinois, 1996) **2**: 665-672.

Song, H., J. Yanch, and R. Klinkowstein (1997). "Accelerator-based fast neutron brachytherapy." Transactions of the American Nuclear Society, TRANSAO 77 1-560, (Published by ANS, Inc., La Grange Park, Illinois, 1997) **77**: 47-48.

Song, H., J. Yanch, and R. Klinkowstein (1997). "An interstitial/intracavity accelerator-based neutron source for fast neutron brachytherapy." Advances in Neutron Capture Therapy, Volume I, Medicine and Physics, (Editors: B. Larsson, J. Crawford, and R. Weinreich): 543-548.

Song, H., J. Yanch, and R. Klinkowstein (1998). "Accelerator-based neutron brachytherapy." Medical Physics. (Submitted).

Warburton, E.K., D.E. Alburger, and D.H. Wilkinson (1963). "Magnetic pair spectrometer studies of electromagnetic transitions in Be^{10} and B^{10}." Physical Review, Vol 132, Number 2, pp. 776-789.

Whittlestone, S. (1977). "Neutron distributions from the deuteron bombardment of a thick beryllium target." J. Phys. D: Appl. Phys., 10, pp. 1715-1723.

Wierzbicki, J. (1991). "Cf-252 for teletherapy and thermalized Cf-252 neutrons for brachytherapy." Nuclear Science Applications, Vol. 4, pp. 361-366.

Wierzbicki, J. (1997). Private communication.

Yanch, J. and R. Zamenhof (1992). "Dosimetry of Cf-252 sources for neutron radiotherapy with and without augementation by BNCT." Radiation Research **131**: 249-256.

Zamenhof, R., B. Murray, G. Brownell, G. Wellum, and E. Tolpin (1975). "BNCT for treatment of cerebral gliomas. 1: Theoretical evaluation of the efficacy of various neutron beams." Medical Physics **2**: 47-60.

Zhou, X. (1990). "A design of an accelerator-based epithermal neutron beam for BNCT." MS Thesis, MIT.

Appendix A
C Code for Calculating the Double Differential Neutron Yield Spectra for the ^{7}Li(p,n) and ^{7}Li(p,n′) Reactions and Generating the SDEF for the MCNP Input File

```
/* MCNP sdef generator for 7Li(p,n),ground state, Ep=1.95-4.1 MeV */
#include <stdio.h>
#include <math.h>
#define EPMAX 4.1
#define DATE "03/15/1998"
#define Filename_out "sdef.output"
#define c 2.997925e8
#define pi 3.14159265358979
#define avoga 6.022045e23
#define qe 1.602189e-19
#define mn 939.5735
#define mh 938.7910
#define mbe_atom 6536.2825
#define mli_atom 6535.4208
#define li7fraction .925
#define me 0.511 /* to get a more accurate value */
#define mp 938.2800
#define rho_li_nat 0.534 /* g/cm3*/
#define Sizeang 38
#define Sizeep 30

  double stoppower(double);

main (void)
{
  int i,j,k,ii,jj,kk;
  double x,y,z,xx,yy,zz,x1,x2,x3,x4;
  double q,mli,mbe,eth,Ip,fluxp, Nli7, ep, r, r_sq, koset, koset_sq, epenconv;
  double dsigdo, theta, yoen, en, dedx,yield, yeth_epmin;
  double atheta[Sizeang]=
    {0.,2.5,7.5,12.5,17.5,22.5,27.5,32.5,37.5,42.5,47.5,52.5,57.5,62.5,
    67.5,72.5,77.5,82.5,87.5,92.5,97.5,102.5,107.5,112.5,117.5,122.5,
    127.5,132.5,137.5,142.5,147.5,152.5,157.5,162.5,167.5,172.5,177.5,
    180.};
  double ayoen[Sizeep][Sizeang],aen[Sizeep][Sizeang];
  double a0,a1,a2,a3,dsigdo0pr,thetapr,dsigdopr,sigconv,p0,p1,p2,p3;
  double aep[Sizeep]={1.95,2.00,2.05,2.10,2.15,2.20,2.25,2.30,2.35,2.40,
            2.45,2.50,2.60,2.70,2.80,2.90,3.00,3.10,3.20,3.30,
            3.40,3.50,3.60,3.70,3.80,3.90,4.00,4.10,4.20};
  double aa0[Sizeep]={1.125,1.425,1.805,1.810,1.380,0.815,0.585,0.475,
            0.460,0.445,0.465,0.490,0.545,0.585,0.590,0.580,
            0.575,0.580,0.585,0.590,0.600,0.620,0.640,0.660,
            0.685,0.710,0.730,0.740};
  double aa1[Sizeep]={-.125,-.430,-.825,-.845,-.435,0.110,0.330,0.430,
            0.440,0.445,0.420,0.400,0.350,0.320,0.330,0.350,
            0.365,0.360,0.355,0.345,0.330,0.305,0.295,0.285,
            0.275,0.250,0.225,0.210};
  double aa2[Sizeep]={0.000,0.005,0.020,0.035,0.055,0.075,0.085,0.095,
            0.100,0.110,0.115,0.110,0.105,0.095,0.080,0.070,
```

```
           0.060,0.060,0.060,0.065,0.070,0.075,0.080,0.095,
           0.105,0.125,0.145,0.175};
  double aa3[Sizeep]={0.,  0.,  0.,  0.,  0.,  0.,  0.,  0.,
           0.,  0.,  0.,  0.,  0.,  0.,  0.,  0.,
           0.,  0.,  0.,  0.,  0.,  0.,  -.015,-.040,
           -.065,-.085,-.100,-.125};
  double adsigdo0pr[Sizeep]={19.,15.,12.1,13.1,22.6,46.7,79.2,83.4,71.4,
              61.2,53.0,47.4,40.5,36.0,34.2,33.0,32.0,
              31.2,30.5,29.9,29.3,28.7,28.2,27.8,27.4,
              27.0,26.7,27.1};
  double adsigT[Sizeep] ={269.,269.,275.,298.,392.,478.,582.,498.,413.,
            342.,310.,292.,277.,265.,253.,241.,232.,227.,
            223.,222.,221.,224.,227.,231.,236.,241.,245.,252.};
  double ayep[Sizeep];

  double yoep, ayoep[Sizeep][Sizeang];
  double sum1[Sizeep], sum2[Sizeang];
  FILE *Fp_o;

  q=fabs(mli_atom+mh-mn-mbe_atom);
  mli=mli_atom-3*me; /*nuclide weight*/
  mbe=mbe_atom-4*me;
  eth=q*(mbe+mn)/(mbe+mn-mp);
  printf ("threshold of reaction = %7.4f\n", eth);

  q=1.644;/* overwrite the calculated q and eth, for comparison*/
  eth=1.881;

  Ip=1e-6; /* for 1 uA of proton current*/
  fluxp=Ip/qe;
  Nli7=rho_li_nat/1000*c*c/(mli_atom*qe*1.0e6)*li7fraction; /* n cm-3*/

/*
dY/domega dEn=yoen =fluxp*Nli7*dsigma/domega'sigconv *epenconv /dedx *1e(-28)
   [unit]= n/sec/sr/MeV. [dedx]=MeV/mm
*/
  for (i=0;i<Sizeang;i=i+1) atheta[i]=atheta[i] *pi /180.;

  for (ii=0;aep[ii]<=EPMAX;ii=ii+1)
    {
    ep=aep[ii];
    a0=aa0[ii];
    a1=aa1[ii];
    a2=aa2[ii];
    a3=aa3[ii];
    dsigdo0pr=adsigdo0pr[ii];

    r_sq=mp*mn/mbe/(mbe+mn-mp)*ep/(ep-eth);
    r=sqrt(r_sq);
    dedx=stoppower(ep);

    ayep[ii]=fluxp*Nli7*adsigT[ii]/dedx*1.0e-28;

    for (i=0;i<Sizeang;i=i+1)
```

```
        {
          theta=atheta[i];
          koset_sq=1/r_sq-sin(theta)*sin(theta);
          koset=sqrt(koset_sq);
          thetapr=theta+asin(r*sin(theta));
          x=cos(thetapr);
          p0=1.;
          p1=x;
          p2=.5*(3*x*x-1);
          p3=.5*(5*x*x*x-3*x);

          dsigdopr = dsigdo0pr * (a0*p0+a1*p1+a2*p2+a3*p3);
          sigconv=r/koset*(cos(theta)+koset)*(cos(theta)+koset);
          dsigdo=dsigdopr*sigconv;
          yoep=fluxp*Nli7*dsigdo/dedx*1.0e-28;
          ayoep[ii][i]=yoep;

          x1=(mbe+mn)*(mbe+mn)*koset*ep;
          x2=cos(theta)+koset;
          x3=mp*mn*ep*koset*x2 + mbe*(mbe+mn-mp)*eth;
          epenconv=x1 / x2 / x3;

          /*yoen= fluxp*Nli7*dsigdo*epenconv/dedx*1.0e-28;*/
          yoen = yoep * epenconv;
          en=mp*mn/(mbe+mn)/(mbe+mn)*(cos(theta)+koset)*(cos(theta)+koset)*ep;

          ayoen[ii][i]=yoen;
          aen[ii][i]=en;
        }
      }

/* end of yield conversions: ayep, ayoep, ayoen
ayep: dy/dep, ayoep: d2y/domega/dep, ayoen: d2y/domega/den
"a" means "array"
*/
  printf ("yield conversions: ayep, ayoep, ayoen\n\n");

/* integrate for total yield using ayep*/

  y=0;
  for (ii=0;aep[ii]<EPMAX;ii=ii+1)
    {
    x=(ayep[ii] +ayep[ii+1])/2.;
    y=y+x*fabs(aep[ii]-aep[ii+1]);
    printf ("using ayep, yield = %10.3e, ep=%6.3f\n", y, aep[ii+1]);
    }


/* integrate for the total yield using ayoep. */

  y=0.; yy=0.;

  for (ii=0;aep[ii]<=EPMAX;ii=ii+1)
    {
```

```
  sum1[ii]=0.;

  for (i=0;i<(Sizeang-1);i=i+1)
   {
    xx=atheta[i];
    x=atheta[i+1];
    x1=(ayoep[ii][i]+ayoep[ii][i+1])/2.;

    sum1[ii]= sum1[ii]+x1*fabs(cos(x)-cos(xx))*2.*pi;
   }
  }


 for (ii=0;aep[ii]<EPMAX;ii=ii+1)
  {
  x1=(sum1[ii]+sum1[ii+1])/2.;
  y=y+x1*fabs(aep[ii] - aep[ii+1]);
  printf ("using ayoep, trapzoid integration, yield=%10.3e ep=%6.2f\n", y,aep[ii+1]);
  }

 printf ("integration by two steps. equivalent to trapzoid method \n");
 y=0.;

 for (ii=0;aep[ii]<EPMAX;ii=ii+1)
  {
  yy=0.;
    for (i=0;i<(Sizeang-1);i=i+1)
   {
    xx=atheta[i];
    x=atheta[i+1];
x1=(ayoep[ii][i]+ayoep[ii+1][i+1]+ayoep[ii][i+1]+ayoep[ii+1][i])/4.;
    yy= yy+x1*fabs(cos(x)-cos(xx))*2. *pi;
/*   printf ("yy=%7.3f theta=%7.3f\n", yy, xx*180./pi); */
   };
  y=y+yy*fabs(aep[ii]-aep[ii+1]);

  printf ("using ayoep, two step integration. yield=%10.3e ep=%6.2f\n", y,aep[ii+1]);
  }
 yield=y;

/*integrate for the total yield using ayoen*/
 y=0.; yy=0.;
 for (ii=0;aep[ii]<EPMAX;ii=ii+1)
  {
  yy=0.;
  for (i=0;i<(Sizeang-1);i=i+1)
   {
    xx=atheta[i];
    x=atheta[i+1];
    zz=aen[ii][i];
    z=aen[ii+1][i];
    x1=(ayoen[ii][i]+ayoen[ii+1][i+1]+ayoen[ii][i+1]+ayoen[ii+1][i])/4.;

    yy= yy+x1 * fabs( (cos(x)-cos(xx)) * (z-zz))* 2.*pi;
```

```
      };
    y=y+yy;
    printf ("using ayoen, yield=%10.3e enmax=%6.3f\n", y,z);

    }
  printf("\n\n");

  Fp_o=fopen(Filename_out, "w");

/* yield estimate for between eth and 1.95*/
  yeth_epmin=fabs(eth-aep[0]) * sum1[0] /2.;
  printf ("yield estimate y(Ep=1.881-1.95) = %10.3e, eth %6.3f, epmin %6.3f\n\n", yeth_epmin,
eth,aep[0]);

  /* output sdef for MCNP*/
  fprintf(Fp_o,"c
c   sdef for 7Li(p,n) at Ep=1.95-%4.1f MeV.\nc   \n",EPMAX);
  fprintf(Fp_o,"c   threshold=%6.3f  q= -%6.3f. \n", eth, q);
  fprintf(Fp_o,"c   Cross section data used:Lisken and Paulsen, 1975,
c   Atomic Data and Nuclear Data Tables 15,57-84.
c
c   7Li(p,n1) to the first excited state is in a separate sdef file,
c              for Ep>2.5 MeV.
c
c   Abundance of 0.925 of 7Li has been taken into account in the
c   total yield calculation. dE/dx for natural lithium metal.
c
c   dE/dx calculated from the empirical log formula with
c   best-fit parameters based on experimental data by
c   Anderson, Zeigler, Hydrogen, 'Stopping Powers and Ranges in All
c   Elements.' Pergamon Press, New York (1985).
c
c   The kinetics algorithm is taken from
c   Chad Lee, 'Thick Target Doubly Differential Neutron Yields for
c   the 7Li(pn) Reaction Near Threshold,' MIT, Oct.,1997. \nc   \n");
  fprintf(Fp_o,"c   The total yield
c   Y(1.95- %4.1f) = %10.2e n/uC. \nc   \n",EPMAX, yield);
  fprintf(Fp_o,"c   Assume Y(1.881)=0. and linear interpolat. between Y(1.95)
c   Y(1.881-1.95)= %10.2e n/uC. \nc   \n",yeth_epmin);
  fprintf(Fp_o,"c      --last updated by Haijun Song, %s. \nc   \n",DATE);
  fprintf(Fp_o,"sdef vec=0 1 0 dir=d11 erg=fdir d12
c   si-sp 1-10 are available for other parameters, e.g., surf, pos.
c   \n");

  j=0;
  fprintf(Fp_o,"si11 a ");
  for (i=(Sizeang-1);i>=0;i=i-1)
    {
    fprintf(Fp_o,"%10.6f",cos(atheta[i]));
    j=j+1;
    if (j%6==0 && i>0) fprintf(Fp_o,"\n      ");
    }
  fprintf(Fp_o,"\n");
```

```
for (i=(Sizeang-1);i>=0;i=i-1)
  {
  y=0;
  for (ii=0;aep[ii]<EPMAX;ii=ii+1)
    {
      x=(ayoep[ii][i]+ayoep[ii+1][i])/2.;
      y=y+x*fabs(aep[ii]-aep[ii+1]);
    }
  sum2[i]=y;
  }
j=0;
fprintf(Fp_o,"sp11   ");

printf ("\n absolute value of angular distribution\n");

for (i=(Sizeang-1);i>=0;i=i-1)
  {
  fprintf(Fp_o,"%10.6f", sum2[i]/sum2[0]);

  printf ("%6.2f %10.4e %10.6f\n", atheta[i]*180/pi, sum2[i], sum2[i]/sum2[0]);

  j=j+1;
  if (j%6==0 && i>0) fprintf(Fp_o,"\n       ");
  }
fprintf(Fp_o,"\nc    sp11 is normalized to angle = 0.\n");
j=0;
k=12;
fprintf(Fp_o,"ds12 q ");
for (i=(Sizeang-1);i>=0;i=i-1)
  {
  k=k+1;
  fprintf(Fp_o,"%10.6f %2d ",cos(atheta[i]), k);
  j=j+1;
  if (j%3==0 && i>0) fprintf(Fp_o,"\n       ");
  }
fprintf(Fp_o,"\n");

k=12;
for (i=(Sizeang-1);i>=0;i=i-1)
  {
  k=k+1;
  j=0;
  fprintf(Fp_o,"si%2d a ",k);
  for (ii=0;aep[ii]<=EPMAX;ii=ii+1)
    {
      fprintf(Fp_o,"%10.6f", aen[ii][i]);
      j=j+1;
      if (j%6==0 && aep[ii]<EPMAX) fprintf(Fp_o,"\n       ");
    }
  fprintf(Fp_o,"\n");

  j=0;
  fprintf(Fp_o,"sp%2d   ",k);
  for (ii=0;aep[ii]<=EPMAX;ii=ii+1)
```

```
        {
          fprintf(Fp_o,"%10.6f", ayoen[ii][i]/ayoen[0][i]);
          j=j+1;
          if (j%6==0 && aep[ii]<EPMAX) fprintf(Fp_o,"\n       ");
        }
      fprintf(Fp_o,"\n");
      }
  fprintf(Fp_o,"c    sp13-50 normalized to dy/domega/dEn at Ep=1.95 MeV.
c    end of source definition
c   \n");

}/**********************end**********************************/

/* stopping power for lithium metal, [stoppower]=MeV/mm, [Ep]=MeV*/
double stoppower (double ep)
{
  double a,b,a0,a1,a2,a3,a4,beta,massp, epk, sum,s,x,rho;
  a=.1328499;
  b=2.147e4;
  a0=-0.5831;
  a1=.562;
  a2=-.1183;
  a3=.009298;
  a4=-.0002498;
  massp=938.28;
  rho=.534;

  beta = sqrt(1.-1./(1.+ep/massp)/(1.+ep/massp));
  epk=ep*1000.; /* Ep in unit of KeV*/
  x=log(epk);
  sum= a0 +a1*x +a2*x*x +a3*x*x*x + a4*x*x*x*x;
  s=a*(log(b*beta*beta/(1.-beta*beta)) -beta*beta-sum)/beta/beta;
  s=fabs(s*rho/10.); /* unit MeV/mm*/
  return s;
}
```

```
/* MCNP sdef generator for 7Li(p,n1),1st excited state, Ep=2.5-4.1 MeV */
#include <stdio.h>
#include <math.h>
#define EPMAX 4.1
#define DATE "03/15/1998"
#define Filename_out "sdef.output"
#define c 2.997925e8
#define pi 3.14159265358979
#define avoga 6.022045e23
#define qe 1.602189e-19
#define mn 939.5735
#define mh 938.7910
#define mbe_atom 6536.2825
#define mli_atom 6535.4208
#define li7fraction .925
#define me 0.511 /* to get a more accurate value */
#define mp 938.2800
#define rho_li_nat 0.534 /* g/cm3*/
#define q 2.075
#define eth 2.373
#define Sizeang 38
#define Sizeep 30

  double stoppower(double);

main (void)
{
  int i,j,k,ii,jj,kk;
  double x,y,z,xx,yy,zz,x1,x2,x3,x4;
  double mli,mbe,Ip,fluxp, Nli7, ep, r, r_sq, koset, koset_sq, epenconv;
  double dsigdo, theta, yoen, en, dedx,yield, yeth_epmin;
  double atheta[Sizeang]=
    {0.,2.5,7.5,12.5,17.5,22.5,27.5,32.5,37.5,42.5,47.5,52.5,57.5,62.5,
    67.5,72.5,77.5,82.5,87.5,92.5,97.5,102.5,107.5,112.5,117.5,122.5,
    127.5,132.5,137.5,142.5,147.5,152.5,157.5,162.5,167.5,172.5,177.5,
    180.};
  double ayoen[Sizeep][Sizeang],aen[Sizeep][Sizeang];
  double a0,a1,a2,a3,dsigdo0pr,thetapr,dsigdopr,sigconv,p0,p1,p2,p3;
  double adsigdo_fromcom[Sizeep][Sizeang];
  double ayep[Sizeep],yoep, ayoep[Sizeep][Sizeang];
  double sum1[Sizeep], sum2[Sizeang];
  double aep[Sizeep]={2.5,2.6,2.7,2.8,2.9,3.0,3.1,3.2,
            3.3,3.4,3.5,3.6,3.7,3.8,3.9,4.0,4.1,4.2};
  double adsigdo0pr[Sizeep]={0.65,1.10,1.45,1.75,2.05,2.25,2.40,2.60,2.75,
              2.85,2.95,3.00,3.05,3.05,3.05,3.05,3.00};
  double aa0[Sizeep]={1.010,1.095,1.275,1.540,1.755,1.885,1.905,1.865,1.780,
            1.700,1.585,1.485,1.390,1.335,1.300,1.280,1.280};
  double aa1[Sizeep]={0.000,-.025,-.080,-.220,-.310,-.355,-.400,-.415,-.440,
            -.470,-.490,-.515,-.535,-.550,-.570,-.585,-.600};
  double aa2[Sizeep]={-.005,-.020,-.050,-.115,-.220,-.315,-.355,-.345,-.275,
            -.210,-.115,-.020,0.125,0.240,0.340,0.420,0.475};
  double aa3[Sizeep]={-.005,-.050,-.145,-.205,-.225,-.215,-.150,-.105,-.065,
            -.020,0.020,0.050,0.020,-.025,-.070,-.115,-.155};
  double adsigT[Sizeep]={8.0,15.0,23.0,33.5,45.0,53.0,58.0,61.0,61.0,60.5,
```

```
              58.5,55.5,53.5,51.5,50.0,49.0,48.0};
  FILE *Fp_o;

  mli=mli_atom-3*me; /*nuclide weight*/
  mbe=mbe_atom-4*me;
  printf ("threshold of reaction = %7.4f\n", eth);

  Ip=1e-6; /* for 1 uA of proton current*/
  fluxp=Ip/qe;
  Nli7=rho_li_nat/1000*c*c/(mli_atom*qe*1.0e6)*li7fraction; /* n cm-3*/

/*
dY/domega dEn=yoen =fluxp*Nli7*dsigma/domega'*sigconv*epenconv/dedx *1e(-28)
   [unit]= n/sec/sr/MeV. [dedx]=MeV/mm
*/
  for (i=0;i<Sizeang;i=i+1) atheta[i]=atheta[i] *pi /180.;

  for (ii=0;aep[ii]<=EPMAX;ii=ii+1)
    {
    ep=aep[ii];
    a0=aa0[ii];
    a1=aa1[ii];
    a2=aa2[ii];
    a3=aa3[ii];
    dsigdo0pr=adsigdo0pr[ii];

    r_sq=mp*mn/mbe/(mbe+mn-mp)*ep/(ep-eth);
    r=sqrt(r_sq);
    dedx=stoppower(ep);

    ayep[ii]=fluxp*Nli7*adsigT[ii]/dedx*1.0e-28;

    for (i=0;i<Sizeang;i=i+1)
      {
        theta=atheta[i];
        koset_sq=1/r_sq-sin(theta)*sin(theta);
        koset=sqrt(koset_sq);
        thetapr=theta+asin(r*sin(theta));
        x=cos(thetapr);
        p0=1.;
        p1=x;
        p2=.5*(3*x*x-1);
        p3=.5*(5*x*x*x-3*x);

        dsigdopr = dsigdo0pr * (a0*p0+a1*p1+a2*p2+a3*p3);
        sigconv=r/koset*(cos(theta)+koset)*(cos(theta)+koset);
        dsigdo=dsigdopr*sigconv;
        adsigdo_fromcom[ii][i]=dsigdo;
        yoep=fluxp*Nli7*dsigdo/dedx*1.0e-28;
        ayoep[ii][i]=yoep;

        x1=(mbe+mn)*(mbe+mn)*koset*ep;
        x2=cos(theta)+koset;
        x3=mp*mn*ep*koset*x2 + mbe*(mbe+mn-mp)*eth;
```

```
          epenconv=x1 / x2 / x3;

          yoen= fluxp*Nli7*dsigdo*epenconv/dedx*1.0e-28;
          /* or yoen = yoep * epenconv;*/
          en=mp*mn/(mbe+mn)/(mbe+mn)*(cos(theta)+koset)*(cos(theta)+koset)*ep;

          ayoen[ii][i]=yoen;
          aen[ii][i]=en;
        }
      }

/* compare the cross section and En conversion with lab data, also from
Liskien and Paulsen. 1975. */
  for (ii=0;aep[ii]<=4.1;ii=ii+1)
    {
    printf("ep=%4.2f \n",aep[ii]);

    for (i=0;i<=(Sizeang-1);i=i+1)
      {
        printf ("%9.2e ", adsigdo_fromcom[ii][i]);
      }
    printf("\ndsigdo above. \n\n");

    for (i=0;i<=(Sizeang-1);i=i+1)
      {
        printf ("%9.2e ", aen[ii][i]);
      }
    printf("\nEn above. \n\n");
    printf("\n\n");
    }


/* end of yield conversions: ayep, ayoep, ayoen
ayep: dy/dep, ayoep: d2y/domega/dep, ayoen: d2y/domega/den
"a" means "array"
*/
  printf ("yield conversions: ayep, ayoep, ayoen\n\n");

/* integrate for total yield using ayep*/

  y=0;
  for (ii=0;aep[ii]<EPMAX;ii=ii+1)
    {
    x=(ayep[ii] +ayep[ii+1])/2.;
    y=y+x*fabs(aep[ii]-aep[ii+1]);
    printf ("using ayep, yield = %10.3e, ep=%6.3f\n", y, aep[ii+1]);
    }


/* integrate for the total yield using ayoep. */

  y=0.; yy=0.;

  for (ii=0;aep[ii]<=EPMAX;ii=ii+1)
```

```
    {
    sum1[ii]=0.;

    for (i=0;i<(Sizeang-1);i=i+1)
      {
        xx=atheta[i];
        x=atheta[i+1];
        x1=(ayoep[ii][i]+ayoep[ii][i+1])/2.;

        sum1[ii]= sum1[ii]+x1*fabs(cos(x)-cos(xx))*2.*pi;
      }
    }


  for (ii=0;aep[ii]<EPMAX;ii=ii+1)
    {
    x1=(sum1[ii]+sum1[ii+1])/2.;
    y=y+x1*fabs(aep[ii] - aep[ii+1]);
    printf ("using ayoep, trapzoid integration, yield=%10.3e ep=%6.2f\n", y,aep[ii+1]);
    }

  printf ("integration by two steps. equivalent to trapzoid method \n");
  y=0.;

  for (ii=0;aep[ii]<EPMAX;ii=ii+1)
    {
    yy=0.;
        for (i=0;i<(Sizeang-1);i=i+1)
      {
        xx=atheta[i];
        x=atheta[i+1];
 x1=(ayoep[ii][i]+ayoep[ii+1][i+1]+ayoep[ii][i+1]+ayoep[ii+1][i])/4.;
        yy= yy+x1*fabs(cos(x)-cos(xx))*2. *pi;
/*      printf ("yy=%7.3f theta=%7.3f\n", yy, xx*180./pi); */
      };
    y=y+yy*fabs(aep[ii]-aep[ii+1]);

    printf ("using ayoep, two step integration. yield=%10.3e ep=%6.2f\n", y,aep[ii+1]);
    }
  yield=y;

/*integrate for the total yield using ayoen*/
  y=0.; yy=0.;
  for (ii=0;aep[ii]<EPMAX;ii=ii+1)
    {
    yy=0.;
    for (i=0;i<(Sizeang-1);i=i+1)
      {
        xx=atheta[i];
        x=atheta[i+1];
        zz=aen[ii][i];
        z=aen[ii+1][i];
        x1=(ayoen[ii][i]+ayoen[ii+1][i+1]+ayoen[ii][i+1]+ayoen[ii+1][i])/4.;
```

```
        yy= yy+x1 * fabs( (cos(x)-cos(xx)) * (z-zz))* 2.*pi;
      };
    y=y+yy;
    printf ("using ayoen, yield=%10.3e enmax=%6.3f\n", y,z);

    }
  printf("\n\n");

  Fp_o=fopen(Filename_out, "w");

/* yield estimate for between eth and 2.5 */
  yeth_epmin=fabs(eth-aep[0]) * sum1[0] /2.;
  printf ("yield estimate y(Ep=2.373-2.5 MeV) = %10.3e, eth %6.3f, epmin %6.3f\n\n", yeth_epmin,
eth,aep[0]);

  /* output sdef */
  fprintf(Fp_o,"c
c   sdef for 7Li(p,n1) at Ep=2.5-%4.1f MeV.\nc   \n",EPMAX);
  fprintf(Fp_o,"c   threshold=%6.3f  q= -%6.3f. \n", eth, q);
  fprintf(Fp_o,"c   Cross section data used:Lisken and Paulsen, 1975,
c   Atomic Data and Nuclear Data Tables 15,57-84.
c
c   7Li(p,n) to ground state state is in a separate sdef file.
c
c   Abundance of 0.925 of 7Li has been taken into account in the
c   total yield calculation. dE/dx for natural lithium metal.
c
c   dE/dx calculated from the empirical log formula with
c   best-fit parameters based on experimental data by
c   Anderson, Zeigler, Hydrogen, 'Stopping Powers and Ranges in All
c   Elements.' Pergamon Press, New York (1985).
c
c   The kinetics algorithm is taken from
c   Chad Lee, 'Thick Target Doubly Differential Neutron Yields for
c   the 7Li(pn) Reaction Near Threshold,' MIT, Oct.,1997. \nc   \n");
  fprintf(Fp_o,"c   The total yield
c   Y(2.5- %4.1f) = %10.2e n/uC. \nc   \n",EPMAX, yield);
  fprintf(Fp_o,"c   Assume Y(2.373)=0. and linear interpolat. between Y(2.5)
c   Y(2.373-2.5)= %10.2e n/uC. \nc   \n",yeth_epmin);
  fprintf(Fp_o,"c      --last updated by Haijun Song, %s. \nc   \n",DATE);
  fprintf(Fp_o,"sdef vec=0 1 0 dir=d11 erg=fdir d12
c   si-sp 1-10 are available for other parameters, e.g., surf, pos.
c   \n");

  j=0;
  fprintf(Fp_o,"si11 a ");
  for (i=(Sizeang-1);i>=0;i=i-1)
    {
    fprintf(Fp_o,"%10.6f",cos(atheta[i]));
    j=j+1;
    if (j%6==0 && i>0) fprintf(Fp_o,"\n       ");
    }
  fprintf(Fp_o,"\n");
```

```
for (i=(Sizeang-1);i>=0;i=i-1)
  {
  y=0;
  for (ii=0;aep[ii]<EPMAX;ii=ii+1)
    {
      x=(ayoep[ii][i]+ayoep[ii+1][i])/2.;
      y=y+x*fabs(aep[ii]-aep[ii+1]);
    }
  sum2[i]=y;
  }
j=0;
fprintf(Fp_o,"sp11   ");

printf ("\n absolute value of angular distribution\n");

for (i=(Sizeang-1);i>=0;i=i-1)
  {
  fprintf(Fp_o,"%10.6f", sum2[i]/sum2[0]);

  printf ("%6.2f %10.4e %10.6f\n", atheta[i]*180/pi, sum2[i], sum2[i]/sum2[0]);

  j=j+1;
  if (j%6==0 && i>0) fprintf(Fp_o,"\n       ");
  }
fprintf(Fp_o,"\nc    sp11 is normalized to angle = 0.\n");
j=0;
k=12;
fprintf(Fp_o,"ds12 q ");
for (i=(Sizeang-1);i>=0;i=i-1)
  {
  k=k+1;
  fprintf(Fp_o,"%10.6f %2d ",cos(atheta[i]), k);
  j=j+1;
  if (j%3==0 && i>0) fprintf(Fp_o,"\n       ");
  }
fprintf(Fp_o,"\n");

k=12;
for (i=(Sizeang-1);i>=0;i=i-1)
  {
  k=k+1;
  j=0;
  fprintf(Fp_o,"si%2d a ",k);
  for (ii=0;aep[ii]<=EPMAX;ii=ii+1)
    {
      fprintf(Fp_o,"%10.6f", aen[ii][i]);
      j=j+1;
      if (j%6==0 && aep[ii]<EPMAX) fprintf(Fp_o,"\n       ");
    }
  fprintf(Fp_o,"\n");

  j=0;
  fprintf(Fp_o,"sp%2d   ",k);
  for (ii=0;aep[ii]<=EPMAX;ii=ii+1)
```

```
      {
        fprintf(Fp_o,"%10.6f", ayoen[ii][i]/ayoen[0][i]);
        j=j+1;
        if (j%6==0 && aep[ii]<EPMAX) fprintf(Fp_o,"\n       ");
      }
    fprintf(Fp_o,"\n");
    }
  fprintf(Fp_o,"c    sp13-50 normalized to dy/domega/dEn at Ep=2.5 MeV.
c   end of source definition
c  \n");

}/***********************end************************************/

/* stopping power for lithium metal, [stoppower]=MeV/mm, [Ep]=MeV*/
double stoppower (double ep)
{
  double a,b,a0,a1,a2,a3,a4,beta,massp, epk, sum,s,x,rho;
  a=.1328499;
  b=2.147e4;
  a0=-0.5831;
  a1=.562;
  a2=-.1183;
  a3=.009298;
  a4=-.0002498;
  massp=938.28;
  rho=.534;

  beta = sqrt(1.-1./(1.+ep/massp)/(1.+ep/massp));
  epk=ep*1000.; /* Ep in unit of KeV*/
  x=log(epk);
  sum= a0 +a1*x +a2*x*x +a3*x*x*x + a4*x*x*x*x;
  s=a*(log(b*beta*beta/(1.-beta*beta)) -beta*beta-sum)/beta/beta;
  s=fabs(s*rho/10.); /* unit MeV/mm*/
  return s;
}
```

Appendix B
The MCNP Input File for the ^{9}Be(d,n) Reaction at E_d=1.5 MeV

```
June 24  1998
c   cell
1   1 -1.0 -1
2   1 -1.0 1 -2
3   1 -1.0 2 -3
4   1 -1.0 3 -4
5   1 -1.0 4 -5
6   1 -1.0 5 -6
7   1 -1.0 6 -7
8   1 -1.0 7 -8
9   1 -1.0 8 -9
10   1 -1.0 9 -10
11   1 -1.0 10 -11
12   1 -1.0 11 -12
13   1 -1.0 12 -13
14   1 -1.0 13 -14
15   1 -1.0 14 -15
16   1 -1.0 15 -16
17   0  16

c   surface
1   so 0.5
2   so 1.0
3   so 1.5
4   so 2.0
5   so 2.5
6   so 3.0
7   so 3.5
8   so 4.0
9   so 4.5
10   so 5.0
11   so 5.5
12   so 6.0
13   so 6.5
14   so 7.0
15   so 7.5
16   so 8.0

mode n p
print
c   Be(d,n) Ed=1.4 MeV yield read off curve of Wittlestone, 1976,
c        by HS, 6-16-98
c   The reference:
c        S. Wittlestone, "Neutron distributions from ...",
c            J. Phys. D:Appli. Phys., Vol. 10, 1977.
c   The yield has been integrated over angle.
c      The yield unit is : n/MeV/uC.
c       The values to be multiplied by 10e8.
c
sdef   erg=d11
si11 a   0.075 0.35 0.475 0.6 0.725 0.85 0.975 1.1
```

```
      1.225 1.35 1.475 1.6 1.725 1.85 1.975 2.1
      2.225 2.35 2.475 2.6 2.725 2.85 2.975 3.1
      3.225 3.35 3.475 3.6 3.725 3.85 3.975 4.1
      4.225 4.35 4.475 4.6 4.725 4.85 4.975 5.1
      5.225 5.35 5.475 5.6 5.725 5.85 5.975 6.1
sp11 d  6.5 4 2.625 0.375 0.75 0.625 0.5 0.5
      0.65 0.875 1.025 1.1 0.9 0.875 0.725 0.4375
      0.25 0.3125 0.4125 0.625 0.75 0.75 0.7375 0.6875
      0.6 0.55 0.55 0.625 0.875 1.0625 1.125 1.025
      1.0625 1.2375 1.3125 1.2875 1.1875 1.0625 0.875 0.725
      0.5625 0.4375 0.3375 0.25 0.1875 0.125 0.0625 0
c    END SOURCE DEFINITION
c
f4:p  1 2 3  4  5  6  7  8  9  10  11  12
      13  14  15  16
fc4  INDUCED PHOTON FLUX IN CELLS OF PHANTOM
de4  0.055 0.3 0.75 1.5 2.5 3.5 4.5 5.5 6.5
df4  7.42e-11 1.51e-10 3.82e-10 6.71e-10 9.63e-10
    1.21e-9 1.43e-9 1.64e-9 1.85e-9
f14:n  1  2 3  4  5  6  7  8  9  10  11  12
      13  14  15  16
fc14  FAST NEUTRON FLUX IN CELLS OF PHANTOM
c    BELOW FOR FAST NETRON DOSE
de14  0.35999e-06 0.36000e-06 0.63000e-06 0.11000e-05
     0.20000e-05 0.36000e-05 0.63000e-05 0.11000e-04
     0.20000e-04 0.36000e-04 0.63000e-04 0.11000e-03
     0.20000e-03 0.36000e-03 0.63000e-03 0.11000e-02
     0.20000e-02 0.36000e-02 0.63000e-02 0.11000e-01
     0.20000e-01 0.36000e-01 0.63000e-01 0.82000e-01
     0.86000e-01 0.90000e-01 0.94000e-01 0.98000e-01
     0.10500e+00 0.11500e+00 0.12500e+00 0.13500e+00
     0.14500e+00 0.15500e+00 0.16500e+00 0.17500e+00
     0.18500e+00 0.19500e+00 0.21000e+00 0.23000e+00
     0.25000e+00 0.27000e+00 0.29000e+00 0.31000e+00
     0.33000e+00 0.35000e+00 0.37000e+00 0.39000e+00
     0.42000e+00 0.46000e+00 0.50000e+00 0.54000e+00
     0.58000e+00 0.62000e+00 0.66000e+00 0.70000e+00
     0.74000e+00 0.78000e+00 0.82000e+00 0.86000e+00
     0.90000e+00 0.94000e+00 0.98000e+00 0.10500e+01
     0.11500e+01 0.12500e+01 0.13500e+01 0.14500e+01
     0.15500e+01 0.16500e+01 0.17500e+01 0.18500e+01
     0.19500e+01 0.21000e+01 0.23000e+01 0.25000e+01
     0.27000e+01 0.29000e+01 0.31000e+01 0.33000e+01
     0.35000e+01 0.37000e+01 0.39000e+01 0.42000e+01
     0.46000e+01 0.50000e+01 0.54000e+01 0.58000e+01
     0.62000e+01 0.66000e+01 0.70000e+01 0.74000e+01
     0.78000e+01 0.82000e+01 0.86000e+01 0.90000e+01
     0.94000e+01 0.98000e+01 0.10500e+02 0.11500e+02
     0.12500e+02 0.13500e+02 0.14500e+02 0.15500e+02
     0.16500e+02 0.17500e+02 0.18500e+02 0.19500e+02
     0.21000e+02 0.23000e+02 0.25000e+02 0.27000e+02
     0.29000e+02 0.29001e+02
df14    0.1e-40 0.39915e-11 0.30255e-11 0.22902e-11
     0.17185e-11 0.13008e-11 0.10200e-11 0.83822e-12
```

```
     0.74959e-12 0.78283e-12 0.96992e-12 0.13931e-11
     0.22914e-11 0.39420e-11 0.67553e-11 0.11681e-10
     0.21001e-10 0.37503e-10 0.64423e-10 0.10871e-09
     0.18933e-09 0.31302e-09 0.48604e-09 0.57658e-09
     0.60727e-09 0.62625e-09 0.64523e-09 0.66321e-09
     0.69460e-09 0.73741e-09 0.77801e-09 0.81664e-09
     0.85415e-09 0.88955e-09 0.92283e-09 0.95620e-09
     0.98633e-09 0.10165e-08 0.10608e-08 0.11171e-08
     0.11662e-08 0.12252e-08 0.12742e-08 0.13240e-08
     0.13649e-08 0.14184e-08 0.14663e-08 0.15349e-08
     0.16689e-08 0.16906e-08 0.16548e-08 0.17126e-08
     0.17716e-08 0.18332e-08 0.18948e-08 0.19537e-08
     0.20022e-08 0.20624e-08 0.21142e-08 0.21695e-08
     0.22364e-08 0.23410e-08 0.25239e-08 0.25592e-08
     0.25373e-08 0.26439e-08 0.27315e-08 0.27787e-08
     0.28538e-08 0.29648e-08 0.30038e-08 0.31285e-08
     0.31463e-08 0.32421e-08 0.32899e-08 0.34205e-08
     0.35717e-08 0.37110e-08 0.38390e-08 0.41820e-08
     0.42670e-08 0.43694e-08 0.43007e-08 0.44285e-08
     0.44386e-08 0.46851e-08 0.45749e-08 0.47860e-08
     0.49020e-08 0.50300e-08 0.52379e-08 0.55138e-08
     0.54495e-08 0.54063e-08 0.55679e-08 0.56697e-08
     0.57173e-08 0.58403e-08 0.59787e-08 0.63920e-08
     0.63770e-08 0.66125e-08 0.68648e-08 0.70318e-08
     0.70804e-08 0.72128e-08 0.73173e-08 0.74422e-08
     0.75855e-08 0.75641e-08 0.75124e-08 0.75391e-08
     0.74094e-08 0.1e-40
f24:n  1 2 3  4  5  6  7  8  9  10  11  12
      13  14  15  16
fc24  THERMAL NEUTRON FLUX IN PHANTOM CELLS
de24  0.25300e-07 0.36000e-07 0.63000e-07 0.11000e-06
     0.20000e-06 0.36000e-06 0.36001e-06
df24  0.14906e-10 0.12626e-10 0.95326e-11 0.72163e-11
     0.53570e-11 0.39915e-11 0.1e-40
f34:n  1 2  3  4  5  6  7  8  9  10  11  12
      13  14  15  16
fc34  BORON DOSE
de34  0.10e-8 0.1e-7 0.25e-7
     0.36000e-07 0.25100e-06 0.68400e-06
     0.18600e-05 0.50000e-05 0.13700e-04 0.37300e-04
     0.10100e-03 0.27500e-03 0.74900e-03 0.20300e-02
df34  1.7448e-9 0.5516e-9 3.4896e-10
     2.90800e-10 1.16800e-10 0.71200e-10
     0.43600e-10 2.62400e-11 1.60000e-11 0.93200e-11
     0.58800e-11 3.59600e-12 2.19200e-12 1.30800e-12
imp:n,p 1 15r 0
phys:p 10 1 0
m1   1001.50 -10.57 6012.50 -13.97 7014.50 -1.84
    8016.50 -72.59 11023.50 -0.14 15031.50 -0.39
    17000.50 -0.14 19000.50 -0.39
c   M1 IS BRAIN TISSUE
nps  1000000
```

```
c    ------------------------------------------------
c    ------------------------------------------------
c     If the f6 tally card is used to calculate the kerma
c         the tally cards are as follows.
c
c    END SOURCE DEFINITION
c
c    the tally part of the MCNP input file using the f6 tally for dose calculations.
f6:p  1 2 3  4  5  6  7  8  9 10 11 12
      13 14 15 16
fc6 induced photon dose, rad
fm6 1.602177e-8
c  fm6 converts f6 from MeV/g to rad
f16:n 1 2 3  4  5  6  7  8  9 10 11 12
      13 14 15 16
fc16 Dn separated by 0.36eV, rad
fm16 1.602177e-8
e16  0.36e-6 10
c    END OF TALLY CARDS
```

Appendix C
Algorithm for Operating the Angular Tilter

The angular tilter composes of two slanting disks, Disks 1 and 2, grinding against each other, as shown in Figure C.1. Either disk can be used for mounting an application device. In here, Disk1 in fixed solidly to the accelerator beam tube and Disk 2 is for mounting the needle tube Prototype II, as described in Chapter Six. The slanting angle is 5° (Figure C.1.a and b).

The axis of Disk 1 makes an angle, θ_0, of 5° with the beam line (Figure C.1.b). With the turning of the disk along the φ angle, φ_1, the axis makes a cone of 5° around the beam line. On a (θ,φ) diagram, where θ is the radius and φ is the angle, the trajectory is a circle with $\theta = \theta_0$. On the (θ,φ) diagram, the trajectories of the axis (which is also angular position of the needle tub Prototype II) of Disk 2 are circles with a radius of θ_0 centered on the circumference of the axis trajectory circle of Disk 1. With the turning of both Disks 1 and 2 along the φ angle, φ_1 and φ_2, the superimposed angular position fills a $\theta=2\theta_0=10°$ circle, which corresponds to a 10° cone along the beam line, as shown in Figure C.1.b and C.1.c.

The relation between the superimposed angular position, θ and φ, the slanting angle, θ_0, and turning of the two disks, φ_1 and φ_2, is illustrated in Figure C.1.d. Note in use with the Prototype II, $(\varphi_1 - \varphi_2)$ is close to 180° so that the net deviation from the beam line is small. The coordinates of the superimposition are

$$\theta_0 (\cos\varphi_1 + \cos\varphi_2,\ \sin\varphi_1 + \sin\varphi_2)$$

in a Cartesian reference frame. Thus,

$$\begin{aligned} \theta/\theta_0 &= [(\cos\varphi_1 + \cos\varphi_2)^2 + (\sin\varphi_1 + \sin\varphi_2)^2]^{1/2} \\ &= [4 \cos^2 \frac{\varphi_1 - \varphi_2}{2}]^{1/2} \\ &= 2 \|\cos \frac{\varphi_1 - \varphi_2}{2}\|. \qquad \text{(C.1)} \\ \tan\varphi &= (\sin\varphi_1 + \sin\varphi_2) / (\cos\varphi_1 + \cos\varphi_2) \\ &= \tan \frac{\varphi_1 + \varphi_2}{2}, \end{aligned}$$

which follows that

$$\varphi = \frac{\varphi_1 + \varphi_2}{2}. \qquad \text{(C.2)}$$

Equations (C.1) and (C.2) can be rewritten as

$$\begin{aligned} \theta &= \theta_0 2 \|\sin \frac{\varphi_1 - \varphi_2^*}{2}\|, \\ &= \theta_0 \|\varphi_1 - \varphi_2^*\| \qquad \text{(C.3)} \\ \varphi &= \frac{\varphi_1 + \varphi_2^*}{2} + \pi/2, \qquad \text{(C.4)} \end{aligned}$$

where φ_2^* is defined as $\varphi_2^* = \varphi_2 - 180°$. Since $(\varphi_1 - \varphi_2)$ is close to 180°, $(\varphi_1 - \varphi_2^*)$ is close to 0°.

The variations of the angular position, $\delta\theta$ and $\delta\varphi$, as a function of the turning, $\delta\varphi_1$ and $\delta\varphi_2^*$ ($\delta\varphi_2$), of the slanting disks are

$$\delta\theta = \theta_0 \ \mathrm{sign}(\varphi_1 - \varphi_2^*) \, (\delta\varphi_1 - \delta\varphi_2^*), \tag{C.5}$$

$$\delta\varphi = \tfrac{1}{2} \, (\delta\varphi_1 + \delta\varphi_2^*). \tag{C.6}$$

Motion in the two orthogonal θ and φ directions can be independently achieved by turning the two slanting disks by the same amount but with different combinations of turning directions. Same sign in $\delta\varphi_1$ and $\delta\varphi_2^*$ results in motion in the φ but not θ direction; opposite sign in $\delta\varphi_1$ and $\delta\varphi_2^*$ results in motion in the θ but not φ direction. Other modes (combinations of turning angles and directions) of motion are also possible.

The slanting disks take around 2180 steps of the step motor to complete a 360° turn.

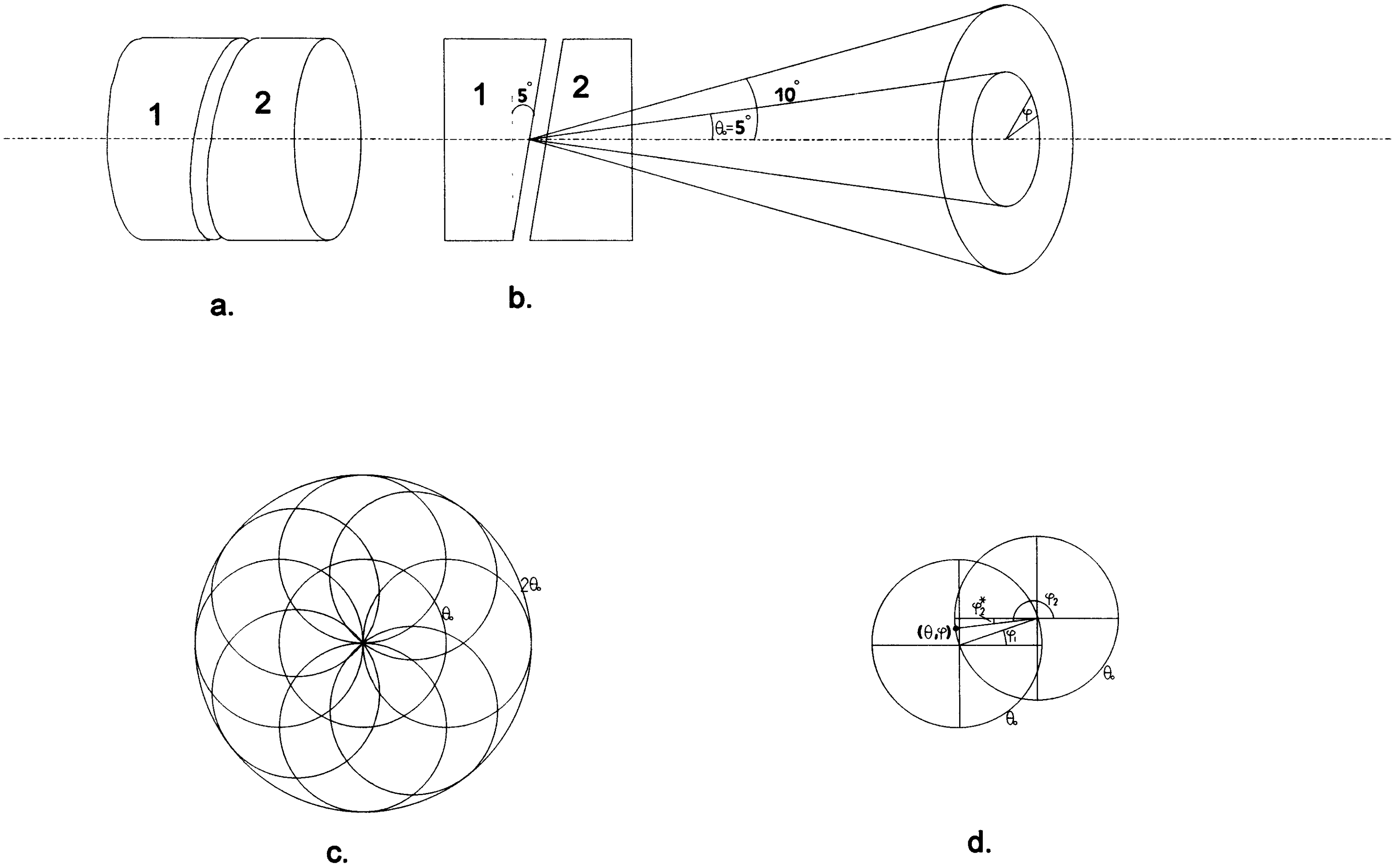

Figure C.1. Demonstration of operation of the angular tilter.

Appendix D
Heat Transfer Analysis

D.1. HEAT TRANSFER FORMULAE

Consider a simplified heat transfer system as shown in Figure D.1. The target is wrapped in a perfect thermal insulator except two surfaces, one exposed to vacuum and the other to a cooling water flow. The vacuum surface is bombarded by an ion beam and a heat load, P, is generated within a very thin layer. A uniform heat flux, q ($=P/A_t$, A_t is the cross section of the target), flows from the vacuum surface to the water surface through heat conduction and to the cooling water through heat transfer across the target-water surface. The temperature, T_{target}, is measured inside the target with a thermocouple.

The two constraints are heat transfer failure along the target-water surface and melting of the target. The heat transfer across the target-water surface is the bottle neck of heat removal from the target. The melting of the target can be checked by making sure the hottest spot in the target, which is the vacuum surface, is lower than the melting point of the target.

The heat conduction within the target is governed by

$$q = -k\, dT/dl\,, \qquad \text{(D.1)}$$

where k is the thermal conductivity of the target, dT/dl is the temperature gradient in the target.

The heat transfer between the target and the cooling water across the target-water surface is governed by the Newton's law of cooling as

$$q_{tw}=h_{tw}\,(T_{tw} - T_b), \qquad \text{(D.2)}$$

where q_{tw} denotes the heat flux across the target-water surface (and in the present model equals the heat flux, q, in the target), h_{tw} the heat transfer coefficient, T_{tw} the temperature on the target-water surface, and T_b the bulk temperature of the cooling water.

The heat transfer coefficient can be calculated with the Dittus-Boelter empirical formula:

$$Nu = 0.023\, Re^{0.8}\, Pr^{0.4}, \qquad \text{(D.3)}$$

where Nu, Re, and Pr are called the Nusselt, Reynolds, and Prandtl numbers respectively and their definitions are to follow. Formula (D.3) is applicable to a fully developed turbulent flow in a smooth tube for liquids with a Prandtl number between 0.6 and 100, and moderate temperature difference between the tube wall and the fluid. The parameters are all evaluated at the bulk temperature.

The Prandtl number is

$$Pr = C_b\, \mu_b / k_b, \qquad \text{(D.4)}$$

where C_b is the specific heat, μ_b the viscosity, and k_b the thermal conductivity of the cooling water.

The Reynolds number is

$$Re = \rho_b\, v_b\, D_h / \mu_b, \qquad \text{(D.5)}$$

where ρ_b is the density of the cooling water, v_b the velocity of the cooling flow at the target-water surface, and D_h is the hydraulic diameter and is defined for the cross section of the cooling flow with an area of A_b as

$$D_h = 4A_b / (\text{wetted perimeter of } A_b). \qquad \text{(D.6)}$$

Finally, the Nusselt number is defined as

$$Nu = h_{tw} D_h / k_b. \qquad (D.7)$$

The following are properties of water, at 20 °C.

C_b=4.2 e3 J/(kg °C), specific heat,
ρ_b=997 kg/m^3, density,
μ_b=9.8 e-4 kg/(m s), viscosity, and
k_b=0.6 W/(m°C), thermal conductivity.

The saturation temperature of water is 100 °C under 1 atmosphere pressure, 121 °C under 2 atmospheres, and 133 °C under 3 atmospheres.

Heat transfer theory predicts that, at low heat flux, the heat transfer across the target-water surface is by single phase convection and the target surface temperature, hence T_{tw}, should increase linearly with heat load for a constant h_{tw}. When the surface is higher but for water within around 5 °C of the saturation temperature of the coolant, nucleation is initiated and two phase heat transfer occurs. This will initially result in improved heat transfer so that the surface temperature and hence T_{tw} will increase with heat flux at less than a linear rate. However, for sufficiently high heat fluxes, a limiting value will be reached, the critical heat flux, a condition under which heat transfer deteriorate.

The critical heat flux (CHF) for water boiling on a platinum wire was demonstrated to be a weak function of water pressure: CHF is between 2-5 MW/m^2 under pressure of 1 to 100 atmosphere (Holman, (1981)). Lekakh, (1996) gives CHF as a function of flow velocity (above 1 m/s) under pressures above 10 atmosphere. The cooling flow velocity near the targets used in the heat removal experiments was 0.7 m/s for Prototype I and 0.3 m/s for Prototype II. The CHF values extrapolated from the curves of Lekakh, (1996) are both around 8 MW/ m^2.

D.2. APPLICATION TO PROTOTYPE I

The heat removal of the target in Prototype I, as described in Chapter Five, is similar to the heat transfer system discussed above. The highest heat load achieved experimentally with this prototype is 38 Watts. The tip portion of Prototype I with details of the copper target and cooling channel is shown in Figure D.2. The heat transfer analysis will be performed in the copper target and along the line (the reference line) on the target-water surface across the center and perpendicular to the cooling flow (Figure D.2). Labels and parameters are listed as follows.

A_t=π/4 2.5^2 mm^2 = 4.91e-6 m^2, target cross section.
A_{tw}=π(3.0^2/4+3.0x0.5) mm^2 = 11.8e-6 m^2, copper in contact with water.
A_b=3x6 mm^2 = 18e-6 m^2, flow cross section (b stands for bulk) at the reference line.
k_{Cu}=380 W/(m °C), averaged thermal conductivity of copper between 0-200 °C.
k_{Be} =~ 200 W/(m °C), approximate thermal conductivity of beryllium between 0-300 °C.
k_{teflon} =2.25 W/(m °C) at 25 °C and 2.5 W/(m °C) at 230 °C.
f= 0.8 l/min = 13.33 e-6 m^3/s, cooling water flow.

Pressure of the cooling water is 1 atmosphere and the saturation temperature is 100 °C.

D.2.1. Bulk Temperature

The temperatures of the cooling water inlet and outlet, T_{bin} (20 °C, given) and T_{bout}, change at the highest head load of 38 Watts by

$$T_{bout} - T_{bin} = P/(\rho_b f C_b) = 0.7 \text{ °C}.$$

Since the change is small, the bulk temperature, T_b, of the cooling water is assumed to be constant at 20 °C.

D.2.2. Reynolds Number

The velocity, v_b, of the cooling flow at the reference line is

$$v_b = f/A_b = 0.741 \text{ m/s}.$$

The hydraulic diameter, D_h, is

$$D = 4A_b/(\text{wetted perimeter of } A_b) = 4\text{e-}3 \text{ m}.$$

The Reynolds number, Re, is

$$Re = \rho_b v_b D_h / \mu_b = 3015,$$

which indicates a turbulent flow.

D.2.3. Prandtl Number

The Prandtl number is

$$Pr = C_b \mu_b / k_b = 6.9.$$

D.2.4. Nusselt Number

The Dittus-Boelter empirical formula (D.3) gives:

$$Nu = 0.023 \, Re^{0.8} \, Pr^{0.4} = 30.$$

D.2.5. Heat Transfer Analysis

From the definition of the Nusselt (D.7), the heat transfer coefficient for a one-phase convection is calculated as

$$h_{Nu} = Nu \, k_b / D_h = 4.5 \text{ e}3 \text{ W/(m}^2 \text{ °C)}.$$

The subscription of Nu to the heat transfer coefficient is to identify it is calculated from the Nusselt number. This value is consistent with the 3500 W/(m^2 °C) value listed for forced convection flow, see e.g., Holman, (1981).

The heat coefficient, h_{tw} (subscription tw to distinguish from h_{Nu}), can also be calculated from the heat transfer equation (D.2) as

$$h_{tw} = q_{tw} / (T_{tw} - T_b).$$

If the power, P, of 38 Watts generated on the target-vacuum surface flows uniformly to the cooling water (i.e., assuming perfect thermal insulation of the teflon sleeve, which is a poor thermal conductor),

$$q_{tw} = P/A_{tw} = 3.22 \text{ e}6 \text{ W/m}^2.$$

(As will be discussed below, the teflon sleeve likely conducts a substantial heat flux due to its thin thickness and the heat flux on the target-water surface should be substantially smaller than the value given above. For comparison, the critical heat flux is estimated to be 8 e6 W/m^2 in Section D.1.) The maximum temperature difference between T_{tw} and T_b is (120-20)°C or 100 °C. So, a lower estimate for h_{tw} is

$$h_{tw} > q_{tw}/100 \text{ °C} = 3.22 \text{ e}4 \text{ W/(m}^2 \text{ °C)}.$$

This is an order of magnitude higher than the 3500 W/(m^2 °C) for the one-phase forced convection regime, but falls in the range of heat transfer coefficients for boiling water flowing in a tube, 5 e3 - 1 e5 W/(m^2 °C) (e.g., Holman, (1981)). If the heat transfer along the target-water surface is by two phase, T_{tw} should be slightly (~5 °C) above 100 °C, the saturation temperature of the cooling water.

Heat conduction calculation in the copper target gives another estimate of T_{tw} from the measured T_{target} (Figure D.2) as

$$T_{tw} = T_{target} - P/A_t\,(l_1/k_{Cu}) - P/A_{tw}\,(l_2/k_{Cu}) = 120 - 40.7 - 4.2 = 75\ °C, \tag{D.8}$$

where l_1 and l_2 (2.0 and 0.5 mm) are the distances between where T_{target} is measured, where the target turns into the shoulder (from diameter 2.5 mm to 3.0 mm), and the target-water surface. This T_{tw} value of 75 °C means that the heat transfer is one phase convection at the heat load of 38 watts.

The contradiction between the one phase and two phase heat transfer could be resolved by either of the following two speculations.

First, T_{target} is measured closer to the target-water surface than it is intended to be. The thermocouple T_{target} was inserted into the 2.5 mm deep hole in the bottom of the copper target and soldered. During the attaching process, the thermocouple might not stay at the deepest position as it is intended to be. If the thermocouple reached only half of the depth of the hole (1.25 mm), T_{tw} would be close to 100 °C according to formula (D.8), assuming still that the teflon sleeve is a perfect thermal insulator.

Second, despite the fact that teflon is a good thermal insulator, the thin thickness may still allow it to be a competitor of heat conduction to copper. The heat flux may still start high from the vacuum surface, which generates a high temperature gradient near the vacuum surface. Spreading out as it flows from the vacuum surface to the cooling water, the heat flux decreases and may be substantially smaller than P/A_t or P/A_{tw} between T_{target} and the water surface. For example, if the heat flux between where T_{target} is measured and the target-water surface is reduce by half, T_{tw} will be 98 °C at the heat load of 38 watts.

Under either of the above two situations, the temperature is close to 100 °C on the target-water surface, and the heat transfer along the surface is likely by two phase at the heat load of 38 watts. The boiling, or nucleation on the target-water surface, would be very localized and does not cause measurable changes in the bulk temperature when the resulting steam bubbles are condensed by the cooling flow. This is called the subcooled nucleate boiling heat transfer regime. The thermocouple T_{liquid} reads the same as the bulk temperature probably because it is not close enough to the target-water surface.

Let us examine the first speculation of mislocation of the target thermocouple but perfect thermal insulation of the teflon sleeve. For this case, the power, $P_{trans,}$ on the target when the transition from one phase to two phase heat transfer occurs, is estimated as

$$P_{trans} =\sim A_{tw}\, h_{Nu}\, 100\ °C = 5.3\ W.$$

At the heat load of $P_{trans,}$ T_{tw} should be slightly (5 °C) above 100 °C. And $T_{target,}$ which is higher than T_{tw}, should be higher than 100 °C. However, at this heat load, T_{target} reads only 33 °C, as shown in Figure D.3. (redrawn from Figure 5.4.) Therefore, the second speculation seems to be more likely.

D.2.6. Highest Temperature In Target

The hottest spot is the vacuum surface of the copper target where the power is generated by the ion beam. From the heat conduction equation (D.1) and the temperature measured with the thermocouple, $T_{target,}$ the temperature on the vacuum surface is calculated as

$$T_{tv} = T_{target} + P/A_t\ dl/k_{Cu} = 146\ °C, \text{ at } P = 38\ W,$$

where d*l* is the distance between the vacuum surface and where T_{target} is measured.

For a beryllium target of identical dimensions of the copper target under the same cooling conditions, the heat transfer on the target-water surface will be the same. The temperature gradient in the beryllium target will be larger since the thermal conductivity of beryllium of around 200 W/(m °C) is lower than that of copper. Starting from 100 °C on the target-water surface, the temperature on the vacuum surface of such a beryllium target is calculated to be

$$T_{tv} = 100\ °C + P/A_t\ dl/k_{Cu} = 247\ °C, \text{ at } P = 38\ W,$$

where d*l* is the length of the target.

D.2.7. Conclusions

The most likely conclusions from the heat transfer analysis on Prototype I are as follows. The thermocouple T_{target} is located in the design position. The thin thickness of the teflon sleeve overcompensates its poor thermal conductivity and conducts a substantial amount of the heat flux. As a result, the heat flux is small close to the target-water surface in the target and so is temperature gradient. The target-water surface temperature, T_{tw}, thus follows very closely to $T_{target.}$ The transition from one phase to two phase heat transfer occurs shortly after T_{target} and hence T_{tw} passes 100 °C. At the maximum heat load of 38 watts achieved with Prototype I, the heat transfer has passed the transition from one phase to two phase heat transfer and is in the subcooled nucleate boiling regime.

The estimated range of T_{tw} is shown in Figure D.3. The lower limit is calculated assuming the teflon is a perfect thermal insulator. The upper limit is based on the reasoning that T_{tw} follows closely to T_{target} up to around 105 °C and flattens and is shown in the shaded triangle in Figure D.3., which is the uncertainty of how close they are.

The highest temperature in the copper target is 146 °C.

D.3. APPLICATION TO PROTOTYPE II

The target in Prototype II is a tube shaped, as shown in Figure D.4. (redrawn from Figure 6.3). A copper and beryllium target was made of the same dimensions. T_{target} of the copper target was 142 °C at maximum tested heat load, P_{max}, of 150 Watts. T_{target} of the beryllium was 220 °C at a P_{max} of 130 Watts. The tests on the two targets were under different cooling flows: 1.4 l/min, 30 °C, and 2 atmospheres of pressure for the copper target and 1.4 l/min, 23 °C, and 3 atmospheres of pressure for the beryllium target. The bulk temperature change is calculated to be 1.5 °C at the heat load of 150 Watts. So the cooling water bulk temperatures are treated as constant. The heat load is generated at the bottom of the tube, the heating spot. The temperature, T_{tv}, is the highest temperature in the target. The total target surface area in contact with the cooling water is

$$A_{total} = \pi\,(0.148^2/4 + 0.148 \times 0.65)\ \text{inch}^2 = 206\ \text{e-6 m}^2 .$$

The average of the total heat load over the total target area, the average heat flux, is

$$q_{avg} = P_{max}/A_{total}.$$

The numbers are 0.7 e6 W/ m^2 for 150 Watts and 0.6 e6 W/ m^2 for 130 Watts. (For comparison, the critical heat flux is estimated to be 8 e6 W/ m^2 in Section D.1.) The highest heat flux along the target-water surface should occur close to the heating spot and could be many times higher than the average flux given above. For convenience, this is called the hot zone, as shown shaded in Figure D.4. The average heat transfer coefficient across the target-water surface is

$$h_{avg} = q_{avg}/(T_{tw} - T_b) > h_{avg.min} = q_{avg}/(T_{sat} - T_b),$$

where T_{sat} is the saturation temperature of the cooling water and $h_{avg.min}$ is the minimum average heat transfer coefficient. The minimum average heat transfer coefficients are calculated to be 8.0 e3 W/(m^2 °C) for the copper target at 150 Watts of heat load and 5.7 e3 W/(m^2 °C) for the beryllium target at 130 Watts of heat load. The two heat transfer coefficients are still higher than a typical value of one-phase convection. It is thus concluded that the heat transfer in the hot zone is by two-phase at the heat load of 130 Watts. Since the bulk temperature change is small, the heat transfer is likely in the subcooled nucleate regime. The heat transfer across the target-water surface close to the teflon sleeve is by one-phase as indicated by the low temperature (40 °C) measured with thermocouple T_2 for both the copper and beryllium targets.

The distances between the heating spot, T_{target}, and the hot zone are roughly equal. One estimate of the temperature at the heating spot, T_{tv}, is given by

$$T_{tv} = 2 \times (T_{target} - T_{sat}) + T_{sat}.$$

This yields 163 °C for the copper target (150 Watts of heat load) and 307 °C for the beryllium target (130 Watts) under the two cooling conditions respectively.

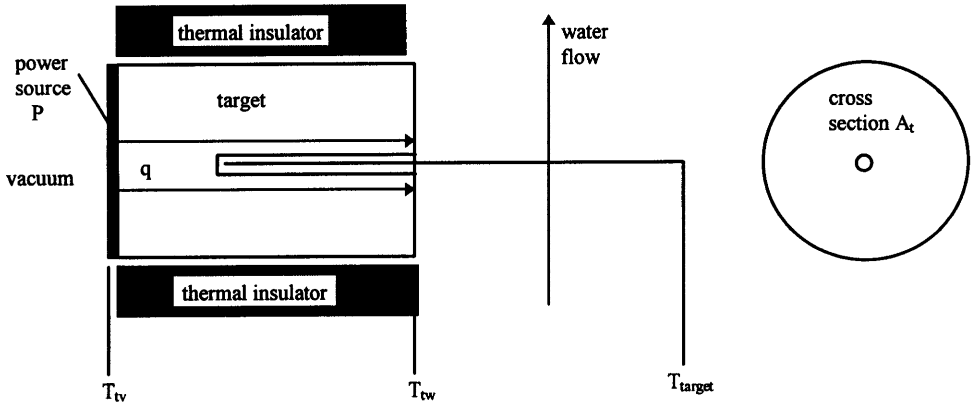

Figure D.1. A heat transfer system.

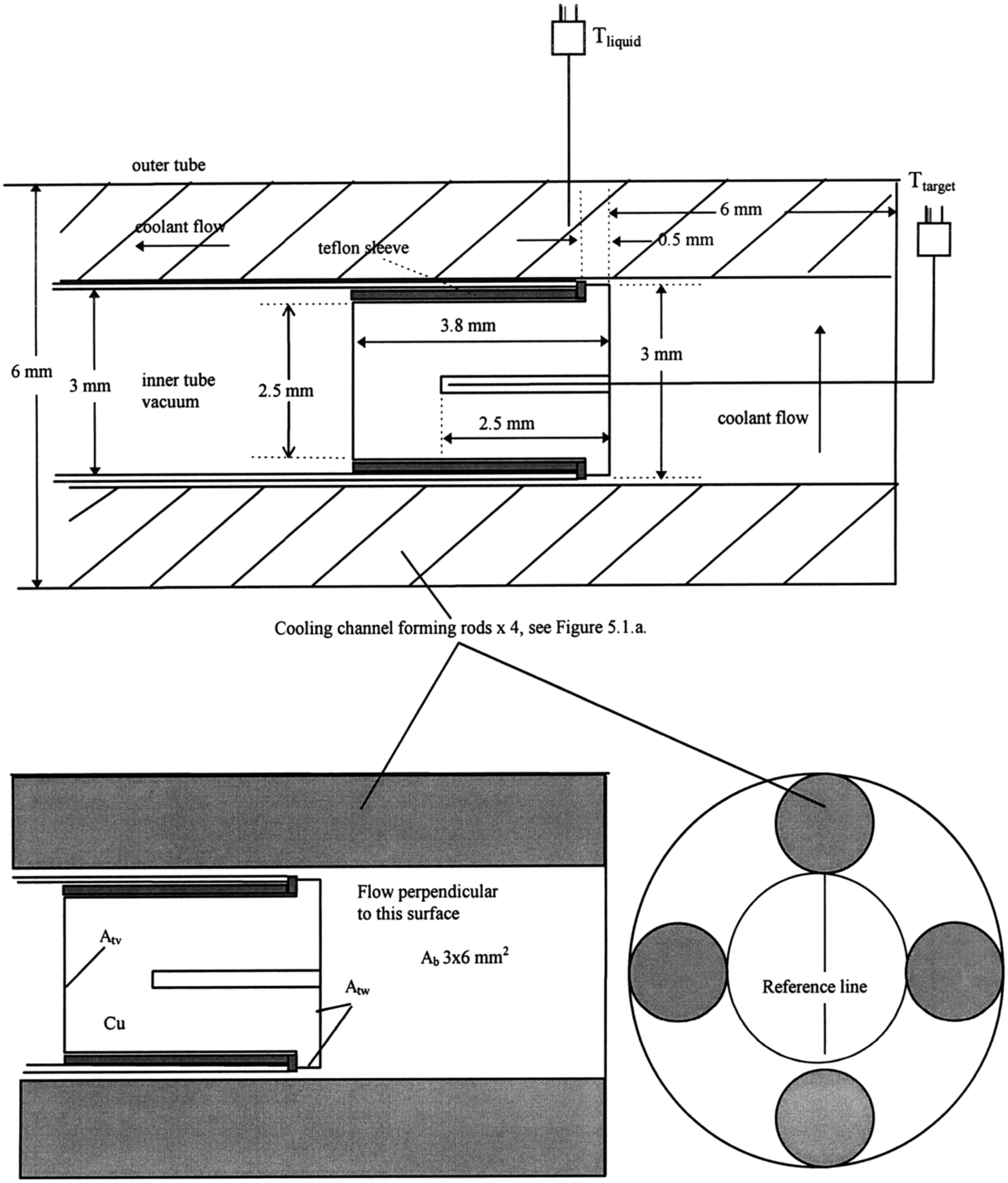

Three areas are shown: A_b, cross section of the cooling flow; A_t, cross section of the copper target body; and A_{tw}, copper in contact with water. Subscription "b" stands for bulk, i.e., the coolant water.

Figure D.2. Schematic of the tip portion of the needle tube Prototype I. The lower part explains some parameters used in the heat transfer calculations.

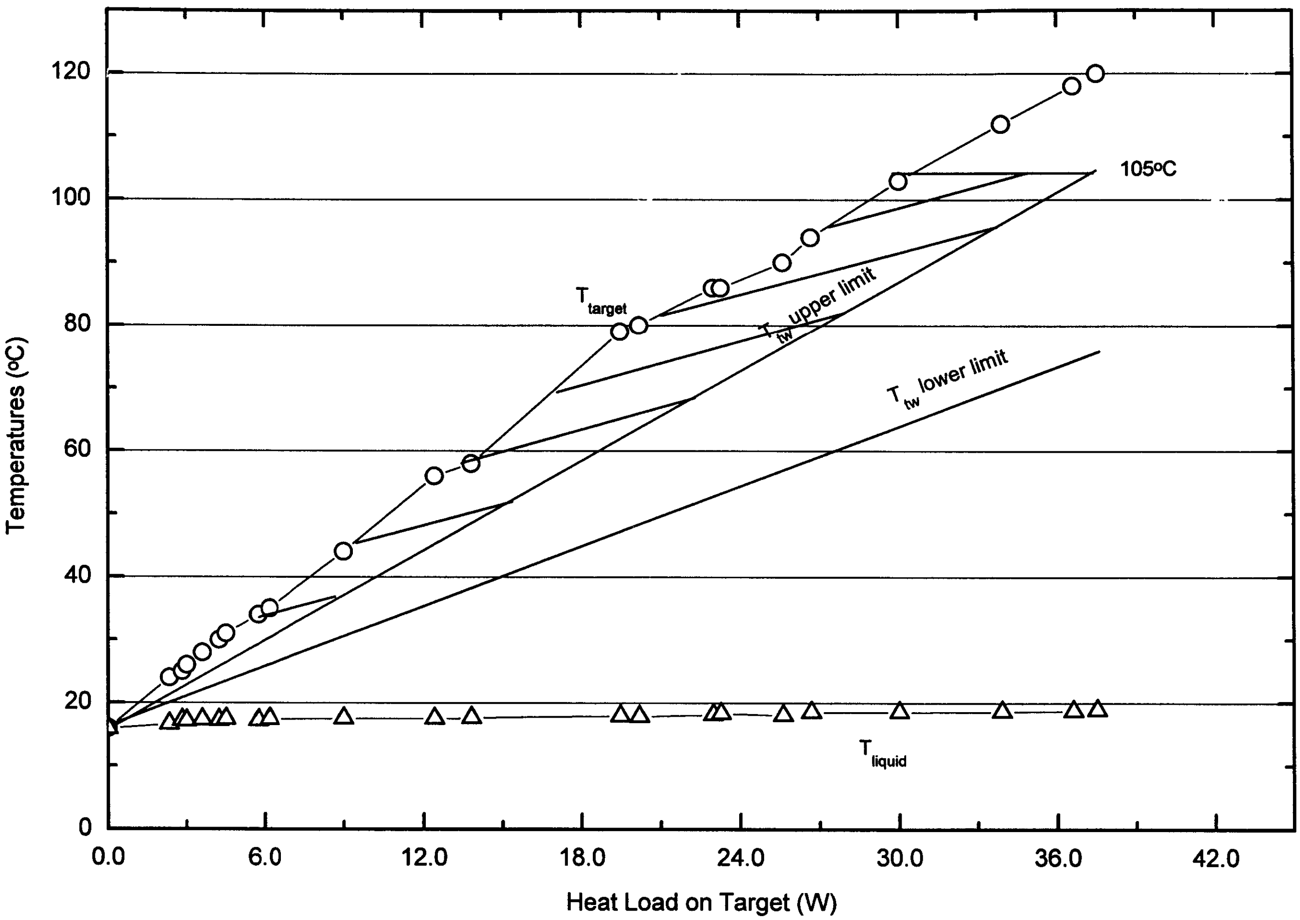

Figure D.3. Temperatures as a function of heat load on target in prototype I. T_{target} and T_{liquid} are measured at locations indicated in Figure D.2. The lower and upper limits of the target-surface temperature, T_{tw}, are shown (see text).

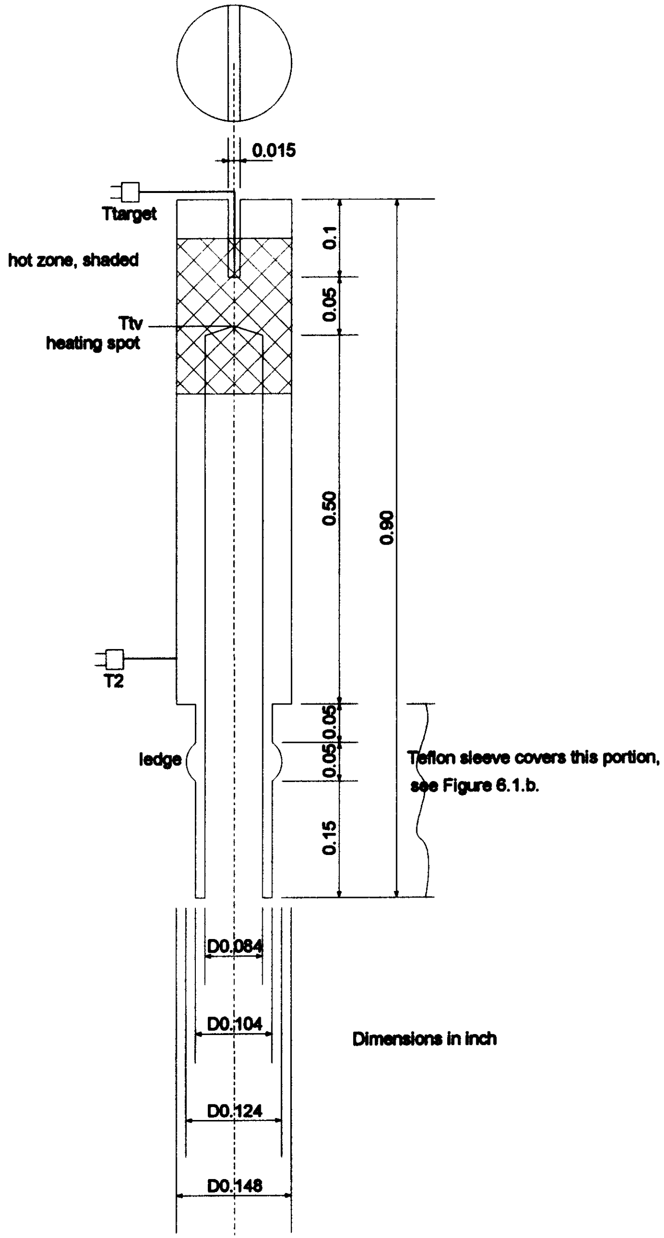

Figure D.4. The Cu and Be target dimensions with symbols for heat transfer analysis.

Appendix E
Dependence of the Effective Center of a Dosimeter on the Gradient of a Radiation Field

Consider the measurement of a radiation field, $D(\vec{r})$, with a dosimeter of a sensitive volume, V. The dose measurement taken with this dosimeter is an average of the dose within the sensitive volume. In attempt to represent the averaged value in the volume, V, with a single point, the effective point, $\vec{r}_{eff}$, is defined as

$$D(\vec{r}_{eff}) = \frac{\int_V D(\vec{r})d\vec{r}}{V} \quad . \tag{E.1}$$

The relations are illustrated in Figure E.1 for the x dimension. The dosimeter's sensitive volume covers from x_0 to x_1 in the x direction. For two different dose distributions, D_1 and D_2, the effective centers, x_{eff1} and x_{eff2}, are different and may both be away from the geometrical center of the dosimeter, x_G. There are situations when the three points converge into one, e.g., a uniform field or a dose distribution linear with coordinates. But generally these three points are different. Theoretically, the distance between the effective point and the geometric center can be up to the size of the detector. For a "smooth" radiation field, they are close. This demonstrates that the effective point is dependent on the gradient of the radiation field and is not a characteristic of the detector alone. It is rather for convenience to call the geometrical center of a dosimeter the "effective center".

However, it is not surprising that the spatial resolution of a dose measurement is the same as the size of the dosimeter.

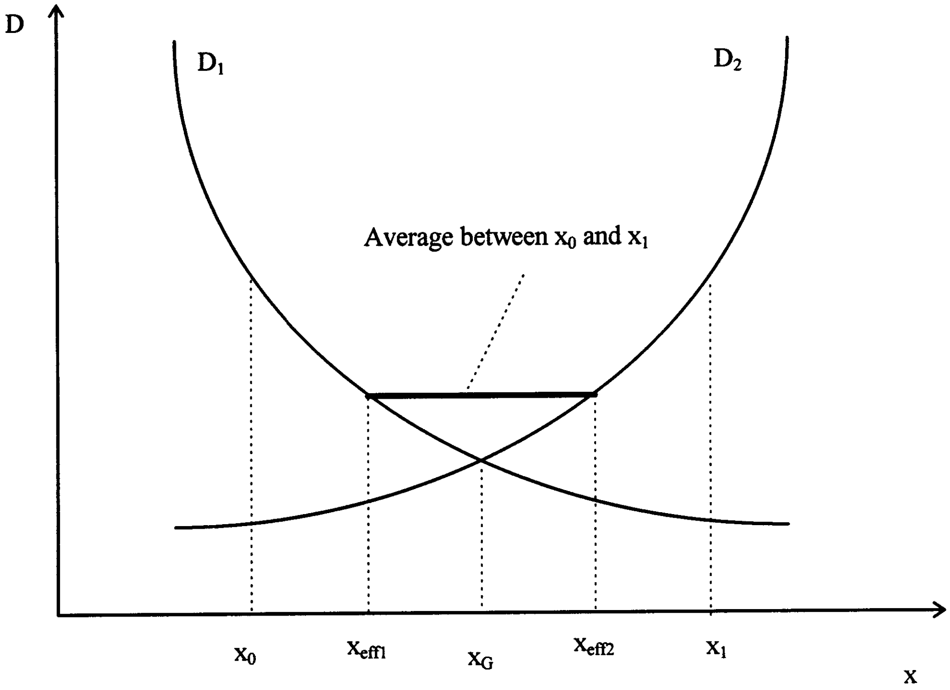

Figure E.1. Illustration of the dependence of the effective center of a dosimeter on the gradient of a radiation field.